CARBON NANOTUBE REINFORCED POLYACRYLONITRILE AND POLY(ETHERKETONE) FIBERS

A Dissertation
Presented to
The Academic Faculty

By

Rahul Jain

In Partial Fulfillment
Of the Requirements for the Degree
Doctor of Philosophy in Polymer, Textile and Fiber Engineering

Georgia Institute of Technology
ATLANTA, GEORGIA

May, 2009

CARBON NANOTUBE REINFORCED POLYACRYLONITRILE AND POLY(ETHERKETONE) FIBERS

Approved by:

Dr. Satish Kumar, Advisor
School of Polymer, Textile, and Fiber Engineering
Georgia Institute of Technology

Dr. Meisha Shofner
School of Polymer, Textile, and Fiber Engineering
Georgia Institute of Technology

Dr. Anselm Griffin
School of Polymer, Textile, and Fiber Engineering
Georgia Institute of Technology

Dr. Gleb Yushin
School of Materials Science and Engineering
Georgia Institute of Technology

Dr. David Bucknall
School of Polymer, Textile, and Fiber Engineering
Georgia Institute of Technology

Date Approved: March 16, 2009

I dedicate this thesis to my grandparents Raghunath Sahai Jain and Sumitra Devi Jain who always believed in me and taught all the good things in life.

ACKNOWLEDGEMENTS

Dr. Kumar, my advisor, was a constant source of encouragement. His constructive criticism always helped in the progress of this research. His questions and comments forced me to think creatively and his personal advice helped me to make the best decisions.

I am thankful to my committee members including Dr. Anselm Griffin, Dr. David Bucknall, Dr. Meisha Shofner, and Dr. Gleb Yushin for their valuable time and suggestions. I am grateful to Dr. Jong Beom Baek for synthesizing all of the PEK and PEK-g-CNT systems and for his friendly advice. I am thankful to Dr. Han Gi Chae and Dr. Asif Rasheed for their help during fiber spinning, to Dr. Marilyn Minus for all the TEM work, to Young Ho Choi for spinning the PEK based fibers. I am thankful to my group members Dr. Dhriti Nepal, Sudhakar Jagannathan, Yaodong Liu, Ericka Ford, and past group members Dr. Jing Liu, Beom Jin Yoon, Dr. Tong Wang, Dr. Shanju Zhang, Dr. Chongfu Zhou, Dr. Huina Guo, and Hong Shen who always provided constructive and valuable criticism and created a friendly environment.

It was great to be around other PTFE graduate students including Wanting Ren, Sharon Wu, Sehoon Chang, Zhan Liu, Pratap Kumar, Deepali Palta, Hongfeng Ren, Jun Jia, Sungwon Ma, Jasmeet Kaur, Srikanth Singamaneni, Ruilan Guo, Mihir Oka, Bilge Hatiboglu, Katie Campbell, Michelle Schlea, Ryan Kincer, Christine Flaherty, Holley Harris, Shamal Mhetre, Vibhor Jain, Sarang Deodhar, Wei Zhang, Xuxia Yao, Ruihua Li, Wenjun Xu, Rodney Averett, Xie Wang, Eric Crawford, and Vivek Sharma who created

a very cordial environment which made the graduate student life at Georgia Tech enjoyable and memorable.

I am grateful to Yubin Shen for being a great friend who was always there when I needed one the most. I was lucky to have friends like Pooja Upreti, Diem Trinh, Claudia Espinosa, Bandana Bhusal, Noriko Kato, Eunhwa Yang, Rakesh Sundriyal, Lakshya Deka, Mélanie Hall, Gokul Narayanan, Ankush Gupta, Karan Kakkar, Amol Khotpal, Dexin Luo, Duane Hahn, Bob Wright, John Hoy, Federico Polo, Srividya Mohan, Nicolas Espinoza, Justyna Wiedemair, Peng Meng Kou, Anne Showman, Valli Subbiah, and Dr. Xiaolan Hu, whose company provided avenues for fun times and helped de-stress the Ph.D. student life.

I am thankful to Georgia Tech Leadershape® members, who helped increase my self-awareness and provided some very good and ambitious friends.

I am very thankful to our administrative staff Angie Abbott, Hope Payne, Linda Robertson, Jay Gallman, and Mike Boyett for making my life easier in PTFE.

I am also thankful to Dr. Haskell Beckham, Dr. Davis Lee, Dr. Donggang Yao, Dr. Karl Jacob, Dr. Yonathan Thio, and Dr. Lisa Detter-Hoskin for personal advice on matters that became important at different times.

I was lucky to have Shivam Goel, Sachin Chaudhry, Abhilash Goyal, Sumit Soni, Debra Cole, and Deia Joel Nourse as room-mates who were very understanding and careful.

I am grateful to NIST for funding this research.

TABLE OF CONTENTS

Page

LIST OF TABLES

LIST OF FIGURES

LIST OF ABBREVIATIONS

AFM	atomic force microscopy
C-fiber	carbon fiber
CNF	carbon nanofiber
CNT	carbon nanotube
CTE	coefficient of thermal expansion
CVD	chemical vapor deposition
DFS	dynamic frequency sweep
DMA	dynamic mechanical analysis/analyzer
DR	draw ratio
DSC	differential scanning calorimetry/calorimeter
DSS	dynamic strain sweep
FTIR	Fourier transform infra-red spectroscopy
FWHM	full width half maximum
f	frequency
$f_{Polymer}$	Herman's orientation factor for polymer
f_{CNT}	Herman's orientation factor for carbon nanotube
$L_{Polymer}$	Crystal size for polymer
L_{CNT}	Crystal size for carbon nanotube
LVR	linear viscoelastic region
MA	methyl acrylate
MMA	methyl methacrylate

MW	molecular weight
MWD	molecular weight distribution
MWNT	multi wall carbon nanotube
NMR	nuclear magnetic resonance
NT	nanotube
PAN	polyacrylonitrile
PDI	polydispersity index
rpm	revolutions per minute
s	second
SEM	scanning electron microscope/microscopy
SRS	strain rate sweep
SWNT	single wall carbon nanotube
TEM	transmission electron microscope/microscopy
T_g	glass transition temperature
TGA	thermogravimetric analysis/analyzer
TMA	thermomechanical analysis/analyzer
VA	vinyl acetate
VC	vinyl chloride
WAXD	wide-angle X-ray diffraction

SUMMARY

Traditionally, polyacrylonitrile (PAN) based carbon fibers have been used for high-temperature and high-strength applications. The graphitic nature, continuous structure, and high mechanical properties of carbon nanotubes (CNTs) make them good candidate for reinforcing PAN fiber. The different types of CNTs including single-wall carbon nanotubes (SWNTs), few-wall carbon nanotubes (FWNTs), and multi-wall carbon nanotubes (MWNTs) differ in terms of their diameter and number of graphitic walls. The carbon nanofibers (CNFs) are another class of carbon nanostructures. The SWNTs, FWNTs, MWNTs, and CNFs have diameter ranges of 0.4 to 4 nm, 2 to 6 nm, 5 to 30 nm, and 50 to 200 nm, respectively. The work in this thesis is mainly focused on MWNT and CNF reinforced PAN composite fibers, and SWNT, FWNT, and MWNT reinforced poly(etherketone) (PEK) composite fibers.

PAN/CNT composite fibers were processed using different concentrations of MWNT (5, 10, 15, and 20 wt.%) and CNF (5, 10, 15, 20, and 30 wt.%). To the best of our knowledge, this is the first study to report the spinning of 20% MWNT or 30% CNF reinforced polymer fiber spun using conventional fiber spinning.

PAN and PAN/MWNT composite fibers were spun using dry-jet wet solution spinning. Fibers reinforced with MWNTs were found to have lower thermal shrinkage, higher glass transition temperature (T_g), and significantly higher Young's modulus (particularly above T_g) than the control PAN fibers. The composite fibers have been compared with neat PAN fiber in terms of over-all crystallinity, PAN crystal size, PAN orientation, MWNT orientation, tensile and dynamic mechanical properties, thermal

stability (in nitrogen and air), and overall char yield. Low (100K) and high molecular weight (MW) (250K and 700K) PAN fibers were spun with different concentrations of CNFs. For low MW PAN, the 5% CNF containing fiber showed the highest mechanical properties and the properties decreased with increase in CNF content. At high CNF content (20%), the mechanical properties improved when high MW PAN was used. The effect of two-stage heat drawing, sonication time for CNF dispersion, and the fiber drying temperature was also studied. Other challenges associated with processing high concentrations of solutions for making composite fibers have been identified and reported. The effect of CNT diameter and concentration on fiber spinnability and electrical conductivity of composite fiber have also been studied. This work suggests that CNT diameter affects the CNT-polymer physical interaction and controls the maximum possible concentration of CNTs in a composite fiber. For a particular type of CNT, as expected, the electrical conductivity increased with increase in CNT concentration. The electrical conductivity also increased with increase in draw ratio. For a particular CNT concentration, the high MW PAN based composite fibers showed higher electrical conductivity. The results show that by properly choosing the type of CNT, length of CNTs, dispersion of CNTs, fiber spinning method, fiber draw ratio or orientation of CNTs, and type of polymer, one can get electrically conducting fibers with wide range of conductivities for different applications.

The PEK/CNT fibers were also spun by dry-jet wet spinning. The PEK fibers were spun with different types of CNTs at different concentrations. This is the first study reporting the PEK-g-CNT fibers. The CNTs were found to be uniformly distributed and dispersed in the composite fibers. The PEK based control and

composite fibers possess high thermal stability with almost no weight loss up to 500 ˚C. PEK and PEK-g-CNT fibers showed a strong exotherm in air at around 290 ˚C, which was absent in N_2. At low CNT concentrations, no significant effect was observed, in the presence of different CNTs, in the crystallinity, crystal size, tensile properties, and dynamic mechanical properties of the fibers. The PEK based fibers showed high toughness which surpassed many of the high-performance fibers like Kevlar® and Zylon®. The energy dissipation behavior of high CNT (≥ 5 wt.%) containing fibers changed above the T_g of the fiber, which was evident from the tan δ curves obtained from DMA experiments. PEK fibers showed negligible thermal shrinkage up to 200 ˚C and a little shrinkage of about 6 % up to 340 ˚C. The 10% FWNT containing fibers were unique in terms of high electrical conductivity and high toughness.

The overall objectives of this thesis were:

- To process PAN based composite fibers with high concentrations of CNTs and CNFs.
- To study the morphology, structure, and properties of high CNT and CNF containing PAN Fibers.
- To study the morphology, structure, and properties of PEK-g-CNT fibers.

Chapter 1 reviews the literature on PAN, CNTs, and PAN/CNT composites. Chapter 2 is devoted to the processing, structure, and properties of PAN/MWNT composite fibers. Chapter 3 covers the results for low molecular weight (MW) PAN/CNF composite fibers and effects of various processing parameters on its tensile

properties. Chapter 4 covers the results for high MW PAN/CNF composite fibers. The effect of CNT diameter and concentration on the fiber spinnability is covered in Chapter 5. The effect of various factors on the electrical conductivity of the PAN/CNT fibers is discussed in Chapter 6. The PEK and PEK-g-CNT synthesis, fiber processing, structure, and properties are discussed in Chapter 7. The overall conclusions of this work are reported in Chapter 8. The details of various PAN/CNT fiber codes are given in Appendix A.

CHAPTER 1

INTRODUCTION

1.1. Polyacrylonitrile (PAN)

Commercially, PAN polymer is synthesized by free radical polymerization [1]. The success of free-radical polymerization over other methods include control over polymerization rate, molecular weight (MW), chain linearity (low branching), and incorporation of comonomers and dye sites. Generally, low MW PAN (~ 45,000 g/mole) is employed for making textile grade fibers and high MW PAN (> 200,000 g/mole) is used for making precursor fibers for carbon fiber, where high strength and modulus are desirable. PAN is rarely used as a homopolymer. The comonomers that are commonly used with acrylonitrile include methyl acrylate (MA), vinyl acetate (VA), and vinyl chloride (VC) [1]. Neutral comonomers, such as MA, methyl methacrylate (MMA), and VA, are used to modify the solubility of polymer in spinning solvents and to modify the fiber morphology [1, 2]. The incorporation of comonomers also modifies the rate of diffusion of solvents, non-solvents, and dyes. The halogenated comonomers that have been used in the past to impart flame resistance to fibers include vinylidene chloride, vinyl bromide, and VC. PAN has high char yield (> 40%) and can be made fire resistant through stabilization, which makes it an attractive candidate for fire barrier applications. Among the textile grade fibers, PAN (after stabilization) has the highest oxygen index of > 40% [3]. ASTM D2863 defines the oxygen index to be the minimum concentration of oxygen in an oxygen/nitrogen mixture that will support a flaming burn in a plastic specimen.

A copolymer with less than 85% PAN is termed modacrylic. The modacrylic fiber may incorporate up to 35-40% of halogenated comonomers to impart high flame resistance [1]. Dehydrohalogenation during processing of modacrylic can lead to the formation of double bonds which results in color formation in the fiber. Additionally, acids such as HCl and HBr may be generated during the hot processing. Liberation of acids makes the fiber corrosive and difficult to process [4]. PAN fibers have also been used as a replacement for asbestos and for reinforcing cement [4]. For such applications, modulus retention under warm-moist conditions, resistance towards alkaline degradation, and bonding ability with cement are some of the desirable properties.

Most semi-crystalline polymers are described to possess a two phase morphology consisting of crystalline and amorphous regions. PAN is described to possess amorphous morphology with a high degree of lateral order [5]. The dipolar interaction in PAN is due to pendant nitrile groups. The interaction can either be attractive or repulsive as shown in Figure 1. The antiparallel and parallel orientations shown in Figure 1 show the case for maximum attraction and maximum repulsion, respectively. The energy of dipolar interaction (E) is a function of dipole moment (μ) and the proximity distance (r) between dipoles.

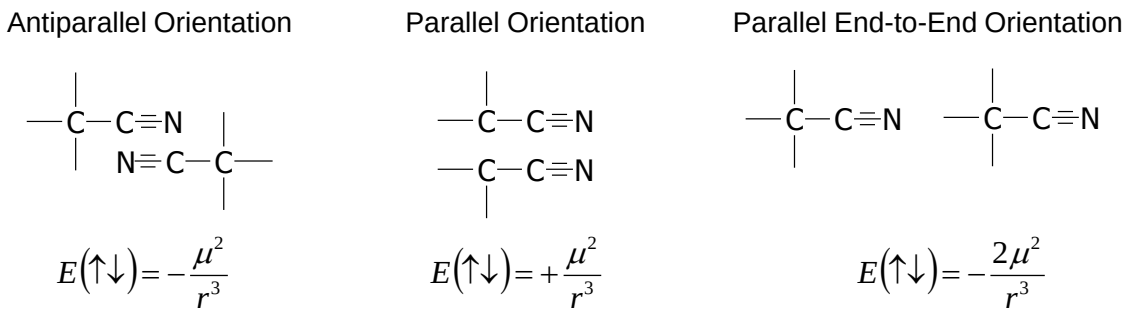

Figure 1. Types of nitrile dipolar interactions in PAN due to different orientations of nitrile groups. (adapted from Olive [6])

PAN chains pack themselves in a hexagonal lattice with each chain occupying a cylinder of about 0.6 nm diameter. Since PAN is generally atactic, the chain conformation within a cylinder is irregular and off-equatorial reflections are generally not observed in X-ray diffraction. The pendant nitrile groups extend beyond that cylinder and participate in lateral nitrile-nitrile dipolar interchain bonding.

As mentioned earlier, for practical reasons PAN homopolymer is rarely used for making commercial grade fibers. The presence of comonomer affects the PAN chain packing. The presence of comonomer tends to decrease both crystal size and perfection. The size and polarity of the comonomers affect the disruption of crystalline morphology. A comparison among MMA, VA, and methacrylonitrile groups showed that full width at half maximum (FWHM) of the most intense peak of PAN (200 reflection) was greatly increased with the increase in molar concentration in case of both MMA and VA, but the increase was not as obvious in case of methacrylonitrile comonomer. The reason being that both MMA and VA are similar in size but larger than methacrylonitrile, and presence of the nitrile dipole in methacrylonitrile does not significantly disrupt the intermolecular dipolar binding between PAN chains [5].

At elevated temperatures PAN undergoes cyclization and degradation before melting. During cyclization, the adjacent nitrile groups form a six-membered ring structure in the chain backbone, and this reaction is exothermic. PAN is the main precursor for carbon fiber. First the PAN fiber is stabilized under an oxidative environment to make the ladder polymer through nitrile polymerization. The nitrile polymerization can be a radical or an ionic process. The nitrile polymerization is also an exothermic process and is very critical in determining the final tensile strength and

modulus of the carbon fiber. Comonomers, such as carboxylic acids or vinyl bromide used for initiating ionic exotherm, help in controlling/moderating the exotherm and lower the onset temperature for nitrile polymerization [4]. A smaller exotherm is desirable from the point of view of eliminating localized heat buildup and preventing the charring in large yarn bundles. Previous research [4] has shown the following monomers to be effective (in reducing and slowing the exotherm): acrylic acid, itaconic acid, methacrylic acid, and vinyl bromide. Comonomers MA and VA do not help in catalyzing the exotherm but they are reported to hinder the nitrile polymerization [4]. For carbon fiber production, the precursor fiber should have small diameter, high tensile strength and modulus, broad exothermic peak during nitrile cyclization, low threshold temperature for cyclization, and high carbon yield (>50 %) [2]. Itaconic acid has been considered to be a superior comonomer for initiating the cyclization reaction at lower temperature [2]. At the onset of cyclization, carboxylic groups of itaconic acid come in the vicinity of pendant nitrile group and initiate the ionic exothermic reaction. Itaconic acid also slows down the propagation of cyclization, which is very fast in PAN homopolymer, where cyclization occurs mainly through radical mechanism. A high exothermic heat flux during cyclization is detrimental for the carbon fiber structure and mechanical properties.

1.1.1. Wet-Spinning and Dry-Jet Wet-Spinning of PAN Fiber

PAN solution gets converted into a rubbery gel if a solution of sufficient polymer concentration is allowed to stand at room temperature. Consequently, the viscosity of the system increases, but this gelation is thermo-reversible and the viscosity can be reduced by increasing the temperature. The gelation is due to the phase separation of polymer

chains and formation of small ordered regions or crystallites, which provide reversible physical crosslinks [5]. To prevent gelation, the solution must be well mixed/stirred.

The wet-spinning of fiber involves the extrusion of polymer solution through a spinneret which is submerged in a coagulation bath. For dry-jet spinning (or dry-jet wet-spinning) there is a finite air-gap, ranging from a fraction of a millimeter to tens of millimeters between the spinneret and the coagulation bath [2, 7]. For PAN fibers, the coagulation bath usually contains a mixture of the spin-solvent and water, which is a non-solvent for PAN. After entering the coagulation bath, the fiber is coagulated during which the solvent comes out and non-solvent goes into the fiber. The rate of diffusion of non-solvent and solvent into and out of fiber can be varied by changing several variables which include: concentration of solvent in coagulation bath, temperature of bath, fiber residence time in bath (by controlling extrusion rate, length of bath, and winding speed), and spinneret diameter. The slight changes in these variables can significantly change the fiber microstructure, polymer morphology, and ultimately its properties.

Generally, multiple coagulation baths are used to achieve complete coagulation, where successive baths are made up of decreasing solvent concentration. The successive stages of fiber formation include washing, heat-drawing, and drying the fiber. Drawing is done to orient the polymer chains in the fiber direction which leads to significant improvement in fiber properties. In addition to the aforementioned factors, the fiber physical properties are dependent on polymer MW, polymer solid content in the spinning solution, and the degree of heat-drawing.

Fiber properties and microstructure are improved when using dry-jet wet-spinning as compared to wet-spinning [2, 7]. Unlike wet-spinning, threadline stresses are not

transferred back to the spinneret in dry-jet wet spinning. Additionally, the air-gap allows the relaxation of oriented molecules and a uniform structure is resulted. The subsequent drawing of fiber leads to polymer chain orientation and high tenacity. A higher solid content in the spinning solution is also possible with dry-jet wet-spinning and the fiber is generally free of pear/finger shaped voids. The heat-drawing is usually conducted in hot or boiling water, but polyhydric alcohols, such as glycerol and ethylene glycol, can be used if heat drawing at high temperatures (>100 ˚C) is desired. Heat drawing in multiple-stages is usually done to achieve high draw-ratios and to improve the fiber properties. The temperature for heat-drawing is increased with each stage.

A number of authors have studied the effect of several processing variables on the fiber microstructure and its physical properties. Baojun *et al.* [8, 9] studied the effects of bath concentration (DMF in water), bath temperature, and jet-stretch on the void formation in PAN fibers by using wet-spinning and dry-jet wet-spinning. For both wet and dry-jet wet-spinning, the fiber shape changed from an irregular or bean shape to a more circular shape with an increase in bath temperature or bath concentration. The increase in circularity of the fiber has to do with slower and more uniform coagulation, which can be achieved with an increase in bath concentration or temperature. In case of wet-spinning, the voids were found to be increased with an increase in bath temperature, or a decrease in bath concentration. The voids moved toward the fiber periphery with an increase in bath concentration. In case of dry-jet wet-spinning, the voids (as observed through the optical microscopy) were found to be absent under the conditions studied (bath temperature from 10-70 ˚C, bath concentration from 0-51%, jet-stretch from 0.55-2.6) [9]. For both wet and dry-jet wet-spinning, the volume porosity decreased with an

increase in polymer solid content and a decrease in bath temperature. In case of dry-jet wet-spinning, the volume porosity decreased with an increase in jet-stretch. The authors [9] emphasized that because of the air gap a thin, dense cuticle is formed which sharply slows down the water diffusion into the fiber and hence no big voids are formed.

Stoyanov [10] studied the effect of dope concentration (solid content in the spinning solution) on the mechanical properties of the fiber for different MWs of PAN. It was implied that a low solid content can slow the coagulation rate resulting in incomplete coagulation and a high solid content can increase the coagulation rate leading to skin-core formation (i.e. a heterogeneous structure). In both extreme cases, the properties (tenacity, loop strength, density) deteriorate. Therefore, an optimum concentration is desirable to achieve uniform and complete coagulation. Invariably, the properties improved with an increase in the MW of PAN.

Dunbleton and Bell [11] discussed the collapse process of voids during the drying of PAN fibers. The fiber made by wet-spinning is a porous structure of networks of rods and fibrils. While drawing (e.g. in boiling water), the network is stretched and voids become elongated in the fiber direction. But during drying, the fiber contracts radially and the voids are collapsed. The fibers in their study were spun using wet-spinning and no spin-draw was applied before drying the fibers. The important parameter in the collapsing of voids was the drying temperature. The collapse occurred near the glass transition temperature (T_g) of fiber. The presence of water lowers the T_g and allows the collapse to occur at lower temperatures. The time and temperature for drying were found to be interchangeable in terms of causing the same change in fiber diameter. The effect same as high temperature over a small period could be achieved at lower temperature

over long period. The radial shrinkage was found to occur near 90 ˚C and was completed when the temperature reached to 130 ˚C. The decrease in porosity with shrinkage was verified by an increase in the sonic modulus of the fiber. The sonic modulus abruptly increased near the temperature at which maximum shrinkage occurred. The compactness of the fiber after shrinkage also determines the resistance to re-swelling. The authors also discussed that PAN molecule adopts a helical conformation. The fibrils in the fiber consist of arrays of helical molecules which posses a lateral order but no longitudinal order. Furthermore, under tension, the fibrils orient during stretching followed by stretching of PAN chain helices. The possibility of molecular slippage also increases above T_g.

Hersh *et al.* [12] studied the influence of processing variables on the physical properties of a wet-spun modacrylic fiber. The fiber tenacity increased with an increase in fiber residence time in the coagulation bath up to 10 s, after which it became constant. The fiber tenacity after stretching was found to be increased with a decrease in the residual content of the solvent in fiber. The authors showed that the effect of stretching in increasing the fiber tenacity decreased with increasing fiber diameter. This effect was attributed to the high solvent content in the large diameter fiber which limited the orientation and hence the properties. At very large diameters, the tenacity decreased with stretching. The drying at higher temperature was believed to cause fast evaporation of solvent and water out of the fiber leading to cracks and flaws which limited the fiber tenacity and elongation. The authors reported no change in fiber properties when the shear rate was changed by varying the solution flow rate or spinneret hole diameter.

Wang *et al.* [13] studied the effect of coagulation conditions on the wet-spun PAN fiber. For a particular bath concentration, the coagulation rate was found to be increased due to increased solvent mobility with an increase in the bath temperature. Additionally, the fiber shape changed from a bean shape to a circular shape with an increase in bath temperature. The reduction in bath temperature led to an increase in bulk density of the fiber, reduction in the number of large voids, and a decrease in elongation and tenacity. The fiber cross-section also changed from a bean shape to a circular shape with increase in solvent bath concentration. Though the bulk density and tenacity increased with an increase in bath concentration, the elongation at break and number of voids reduced.

Hou *et al.* [14] studied the diffusion of non-solvent (water) in the formation of PAN fiber using wet-spinning. The diffusion of water into the fiber was found to be reduced with an increase in the dope solid content. The reason was attributed to an increase in the polymer viscosity which slows the diffusion of solvent and non-solvent across in the fiber. Additionally, with an increase in the solid content, the concentration gradient of solvent in the fiber and coagulation bath decreases, this further slowed the diffusion of both solvent and non-solvent in the fiber. The diffusion of water increased with an increase in the bath temperature. The change in diffusion becomes less significant beyond 60 ˚C which could be due to reduction of polar interactions among the PAN chains (due to nitrile groups) above that temperature. The diffusion of water was also found to be increased with an increase in the jet stretch minus ratio which was attributed to a possible decrease in the bulk density of the fiber and an increase in the number of voids in the fiber.

Chen *et al.* [15] studied the formation of PAN fibers using wet-spinning. It was measured that DMSO diffusion from the fiber to the H_2O/DMSO coagulation bath was rapid at first which decreased with increasing time and became stable after 24 s. Furthermore, with an increase in the coagulation time, the fibers became denser and had fewer inner defects gradually. However, after 24 s the fiber developed transverse stripes on the surface which got deeper with increasing time. It was implied that transverse stripes develop when the polymer chains in the skin region rupture beyond a critical value of stretching. These transverse stripes are detrimental to the tensile strength of the fiber as well. To control the same, a minus stretch ratio is desired during the coagulation process.

Several patents [16-19] have mentioned the production method for making high strength and high modulus PAN fibers. These methods emphasize the use of high MW PAN ($\geq$ 400,000 g/mole) with a polydispersity index (PDI) of less than five and applying multistage stretching at temperatures such that the later the stretching stage higher the temperature, and then drying the fiber under tension at a temperature below 130 ˚C. Polymer solution concentration should be such that the chains are sufficiently disentangled and can be oriented and extended during the spinning, coagulating, and drawing operations. The removal of any air bubbles from the solution under reduced pressure was another factor mentioned for improving the solution quality and fiber properties. The dissolution temperature of polymer was suggested to be between 70-130 ˚C and the dynamic viscosity at 30 ˚C between 500-10000 Pa.s. The presence of air bubbles in the solution hinders the parallel arrangement and orientation of chains and causes formation of defects in the fiber. The attainment of slow, uniform and complete coagulation was suggested through the use of multiple coagulation baths with increasing

concentration of non-solvent. For the same reason, finer diameter fibers were suggested to be desirable. If a polyhydric alcohol is used for drawing at higher temperatures, then the fiber should be washed, for example with warm water at 60 ˚C, to an alcohol content of less than 0.5 wt%. The drying was suggested to be conducted below 120 ˚C under constant length.

In one patent [19], the use of high MW PAN and high solid content dope with a viscosity of preferably between 260 and 450 Pa.s (determined at 80 ˚C in DMF) was suggested. The dope solution filtration and degassing was suggested to remove any gel particle, contaminants, and bubbles from the solution. For high solid content, the solution can be heated to 80-130 ˚C to lower the viscosity to a desired value, but the spinning pressure should be kept to at least 20 bar. The exit velocity of the solution coming out of the spinneret should be controlled so that the fiber stream does not bend while entering the coagulation bath. The preferred exit velocity for the solution is 15-35 m/min. For a stable spinning under the suggested conditions the spinneret orifice diameter should preferably be 60-120 μm and the air-gap should be less than 10 mm. The solvent concentration in the coagulation bath and the coagulation bath temperature should preferably be 20-50% and 60-85 ˚C, respectively. The length of the coagulation bath should be at least 0.5 m. The total draw ratio should be between 10 and 25.

1.2. Carbon Nanotubes (CNTs)

Carbon nanotubes (CNTs) are cylindrical shape supra-molecular structures which are only comprised of carbon atoms. The carbon atoms in a cylinder are attached to each other through sp^2 hybridized bonding. As shown in Figure 2, CNTs can exist in the form

of single-walled carbon nanotube (SWNT), double-walled carbon nanotube (DWNT), and multi-walled carbon nanotube (MWNT). Different types of CNTs can be synthesized by various methods. Chemical vapor deposition (CVD), arc discharge, and laser ablation are some of the main methods for CNT synthesis. Of these, CVD is the most commonly used method for mass production of different types of CNTs.

The excellent electrical conductivity of CNTs presents an important avenue for CNT reinforced composite fibers, especially when the CNT content is high (>20 %). Therefore CNTs can impart electrical conductivity to the composite fiber, and if correctly engineered the fiber can be used in applications where electrical, thermal, and mechanical properties are desirable. At sufficiently high concentrations, CNTs in a composite fiber can carry high current density.

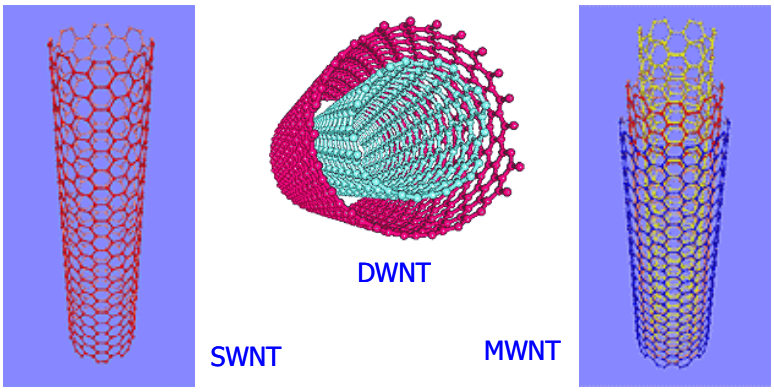

Figure 2. Images representing the structure of SWNT, DWNT, and MWNT. (images from [20])

1.2.1. Carbon Nanofibers (CNFs)

CNFs can be classified as a special category of MWNTs with larger diameters. CNFs are cheaper than other CNTs, yet possess many similar characteristics. CNF has diameter in the range of 50-200 nm and length of the order of tens of micrometers. This

CNF geometry results in aspect ratios of 150-2000. Figure 3 shows the SEM images of herringbone (stacked-cup) and bamboo type of structures for CNFs.

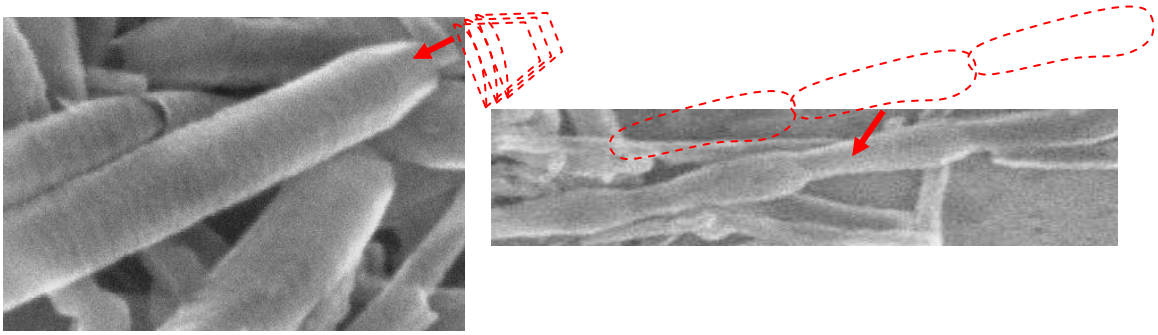

Figure 3. SEM images of different types of CNFs. Left: herringbone (stacked-cup geometry); Right: bamboo type of structure.

1.2.2. SWNT Density

Few questions come to the mind while thinking about the SWNTs and their structures. Some of these are:

- Do molecular weight and density (ρ) of a SWNT depend on its chirality?
- What is the molecular weight and density of a SWNT of given diameter and length?

Carbon atoms in a SWNT are arranged in a hexagonal pattern as shown in Figure 4. A hypothetical unit cell of 32 carbon atoms occupies an area of 0.838368 nm^2. Now, the total number of carbon atoms in a tube of diameter d_t and length h can be calculated from equation 1. Knowing that the atomic weight of a C-atom is 12.011 atomic mass units, the molecular weight of a SWNT can be calculated using equation 2. For example, the molecular weight of a SWNT with 1 nm diameter and 10 μm length is given in equation 3.

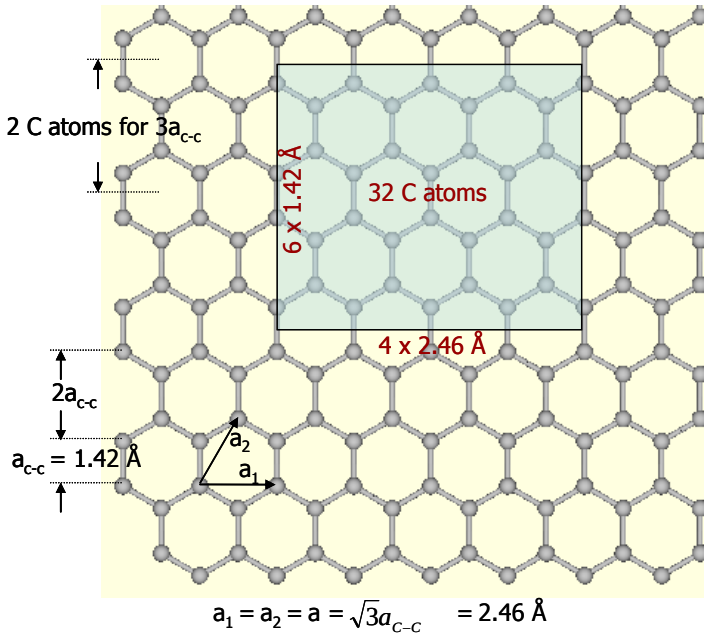

Figure 4. Hexagonal arrangement of carbon atoms on the surface of a SWNT. The lattice parameters and a hypothetical unit cell of 32 carbon atoms are also shown.

$$Number\ \ of\ \ carbon\ \ atoms = \pi d_t h \times \frac{32}{0.838368} \tag{1}$$

$$MW\ \ of\ \ a\ \ SWNT = \pi d_t h \times \frac{32}{0.838368} \times 12.011\ \ g.mol^{-1} \tag{2}$$

$$MW\big|_{1nm\ dia\ \&\ 10\mu m\ length} \approx 1.44 \times 10^7\ \ g.mol^{-1} \tag{3}$$

Since this calculation does not take chirality into account, it is clear that the MW of a SWNT is independent of its chirality!

The density of a NT can be calculated using equation 4.

$$\rho_t = \frac{MW}{N_{Av} \times V_t} \tag{4}$$

where N_{Av} is the Avogadro's number and V_t is the volume of SWNT.

Assuming that the SWNTs arrange in a triangular unit cell in a bundle of SWNTs and the van der Waals separation between SWNTs in a bundle is 0.334 nm (Figure 5), the equilateral triangle shown in Figure 5 shows the area covered by C-atoms in SWNT (overlapping area between circles and the triangle) and the total area occupied in that arrangement for density calculation. As shown in Figure 5, one triangle occupies only half of a SWNT in its area. The density of SWNT's can be calculated using equations 2 and 5. For example, the density of a SWNT with 1 nm diameter is given in equation 6. A relationship between SWNT diameter (ranging from 0.4 nm to 4 nm) and its density is shown in Figure 6. A tube with a diameter of more than 2 nm has a density of less than water, which suggests that materials made from such tubes can be made to float on water.

$$\rho_{NT} \propto \frac{Weight\ \ of\ \ C-atoms\ \ in\ \ A_{half\ NT}}{A_{eq.\ \Delta}} \qquad \left[A_{eq.\ \Delta} = \frac{\sqrt{3}}{4}\left(d_t + 0.334\right)^2 \right] \tag{5}$$

$$\rho\big|_{1nm\ dia\ NT} = \frac{\frac{\pi d_t h}{2} \times \frac{32}{0.838368} \times 12.011}{N_{Av} \times \frac{\sqrt{3}}{4}\left(d_t + 0.334\right)^2 h} \approx 1.552\ \ g.cm^{-3} \tag{6}$$

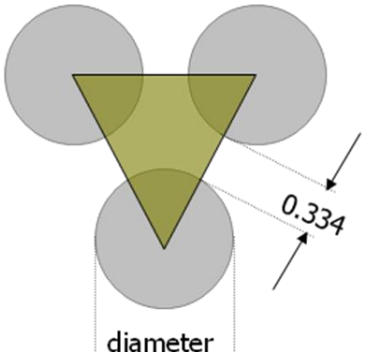

Figure 5. A triangular unit cell showing the arrangement of three SWNTs and separation between them.

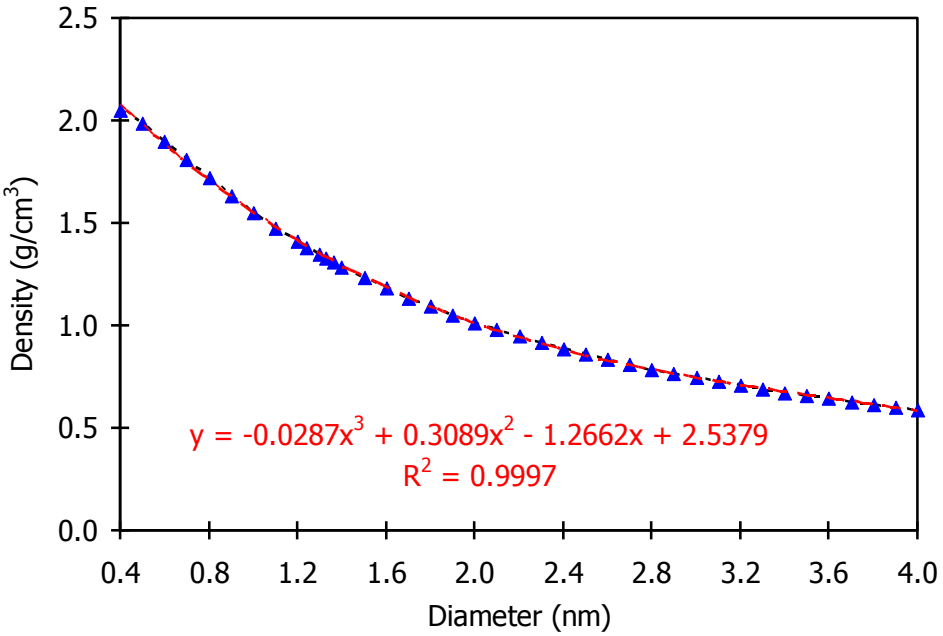

Figure 6. SWNT density as a function of its diameter. (Assumption: the van der Waals separation between SWNTs in a bundle is 0.334 nm).

The parameters used in the above equations for density calculation assume an interlayer spacing of 0.334 nm, whereas this spacing could be slightly different and is a function of SWNT chirality. The inside mass of the SWNT (if any gas molecules in an open ended tube!) is also ignored for the molecular weight and density calculations.

1.3. PAN/CNT Composites

A number of studies have been devoted to the study of CNT reinforced PAN fibers. Sreekumar *et al.* [21] spun the SWNT/PAN composite fibers with SWNTs concentrations of 5 and 10 wt%. As compared to neat PAN fibers, the 10 wt% composite fibers were reported to exhibit 100% increase in tensile modulus at room temperature and an order of magnitude increase in storage modulus at 150 ˚C. The glass transition temperature (T_g) of 10 wt% composite fiber increased by 40 ˚C as compared to neat PAN

fiber. The 10 wt% loading of SWNTs in the fiber significantly reduced the shrinkage at 200 ˚C. The composite fibers showed lower solubility (higher chemical stability) over neat PAN fiber in DMF and DMAc. The SWNT orientation in the composite fibers was evaluated from the Raman spectroscopy. Various results from the study corroborated that SWNT shows good interaction with PAN chains.

In continuation of the previous study [21], Min *et al.* [22] oxidatively stabilized the 5 and 10 wt% SWNT containing composite fibers under continuous air flow at 250 ˚C for 10 h. All the tensile mechanical properties were improved by the addition of SWNTs. Particularly the 10 wt% SWNT loaded oxidized fibers showed 100%, 160%, and 115% increase in tensile strength, modulus, and strain to failure, respectively, over the oxidized neat PAN fiber. However, the absolute mechanical properties of all the fibers were reduced after the oxidation. The composite fibers also showed a lower stress build-up during the isothermal heating of fibers at 250 ˚C for 4 hours at constant length.

Chae *et al.* [23] compared the reinforcement efficiency of SWNTs, MWNTs, DWNTs, and CNFs in PAN at 5 wt% loading. The thermogravimetric analysis (TGA) studies of different CNTs showed that the CNTs containing inner walls (MWNTs) or a layered structure (CNFs) have higher thermal stability (both in air and nitrogen) than CNTs with fewer walls (SWNTs, DWNTs). The CNT containing fibers showed improvements in properties over neat PAN fiber. The SWNTs reinforced fibers showed a significant increase in the low strain properties (75% increase in modulus, 50% reduction in shrinkage) and the MWNTs reinforced fibers showed improvements in high strain properties (75% increase in tensile strength, 110% increase in strain to failure, 230% improvement in work of rupture). The orientation of PAN chains, as measured from

WAXD, was higher in composite fibers than in neat PAN fiber. The crystal size of PAN in composite fiber was found to be larger but the crystallinity was found to be decreased. The improvement in low strain properties with SWNTs was attributed to good interaction between PAN and SWNTs and improvements with MWNTs was partly attributed to the MWNTs' long length.

The introduction of SWNTs into PAN has led to the development of composite films with unique combination of properties [24]. Above T_g, the composite films showed a 40 times increase in the storage modulus over neat PAN film. The PAN was found to be coated on to SWNTs, which increased the rope diameter of SWNTs from 26 nm to 40 nm. The composite films showed lower thermal expansion at high temperatures and lower dissolution of PAN in DMF from the composite films as compared to neat PAN films.

Electrospinning has also been used for making nanofiber composites. Liu *et al.* [25] made composite core-shell nanofibers with SWNT core and PAN shell. The nanofibers showed potential for developing nanowires and nanoelectrodes with conducting core and insulating shell and as probe tips for atomic force microscopy (AFM). Ko *et al.* [26] also made composite nanofibers of SWNT/PAN using electrospinning. They showed good distribution and alignment of SWNT in the composite fibers. Upon oxidation and carbonization of the fibers, the nanofibers maintained their shape but the PAN shrank around CNTs and led the CNTs to be sticking out, as observed through TEM images.

Pirlot *et al.* [27] made composite films of MWNTs and PAN and found horn-sonication over bath sonication to be a better method for MWNT dispersion in PAN.

However, they did not evaluate the effect of dispersion methods on CNT length curtailment or on final mechanical properties of the films. Petrov *et al.* [28] grafted the PAN chains onto MWNTs surface and found that the PAN chains provided a steric barrier against CNT reagglomeration. The corresponding system provided a stable dispersion in DMF. However, the period of stability of dispersion was not reported.

Ge *et al.* [29] made the composite nanofiber sheets of PAN and MWNTs (with CNT loading of 0, 2, 3, 5, 10, and 20 wt%) using electrospinning. Through transmission electron microscopy (TEM) studies, MWNTs were observed to be aligned along the fiber direction. Both TEM images and AFM height and phase images obtained under tapping mode revealed that neat PAN nanofibers had smooth surface, whereas MWNT/PAN composite nanofibers had a rough surface. WAXD patterns of PAN and MWNT/PAN nanofiber sheets showed good orientation of both PAN and MWNTs along the winding direction. The MWNTs orientation (f_{MWNT} = 0.90) was much higher than the PAN (f_{PAN} = 0.62) orientation in the 10 wt% MWNT/PAN composite nanofiber. The tensile strength and modulus increased with increasing percentage of MWNTs in the composite nanofiber sheets while the strain to failure decreased. The degradation temperature of the nanofiber sheets, as measured using TGA under nitrogen atmosphere, was found to be shifted from 268 ˚C for the neat PAN to 292 ˚C for the 5 wt% MWNT composite which was accompanied by an improvement in the char yield at 600 ˚C. The composite nanofiber sheets also showed lower extension when heating under tension using TMA and the temperature for extension/softening was found to be shifted to higher temperatures with increasing percentage of CNTs. The coefficient of thermal expansion (CTE) was reported

to be decreased by more than an order of magnitude for 10 and 20% MWNTs nanofiber sheets over neat PAN nanofiber sheets.

Koganemaru and co-workers [30] made the MWNT/PAN composite films by gelation with MWNTs concentrations of 0, 5, 7, and 10 wt%. The composite films were also drawn, stabilized, and carbonized to convert into carbon-carbon composite films. Though a finite tension was applied during the stabilization process, the magnitude was not reported. The development of diffraction arcs in the WAXD patterns in drawn (10x) films suggested the orientation of both PAN chains and MWNTs. However, the degree of orientation, percentage crystallinity, and crystal size were not quantified. The storage modulus of 10x drawn films, as measured from DMA, was found to increase with increasing concentration of MWNTs. The magnitude of tan δ peaks decreased with increase in MWNT content but there was no shift in the tan δ peak position (i.e. T_g remained unchanged with increasing percentage of MWNTs). Though electrical conductivity increased after the addition of MWNTs and reached the percolation threshold at 5 wt% loading, the drawing seemed to create no effect on the electrical conductivity of the films. Up to the stabilization stage of the films, the MWNTs containing films showed much higher electrical conductivity, but at the carbonized stage all films (0, 5, 7, 10 wt% MWNT) showed almost the same conductivity. The modulus of the 10x drawn films increased with increasing percentage of MWNTs, and this trend was consistent at all stages of processing (untreated, stabilized, carbonized). The modulus was found to be slightly reduced after stabilization, but it increased by almost three times after carbonization.

Ye *et al.* [31] studied the reinforcement and rupture behavior of CNT/PAN composite nanofibers with CNT concentration of 1 wt%. A two stage rupture behavior was reported to be observed in both SWNT and MWNT composite nanofibers. The first stage of PAN matrix crazing was followed by CNT pull-outs. The polymer crazing was hindered by the presence of CNTs which reduced the stress concentration and ultimately CNTs helped in the higher energy dissipation through the pull-out mechanism. Though higher toughness was suggested for composite nanofibers, but no quantitative studies were conducted to support the same point.

Hou and Renekar [32] carbonized the electrospun PAN nanofibers and subsequently used them as substrate for MWNT growth to make nanotubes on nanofibers. Fe(acetylacetonate)$_3$ was added to the PAN/DMF solution before electrospinning which later led to the formation of iron catalyst particles and served as nucleating points for MWNT growth. The tip growth mechanism was attributed for the MWNT growth and the ultimate length was a function of the growth time. The MWNTs synthesized at lower temperature (~ 700 ˚C) were found to be curved and kinked, whereas the MWNTs grown at higher temperature (~ 850 ˚C) seemed to be straighter.

Ra and coworkers [33] fabricated the MWNT/PAN composite nanofiber paper using electrospinning. The diameter of the nanofibers was found to be decreased with increasing concentration of MWNTs. The composite papers were further stabilized and carbonized. The electrical conductivity was found to be increased with increasing carbonization temperature (800, 900, and 1000 ˚C). Unlike the pure PAN based paper, the electrical conductivity of the carbonized composite paper in winding direction was three times of the conductivity in lateral direction. This observation and TEM images

suggested that MWNTs were preferentially oriented in the winding direction during the electrospinning.

Hou *et al.* [34] electrospun the composite nanofiber sheets of PAN reinforced with different concentrations of MWNTs (0, 2, 3, 5, 10, 20, 35 wt%) treated with 6M nitric acid. The sheets were subsequently stabilized in air and then carbonized in argon at 850 ˚C. The IR spectroscopy of HNO_3 treated MWNTs confirmed the presence of carboxylic groups, and TEM observation revealed that the surface of MWNTs remained unchanged after treatment. SEM images revealed that the surface roughness of the nanofibers increased with increasing percentage of MWNTs and TEM images showed MWNTs protruding out of the nanofibers in case of high content MWNT nanofibers. TEM images further confirmed the orientation of MWNTs along the fiber axis and a requirement of un-deformed or un-kinked MWNTs was suggested for making nanofibers with smoother surface. The tensile modulus of the composite sheets increased and strain to failure consistently decreased with increasing percentage of MWNTs. However, the tensile strength first increased and then decreased beyond 5% loading of MWNTs. Poor dispersion and poor interfacial contact between CNTs and PAN was suggested to be a reason for decreased tensile strength at higher concentrations of MWNTs. The shrinkage of composite nanofiber sheets decreased with increasing percentage of MWNTs when heated up to 850 ˚C. The shrinkage reduction was more in the axial direction than in the transverse direction.

Chae *et al.* [35] spun SWNT/PAN composite fibers using gel spinning with three different concentrations of SWNT (0, 0.5, and 1%). The SWNT/PAN composite fibers showed higher resistance towards electron beam radiation and chemical attack by DMF.

Exfoliation of SWNTs in the fiber was observed from van Hove transitions in UV-Vis spectra and was confirmed from the high resolution transmission electron microscopy (HRTEM) images. The tensile modulus of the composites fibers exceeded the values predicted by simple rule of mixtures. A change in the PAN morphology and structure in the presence of SWNTs was suggested to be the cause for improved properties. In a subsequent study [36], Chae *et al.* studied the stabilization and carbonization of 0 and 1% SWNT reinforced PAN fibers. The HRTEM and Raman spectroscopy of carbonized fibers suggested the existence of well developed graphitized regions in case of SWNT reinforced fibers and only the presence of disordered carbon in case of control PAN fibers. The tensile modulus and strength of the carbonized composite fibers was improved by 49% and 64%, respectively, just by the addition of 1% SWNTs. SWNT/PAN composites have also been made as films and carbonized and explored for electrochemical capacitor electrode applications [37].

The PAN based fibers have also been used in fire barrier applications [3]. The existing fiber candidates for fire barrier applications include cotton, aramid, melamine/aramid, novoloid, and acrylic based, such as OxyPAN [38]. OxyPAN is an oxidized version of the PAN fiber. PAN can be converted to OxyPAN by heating it in an oxygenated atmosphere, such as air [39]. The heating should be controlled to prevent PAN degradation. This process of heating in an oxygenated atmosphere is referred to as stabilization. It is during the stabilization, when the PAN linear structure transforms to a ladder type aromatic structure. Due to molecular orientation of PAN chains during the fiber processing (especially during drawing), the entropic shrinkage occurs when PAN is heated. The shrinkage can be reduced by applying tension to the fiber during heating.

This ensures that subsequent ladder structure adopts a linear and oriented conformation. This linear and oriented structure is also the key for high strength and modulus. A number of parameters including gas flow rate, heating temperature, tension, and time of heating play a role in the thermo-mechanical characteristics of the final stabilized fiber.

CNTs are among the longest supra-molecules which can be produced with high degree of perfection. The carbonaceous nature, negligible contraction/expansion upon heating, and higher mechanical properties make CNTs an interesting candidate for reinforcing and modifying the PAN fiber for fire barrier applications.

The modified version of the OxyPAN may be referred as OxyPAN/CNT. The main difference is that precursor PAN fiber is reinforced with CNTs (SWNT/MWNT/CNF). Modified PAN fiber (PAN/CNT) can be further stabilized in a similar manner as mentioned for OxyPAN. The presence of CNTs can change the parameters that need to be controlled. Since CNTs are in the form of long graphitic cylinders, it is expected that they will act as a template for the ladder formation of the PAN molecules and assist the stabilization process. The template mechanism can further contribute to the formation of longer and highly oriented crystals of PAN. Due to their peculiar combination of properties (high tensile strength and modulus, high thermal stability, and high thermal and electrical conductivity) it is expected that CNTs will improve the final thermo-mechanical properties of the fiber.

The use of high concentrations of CNTs in PAN films led to the creation of composite films with unique combination of properties [24]. The different types of CNTs and CNFs possess different physical characteristics and therefore they interact differently with a particular polymer system. This results in composites with different combinations

of properties (mechanical strength, electrical conductivity, etc.). Even for a particular type of CNT or CNF, the solution properties (steady and dynamic rheological properties) and the final material properties and characteristics differ widely with filler concentration. Particularly at high concentrations, due to the rigid nature of these carbonaceous fillers, the processing of fibers with these composites systems becomes very difficult. Nevertheless, the high CNTs and CNFs content composite fibers provide the potential for creating materials with unique combination of properties and characteristics (high tensile strength and modulus, high thermal stability, high electrical and thermal conductivity). Additionally, the high aspect ratio of these filler materials can lead to unique structures (uniformly aligned, porous and flexible structures) with very special properties (breathability, reservoir for gases and liquids, and high thermal stability) and applications (scaffold/template for directional growth of tissue, cell and neuron, filtration media, and electrodes for electrochemical capacitors).

1.3.1. Rheology of PAN/CNT Composites

CNTs possess high aspect ratios, are rigid in nature, and are cylindrical in shape. Due to these physical characteristics, the interaction between polymer-CNT and polymer-polymer becomes very different. In fact, the presence of CNTs in a system can very much affect the polymer-polymer interaction on a global level. The presence of CNTs in a polymer system can impede polymer chain motion, affect chain entanglement, and affect viscoelasticity of the system. A number of studies have been conducted to study the rheology of CNT reinforced systems.

Hu *et al.* [40] studied the rheological and electrical percolation of MWNTs in PET based composites. As compared to electrical percolation, the rheological percolation threshold was found to be very low. The reason being that the electrical conductivity requires the closer proximity of CNTs (dense network required for electron hopping/tunneling), whereas even the farther apart CNTs (not so dense network), can impede polymer mobility. The other reason for high percolation requirement for electrical conductivity is that it can be severely affected by defects in CNTs and chirality of CNTs, the rheological characteristics may not be affected at all by those factors. The dynamic frequency sweep (DFS) tests showed that for MWNT reinforced samples, the viscosity at lower frequency increased with an increase in MWNT content. Additionally, whereas the viscosity of PET sample showed no dependence on the frequency, the MWNTs containing sample showed a shear thinning behavior, which became stronger with an increasing concentration of MWNTs. Both storage modulus (G') and loss modulus (G") increased with an increase in MWNT percentage in the system.

Potschke and co-workers [41-44] studied the rheology of melt mixed MWNT/polycarbonate systems. The viscosity of the composite systems at low frequencies was greater but became similar to the pure polycarbonate viscosity at high frequencies. Whereas the viscosity of pure polycarbonate showed independence on the frequency (between 0.1 to 100 Hz), the composite systems showed a shear-thinning behavior which became stronger with higher concentration of MWNTs. Both G' and G" increased with an increase in the MWNT concentration. Furthermore, though the absolute values of the viscosities decreased with an increase in the measurement temperature, the

rheological percolation threshold was found to decrease from 5 to 0.5% when the temperature was increased from 170 to 280 ˚C.

Du *et al.* [45] studied the rheology of SWNT/PMMA for different molecular weight PMMA. They observed that alignment of SWNTs in the system reduced the G' at low frequencies, which was due to the fact that tube-tube contact decreases with an increase in the alignment of SWNTs. The high MW PMMA chains were found to be facilitating the nanotube efficacy in impeding the mobility of polymer chains.

Wu *et al.* [46] studied the linear and non-linear rheological properties of the MWNT/PBT composites. In dynamic strain sweep (DSS) experiment, the G' increased with an increase in the MWNT content. However, the linear viscoelastic region (LVR) became shorter and shorter with increasing percentage of MWNTs in the system. In DFS experiment, the viscosity at low frequency increased with MWNTs loading, but unlike the pure PBT system which showed a constant viscosity over a long range of frequency, the MWNTs loaded systems showed more of a shear thinning behavior. In the study of non-linear rheology of the system, the authors measured the dynamic moduli of the pre-sheared samples. It was observed that the dynamic modulus of the presheared sample decreased with increasing rate of pre-shear. For the presheared samples, the G" was higher than G' at all frequencies and the system behavior was more liquid like than solid like. This was attributed to the fact that the percolation network of high aspect ratio fillers, such as MWNTs, depends on the orientation of the fillers. The pre-shear increased the orientation of MWNTs and decreased the network density and hence particle-particle interactions reduced, which explains the observed behavior.

Wang and co-workers [47] studied the rheology of PAN/MWNTs spinning dopes. The composite systems were made by in-situ polymerization of acrylonitrile in the presence of MWNTs. The MW of the synthesized resin decreased with an increase in MNWT loading. The apparent viscosity was found to be decreased with an increase in the MWNT content, which was mainly attributed to the decrease in PAN MW. The systems showed a shear thickening behavior when the MWNT content was 0.53 wt%. Of course, this number has no significance, unless the effects of MWNT purity and quality (kinks, etc.), length and diameter of MWNTs, MWD of polymer, and the total solid content of composite solution system are properly characterized. The differences in the MWNT containing samples could have originated from any or a combination of aforementioned factors. While the complex viscosity of the pure PAN solution decreased continuously with increasing frequency (shear thinning), the MWNTs containing systems showed an initial increase in the lower frequency range, and then a continuous decrease at higher frequencies. This was attributed to the reduced mobility of PAN chains in the neighborhood of MWNTs at lower frequencies and then the possible orientation of MWNTs and PAN chains at higher frequencies.

1.3.2. Electrical Conductivity of Polymer/CNT Composites

In an insulating matrix, the conductivity results from the fact that fillers like CNTs provide a continuous conductive path to the flow of electrons. The minimum concentration of filler at which a continuous conductive path is created is called percolation threshold. The percolation threshold has a strong dependence on the aspect ratio of filler. For example, an infinitely long SWNT (with infinite aspect ratio)

containing composite fiber will show a very low percolation threshold than a composite fiber containing SWNT with a finite aspect ratio (e.g. 100). CNTs have been reported to possess electrical conductivity of around 10^5-10^8 S/m [48-50]. SWNT, DWNT, and MWNT have very high current carrying capacity of around 10^8-10^9 A/cm^2 [51-53], but can still show electrical breakdown if exposed to high enough electric potential [54]. The reason for such a large range of reported electrical conductivity and current density is that these properties are not only influenced by the inherent electronic structure of CNT (chirality), but also by external factors such as temperature and chemical environment [50, 55]. The CNTs show voltage induced electrostatic charging with charges distributed uniformly on the surface of the tube and very high concentration of charges at tube ends [56, 57].

Inasmuch as CNTs have a strong tendency for aggregation or agglomeration, the degree of exfoliation and/or dispersion is important for the percolation of nanotube-polymer composite system. Furthermore, the quality and purity of tubes and the density of defects strongly affect the results. Chemical pre-treatments and/or functionalization of nanotubes will alter the results. Since previous researchers studied effects in different matrices, different results would be expected because the overall conductivity should be a function of both nanotube and matrix's conductivity. Obviously, then volume fraction for electrical percolation should be lower in case of conducting polymers than in case of insulating polymers.

In essence, factors such as geometrical placement of tubes, type (metallic, semi-conducting), length, orientation, conformation (elongated/coil), degree of exfoliation, degree/density/type of defects, chemical functionalization, and different matrices could

be the reasons for differences in values of volume fraction for electrical percolation. Sandler *et al.* [58] reported very low percolation threshold of 0.0025 wt% with MWNTs in epoxy matrix and Bryning *et al.* [59] reported very low percolation threshold of 0.000052 wt% with SWNTs in epoxy matrix. Whereas Coleman *et al.* [60] reported a very high concentration of ~ 9 wt% for percolation threshold of SWNT in poly-p-phenlyenevinylene-co-2,5-dioctoxy-m-phenylenevinylene (PmPV) matrix. Kymakis *et al.* [61] reported a very high concentration of ~ 11% for percolation threshold of SWNT in poly(3-octylthiophene). Generally, CNT based composites show electrical conductivity within the range of 10^{-2} to 10^{-5} S/m [62, 63], but significantly high values of around 480 S/m [64], 1600 S/m [65], 5780 S/m [66], 15000 S/m [24] have also been reported.

Du *et al.* [67] studied the percolation threshold in a SWNT/PMMA melt spun composite fiber and found alignment and concentration to be main factors affecting percolation. The highest conductivity was observed for slightly aligned, rather than isotropic, SWNTs. There are studies which show opposite trends about the effect of CNT alignment on electrical conductivity of composites [68, 69].

In this work, different CNT containing composite fibers were made which can be used in many applications where a moderate electrical conductivity is required. The semiconducting nature of composite fiber can be used to make antistatic materials (electronics housing, cabinets, etc.). Electrostatic discharge (ESD) due to a high voltage surge can be damaging for electronic components. For this reason, the electronic components are shipped inside antistatic materials. In case of plastics, the main materials that are currently used include ionic conductors, carbon black filled plastics and vacuum metalized plastics [70]. Ionic conductors absorb the moisture from atmosphere and form

a conductive surface. A low humidity or dry atmosphere can render them ineffective. The re-use of the container is limited because the material can be washed-off. Carbon black particles can wear off from the surface and loose performance and create pollution (in clean room environment). In case of metalized plastics, the adhesion to the polymer is difficult to achieve.

The carbon nanotubes provide an attractive alternative to the aforementioned materials. When properly incorporated and dispersed, because of their large aspect ratio, the carbon nanotube are entangled and/or bound with the polymer system. Therefore the CNTs will not wear-off with time and a reasonable conductivity can be achieved at very low percolation. The conductivity of the composite can actually be tailored within wide ranges by changing the length, concentration, orientation, and type of nanotubes.

In this study, PAN/CNT and PEK/CNT fibers were processed with different types of CNTs in different concentrations. The processing, structure, and properties of various PAN/CNT fibers are discussed in Chapters 2, 3, and 4. The effect of CNT diameter and concentration on PAN/CNT fiber spinnability and electrical conductivity are discussed in Chapters 5 and 6. The processing, structure, and properties of PEK/CNT fibers are discussed in Chapter 7.

1.4. References

1. Wade B and Knorr R. "Acrylic Fiber Technology and Applications" (edited by J C Masson), Marcel Dekker, Inc., New York 1995:37-67.

2. Bajaj P. "Manufactured Fibre Technology" (edited by V. B. Gupta and V. K. Kothari), Chapman and Hall, London 1997:406-456.

3. Zoltek. Pyron Brochure: http://www.zoltek.com/pdf/PyronBrochure.pdf (accessed on 08/03/2008).

4. Masson JC. Acrylic Fiber Technology and Applications (edited by J C Masson) 1995:167-195.

5. Frusher BG. "Acrylic Fiber Technology and Applications" (edited by J C Masson), Marcel Dekker, Inc., New York 1995:197-257.

6. Henrici-Olivé G and Olivé S. Advances in Polymer Science 1979;32:123-152.

7. Capone GJ. "Acrylic Fiber Technology and Applications" (edited by J C Masson), Marcel Dekker, Inc., New York 1995:69-103.

8. Baojun Q, Jian Q, and Lhanlong Z. Textile Asia 1989;20(4):40-56.

9. Baojun Q, Ding P, and Zhenqiou W. Advances in Polymer Technology 1986;6(4):509-529.

10. Stoyanov AI. Journal of Applied Polymer Science 1982;27(1):235-238.

11. Dumbleton JH and Bell JP. Journal of Applied Polymer Science 1970;14(9):2402-2406.

12. Hersh SP, Higgins TD, and Krause HW. Journal of Applied Polymer Science 1963;7(2):411-442.

13. Wang Y-X, Wang C-G, and Yu M-J. Journal of Applied Polymer Science 2007;104(6):3723-3729.

14. Hou C, Liang Y, and Wang CG. Journal of Polymer Research 2005;12(1):49-52.

15. Juan Chen H-YG, Xing-Guang Dong, Cheng-Guo Wang,. Journal of Applied Polymer Science 2007;106(1):692-696.

16. Kobashi T and Takao S. US Patent 4535027 1985.

17. Kobashi T and Takao S. US Patent 4658004 1987.

18. Kobashi T and Takao S. US Patent 4659529 1987.

19. Neuert R. US Patent 6228966 B1 2001.

20. JST. http://www.jst.go.jp/kisoken/nano/ryoikisites/fukusites/theme-e/subject/03-shinohara.html (accessed on 08/03/2008).

21. Sreekumar TV, Liu T, Min BG, Guo H, Kumar S, Hauge RH, and Smalley RE. Advanced Materials 2004;16(1):58-61.

22. Min BG, Sreekumar TV, Uchida T, and Kumar S. Carbon 2005;43(3):599-604.

23. Chae HG, Sreekumar TV, Uchida T, and Kumar S. Polymer 2005;46(24):10925-10935.

24. Guo H, Sreekumar TV, Liu T, Minus M, and Kumar S. Polymer 2005;46(9):3001-3005.

25. Liu J, Wang T, Uchida T, and Kumar S. Journal of Applied Polymer Science 2005;96(5):1992-1995.

26. Ko F, Gogotsi Y, Ali A, Naguib N, Ye H, Yang GL, Li C, and Willis P. Advanced Materials 2003;15(14):1161-1165.

27. Pirlot C, Willems I, Fonseca A, Nagy JB, and Delhalle J. Advanced Engineering Materials 2002;4(3):109-114.

28. Petrov P, Lou XD, Pagnoulle C, Jerome C, Calberg C, and Jerome R. Macromolecular Rapid Communications 2004;25(10):987-990.

29. Ge JJ, Hou H, Li Q, Graham MJ, Greiner A, Reneker DH, Harris FW, and Cheng SZD. J. Am. Chem. Soc. 2004;126(48):15754-15761.

30. Koganemaru A, Bin Y, Agari Y, and Matsuo M. Advanced Functional Materials 2004;14(9):842-850.

31. Ye H, Lam H, Titchenal N, Gogotsi Y, and Ko F. Applied Physics Letters 2004;85(10):1775-1777.

32. Hou HQ and Reneker DH. Advanced Materials 2004;16(1):69-+.

33. Ra EJ, An KH, Kim KK, Jeong SY, and Lee YH. Chemical Physics Letters 2005;413(1-3):188-193.

34. Hou H, Ge JJ, Zeng J, Li Q, Reneker DH, Greiner A, and Cheng SZD. Chem. Mater. 2005;17(5):967-973.

35. Chae HG, Minus ML, and Kumar S. Polymer 2006;47(10):3494-3504.

36. Chae HG, Minus ML, Rasheed A, and Kumar S. Polymer 2007;48(13):3781-3789.

37. Liu T, Sreekumar TV, Kumar S, Hauge RH, and Smalley RE. Carbon 2003;41(12):2440-2442.

38. Exploratory Tests for Fire Barrier Materials-United States Consumer Product Safety Commission. http://www.cpsc.gov/library/foia/foia05/os/uff8.pdf (accessed on 02/24/2009) 2004.

39. Perepelkin KE. Fibre Chemistry 2003;35(6):409-416.

40. Hu G, Zhao C, Zhang S, Yang M, and Wang Z. Polymer 2006;47(1):480-488.

41. Potschke P, Fornes TD, and Paul DR. Polymer 2002;43(11):3247-3255.

42. Potschke P, Abdel-Goad M, Alig I, Dudkin S, and Lellinger D. Polymer 2004;45(26):8863-8870.

43. Abdel-Goad M and Potschke P. Journal of Non-Newtonian Fluid Mechanics 2005;128(1):2-6.

44. Lin B, Sundararaj U, and Potschke P. Macromolecular Materials and Engineering 2006;291(3):227-238.

45. Du FM, Scogna RC, Zhou W, Brand S, Fischer JE, and Winey KI. Macromolecules 2004;37(24):9048-9055.

46. Defeng Wu LW, Ming Zhang,. Journal of Polymer Science Part B: Polymer Physics 2007;45(16):2239-2251.

47. Wang B, Li J, Wang H, Jiang J, and Liu Y. Macromolecular Symposia 2004;216(1):189-194.

48. Kasumov AY, Khodos II, Ajayan PM, and Colliex C. Europhysics Letters 1996;34:429-434.

49. McEuen PL, Fuhrer MS, and Hongkun P. Nanotechnology, IEEE Transactions on 2002;1(1):78-85.

50. Ebbesen TW, Lezec HJ, Hiura H, Bennett JW, Ghaemi HF, and Thio T. Nature 1996;382(6586):54-56.

51. Chen YF and Fuhrer MS. Current-carrying capacity of semiconducting carbon nanotubes. 2006. pp. 3403-3407.

52. Wei BQ, Vajtai R, and Ajayan PM. Applied Physics Letters 2001;79(8):1172-1174.

53. Moon S, Song W, Kim N, Lee JS, Na PS, Lee SG, Park J, Jung MH, Lee HW, Kang KH, Lee CJ, and Kim J. Nanotechnology 2007;18(23).

54. Umnov AG and Mordkovich VZ. Applied Physics a-Materials Science & Processing 2001;73(3):301-304.

55. Collins PG, Bradley K, Ishigami M, and Zettl A. Science 2000;287(5459):1801-1804.

56. Li CY and Chou TW. Applied Physics Letters 2006;89(6).

57. Ke CH and Espinosa HD. Journal of Applied Mechanics-Transactions of the Asme 2005;72(5):721-725.

58. Sandler JKW, Kirk JE, Kinloch IA, Shaffer MSP, and Windle AH. Polymer 2003;44(19):5893-5899.

59. Bryning MB, Islam MF, Kikkawa JM, and Yodh AG. Advanced Materials 2005;17(9):1186-1191.

60. Coleman JN, Curran S, Dalton AB, Davey AP, McCarthy B, Blau W, and Barklie RC. Physical Review B 1998;58(12):R7492.

61. Kymakis E, Alexandou I, and Amaratunga GAJ. Synthetic Metals 2002;127(1-3):59-62.

62. Kilbride BE, Coleman JN, Fraysse J, Fournet P, Cadek M, Drury A, Hutzler S, Roth S, and Blau WJ. Journal of Applied Physics 2002;92(7):4024-4030.

63. McNally T, Pötschke P, Halley P, Murphy M, Martin D, Bell SEJ, Brennan GP, Bein D, Lemoine P, and Quinn JP. Polymer 2005;46(19):8222-8232.

64. Ramasubramaniam R, Chen J, and Liu H. Applied Physics Letters 2003;83(14):2928-2930.

65. Guo H, Rasheed A, Minus ML, and Kumar S. Journal of Materials Science 2008;43(13):4363-4369.

66. Liu J, Rasheed A, Minus ML, and Kumar S. Journal of Applied Polymer Science 2008;xxx(xxx):NA.

67. Du F, Fischer JE, and Winey KI. Physical Review B (Condensed Matter and Materials Physics) 2005;72(12):121404-121404.

68. Haggenmueller R, Gommans HH, Rinzler AG, Fischer JE, and Winey KI. Chemical Physics Letters 2000;330(3-4):219-225.

69. Choi ES, Brooks JS, Eaton DL, Al-Haik MS, Hussaini MY, Garmestani H, Li D, and Dahmen K. Journal of Applied Physics 2003;94(9):6034-6039.

70. Wallace GG, Spinks GM, Kane-Maguire LAP, and Teasdale PR. "Conductive Electroactive Polymers: Intelligent Materials Systems" 2002:11-12.

CHAPTER 2

PAN/MWNT COMPOSITE FIBERS

PAN/MWNT composite fibers were spun using dry-jet wet spinning. The composite fibers were characterized and compared with control PAN fiber in terms of thermal shrinkage and heat exotherms related to PAN cyclization. The dispersion of MWNTs in PAN matrix and interaction between PAN and MWNTs are also discussed. The effect of MWNT on PAN crystallinity, PAN crystal size and orientation of both PAN and MWNTs was studied using WAXD, and is reported here. The effects of thermal stabilization on composite fiber microstructure and tensile properties are also reported and discussed.

2.1. Experimental

2.1.1. Materials

PAN with a viscosity average molecular weight of 100,000 g/mol (100K) was obtained from Japan Exlan Co. Ltd. The PAN polymer contains methyl acrylate (MA) as comonomer in 6-7 mole %. The MWNTs powder (purity 95%) was obtained from Iljin Nanotech Co. (Korea). Reagent grade DMF (purity 99.8%) was obtained from Sigma-Aldrich.

2.1.2. PAN/MWNT Solution Preparation

PAN powder was dried under vacuum at around 80 to 90 ˚C for over 2 days. PAN powder was dissolved in DMF (~ 20 g PAN in 100 ml DMF) using an impeller while

keeping the solution temperature below 90 ˚C. For MWNT dispersion in DMF, 1 g MWNT powder was sonicated in 300 ml DMF for 24 h (bath sonicator, Branson 3510-MT, 100W, 42 kHz). The sonicated dispersion of MWNT/DMF was added into the PAN/DMF solution, while stirring at above 300 rpm. Since MWNTs were sonicated in dilute concentrations in DMF, to achieve the desired MWNTs concentration in PAN/MWNT/DMF solution, the MWNT/DMF dispersion was added in batch-wise manner. Stirring was continued and excess DMF was removed using vacuum distillation while keeping the solution temperature below 90 ˚C. Figure 7 shows the set-up for solution preparation. A solution with a final desired solid content (PAN + MWNT) in PAN/MWNT/DMF was used for fiber spinning.

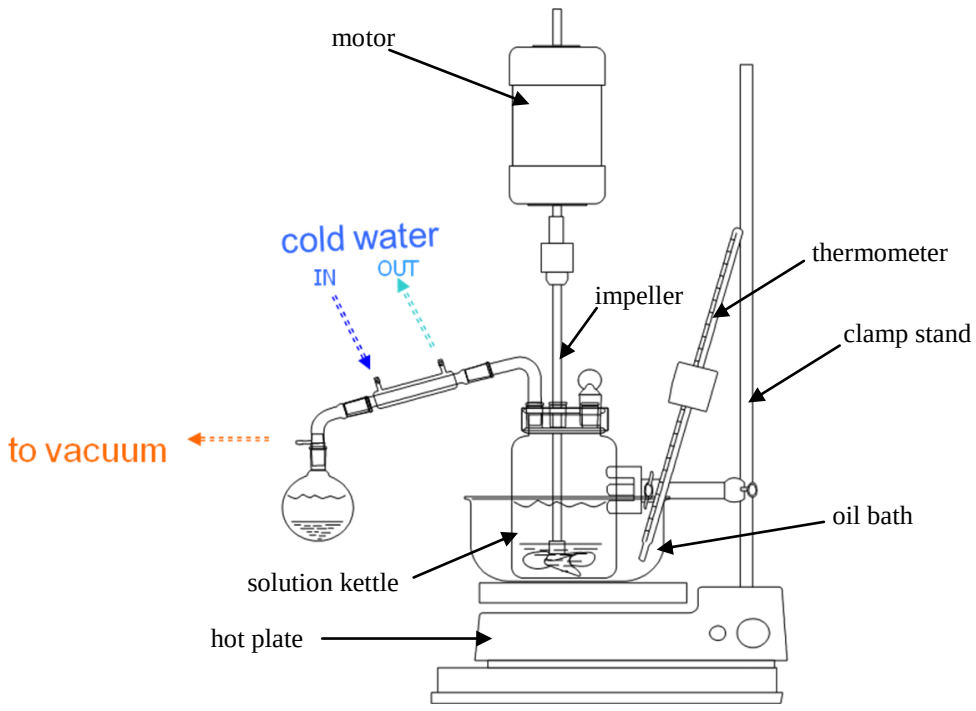

Figure 7. Set-up for solution preparation.

2.1.3. PAN/MWNT Fiber Spinning

The composite fibers with four different concentrations of MWNTs (5, 10, 15, and 20 % MWNT w.r.t. PAN) were spun using dry-jet wet-spinning. The PAN/MWNT/DMF solution was poured into the barrel (with 16 mm internal diameter). The solution was extruded through a spinneret of 250 µm diameter. Figure 8 shows the fiber spinning set-up. The ratio of DMF/water for coagulation baths is also shown in Figure 8. The coagulation baths were kept at room temperature. The continuous fiber spinning was achieved by optimizing temperature of the barrel, polymer extrusion rate through spinneret, and fiber take-up speeds. The fiber spinning conditions and parameters are listed in Table 1. Heat drawing was conducted in between first and second take-up systems in boiling water. The high MWNT containing fibers could not be drawn as much as control PAN fiber and the draw ratio decreased with increase in MWNT content. Fibers were dried in a vacuum oven at 50 ˚C for 7 days.

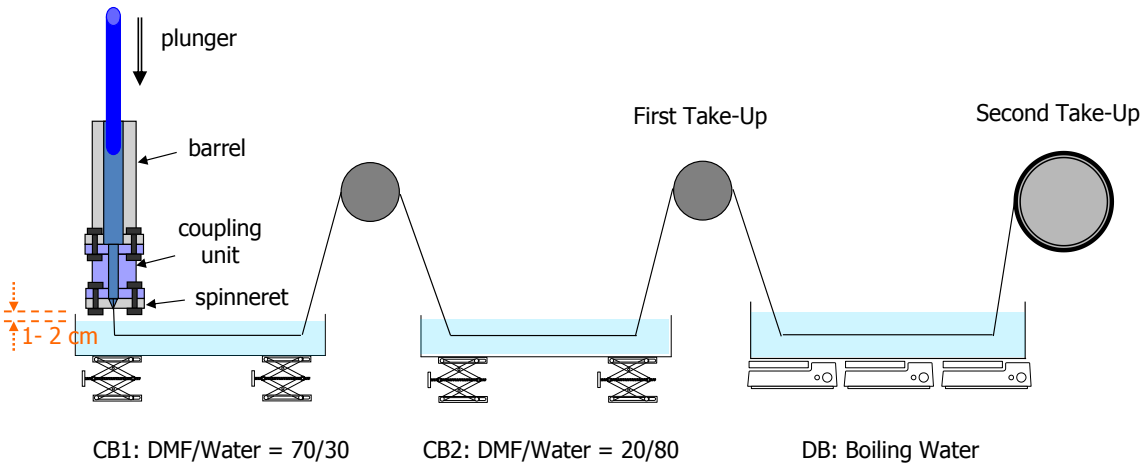

Figure 8. Solution spinning set-up for MWNT/PAN composite fiber. CB1: first coagulation bath; CB2: second coagulation bath; DB: drawing bath.

Table 1. Processing Parameters for Different PAN/MWNT Fiber Spinning

MWNT (%)*	**0**	**5**	**10**	**15**	**20**
Solid Content** (g/100ml DMF)	22	20	20	~17.7	16
Plunger Rate (mm/min)	4.45	2	2.5	4	7.23
Spinning Temperature (˚C)	18	18	50[$]	18	18
Drawing Spools Speed[$$] (m/min)	8 → 48	8 → 48	8 → 40	8 → 32	35 _8 → 20
Heat Draw Ratio in Boiling Water*** (~ 100 ˚C)	6	6	5	4	2.5

* MWNT weight percentage with respect to PAN weight
** Total amount of PAN and MWNT in DMF
[$] Temperature was increased to 50 ˚C in order to decrease solution viscosity to achieve continuous spinning. For other high MWNT solutions, solid content was reduced.
[$$] Drawing spools speed represents the speeds of first and second take-up rolls
*** Heat draw ratio is the ratio of the speeds of second and first take-up roll

2.1.4. Fiber Embedding and Cross-Section Using Microtomy

A mixture of methyl-methacrylate (75 ml), dibutyl phthalate (15 ml), and benzoyl peroxide (2.5 g) was prepared and mechanically shaken for 10 minutes (to completely dissolve benzoyl peroxide and homogeneously mix the solution). A bundle of fibers mounted on a fiber tab was placed into a small polypropylene bottle. The bottle was filled with the embedding solution and left to cure at 35 – 40 ˚C for 1 day. After being cured, the fiber cross-sections were microtomed (using Microm HM 355 S rotary microtome, Thermo Scientific) into thin sections of 5 – 10 μm. The cutting blade was made up of tungsten carbide. The thin slices were mounted on to a SEM stub for image analysis. The aforementioned procedure was used for making cross-sections of all the fibers made for this study. Figure 9 shows the SEM images of the cross-sections of various composite fibers.

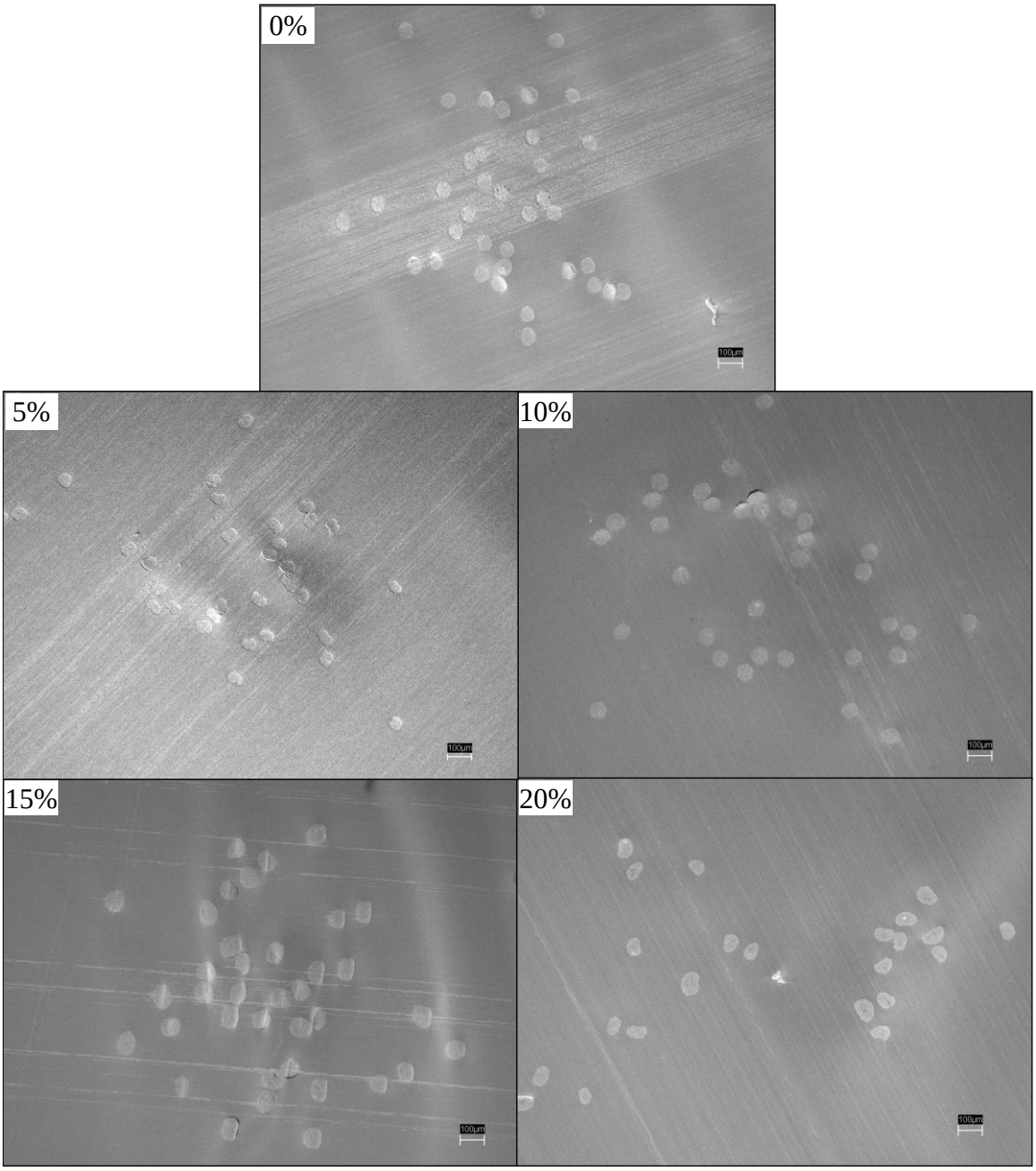

Figure 9. SEM images of the cross-sections of 0, 5 10, 15, and 20% MWNT reinforced PAN fibers. Scale bar in each image is 100 μm long.

2.1.5. PAN/MWNT Fiber Stabilization

The fibers were stabilized in a box furnace (Lindberg, 51668-HR Box Furnace 1200 C, Blue M Electric) in air. Figure 10 shows the set-up for fiber stabilization where

the fiber bundles are hung over quartz rods. A stress of 2 MPa was applied through the clamps to keep the fibers under tension. For stabilization, the furnace is heated from room temperature (~ 25 ˚C) to 260 ˚C at the rate of 1 ˚C/min then kept at 260 ˚C for 8 h before being cooled down to room temperature. Figure 11 shows the thermal cycle for the stabilization process.

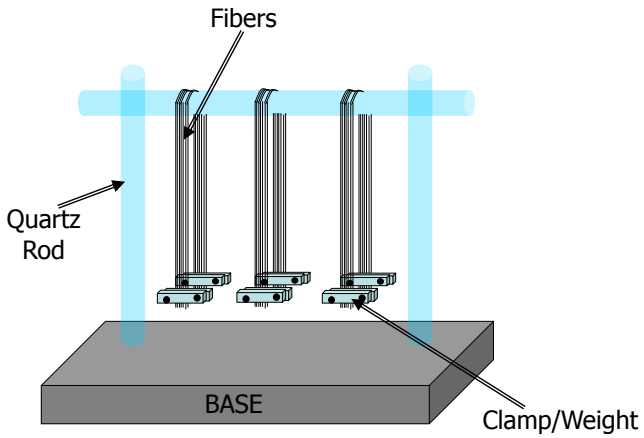

Figure 10. Set-up for fiber stabilization.

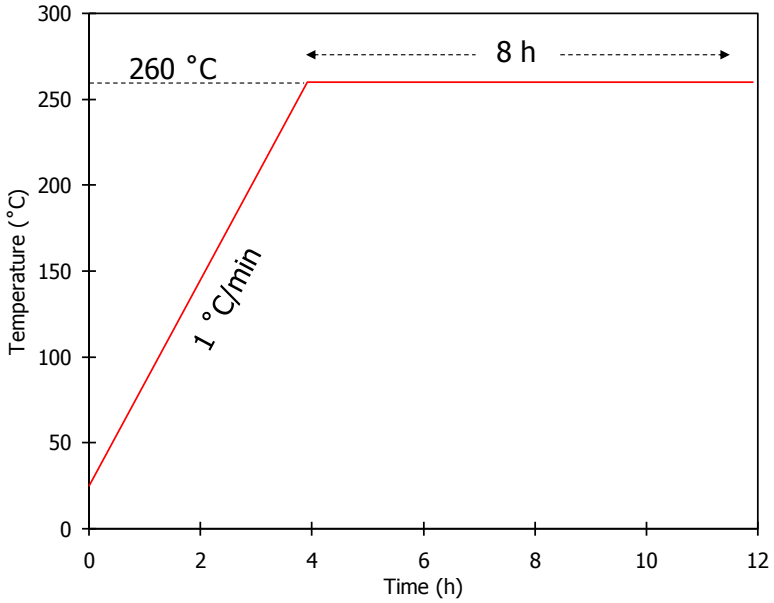

Figure 11. Thermal cycle for fiber stabilization.

2.2. Testing and Characterization of Composite Fibers

The linear density of the fiber was measured in the unit of tex, where 1 tex equals the weight of 1000 m long fiber in grams. The tensile properties and dynamic mechanical properties of the fibers were obtained using RSA III solids analyzer (Rheometric Scientific Co.). A gauge length of 25 mm was used for both tensile and dynamic-mechanical tests. For tensile testing, 10-20 specimens were tested for each fiber sample. A crosshead speed of 0.25 mm/s was used for tensile testing. The dynamic mechanical properties were measured between -120 to 150 ˚C at three different frequencies of 0.1, 1 and 10 Hz at 1 ˚C/min heating rate. The fiber shrinkage was measured using thermomechanical analyzer (TMA 2940, TA Instruments) when the fiber was heated from 40 to 180 ˚C under nitrogen or air (flow rate of 50 ml/min). The stress development/relaxation in the fiber, as the fiber is heated under isostrain conditions, was also studied using TMA. The thermal stability and char yield in nitrogen and air atmosphere was measured using thermogravimetric analyzer (TGA). Unless otherwise specified, the fibers were heated in a platinum pan at a heating rate of 5 ˚C/min up to 1000 ˚C. The DSC was used to study exothermic reactions during PAN stabilization.

The PAN crystallinity, crystal size, orientation, and MWNT orientation were measured using wide-angle X-ray diffraction (WAXD) on a multi-filament bundle using Rigaku Micromax-002 (operated at 45 kV, 0.66 mA, and λ = 1.5418 Å). Diffraction patterns were obtained using Rigaku R-axis IV + + detection system. The diffraction patterns were analyzed using AreaMax V. 1.00 and MDI Jade 6.1. A LEO SEM (Model 1530; operated between 5 to 15 kV) was used for the microstructure analysis (fiber surfaces, tensile fracture surfaces, MWNTs or CNFs imaging, MWNT or CNFs

dispersion in PAN matrix). The specimens were coated with a thin gold film (using sputtering method) to conduct away impinging electrons and to prevent the examined region from localized heating. The ac electrical conductivity of the composite fiber was measured at 60 Hz using a four-probe (four point probe head made by Signatone) coupled with Keithley 2400 Sourcemeter. Figure 12 shows the representative image of a fiber sample with four silver point contacts at ~ 2 mm apart. The voltage was measured as the current was increased from 1 nA to 0.5 mA. The maximum current and voltage limits for the set-up were 0.5 mA and 210 V, respectively.

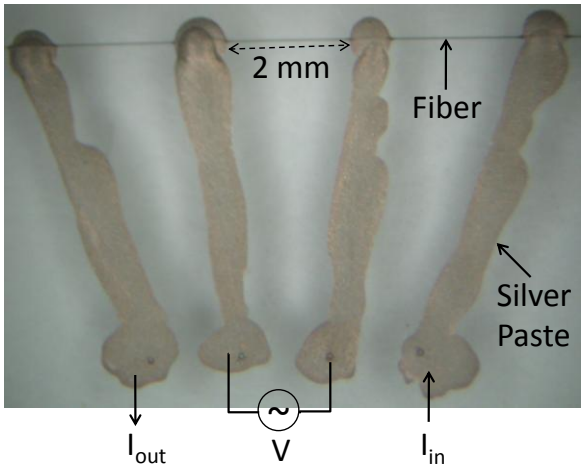

Figure 12. Four-point contact for electrical conductivity measurement.

2.3. Results and Discussion

2.3.1. Thermogravimetric Analysis (TGA)

TGA was conducted in both nitrogen and air on PAN composite fibers reinforced with different concentrations of MWNTs. Figure 13 shows the TGA results of various fibers under nitrogen atmosphere. Assuming that all the DMF traces are removed when the temperature reaches at 170 ˚C (boiling point of DMF is 153 ˚C), from the mass loss

by 170 ˚C it was observed that fibers containing MWNTs had only 1% DMF and the neat PAN fiber had 5% DMF. Since all the fibers were dried under vacuum for 7 days at 50 ˚C, it can be concluded that somehow MWNT reinforced fibers had lower affinity for DMF (that's why most of the DMF was removed during drying). This could be due to the difference in the microstructures of control PAN and composite fibers.

A compact microstructure would exclude the DMF molecules in order to be compact and a more open amorphous region would easily release DMF under vacuum. The composite fibers could have a combination of both compacted regions and open microstructure. This point is further discussed later (Section 2.5). Figure 14 shows the TGA of various fibers under air. A similar DMF loss before 170 ˚C was observed under air also.

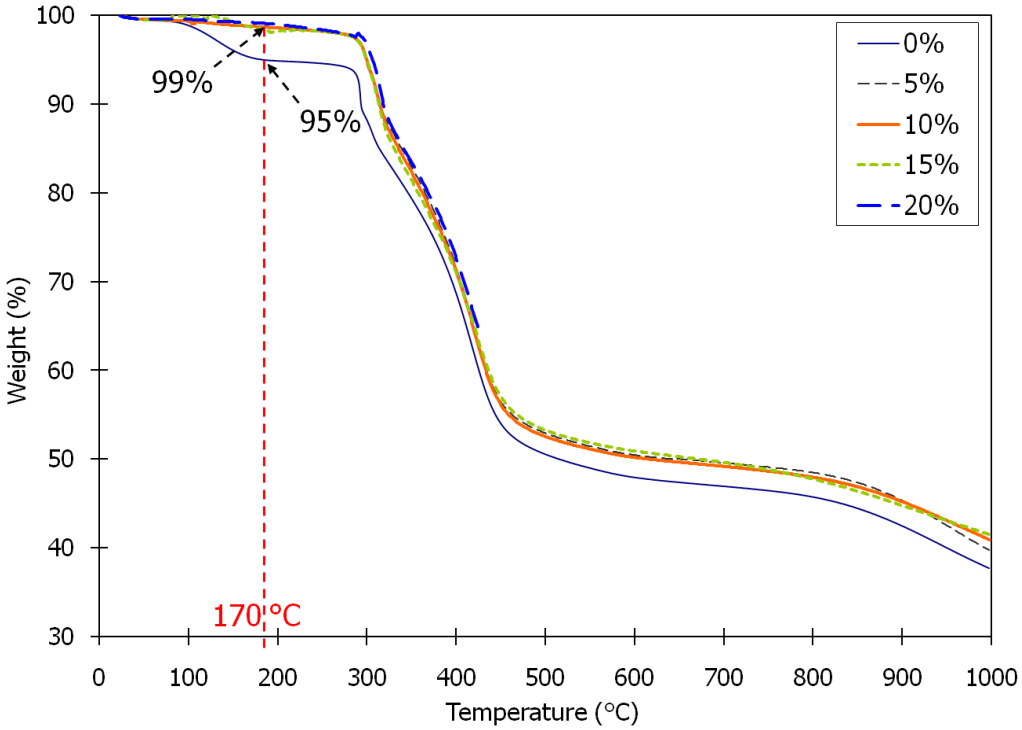

Figure 13. TGA of PAN/MWNT composite fibers under nitrogen (temperature ramp rate: 5 ˚C/min). 0, 5, 10, 15 and 20% correspond to samples A1d, B1a, B2a, B3a, and B4a in Tables 2 and 3.

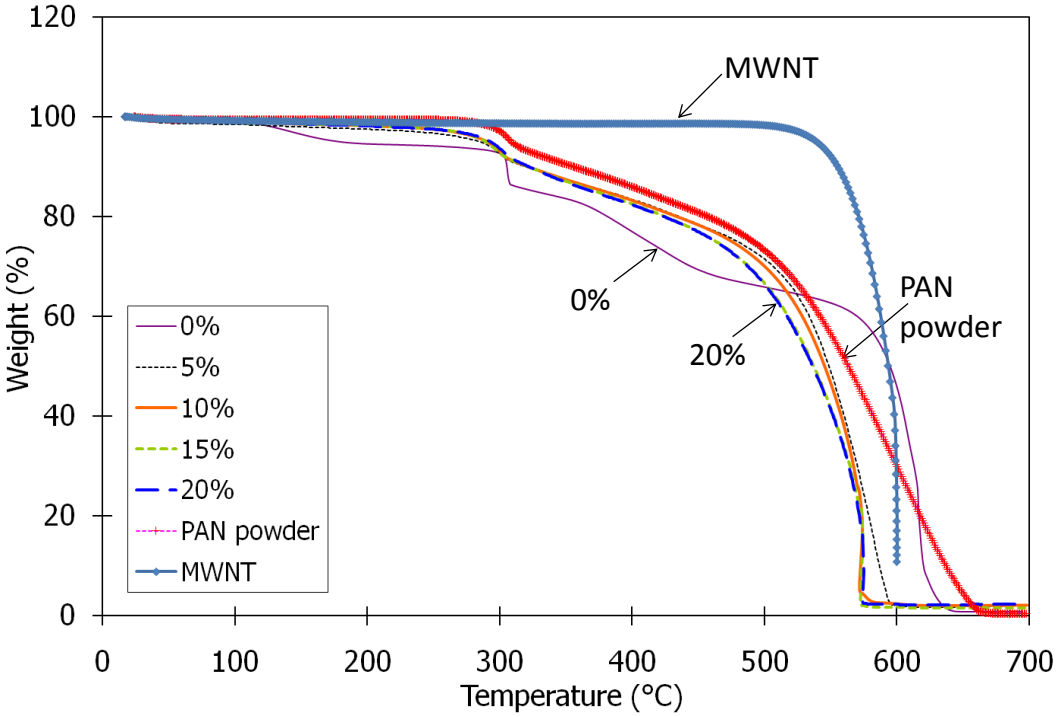

Figure 14. TGA of PAN/MWNT composite fibers under air (temperature ramp rate: 5 ˚C/min). 0, 5, 10, 15 and 20% correspond to samples A1d, B1a, B2a, B3a, and B4a in Tables 2 and 3.

Under nitrogen, all composite fibers have higher thermal stability and char yield than control PAN fiber, but degradation behavior is similar for all the fibers. In air atmosphere, the final degradation temperature was highest for the control PAN fiber. The composite fibers showed lower degradation temperature than control PAN fiber. All the composite fibers showed a two-step degradation behavior, which was similar to the degradation behavior of PAN powder. The control PAN fiber showed a three-step degradation behavior. The lower degradation temperature of MWNTs than control PAN suggests that MWNTs degradation must have catalyzed the degradation in composite fibers, which consequently reduced their degradation temperature.

Table 2. Tensile Properties of Control PAN 100K Fibers

Sample	DR	Linear Density (tex)	Tensile Strength (N/tex)	Tensile Modulus (N/tex)	Strain to Failure (%)	Toughness (N/tex)
A1a	3	5.3	0.13 ±0.00	5.5 ±0.2	10.6 ±0.4	--
A1b	4	3.9	0.18 ±0.01	6.7 ±0.2	10.4 ±0.5	0.013 ±0.001
A1c	5	3.2	0.24 ±0.01	7.5 ±0.3	10.8 ±0.6	--
A1d	6	3.0	0.25 ±0.00	8.0 ±0.0	9.3 ±0.0	0.015 ±0.001
A1e	7	3.4	0.34 ±0.01	9.4 ±0.3	9.8 ±0.4	--
A1f	8	2.0	0.36 ±0.01	10.9 ±0.4	7.4 ±0.7	0.017 ±0.002
A1g	9	3.0	0.34 ±0.01	10.0 ±0.3	6.9 ±0.4	--
A1h	10	3.3	0.39 ±0.01	9.7 ±0.2	8.4 ±0.3	0.019 ±0.001

Table 3. Tensile Properties of PAN/MWNT Composite Fibers After Heat-Drawing

Sample	MWNT (%)	DR	Linear Density (tex)	Tensile Strength (N/tex)	Tensile Modulus (N/tex)	Strain to Failure (%)	Toughness (N/tex)
B1a	5	6	1.5	0.34 ±0.01	10.8 ±0.2	6.8 ±0.4	0.014 ±0.002
B2a	10	5	2.1	0.23 ±0.01	8.9 ±0.5	5.7 ±0.5	0.008 ±0.001
B3a	15	4	3.6	0.20 ±0.01	7.9 ±0.5	5.8 ±0.5	--
B4a	20	2.5	2.0	0.14 ±0.00	7.3 ±0.3	3.5 ±0.3	--

2.3.2. Differential Scanning Calorimetry (DSC) Studies

DSC showed the exotherms (Figure 15) related to PAN stabilization and cyclization. Since the polymer used in this case is not a homopolymer, both free radical and ionic type of nitrile cyclization reactions occur which lead to observed exotherms. Figure 16 shows the mechanisms of the two types of reactions. For a homopolymer, only a single exotherm is expected which occurs through free-radical mechanism at relatively high temperature. Chae *et al.* [1] used PAN homopolymer and showed a single exotherm with a peak at around 280 ˚C. The presence of comonomers allows the nitrile copolymerization to occur through ionic route which can occur at relatively lower

temperature. Though the ionic mechanism requires lower energy to start and can occur at a lower temperature, the reaction itself is slower than the radical mechanism. Therefore, the two mechanisms can overlap or occur simultaneously during a particular temperature range. Invariably, the composite fibers showed a larger total heat of exotherm than the control PAN fiber. The heats of exotherm for 0, 5, 10, and 15% MWNT containing fibers were 2230, 4040, 2390, and 4630 J/g, respectively. The corresponding peak temperatures for the exotherm were 264, 264, 268, and 267 ˚C, respectively.

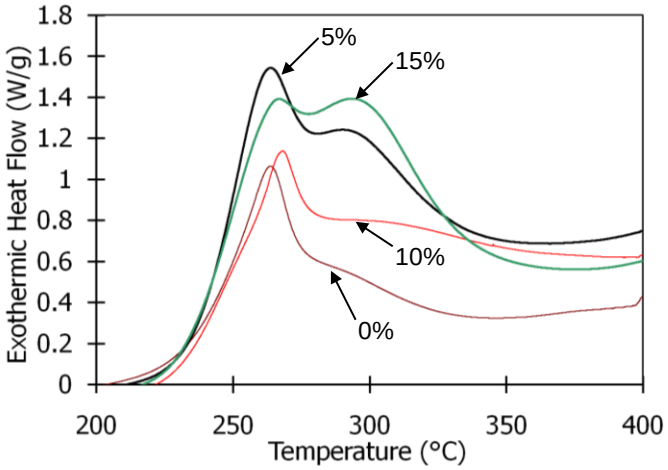

Figure 15. DSC plots of PAN/MWNT composite fibers in air at a heating rate of 1 ˚C/min. 0, 5, 10, and 15% correspond to samples A1d, B1a, B2a, and B3a in Tables 2 and 3.

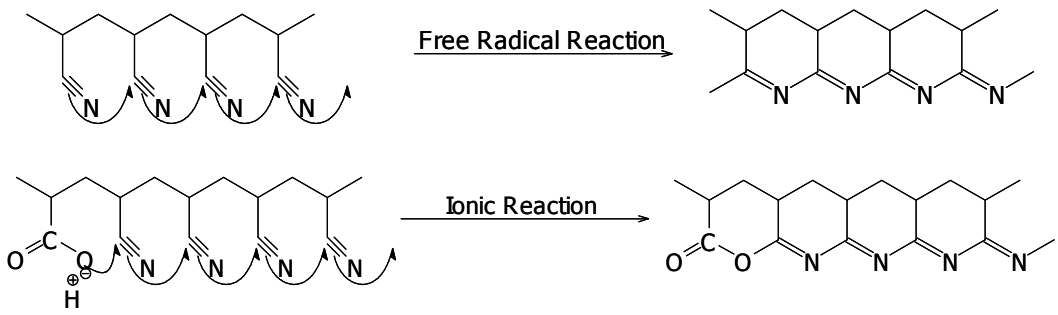

Figure 16. Mechanisms of the PAN exothermic reactions during cyclization. (adapted from [2])

2.3.3. Thermomechanical Analysis (TMA)

As shown in Figure 17, the composite fibers showed lower shrinkage than the neat PAN fiber. The lower shrinkage can be attributed to the presence of MWNTs, which constrained the movement of PAN molecular chains. Additionally, the onset of fiber shrinkage shifted to higher temperature (delayed shrinkage) after the addition of MWNTs. In the presence of MWNTs, a lot of polymer chains come in contact with MWNTs and consequently their movement is constrained. This also increases the T_g of polymer (shown in Section 2.3.6). The shrinkage, which begins at around T_g, is therefore delayed in the presence of MWNTs.

Chae *et al.* [3] reported the thermal shrinkage for control PAN and 5 wt.% MWNT/PAN composite fiber to be around 14 and 8 %, respectively. These values are much smaller than reported here, which is due to the fact that Chae *et al.* [3] used a much higher stress (~ 15 MPa) during the testing than that is used in this study (~ 1 MPa). Layden [4] studied the effect of stress on the thermal shrinkage of PAN fiber and found that shrinkage decreased with increase in applied stress.

2.3.4. Linear Density of Fibers After Heat-Drawing and After Thermal Stabilization

Figure 18 shows the linear density of various fibers before and after stabilization. The variation in linear density of fibers at the heat drawn stage is due to variation in the diameter of the fibers. The linear fiber density after stabilization was found to increase. This increase is due to several factors including the conversion of linear PAN molecules into ladder type of structure and an increase in fiber diameter due to axial shrinkage. During the formation of ladder type structure, lighter elements like hydrogen are removed

by forming volatile products. Stabilization in air atmosphere also introduces heavier elements like oxygen into the ladder structure which leads to an increase in fiber density.

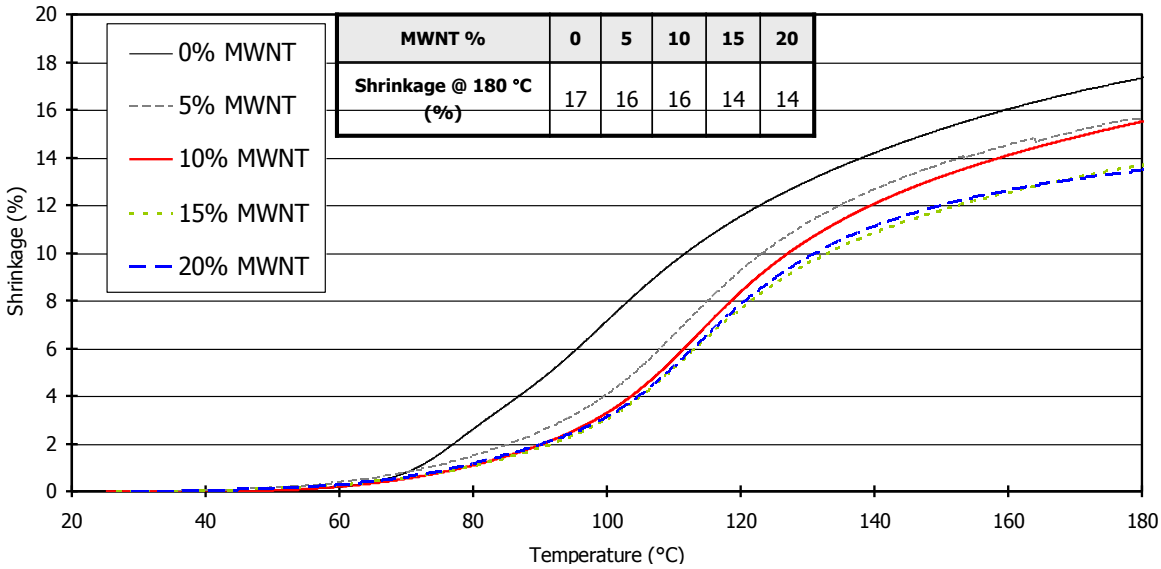

MWNT %	0	5	10	15	20
Shrinkage @ 180 °C (%)	17	16	16	14	14

Figure 17. Fiber shrinkage measured from the TMA (N_2 flow rate: 50 ml/min; temperature ramp rate: 5 °C/min; preload: ~ 1 MPa). 0, 5, 10, 15 and 20% correspond to samples A1d, B1a, B2a, B3a, and B4a in Tables 2 and 3.

PAN polymer degradation leads to the emission of volatile products, CO, CO_2, H_2O, HCN, H_2 and leads to weight loss in the fiber. PAN polymer degradation [5-12], volatile product emanation during stabilization [10-12], and the mechanism of stabilization [5-7, 13-28] have been extensively studied. These physico-chemical processes are strongly influenced by the physical conditions and chemical environment during stabilization [1, 18, 21, 23, 24, 29-41]. The physical factors include tension applied to the fiber and the chemical environment includes purity of air, percentage of oxygen in the air, gas flow rate, and basic/acidic environment of the stabilization.

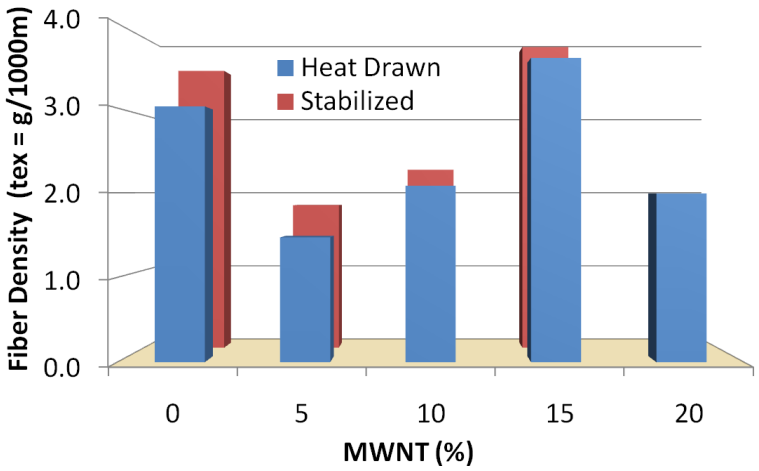

Figure 18. Linear density of different PAN/MWNT composite fibers before and after stabilization. 0, 5, 10, 15 and 20% correspond to samples A1d, B1a, B2a, B3a, and B4a in Tables 2 and 3.

Figure 19 shows the shrinkage and weight loss measurements of the various PAN/MWNT composite fibers after stabilization. The 5% and 10% MWNT composite fibers showed larger shrinkage as compared to the control PAN fiber. These results should not be compared with previous results where a lower shrinkage was observed in the case of composite fibers when the fibers were heated under an inert atmosphere of nitrogen (TMA studies). This is due to the fact that a different load, atmosphere, heating rate, and ultimate temperature were used in two cases. A significantly higher weight loss was observed during stabilization in case of 10% and 15% MWNT fiber whereas 0% and 5% showed almost the same percentage weight loss. A higher weight loss can be due to inefficient stabilization and degradation of PAN in case of 10 and 15% MWNT fiber, because a stabilized ladder type of structure has higher thermal stability at elevated temperatures. This further suggests that high MWNT containing fibers have more defective structure than low or no MWNT containing fibers. As shown in Section 2.3.8,

the agglomerated regions of MWNTs were observed in 10% and higher MWNT containing fibers.

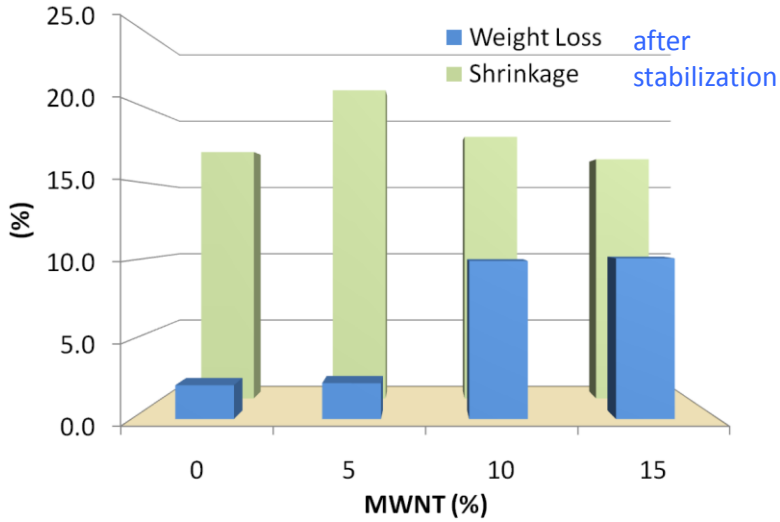

Figure 19. Shrinkage and weight loss in various PAN/MWNT composite fibers after stabilization (initial stress during stabilization ~ 2 MPa). 0, 5, 10, and 15% correspond to samples A1d, B1a, B2a, and B3a in Tables 2 and 3.

2.3.5. Tensile Properties of Fibers After Heat-Drawing and After Thermal Stabilization

The fiber tensile properties after heat-drawing and stabilization are listed in Tables 2 to 4. Generally, for heat-drawn control PAN fiber, both tensile strength and modulus increased with an increase in draw ratio (DR), and strain to failure decreased. A decrease in the tensile properties after DR 8 suggests that DR 8 is the optimum DR for control PAN fiber made in this study. For control PAN fibers, the toughness was found to improve with an increase in DR, and 5% MWNT containing fibers showed similar toughness as control PAN, but 10% MWNT containing fiber showed lower toughness than both control PAN and 5% MWNT composite fiber. After heat drawing, the 5%

MWNT composite fiber showed the highest strength and modulus among all the composite fibers.

Comparing the values in Tables 2 and 3, it is clear that at the same DR, the tensile strength and modulus of a composite fiber is either better or comparable with the control PAN fiber (e.g. 15% MWNT fiber at a DR of 4 has a tensile strength and modulus of 0.20 N/tex and 7.9 N/tex, which are higher than control PAN 100K fiber at DR 4 which has a tensile strength and modulus of 0.18 N/tex and 6.7 N/tex). The tensile strength of the 5% MWNT containing fiber (0.34 N/tex) is higher than 5% SWNT containing fiber (0.30 N/tex) spun by Sreekumar *et al.* [42] and 5% SWNT (0.28 N/tex), 5% DWNT (0.26 N/tex), and 5% CNF (0.27 N/tex) fibers spun by Chae *et al.* [3]. However, for 5% MWNT containing fibers, Chae *et al.* [3] reported a similar value of 0.34 N/tex.

The overall tensile properties were found to be reduced after the stabilization (Table 4). This reduction in properties can be understood from the microstructural changes that take place during the stabilization process, which include voids and crack formation due to volatile products emanation and structural shrinkage. After stabilization, both 0 and 5% MWNT fibers showed comparable tensile strength and strain to failure, but these properties decreased with further addition of MWNTs (10% and 15%). However, the modulus was found to be increased with increasing percentage of MWNTs. This is despite lower draw ratio for the high CNT containing fibers. The 20% MWNT composite fiber being very brittle could not be stabilized in the present geometry. The tensile strength of the 5 and 10% MWNT containing stabilized fibers were higher than 5 and 10% SWNT containing stabilized fibers (0.08 N/tex and 0.11 N/tex) by Sreekumar *et al.* [43].

Figure 20 shows the SEM images of the tensile fractured specimens. A fibrillated failure was observed in case of 0, 5, 10, and 15 % MWNT reinforced fiber but the 20 % MWNT fiber showed a more brittle type of failure.

Table 4. Tensile Properties of PAN/MWNT Composite Fibers After Stabilization

Sample	MWNT (%)	DR	Linear Density (N/tex)	Tensile Strength (N/tex)	Tensile Modulus (N/tex)	Strain to Failure (%)
A1d	0	6	3.6	0.14 ±0.00	6.4 ±0.3	5.1 ±0.4
B1a	5	6	1.8	0.14 ±0.00	6.6 ±0.3	5.1 ±0.7
B2a	10	5	2.3	0.13 ±0.01	7.1 ±0.5	3.5 ±0.4
B3a	15	2.5	3.9	0.11 ±0.00	7.1 ±0.4	2.3 ±0.4

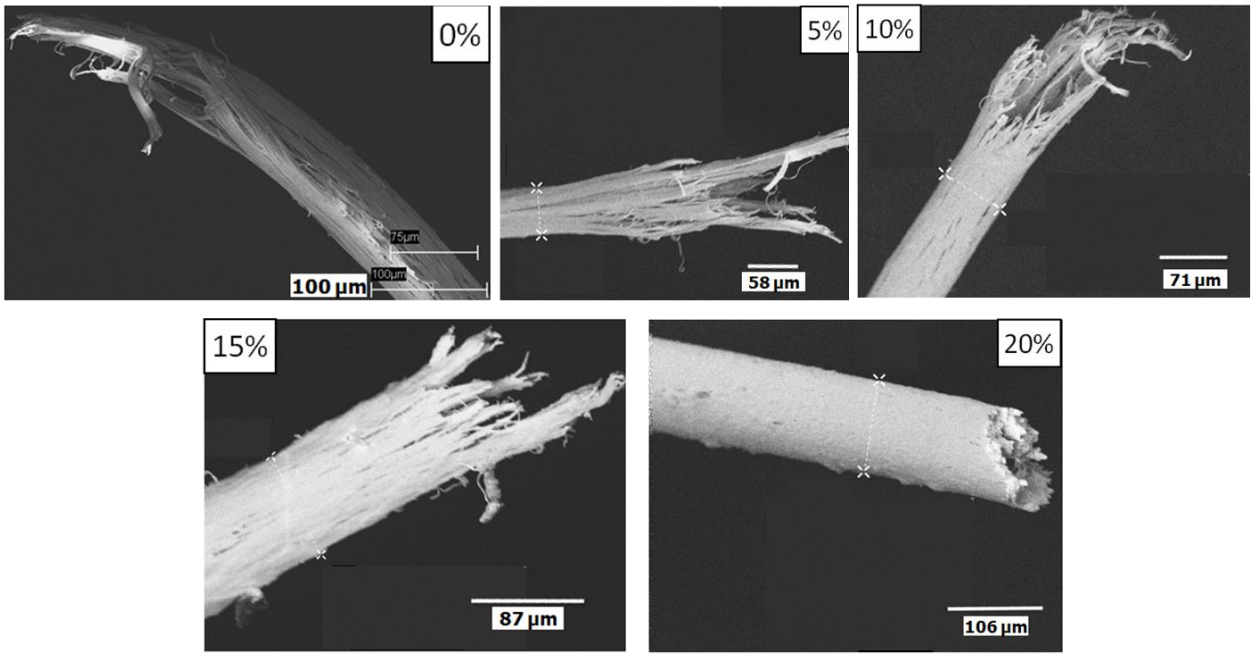

Figure 20. SEM images of tensile fracture specimens of various heat-drawn PAN/MWNT fibers. 0, 5, 10, 15 and 20% correspond to samples A1d, B1a, B2a, B3a, and B4a in Tables 2 and 3.

Figures A1 through A4 in Appendix A show the SEM images of the cross-sections of the tensile fractured specimens of the stabilized fibers. The stabilized fibers did not show a fibrillated type of failure but showed more of a brittle type of failure, which is characteristic of the stabilized fibers. The higher weight loss in the MWNT containing composites fibers at higher loadings of MNWTs (as mentioned in the Section 2.3.4) was evident from the larger voids seen in the MWNT containing fibers. The voids are larger near the periphery and smaller near the core region of the fiber. Additionally, the larger voids near the periphery are elongated in a direction perpendicular to the periphery. The fact that stabilization progresses from the surface to the core, the outer region of the fiber is more exposed to air and volatile products therefore larger voids are created.

2.3.6. Dynamic Mechanical Analysis (DMA)

The storage modulus trend (Figure 21) for different concentration of MWNTs is in agreement with values obtained from the tensile test (Table 3). For control PAN fiber, only the fiber with DR 6 was tested for dynamic mechanical properties. At lower temperatures, the dynamic mechanical properties of the neat PAN fiber were found to be close to the 15% MWNT reinforced PAN fibers. However, both 5% and 10% MWNT reinforced fibers showed higher modulus than the control PAN fiber. At temperatures higher than 40 ˚C, all composite fibers showed significantly higher modulus than neat PAN fiber. The modulus of all composite fibers at 100 ˚C is nearly 5 times than that of control PAN fiber. The difference in the moduli among different MWNT content composite fibers decreased with increase in temperature. At nearly 100 ˚C, all composite

fibers had nearly the same storage modulus. The reported DMA results are for 1 Hz frequency, but DMA testing was also conducted at other frequencies (0.1 Hz and 10 Hz). Similar trend in dynamic mechanical properties was observed at other frequencies (0.1 Hz and 10 Hz).

T_g was measured from tan δ peaks from DMA (Figure 22). T_g was found to be increased by 14 ˚C for 5% composite fiber and it further increased with the successive addition of MWNTs. The magnitude of tan δ peak also reduced for composite fibers. Since tan δ is the ratio of loss modulus to storage modulus, a decrease in the magnitude of tan δ peak suggests that elastic component of the viscoelastic fiber is increased in the presence of MWNTs. This also suggests that PAN chain motion is hindered in the presence of MWNTs. Similar decrease in tan δ peak magnitude for composite fiber was also observed by others [3, 42, 44].

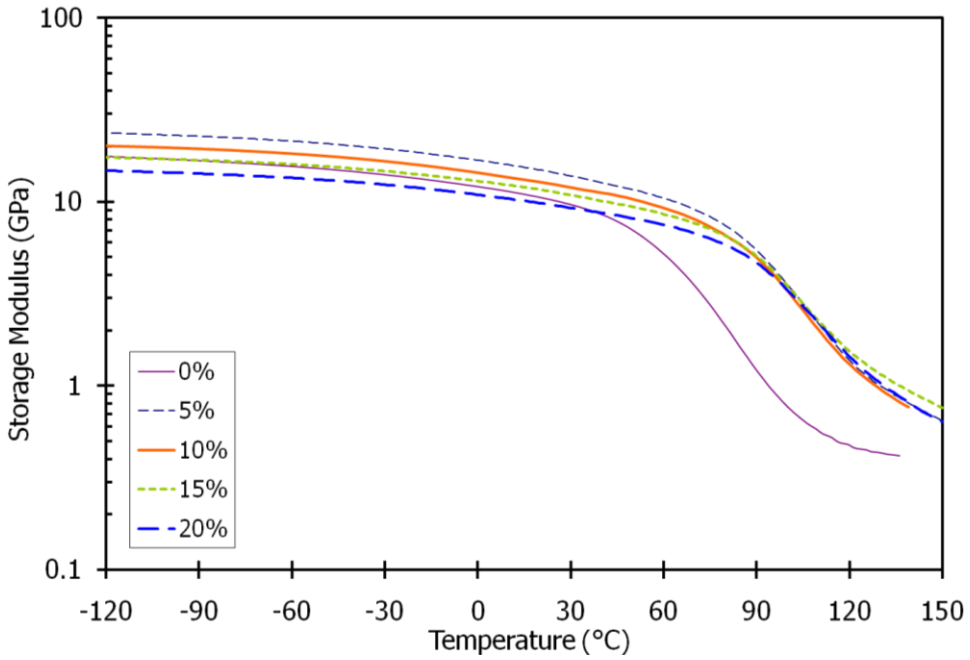

Figure 21. Storage modulus of PAN/MWNT composite fibers as measured from DMA (at 1 Hz frequency). 0, 5, 10, 15 and 20% correspond to samples A1d, B1a, B2a, B3a, and B4a in Tables 2 and 3.

The Arrhenius equation, which relates the frequency (f) with temperature (T) and activation energy (E_a) is represented by equation 7, and was used to calculate the activation energy for T_g. No particular trend was observed in the activation energies for T_g for different composite fibers.

$$f = Ae^{\frac{-E_a}{RT}} \tag{7}$$

Where, A is a constant and R is the gas constant (0.001987 kcal/mol.K).

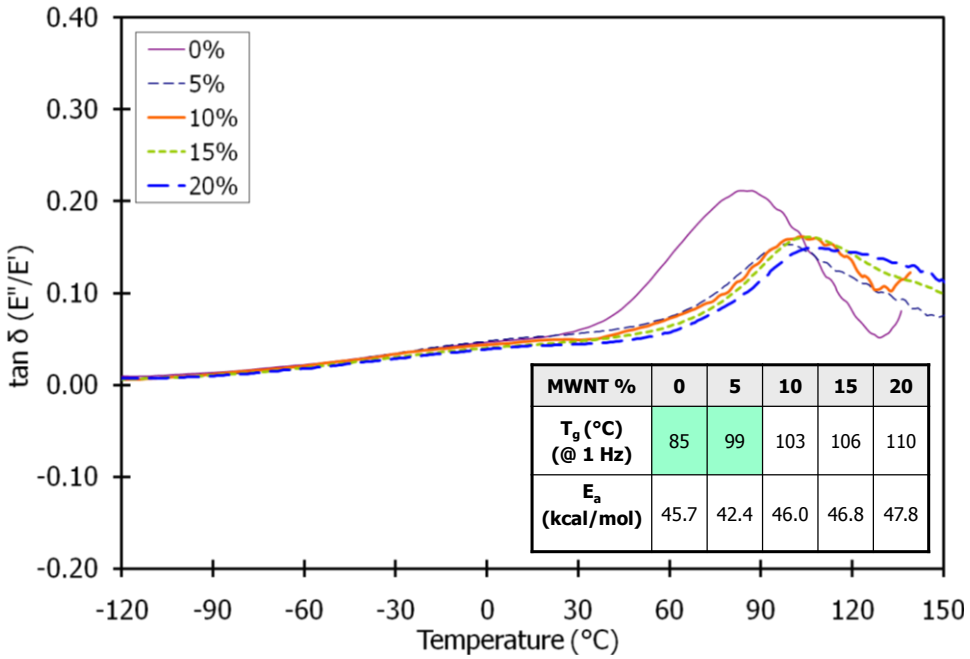

MWNT %	0	5	10	15	20
T_g (°C) (@ 1 Hz)	85	99	103	106	110
E_a (kcal/mol)	45.7	42.4	46.0	46.8	47.8

Figure 22. Tan δ curves (E"/E') measured from DMA at 1 Hz frequency. The trend was same for both 0.1 and 10 Hz frequency (tan δ curves were shifted to lower temperatures for 0.1 Hz and shifted to higher temperatures for 10 Hz). 0, 5, 10, 15 and 20% correspond to samples A1d, B1a, B2a, B3a, and B4a in Tables 2 and 3.

2.3.7. Wide Angle X-ray Diffraction (WAXD) Studies

The WAXD patterns for various control PAN (with different DR) and PAN/MWNT composite fibers (5, 10, 15, and 20%) are shown in Figures 23 and 24, respectively. The corresponding integrated radial scans and deconvoluted profiles for

both control and composite fibers are shown in Figures 25 and 26. The Herman's orientation factor for PAN chains and MWNTs was calculated using equations 8 to 11. The PAN crystal size (CS) was calculated using Scherrer's equation 12. The percentage crystallinity for PAN in the fiber was calculated from the ratio of area under PAN's crystalline peaks and area under both crystalline and amorphous peaks.

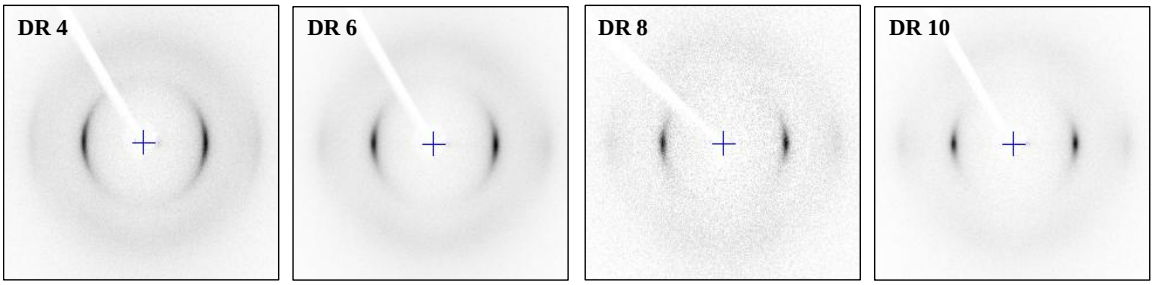

Figure 23. WAXD patterns of control PAN 100K fibers for different draw ratios. DR 4, 6, 8, and 10 correspond to samples A1b, A1d, A1f, and A1h in Table 2.

$$f_c^{hkl} = \frac{\left(3\left\langle \cos^2 \phi_{hkl} \right\rangle - 1\right)}{2} \tag{8}$$

where, $\left\langle \cos^2 \phi_{hkl} \right\rangle = 1 - 2\left\langle \cos^2 \phi \right\rangle$ (9)

where, ϕ is the azimuthal angle and $\left\langle \cos^2 \phi \right\rangle = \frac{\int_0^{\pi/2} I(\phi) \sin\phi \cos^2 \phi \; d\phi}{\int_0^{\pi/2} I(\phi) \sin\phi \; d\phi}$ (10)

This relation (equation 9) was derived from Wilchinsky's relation (equation 11) [45], which relates the three components of the orientation vector.

$$\left\langle \cos^2 \alpha \right\rangle + \left\langle \cos^2 \beta \right\rangle + \left\langle \cos^2 \gamma \right\rangle = 1 \tag{11}$$

For PAN, which has a hexagonal structure ($\alpha = \beta = \phi$, and $\gamma = \phi_{hkl}$), the equation 11 is reduced to equation 9.

$$CS = \frac{K\lambda}{(B\cos\theta)} \tag{12}$$

where, K = 0.9, λ = X-ray wavelength, B = FWHM, and θ = radial angle.

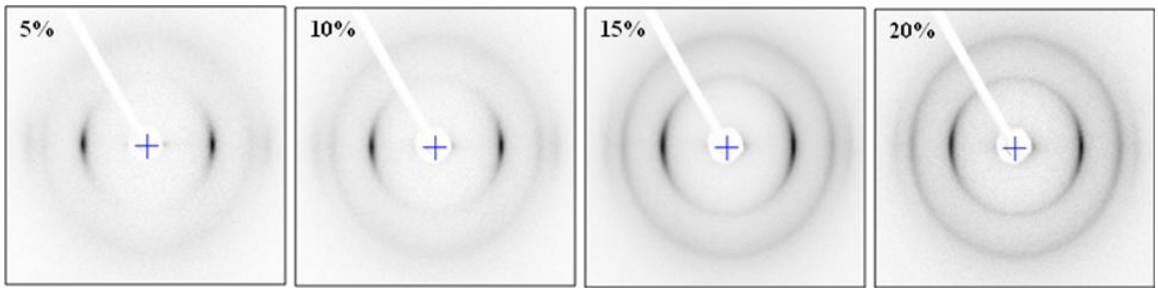

Figure 24. WAXD patterns of PAN/MWNT composite fibers with different concentration of MWNTs. 5, 10, 15 and 20% correspond to samples B1a, B2a, B3a, and B4a in Table 3.

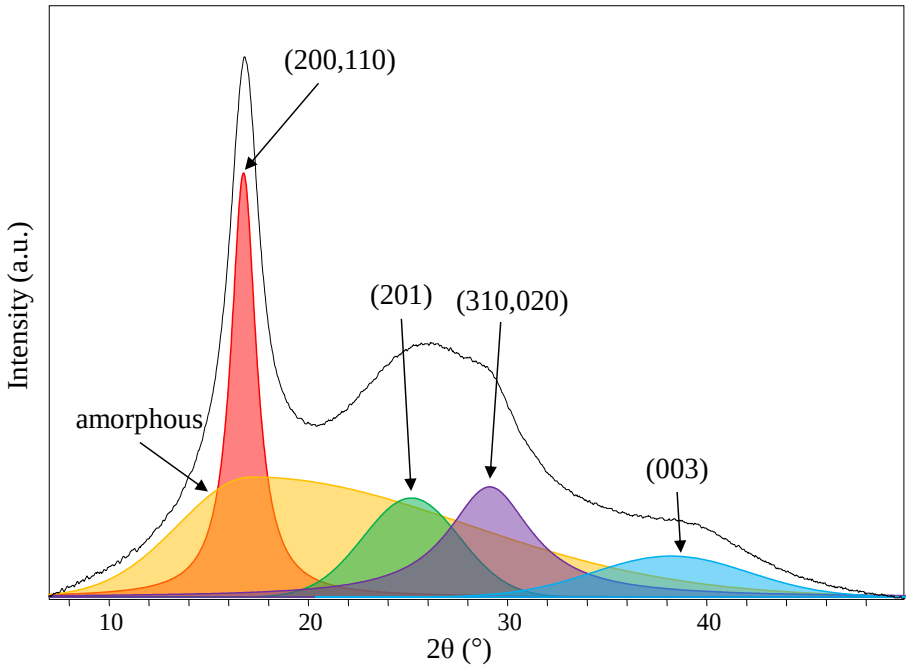

Figure 25. Integrated radial profile of the control PAN fiber of DR6. The deconvoluted profiles of the best fit are also shown. The ingrated raidal profiles of PAN fibers DR 4, 8, and 10 also looked similar.

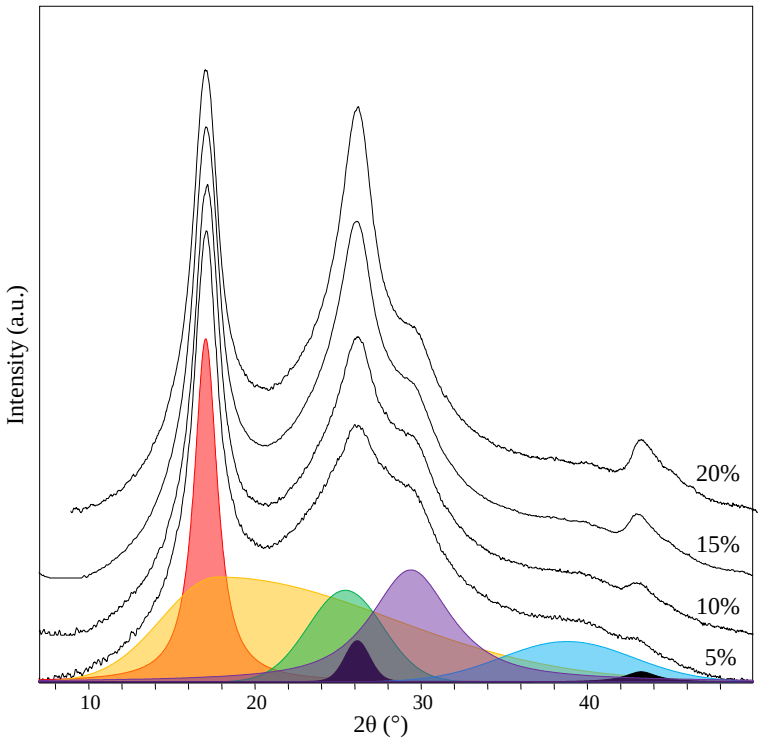

Figure 26. Integrated radial profile of the 5, 10, 15, and 20% MWNT containing PAN fibers. The representative deconvoluted profiles are also shown. The (002) MWNT peak at ~ 26˚ increased with increase in MWNT content. 5, 10, 15 and 20% correspond to samples B1a, B2a, B3a, and B4a in Table 3.

The WAXD results are tabulated in Table 5. For control PAN fibers with different draw ratios, there was no significant change or trend in the crystallinity, crystal size, or d-spacing of the fibers. However, as expected, the orientation was found to be increased with increase in heat draw-ratio. As compared to the control PAN fibers, the MWNT containing composite fibers did not show any significant change in PAN crystallinity or crystal size. In general, the d-spacing was found to be decreased in MWNT containing fibers. This could be due to a thick interphase region between MWNTs and bulk PAN. The PAN chains in the interphase region are more compact than the bulk PAN, which reduced the overall d-spacing of PAN for the MWNT containing fibers. The PAN and MWNT orientation was found to decrease with increasing MWNT content in the

composite fiber. This is attributed to the fact that fibers with increasing MWNT content could be heat-drawn with lower and lower draw ratios. The MWNT orientation was found to be lower than what has been reported before by Chae *et al.* [3]. The low orientation could due to poor dispersion and/or agglomerations of MWNTs in the fiber, which could not be oriented in the fiber drawing process (Section 2.3.8). As discussed in Section 2.3.5, large defects along with lower orientation due to lower draw ratio, in the high MWNT containing fibers, also contributed to the decrease in overall tensile properties of the fibers.

Table 5. WAXD Results for Various PAN and PAN/MWNT Composite Fibers

PAN	CNT (%)	DR	Sample	Crystallinity[1] (%)	d-spacing (PAN 2θ~17°) (Å)	f_{PAN}[2] (2θ~17°)	f_{MWNT}[2] (2θ~26°)	L_{PAN}[3] (2θ~17°) (Å)	L_{MWNT}[3] (2θ~26.3°) (Å)
100K	**0**	**4**	**A1b**	48	5.25	0.66	---	59	---
100K	**0**	**6**	**A1d**	52	5.24	0.74	---	54	---
100K	**0**	**8**	**A1f**	55	5.25	0.77	---	59	---
100K	**0**	**10**	**A1h**	48	5.26	0.81	---	60	---
100K	**5**	**6**	**B1a**	51	5.17	0.79	0.83	59	36
100K	**10**	**5**	**B2a**	48	5.12	0.73	0.60	59	35
100K	**15**	**4**	**B3a**	47	5.12	0.64	0.40	55	34
100K	**20**	**2.5**	**B4a**	54	5.13	0.55	0.32	58	38

[1] Calculated by deconvolution of integrated scan; [2] Herman's orientation factor;
[3] Calculated using Scherrer's equation from equatorial scan

2.3.8. Dispersion State of MWNTs in Composite Fibers

MWNT dispersion in the fiber was studied from SEM of the fiber cross-sections. For SEM imaging, thin slices of microtomed fiber cross-sections were used. Figure 27 shows the SEM images of fiber cross sections for different composite fibers. It seems that in case of higher concentration MWNT fibers (> 5%), in certain regions, MWNTs are

entangled with each other. However, nanotubes seem to be very well wetted with the polymer.

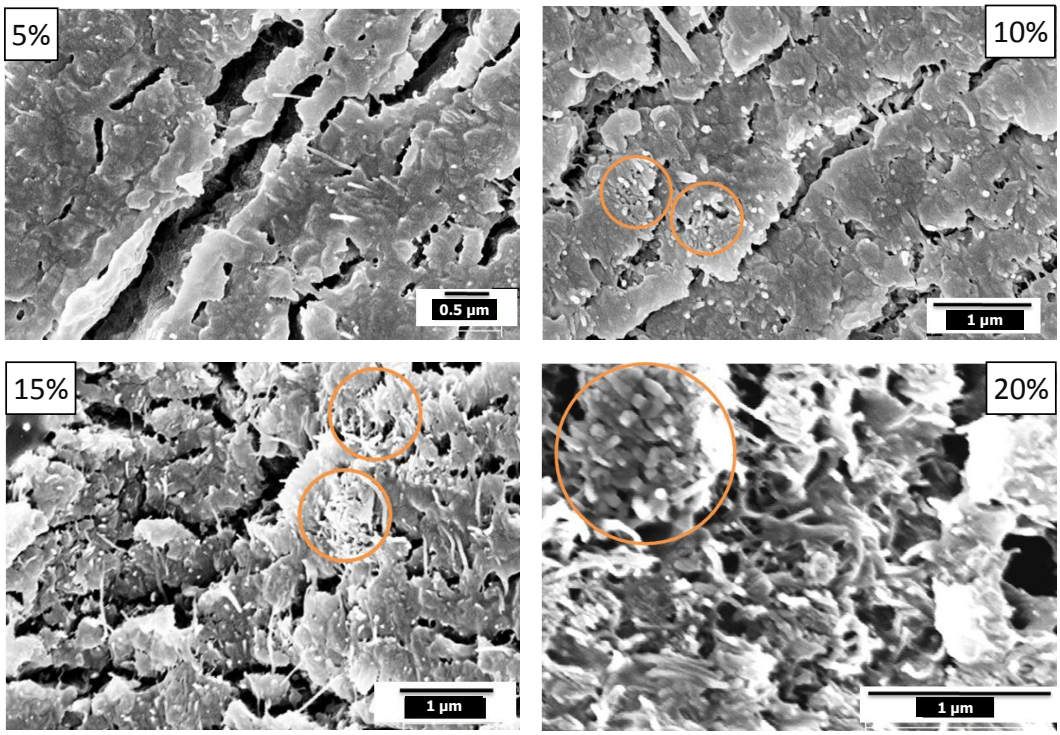

Figure 27. SEM images of the different PAN/MWNT composite fibers showing the MWNTs agglomeration in certain areas. 5, 10, 15 and 20% correspond to samples B1a, B2a, B3a, and B4a in Table 3.

To better understand the PAN/MWNT nanotube interaction and PAN coating on MWNTs, the 15% composite fiber was treated with DMF at room temperature (25 ˚C) and at 155 ˚C (boiling DMF). In each case, the resulting dispersion was poured onto a poly(tetrafluoro-ethylene) (PTFE) filter paper to collect MWNTs. MWNTs on the filter paper were repeatedly washed with excess of DMF (using both DMF at room temperature and at boiling state) to dissolve away as much as PAN polymer as possible and retain MWNTs on the filter paper. MWNTs on the filter paper were imaged using

SEM. 50 MWNTs were randomly selected from the SEM images (Figure 28) and their diameters were measured.

The SEM images of the collected MWNTs ascertained the presence of PAN coating onto the MWNTs when the MWNTs were washed with DMF at room temperature. The average diameters/thicknesses of MWNTs from neat MWNT sample, fiber dissolved and washed with room temperature DMF, and fiber dissolved and washed with boiling DMF were 27 ± 6 nm, 56 ± 10 nm, and 32 ± 7 nm, respectively. This means that the thickness range for the PAN coating on MWNTs in the case of room temperature dissolution in DMF is between 6 to 23 nm. Bar diagram in Figure 28 shows the diameter distribution of MWNTs when washed under two different conditions. A little PAN remained coated when boiled DMF was used for dissolution and washing. It is possible that molecular chains of PAN that are in the vicinity of a MWNT are more compact (lower d-spacing) and wrapped around the MWNTs, while the molecular chains away from it are not compact. It may the compacted PAN around MWNTs that remain coated onto MWNTs when washed with DMF at room temperature.

The TEM images of the sample treated with DMF at room temperature showed a coating of PAN onto MWNTs (Figure 29). Whereas the sample treated with boiling DMF showed little or no coating (Figure 30). The MWNTs seemed to be very irregular in shape and showed lot of kinks. MWNTs with bamboo type of morphologies were also observed in these samples. These defective morphologies may have direct impact on the dispersion and alignment of MWNTs in the PAN matrix and may negatively affect the fiber mechanical properties.

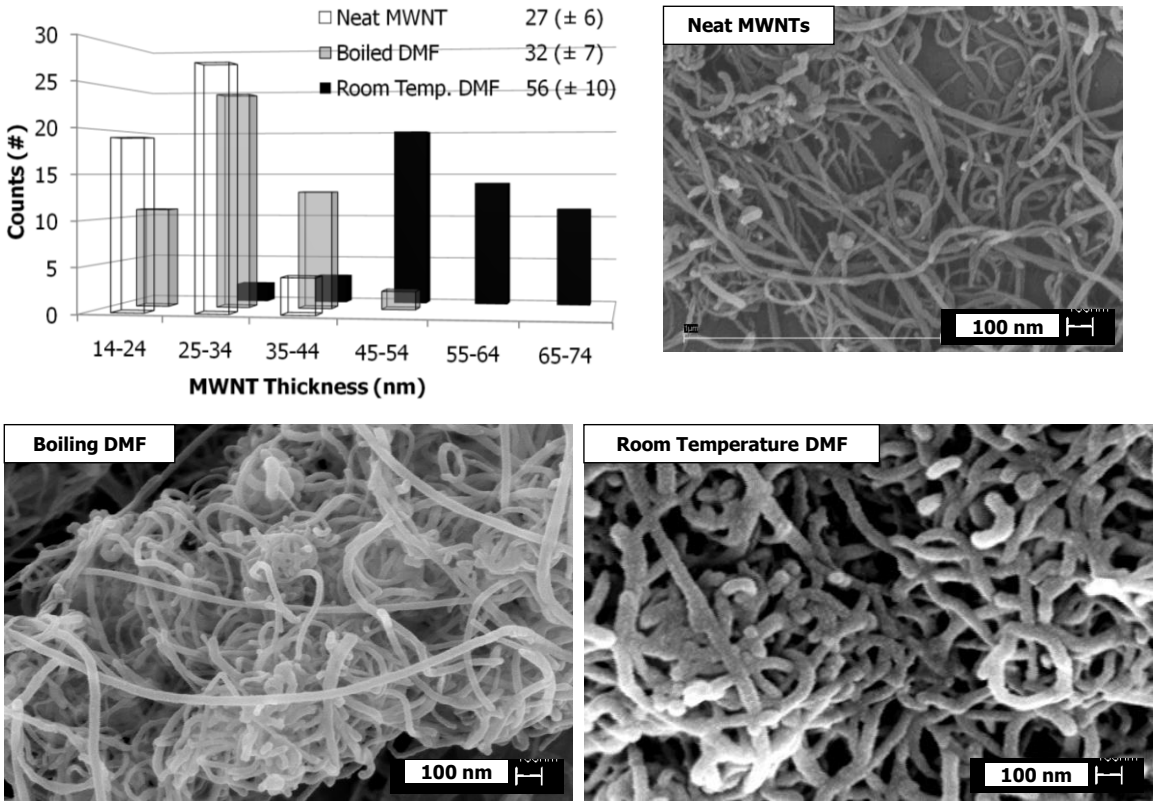

Figure 28. Top left: Diameter distribution of MWNTs for 50 random tubes from SEM images; top right: neat MWNTs; bottom left: MWNTs recovered on a PTFE filter by dissolving the 15% MWNT fiber (Sample B1c in Table 3) with boiling DMF; bottom right: MWNTs recovered on a PTFE filter by dissolving the 15% MWNT fiber with DMF at room temperature.

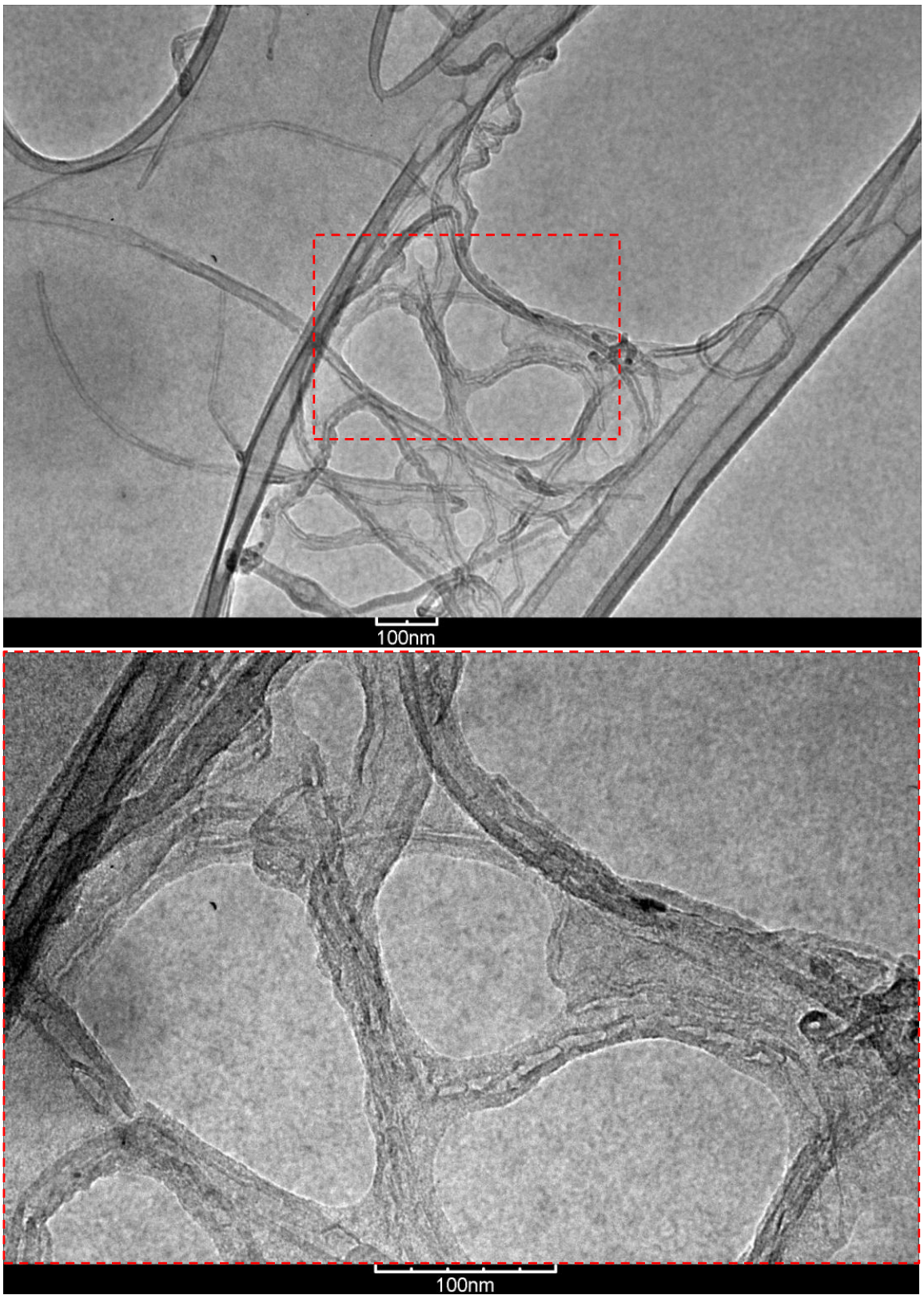

Figure 29. TEM images of the MWNTs (at different magnifications) from the 15% MWNT fiber after treatment with room temperature DMF.

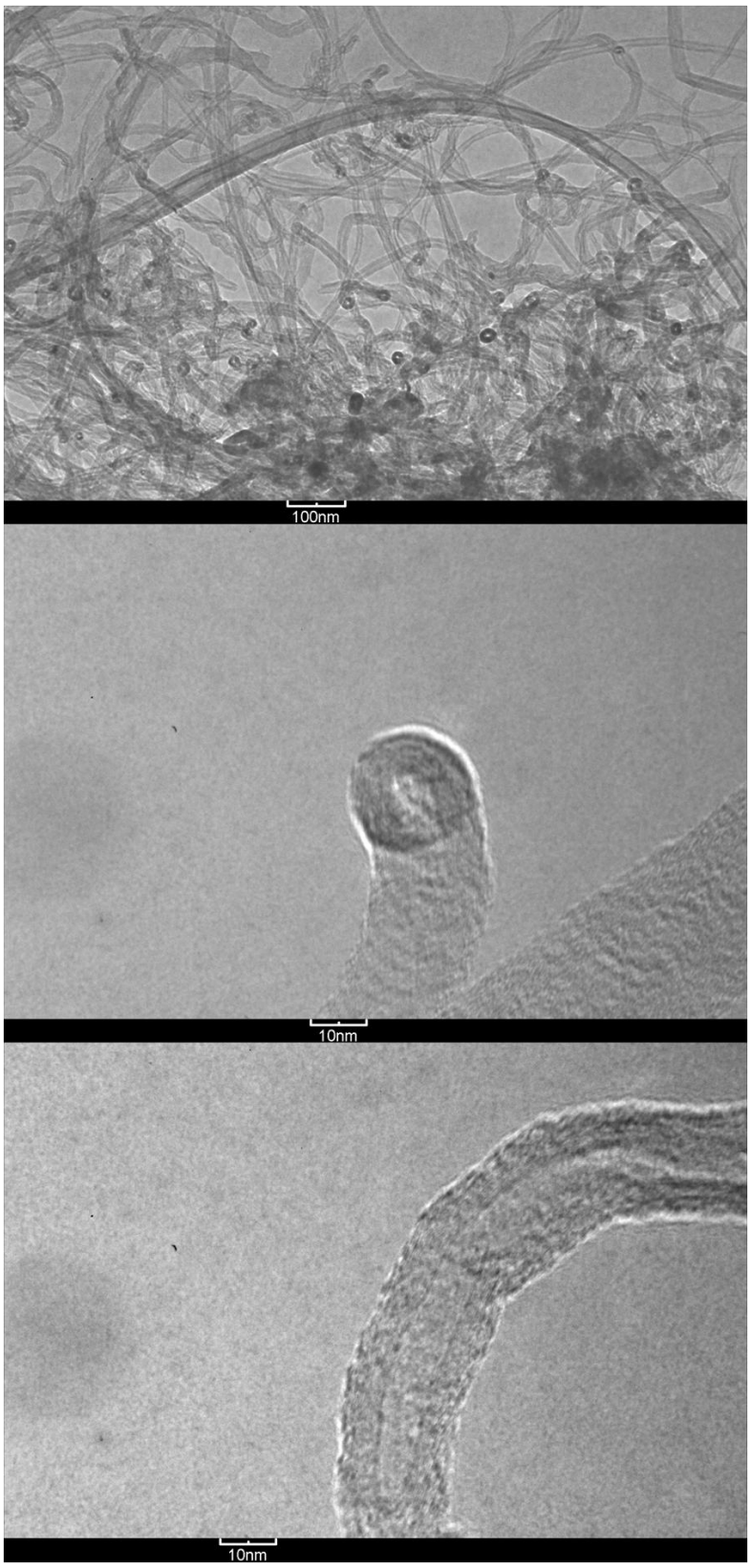

Figure 30. TEM images of the MWNTs (at different magnifications) from the 15% MWNT fiber after treatment with boiling DMF.

2.3.9. Fiber Surfaces of Different Composite Fibers

The fiber surfaces of 0, 5, 10, 15, and 20% MWNT loaded PAN fibers are shown in Figure 31. As compared to control and 5% MWNT composite fibers, the 10, 15, and 20% MWNT composite fibers showed the presence of elongated voids on the surface. The concentration of surface voids and defects increased with an increase in MWNT concentration. Along with the MWNT entanglement mentioned in the previous section, the voids and defects reduce the mechanical properties of the high MWNT containing composite fiber. As will be mentioned in section 3.2.3, similar type of voids increased with increase in CNF concentration.

2.3.10. Electrical Conductivity of PAN/MWNT Composite Fibers

The electrical conductivities of the composite fibers are listed in Table 6. The 5% MWNT composite fiber was not conductive enough to be measured by the available instrument. The 15% MWNT composite fiber showed the highest electrical conductivity, which was almost four orders of magnitude higher than that of the 10% MWNT fiber. Within the measurement error, the 20% MWNT containing fiber showed conductivity similar to that of the 15% MWNT fiber.

Table 6. Electrical Conductivity of Heat-Drawn Composite Fibers

Sample	MWNT (%)	DR	Electrical Conductivity (S/m)
B2a	10	5	$1.04 \times 10^{-4} \pm 4.22 \times 10^{-6}$
B3a	15	4	1.24 ± 1.01
B4a	20	2.5	0.61 ± 0.80

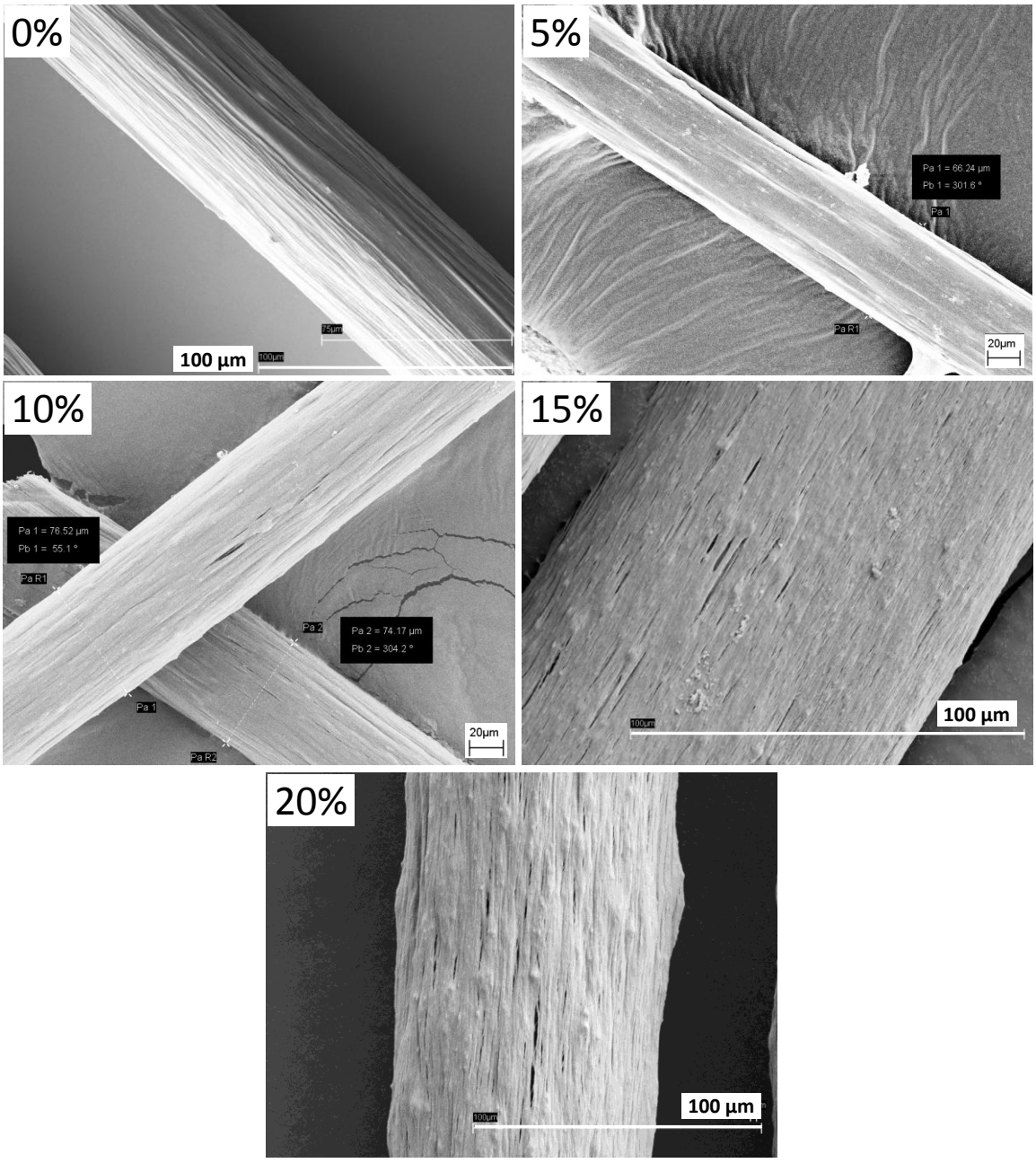

Figure 31. SEM images of the surface of 0, 5, 10, 15 and 20% MWNT containing PAN fibers. 0, 5, 10, 15 and 20% correspond to samples A1d, B1a, B2a, B3a, and B4a in Tables 2 and 3.

2.4. Second Trial of PAN/MWNT Composite Fiber Spinning

Dr. Han Gi Chae spun the 5 and 10% MWNT containing fibers using different MWNTs and PAN. Some changes were also made in the solution preparation and fiber

spinning. The new control and 5% composite fibers showed significantly high moduli than obtained before (section 2.3.5). The processing, structure, and properties of the new fibers are discusses next.

2.4.1. Materials and Fiber Spinning

The MWNTs were obtained from cheaptubes.com and PAN 100K polymer from Japan Exlan Co. Ltd. The PAN polymer contains methacrylic acid as comonomer in 3-4 mole%. Reagent grade dimethylacetamide (DMAc) (purity 99.8%) was obtained from Sigma-Aldrich.

The method for PAN/MWNT solution preparation and fiber spinning was same as reported before [3]. The 0, 5, and 10% MWNT containing fibers were drawn in two stages. In the first stage, the fibers were drawn using boiling water, and in the second stage, the fibers were drawn over a hot plate. The hot plate temperature for 0 and 5% MWNT fibers was kept at 130 ˚C and for 10% MWNT fibers it was kept at 160 ˚C.

Figure 32 shows the SEM images of the surface of 5% MWNT fiber. The fiber surface appears to be rough, which may affect the mechanical properties. The fiber surface of 10% MWNT fiber (Figure 33) appeared to be smoother than 5% MWNT fiber (Figure 32). For the 10% MWNT fiber, the fiber surface showed the presence of voids, which were similar in appearance as for the previously spun 10% MWNT fiber (Figure 31). Figure 34 shows cross-sectional images of 10% MWNT fiber. The MWNTs appeared to be well dispersed, except the fact that in one cross-section, the MWNT concentration appeared to be higher than in other cross-section.

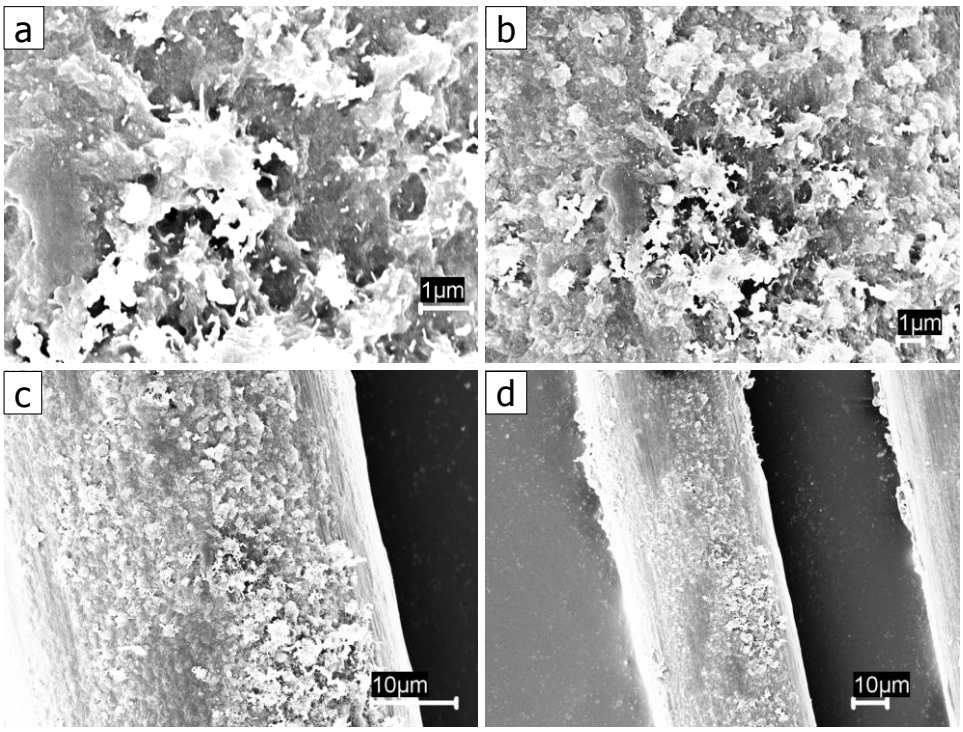

Figure 32. SEM images of the surface of 5% MWNT containing PAN fiber (sample H2a in Table 8).

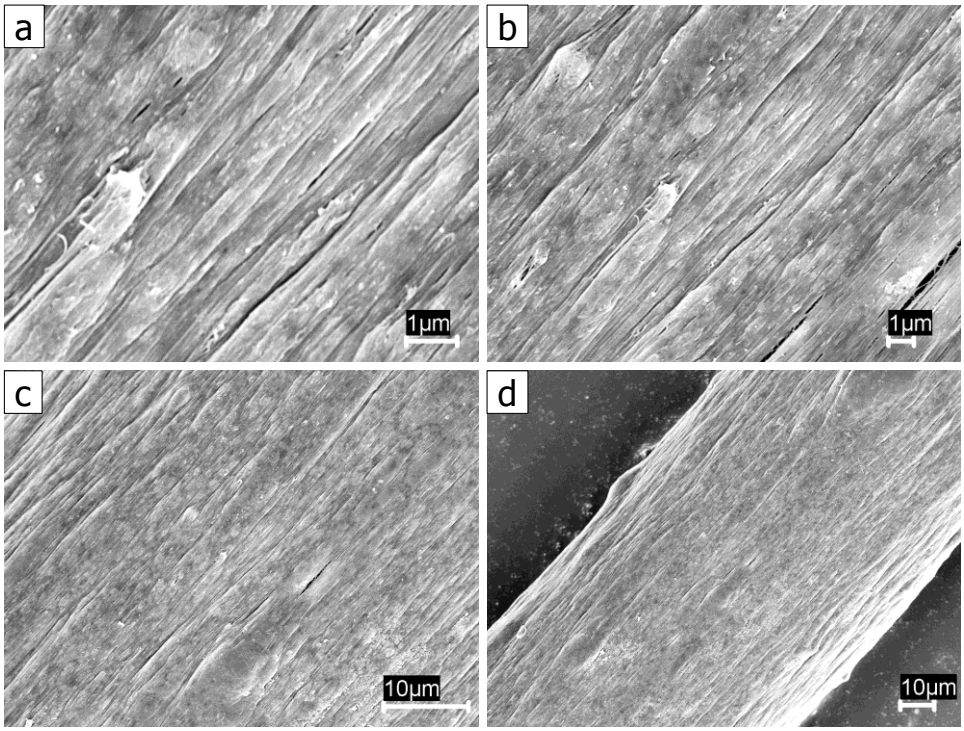

Figure 33. SEM images of the surface of 10% MWNT containing PAN fiber (sample H3a in Table 8).

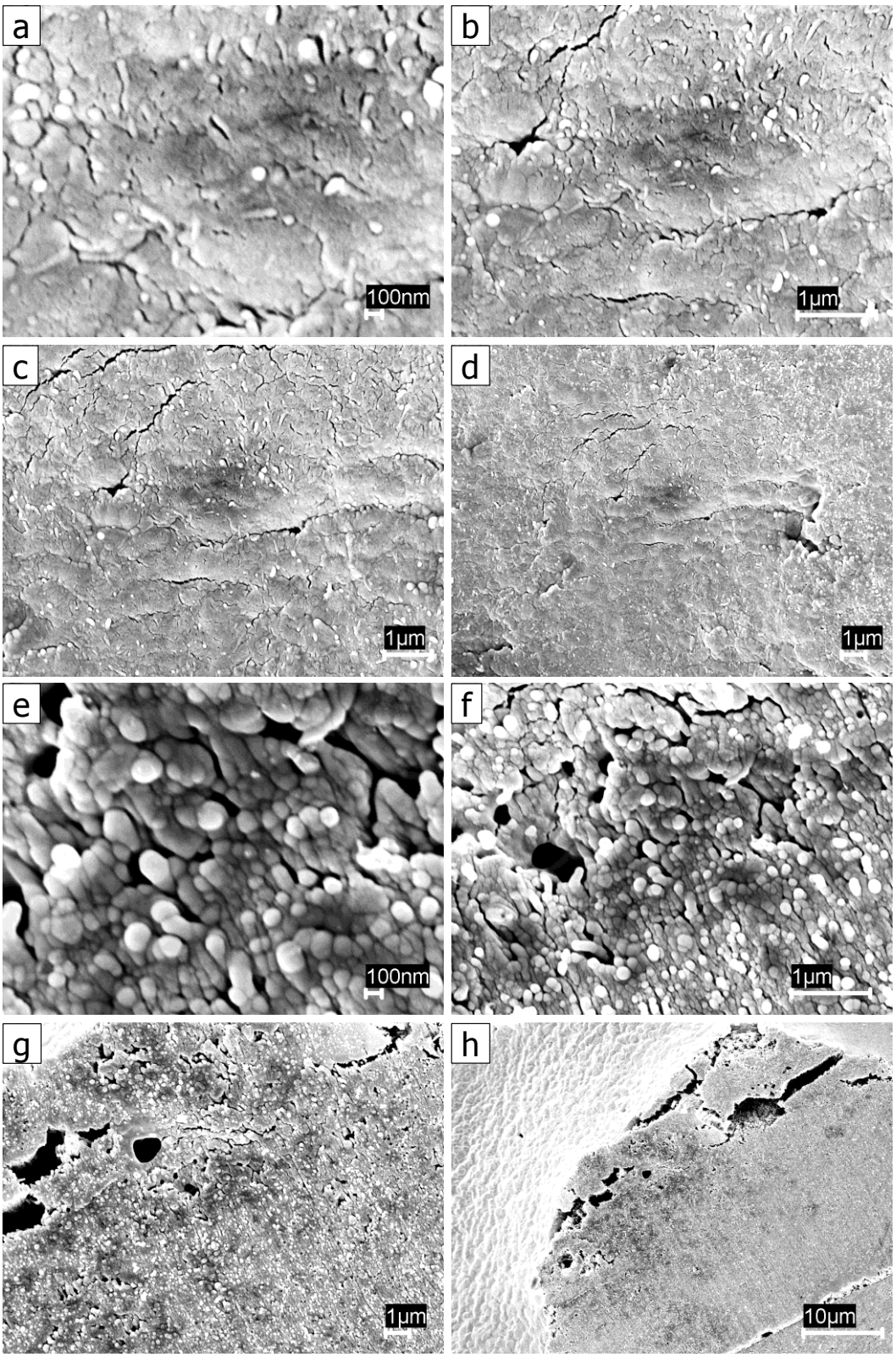

Figure 34. SEM images of the cross-section of 10% MWNT containing PAN fiber (sample H3a in Table 8). Images a, b, c, and d belong to one cross-section, and images e, f, g, and h belong to other cross-section.

2.4.2. Tensile Properties of PAN/MWNT Composite Fibers

The tensile properties of 0, 5, and 10% MWNT fibers are listed in Table 7. The tensile strength and toughness of both control PAN and 5% MWNT fiber were comparable to each other, but the tensile modulus of 5% MWNT fiber was 23% higher than that of the control PAN fiber. The tensile properties of the 10% MWNT fiber were found to be significantly decreased. The properties decreased because the 10% MWNT fiber could not be drawn to high draw ratio. The tensile strength and modulus of both control PAN and 5% MWNT fiber was higher than previously spun fibers (compare values in Table 7 to Tables 2 and 3). The toughness value for the new control PAN (draw ratio ~13) was similar to previously spun PAN fiber (draw ratio 10). The toughness value of the new 5% MWNT fiber (draw ratio ~11) was almost 29% higher than previously spun fiber (draw ratio 6). Compared to previously spun 10% MWNT fiber (Table 3), the new 10% MWNT fiber (Table 7) showed similar tensile strength, 25% increase in tensile modulus, and 37% decrease in strain to failure.

Table 7. Tensile Properties of PAN/MWNT Composite Fibers After Heat-Drawing

Sample	MWNT (%)	DR	Linear Density (tex)	Tensile Strength (N/tex)	Tensile Modulus (N/tex)	Strain to Failure (%)	Toughness (N/tex)
H1a	0	12.8	1.3	0.42 ±0.02	12.8 ±2.7	7.4 ±0.5	0.019 ±0.002
H2a	5	10.7	1.5	0.44 ±0.00	15.8 ±1.0	6.3 ±0.7	0.018 ±0.003
H3a	10	3.9	3.6	0.21 ±0.00	11.1 ±0.5	3.6 ±0.4	--

2.4.3. WAXD Studies

The crystallinity, crystal size, PAN and MWNT orientation for this batch of fibers are listed in Table 8. The corresponding WAXD patterns and integrated radial profiles are

shown in Figures 35 and 36, respectively. The 0, 5, and 10% MWNT fibers showed almost similar crystallinity, but the PAN crystal size increased for the MWNT containing fibers. Even for the control PAN fiber, the crystal size was almost 20% larger than that of the previously spun PAN fiber (Table 5) and reported in the literature [3]. Over the control PAN fiber, the PAN crystal size was almost 43% larger for the 5% MWNT fiber and 18% for the 10% MWNT fiber. For the 5% MWNT fiber, the PAN crystal size was almost 80-100% larger than previous solution spun PAN, PAN/MWNT, and PAN/CNF fibers, and than the values reported in the literature [3] for solution spun PAN and PAN/CNT fibers. The PAN crystal size of the 5%MWNT fiber was similar in values obtained by Chae *et al.* [44] for the gel-spun PAN and PAN/SWNT fibers.

Table 8. WAXD Results for PAN/MWNT Composite Fibers

Sample	CNT (%)	DR	Crystallinity[1] (%)	d-spacing (PAN 2θ~17°) (Å)	f_{PAN}[2] (2θ~17°)	f_{MWNT}[2] (2θ~26°)	L_{PAN}[3] (2θ~17°) (Å)	L_{MWNT}[3] (2θ~26.3°) (Å)
H1a	0	12.8	42	5.24	0.85	--	74	--
H2a	5	10.7	39	5.20	0.83	0.87	106	41
H3a	10	3.9	42	5.22	0.55	0.63	87	35

[1] Calculated by deconvolution of integrated scan; [2] Herman's orientation factor;
[3] Calculated using Scherrer's equation from equatorial scan

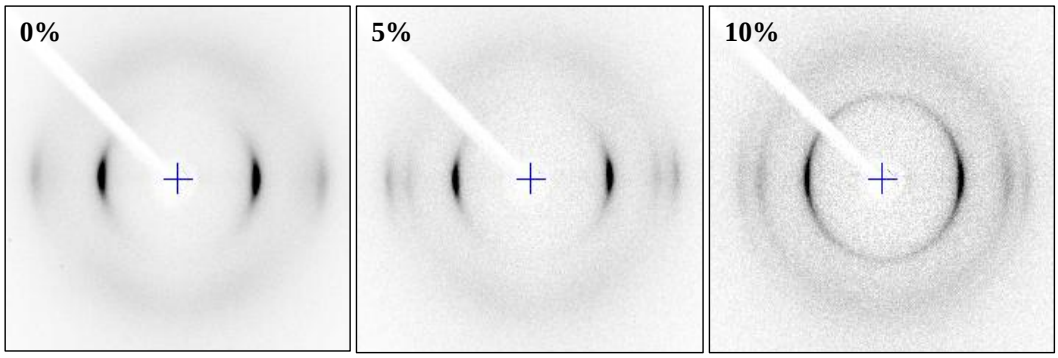

Figure 35. WAXD patterns of PAN/MWNT composite fibers with different concentration of MWNTs. 0, 5, and 10% correspond to samples H1a, H2a, and H3a in Table 8.

The PAN and MWNT orientation decreased with increase in MWNT concentration, which is due to the fact that draw ratio decreased with an increase in MWNT concentration. The PAN orientation values for both 0 and 5% MWNT fiber were higher than previously spun fiber (Table 5). The 10% MWNT fiber was drawn less than previously (DR 3.9 vs. DR 5) and showed lower PAN orientation than previous 10% MWNT fiber. However, the MWNT orientation for 10% MWNT fiber was higher than obtained before (0.63 vs. 0.60). This could be due to the fact that MWNT dispersion was better than obtained before (compare Figures 27 and 34). In conformation to previous results (Table 5), the d-spacing was found to be reduced for the MWNT containing fibers, but not as much as it decreased before.

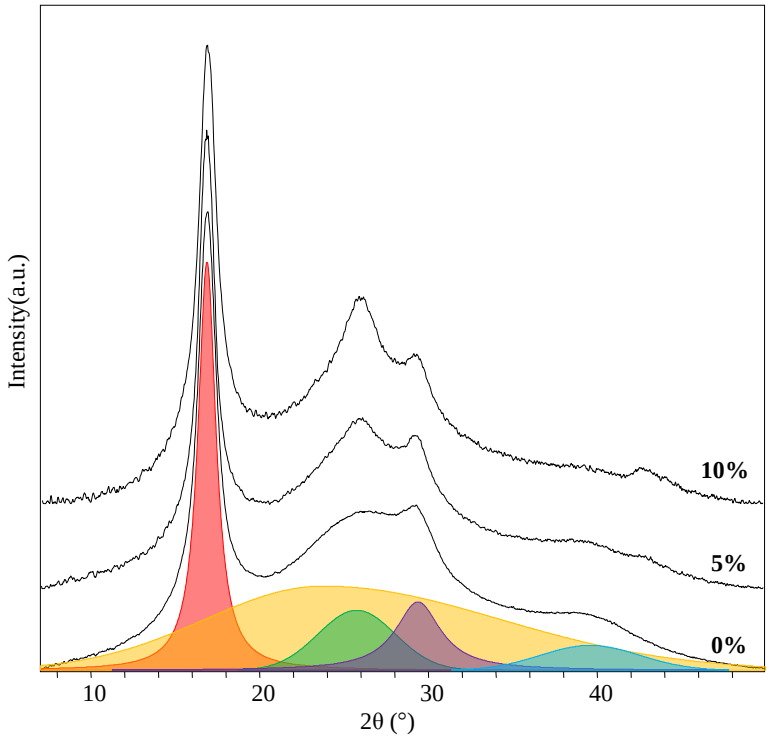

Figure 36. Integrated radial profiles of PAN/MWNT composite fibers. The representative deconvoluted profiles are also shown. 0, 5, and 10% correspond to samples H1a, H2a, and H3a in Table 8.

2.4.4. Theoretical and Experimental Tensile Moduli

The theoretical modulus of composite fibers was calculated using simple rule-of-mixtures equation 13.

$$E_c = E_{PAN} W_{PAN} + E_{CNT} W_{CNT} \tag{13}$$

where E_c is the modulus of composite fiber, E_{PAN} is the modulus of control PAN fiber at a particular draw ratio, W_{PAN} is the weight fraction of PAN in the fiber, E_{CNT} is the modulus of CNT (here MWNT) for a particular orientation, and W_{CNT} is the weight fraction of CNT in the fiber.

E_{CNT} for a particular orientation is correlated with the intrinsic mechanical properties of the CNT through equations 14 and 15 [3, 46, 47]. The angle ϕ (here $\phi = \phi_{hkl}$) is related to the Herman's orientation factor through equation 8. The values for the longitudinal modulus (E_1), transverse modulus (E_2), in-plane shear modulus (G_{12}), and Poisson's ratio (ν_{12}) for SWNT, MWNT, and CNF were taken from the published literature [46] and are listed in Table 9. The moduli values in N/tex were obtained by dividing the moduli in GPa by the density of CNT.

$$\frac{1}{E_{CNT}} = \frac{1}{E_1}\left\langle \cos^4 \phi \right\rangle + \frac{1}{E_2}\left\langle \sin^4 \phi \right\rangle + \left(\frac{1}{G_{12}} - \frac{2\nu_{12}}{E_1} \right)\left\langle \sin^4 \phi \cos^2 \phi \right\rangle \tag{14}$$

$$\frac{1}{E_{CNT}} = \frac{1}{E_2} + \left(\frac{1}{G_{12}} - \frac{2\nu_{12}}{E_1} - \frac{2}{E_2} \right)\left\langle \cos^2 \phi \right\rangle + \left(\frac{1}{E_1} + \frac{1}{E_2} - \frac{1}{G_{12}} + \frac{2\nu_{12}}{E_1} \right)\left\langle \cos^4 \phi \right\rangle \tag{15}$$

The theoretical and experimental values of tensile moduli for different fibers are listed in table 10. Invariably, the experimental values were found to be higher than the theoretically expected values. This suggests that PAN in the interphase region has better morphology that is not present in control PAN fiber. That is why the actual values are higher than expected. The better morphology improves the modulus of PAN which

ultimately helps improve the modulus of composite fiber. These results suggest that properties can be further enhanced by optimizing the interphase region. Chae *et al.* [44] also observed a significant improvement in the tensile properties than expected, and attributed those to improved interphase region.

Table 9. Mechanical Constants for Different CNTs

	SWNT	**MWNT**	**CNF**
ρ (g/cm^3)	1.3 [48]	1.8 [49]	1.95 [49]
E_1 (GPa)	640 [48, 50-52]	1060 [53, 54]	50 [55]
E_1 (N/tex)	492	589	26
E_2 (GPa)	15 [52]	50 [56]	36.5 [55]
E_2 (N/tex)	12	28	19
G_{12} (GPa)	19.5 [57]	4 [56]	4 [3, 55]
G_{12} (N/tex)	15	2	2
ν_{12}	0.17 [52]	0.14 [54]	0.3 [55]

Moduli values in N/tex were obtained by dividing the moduli in GPa by the density of CNT in g/cm^3.

Table 10. Theoretical and Experimental Tensile Moduli of Different PAN/MWNT Fibers

Sample	**MWNT (%)**	**DR**	**f_{CNT}**	**E_{PAN} (N/tex)**	**$E_{CNT}^{\parallel}$ (N/tex)**	**$E_{c\ (Theoretical)}$ (N/tex)**	**$E_{c\ (Experimental)}$ (N/tex)**
B1a	5	6	0.83	8.0	21.3	8.6	10.8 ±0.2
B2a	10	5	0.60	7.5	10.9	7.8	8.9 ±0.5
B3a	15	4	0.40	6.7	8.8	7.0	7.9 ±0.5
B4a	20	2.5	0.32	5.5	8.4	6.1	7.3 ±0.3
H2a	5	10.7	0.87	12.8	26.8	13.5	15.8 ±1.0
H3a	10	3.9	0.63	6.7*	11.5	7.3	11.1 ±0.5

$E_{CNT}^{\parallel}$ (parallel to the fiber axis) was determined using equation 15.
* This value is for PAN 100K with DR 4 (from Table 2).

2.4.5. Electrical Conductivity of PAN/MWNT Fibers

The electrical conductivity of 5 and 10% MWNT fiber were 9.2×10^{-5} and 8.2×10^{-5} S/m. A similar value was obtained for the previously spun 10% MWNT fiber (Table 6).

2.5. Conclusions

The presence of MWNTs constrained the movement of PAN chains, which increased the T_g and reduced the entropic thermal shrinkage in PAN fiber. Among all the composite fibers, the 5% MWNT fiber showed the maximum modulus and strength (at the heat drawn stage). After stabilization, the modulus of the composite fibers increased with increasing percentage of MWNTs. The possible factors which seem to be detrimental to the mechanical properties of the composite fibers include MWNTs entanglements at high MWNT loading (> 5%) and void formation in the fiber. The tensile modulus of the composite fibers was found to be higher than theoretically expected. This improvement is attributed to the improved PAN morphology in the interphase region.

The MWNTs were found to be very well coated/wetted with PAN polymer, which suggests good interaction between PAN polymer and MWNT. The presence of MWNTs showed no particular affect on the crystallinity, crystal size, and orientation of PAN. In general, the PAN orientation increased with an increase in heat draw-ratio. The 15% MWNT fiber showed an electrical conductivity which was four orders of magnitude higher than the 10% MWNT fiber.

The mechanical properties of the fibers could be enhanced (Section 2.4) by changing some of the processing parameters. To date, the obtained tensile properties are higher than any solution spun PAN/MWNT fibers reported in literature.

Based on the observed structure and properties of the fiber, following conclusions were derived to explain the observed structure-property relationship.

Structural-Property Relationship of PAN/MWNT Fibers

- During heat-drawing and vacuum drying of fibers, PAN chains are compacted around MWNTs. Since the overall macroscopic geometry of the fiber is not distorted, this compaction leads to more free volume and voids in the fiber.
- Compaction leads to DMF removal from inter-chain spacing and DMF in the free volume and voids is easily removed (under vacuum drying). That is why the fibers with MWNTs showed ultimately lower content of DMF (TGA studies).
- Higher distributed free volume and voids leads to microscopic defects in the fiber. Therefore, fibers with higher percentage of MWNTs show decreasing mechanical properties. The decrease in mechanical properties with increase in MWNT concentration is also due to low draw ratio and non-uniform MWNT dispersion.
- The voids and defects in higher percentage MWNTs fibers is easily attacked by DMF solvent. Therefore, fibers with MWNTs dissolved readily in DMF (video not included in this document, but the images are shown in Figures A13 through A18 in Appendix A). The compacted PAN around MWNTs did not fully dissolve and was observable from SEM images (MWNT thickness measurements from SEM images).
- During stabilization, the MWNTs containing fibers (especially higher percentage MWNTs), because of more distributed voids, got easily oxidized and showed a higher weight loss. Higher weight loss led to more and bigger voids which decreased the mechanical properties of the fibers (voids visible through SEM images).

- Stabilization progresses from the outer surface towards the core of the fiber. Large diameter fibers of PAN were found to be incompletely oxidized near the core. The size of the voids decreased from the surface towards the core. Since the microstructure is more open in case of high MWNT concentration fibers, the degree of stabilization is higher in composite fibers (oxygen molecules can easily get through the open structure). Consequently, the composite fiber were found to be more brittle and showed lower strain to failure.

2.6. References

1. Chae HG, Minus ML, Rasheed A, and Kumar S. Polymer 2007;48(13):3781-3789.
2. Gupta AK, Paliwal DK, and Bajaj P. Polymer Reviews 1991;31(1):1 - 89.
3. Chae HG, Sreekumar TV, Uchida T, and Kumar S. Polymer 2005;46(24):10925-10935.
4. Layden GK. Journal of Applied Polymer Science 1971;15(7):1709-1715.
5. Ayrey G, Chadda SK, and Poller RC. Journal of Polymer Science Part a-Polymer Chemistry 1982;20(8):2249-2258.
6. Ayrey G, Chadda SK, and Poller RC. European Polymer Journal 1983;19(4):313-315.
7. Bashir Z. Carbon 1991;29(8):1081-1090.
8. Ko TH. Journal of Applied Polymer Science 1991;43(3):589-600.
9. Ko TH. Journal of Applied Polymer Science 1991;42(7):1949-1957.
10. Surianarayanan M, Vijayaraghavan R, and Raghavan KV. Journal of Polymer Science Part a-Polymer Chemistry 1998;36(14):2503-2512.
11. Salary D, Alizadeh S, Massoumi B, and Entezami A. Journal of Polymer Materials 2002;19(4):335-342.
12. Xue TJ, McKinney MA, and Wilkie CA. Polymer Degradation and Stability 1997;58(1-2):193-202.

13. Perkins JS, Sacher RE, Shuford RJ, Thomas GR, and Gaulin CA. Abstracts of Papers of the American Chemical Society 1973:85-&.

14. Andreeva OA, Burkova LA, and Firsov YI. Vysokomolekulyarnye Soedineniya Seriya A 1987;29(3):622-629.

15. Dunham MG and Edie DD. Carbon 1992;30(3):435-450.

16. Wang PH, Liu J, Yue ZR, and Li RY. Carbon 1992;30(1):113-120.

17. Tarakanova NV, Bondarenko VM, and Azarova MT. Fibre Chemistry 1995;27(1):15-17.

18. Gupta AK, Paliwal DK, and Bajaj P. Journal of Applied Polymer Science 1995;58(7):1161-1174.

19. Kakida H, Tashiro K, and Kobayashi M. Polymer Journal 1996;28(1):30-34.

20. Kakida H and Tashiro K. Polymer Journal 1997;29(7):557-562.

21. Lee JK, Shim HJ, Lim JC, Choi GJ, Kim YD, Min BG, and Park D. Carbon 1997;35(6):837-843.

22. Kakida H and Tashiro K. Polymer Journal 1997;29(4):353-357.

23. Kakida H and Tashiro K. Polymer Journal 1998;30(6):463-469.

24. Kakida H and Tashiro K. Polymer Journal 1998;30(6):474-478.

25. Dalton S, Heatley F, and Budd PM. Polymer 1999;40(20):5531-5543.

26. Lu CX, Wu GP, Lu YG, Li KX, Li YH, Liang XY, He F, and Ling LC. New Carbon Materials 2003;18(3):186-190.

27. Ouyang Q, Cheng L, Wang HJ, and Li KX. Polymer Degradation and Stability 2008;93(8):1415-1421.

28. Hou YP, Sun TQ, Wang HJ, and Wu D. Journal of Materials Science 2008;43(14):4910-4914.

29. Kiminta DM. International Journal of Polymeric Materials 1993;23(1-2):57-65.

30. Ogawa H. Nippon Kagaku Kaishi 1994(10):921-926.

31. Gupta AK, Paliwal DK, and Bajaj P. Journal of Applied Polymer Science 1996;59(12):1819-1826.

32. Mittal J, Mathur RB, Bahl OP, and Inagaki M. Carbon 1998;36(7-8):893-897.

33. Wang PH. Journal of Applied Polymer Science 1998;67(7):1185-1190.

34. Wu GP, Lu CX, Li YH, Lu YG, He F, and Ling LC. New Carbon Materials 2003;18(1):25-30.

35. Wu GP, Lu CX, Zhang R, Wu XP, Ren FZ, Li KX, He F, and Ling LC. Journal of Materials Science 2004;39(8):2959-2960.

36. Wu GP, Lu CX, Ling LC, Hao AM, and He F. Journal of Applied Polymer Science 2005;96(4):1029-1034.

37. Yu MJ, Wang CG, Bai YJ, Wang YX, and Zhu B. Journal of Applied Polymer Science 2006;102(6):5500-5506.

38. Yu MJ, Wang CG, Bai YJ, Wang YX, and Xu Y. Polymer Bulletin 2006;57(5):757-763.

39. Sreekumar TV, Chandra L, Srivastava A, and Kumar S. Carbon 2007;45(5):1114-1116.

40. Hou YP, Sun TQ, Wang HJ, and Wu D. Textile Research Journal 2008;78(9):806-811.

41. Yu MJ, Wang CG, Bai YJ, Xu Y, and Zhu B. Journal of Applied Polymer Science 2008;107(3):1939-1945.

42. Sreekumar TV, Liu T, Min BG, Guo H, Kumar S, Hauge RH, and Smalley RE. Advanced Materials 2004;16(1):58-61.

43. Min BG, Sreekumar TV, Uchida T, and Kumar S. Carbon 2005;43(3):599-604.

44. Chae HG, Minus ML, and Kumar S. Polymer 2006;47(10):3494-3504.

45. Samuels RJ. "Structured Polymer Properties: The Identification, Interpretation, and Application of Crystalline Polymer Structure." John Wiley & Sons, New York 1974.

46. Liu T and Kumar S. Nano Lett. 2003;3(5):647-650.

47. Ward IM and Sweeney J. "An Introduction to The Mechanical Properties of Solid Polymers", John Wiley & Sons, Ltd., England 2005:153.

48. Lu JP. Physical Review Letters 1997;79(7):1297-1300.

49. Provided by the Manufacturer.

50. Gao GH, Cagin T, and Goddard WA. Energetics, structure, mechanical and vibrational properties of single-walled carbon nanotubes. Iop Publishing Ltd, 1998. pp. 184-191.

51. Sinnott SB, Shenderova OA, White CT, and Brenner DW. Carbon 1998;36(1-2):1-9.

52. Popov VN, Van Doren VE, and Balkanski M. Solid State Communications 2000;114(7):395-399.

53. Pan ZW, Xie SS, Lu L, Chang BH, Sun LF, Zhou WY, Wang G, and Zhang DL. Applied Physics Letters 1999;74(21):3152-3154.

54. Shen LX and Li J. Physical Review B 2005;71(3):10.

55. Uchida T, Anderson DP, Minus ML, and Kumar S. Journal of Materials Science 2006;41(18):5851-5856.

56. Koerner H, Liu WD, Alexander M, Mirau P, Dowty H, and Vaia RA. Polymer 2005;46(12):4405-4420.

57. Salvetat JP, Briggs GAD, Bonard JM, Bacsa RR, Kulik AJ, Stockli T, Burnham NA, and Forro L. Physical Review Letters 1999;82(5):944-947.

CHAPTER 3

PAN/CNF COMPOSITE FIBERS

PAN/CNF composite fibers with different concentration of CNFs (5, 10, 15, 20, and 30 wt.%) were spun using dry jet wet-spinning. The effect of CNF concentration on dispersion and the challenges associated with the fiber processing of high CNF loading solutions were identified. The effect of sonication time on CNF dispersion in PAN matrix and effect of fiber drying temperature on the tensile properties were also studied. The composite fibers were characterized and compared with control PAN fiber in terms of thermal stability and tensile properties. The idea of creating flexible, porous, and aligned CNF structure is also presented. Previous to this study, Chae *et al.* [1] reported the PAN/CNF composite fibers with 5 wt.% CNF concentration. This is the first study reporting the processing of CNF reinforced continuous polymer fiber with CNF concentration as high as 30 wt.%.

3.1. Experimental

3.1.1. Materials

CNF powder (Pyrograf III, PR-24-HHT LD, heat treated at 2850 ˚C) was obtained from Applied Sciences, Inc. (Cedarville, OH). The manufacturer reported that CNF powder has 98 wt.% carbon, an iron content of no more than 400 ppm, and a sulfur content of less than 0.8 wt.%. The manufacturer reported the average diameter of CNFs to be ~ 100 nm (from SEM image). All other materials were same as in Section 2.1.1.

In addition to the two types of truncated cone geometry, reported by Uchida *et al.* [2], these CNFs also possess bamboo type of morphology (Figure 3). Uchida [2]

calculated the tensile modulus of the two types of truncated geometry CNFs to be 50 GPa and 100-775 GPa. Lawrence *et al.* [3] measured the elastic modulus of CNFs and reported the values between 6 and 207 GPa. The tensile modulus of CNF with bamboo type of morphology is expected to be lower than 50 GPa.

3.1.2. PAN/CNF Solution Preparation

For CNF dispersion in DMF, 1 g of CNF powder was sonicated in 200 ml DMF for about 5 h (bath sonicator, Branson 3510-MT, 100W, 42 kHz). To study the effect of long and short sonication times or to study the effect of CNF length, 5 and 20% CNF containing CNF/PAN/DMF solutions were prepared in which the CNF sonication time was 48 h. The rest of the solution preparation method was the same as described in Section 2.1.2.

3.1.3. PAN/CNF Fiber Spinning

Composite fibers with five different concentrations of CNFs (5, 10, 15, 20 and 30 %) were spun using dry-jet wet spinning. An approach and set-up similar to the one used for PAN/MWNT fiber spinning (described in Section 2.1.3.) was used for PAN/CNF fiber spinning. The continuous fiber spinning was achieved by optimizing temperature of the barrel, polymer extrusion rate through spinneret, and fiber take-up speeds. For example, the 30% CNF containing fiber could only be spun when the plunger speed was increased to double the speed used for lower CNF containing solutions. The fiber spinning conditions and parameters are listed in Table 11. The high CNF containing fibers seemed to be brittle and could only be drawn to very low draw ratios.

Table 11. Processing Parameters for Different PAN/CNF Fiber Spinning

CNF (%)*	5	10	15	20	30
Solid Content** (g/100ml DMF)	27.8	25.5	21.7	24.6	19.9
Plunger Rate (mm/min)	2.5	2.85	2.71	2.74	5
Spinning Temperature (˚C)	20	20	20	20	20
Drawing Spools Speed[$] (m/min)	4 → 36	6 → 60	8 → 48	6 → 30	8 → 28
Heat Draw Ratio in Boiling Water*** (~ 100 ˚C)	9	10	6	5	3.5

* CNF weight percentage with respect to PAN weight
** Total amount of PAN and CNF in DMF measured using TGA (weight loss at 200 ˚C corresponded to DMF weight)
[$] Drawing spools speeds represent the speeds of first and second take-up rolls
*** Heat draw ratio is the ratio of the speeds of second and first take-up roll

3.2. Results and Discussion

3.2.1. Thermogravimetric Analysis

Figure 37 shows the TGA of various composite fibers in nitrogen atmosphere. The char yield of various fibers is listed in Table 12. Composite fibers showed higher thermal stability than the control PAN fiber. In general, the CNF filler increased the char yield of the composite fibers. However, at higher temperatures (> 800 ˚C) the fibers with higher CNF loading (20% and 30%) showed a sharp decrease in the char yield (Table 12). Theoretically, the weight loss of the composite should follow the simple rule of mixtures. Therefore, at a particular temperature, the weight loss for a composite should be equivalent to the combined weight fraction loss for the two components (PAN and CNF). At up to 15% CNF loading, the experimental value for the char yield was similar to the theoretically expected value (Table 7). However, at higher CNF loading, the experimental values were much lower than theoretically expected. This suggests that char

in higher CNF loading fibers is less thermally stable, which leads to a decrease in the ultimate char yield at 1000 ˚C. However, the char yield of the composite fiber was still higher than that of the control PAN fiber. Lower thermal stability could be due to a less compacted structure or more defective structure (voids and cracks) in case of higher CNF containing fibers.

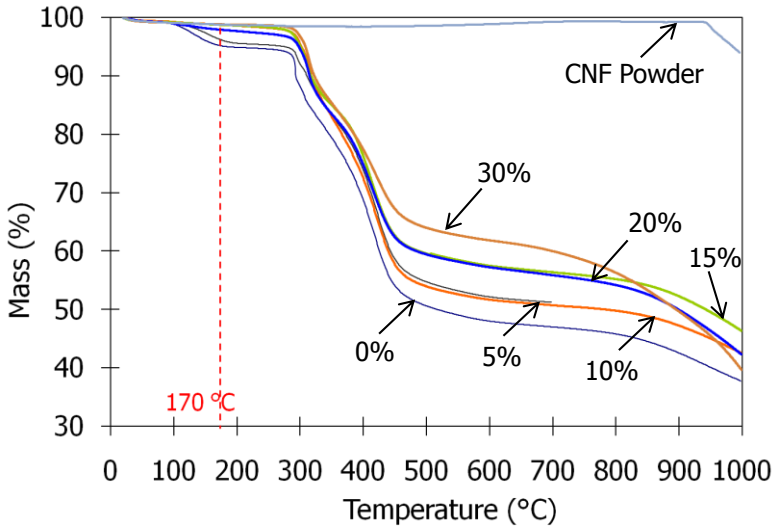

Figure 37. TGA of PAN/CNF composite fibers in nitrogen at a heating rate of 5 ˚C/min. (0, 5, 10, 15, 20, and 30% correspond to samples A1d, C1b, C2a, C3a, C4a, and C5a, respectively).

Table 12. Char Yield of Various PAN/CNF Composite Fibers as Measured Using TGA in N_2

CNF	**Sample**	**Char Yield (%)**		
(%)		@ 170 °C	@ 600 °C	@ 1000 °C
0	A1d	95	48	38
5	C1b	96	52 *(51)*	43 *(41)*
10	C2a	99	52 *(53)*	43 *(43)*
15	C3a	99	57 *(56)*	46 *(46)*
20	C4a	98	57 *(58)*	43 (49)
30	C5a	99	63 *(64)*	39 *(55)*
100	CNF powder	100	100	94

(theoretically expected value from rule of mixtures)

3.2.2. CNF Dispersion in Fibers

To study CNF dispersion, fiber cross-sections were observed in SEM. Thin slices of fiber cross-sections were prepared using microtomy as described in Section 2.1.4. Figure 38 shows the cross-sections of 5, 10, 15, 20, 30, and 40% CNF loaded PAN composite fibers. The 40% fibers could not be spun and drawn in a continuous manner; therefore no further characterization was done on this fiber. However, it helped in the investigation and understanding of relationship between processing and dispersion, and it highlights the challenges associated with the processing of high CNF containing fibers.

Figure 39 shows the schematics for two possible scenarios of the state of dispersion of CNFs in different fibers. Scenario I describes the uniform dispersion of CNFs whereas scenario II describes the bundling of CNFs in the matrix. Figures 40 and 41 show the cross-sections of 5% and 10% CNF loaded fiber, respectively. The CNFs seem to be uniformly distributed in the PAN matrix in both 5 and 10% CNF composite fibers and the dispersion state can be represented by scenario I. Figure 42 shows the cross-section of 15% CNF composite fiber. The dispersion state show regions which can be classified under both scenarios I and II, but to a large degree scenario I seem to be dominant. Figure 43 shows the cross-section of 20% CNF composite fiber. The distribution of CNFs suggests that both scenarios I and II are equally present. Figure 44 shows the cross-section of 30% CNF composite fiber. The fiber cross section shows two distinct regions with a very high gradient in the CNF concentration in the two regions and scenario II seems to be dominant. The bundling of CNFs (as in Scenario II) is also evidenced by the SEM images of the charred fiber (Figure 66). The sharp gradient in the CNFs dispersion within the same cross-section may result from the phase separation of

CNF-rich polymer from the CNF-poor polymer. The phase separation could have possibly occurred during the composite solution preparation or during coagulation during fiber spinning. Table 13 gives the summary of dispersion states of CNFs in different composite fibers.

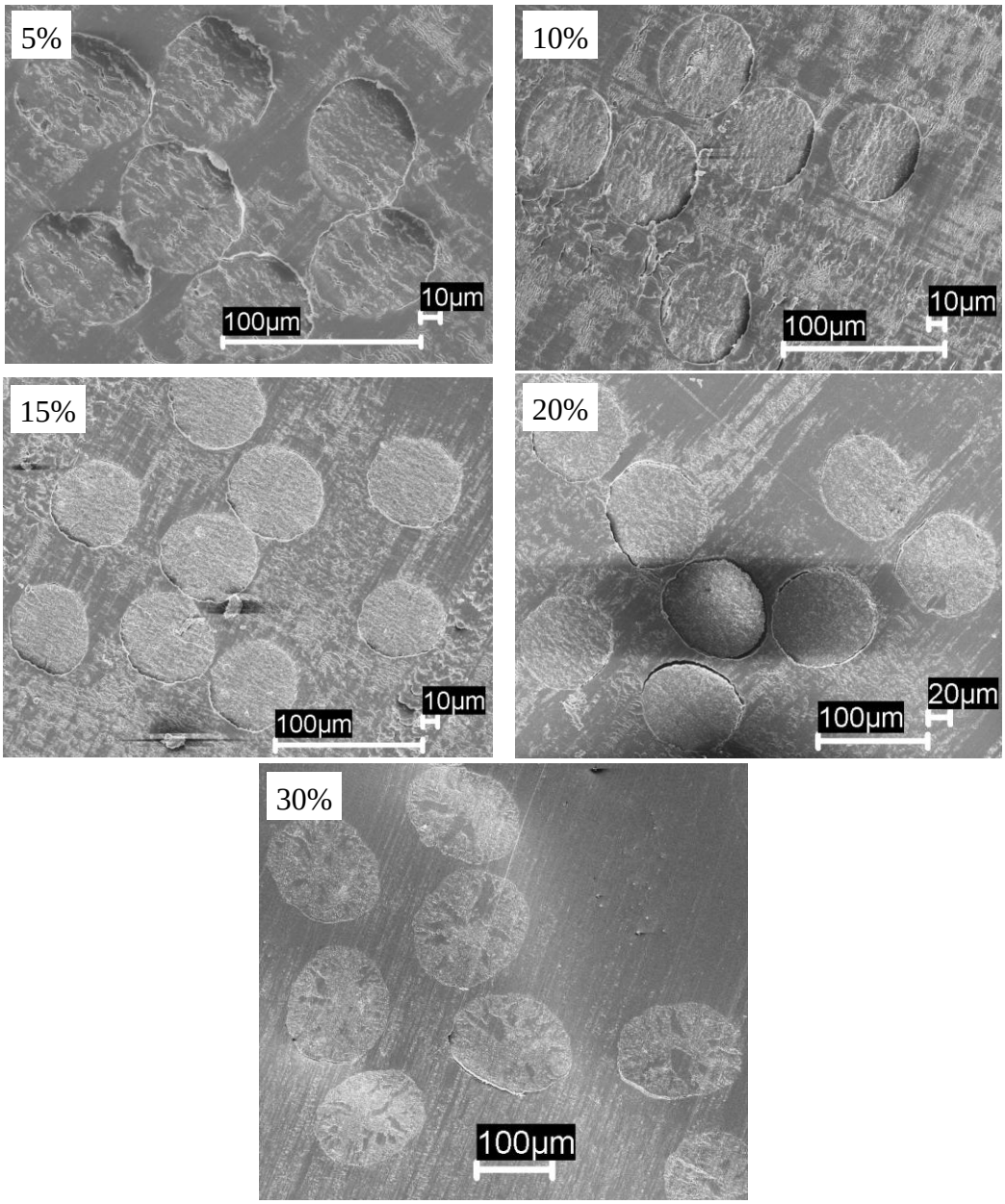

Figure 38. Low magnification SEM images of the cross-sections of PAN/CNF composite fibers. (5, 10, 15, 20, and 30% correspond to samples C1b, C2a, C3a, C4a, and C5a, respectively).

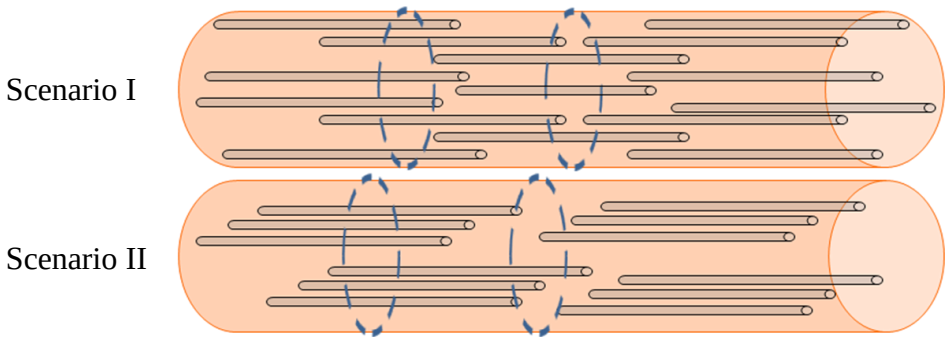

Figure 39. Two possible scenarios of the state of dispersion of CNFs in the PAN matrix. Scenario I represents uniform dispersion and scenario II represents bundling of CNFs. The two dashed circles in the same fiber represent the fiber cross-sections at two different locations.

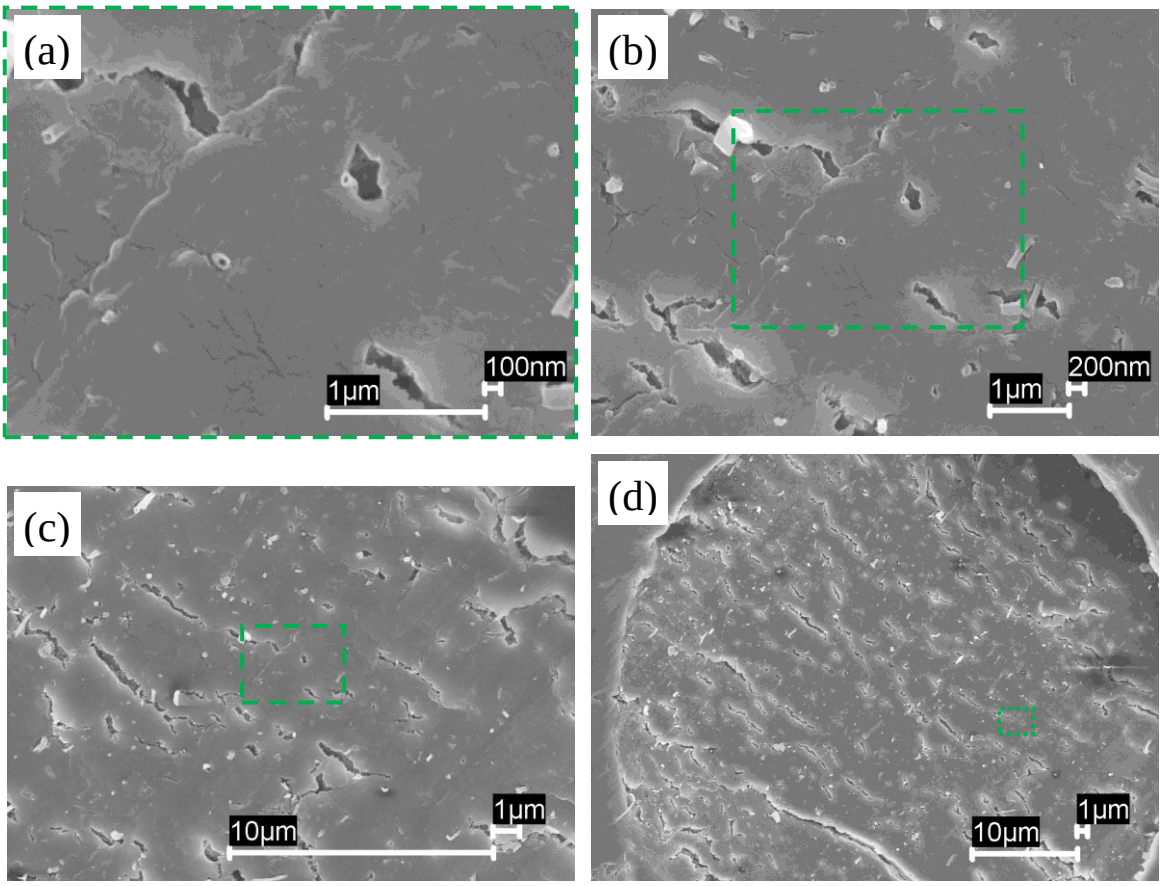

Figure 40. Cross-section (at different magnifications) of 100K PAN/CNF (95/5) composite fiber (sample C1b).

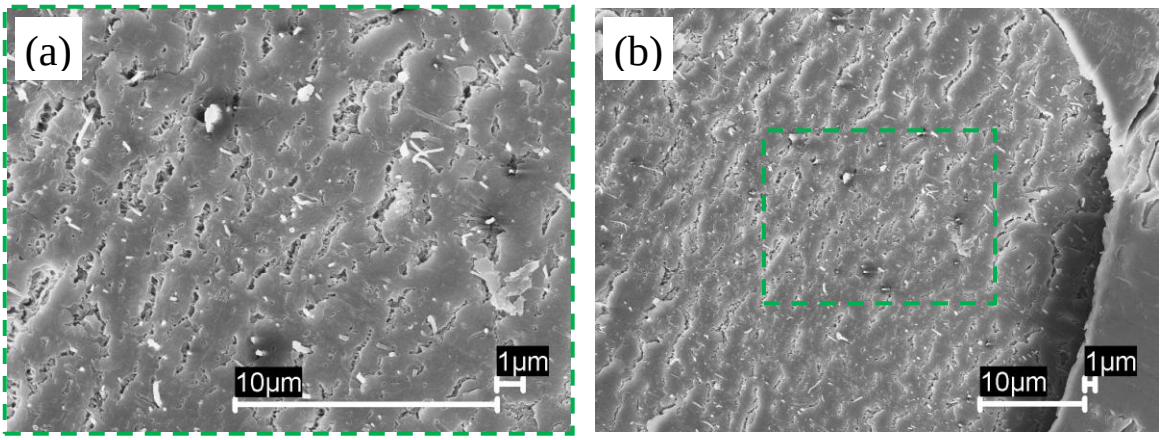

Figure 41. Cross-section (at different magnifications) of 100K PAN/CNF (90/10) composite fiber (sample C2a).

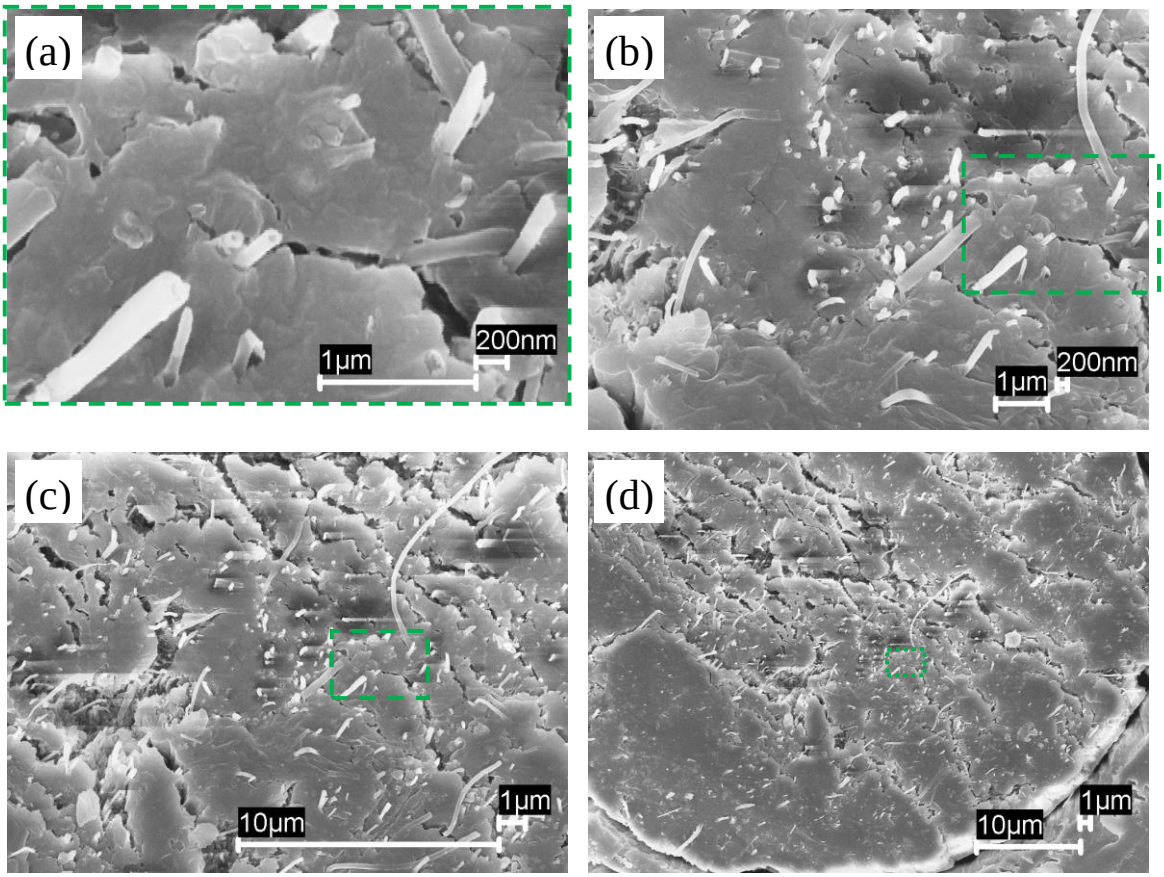

Figure 42. Cross-section (at different magnifications) of 100K PAN/CNF (85/15) composite fiber (sample C3a).

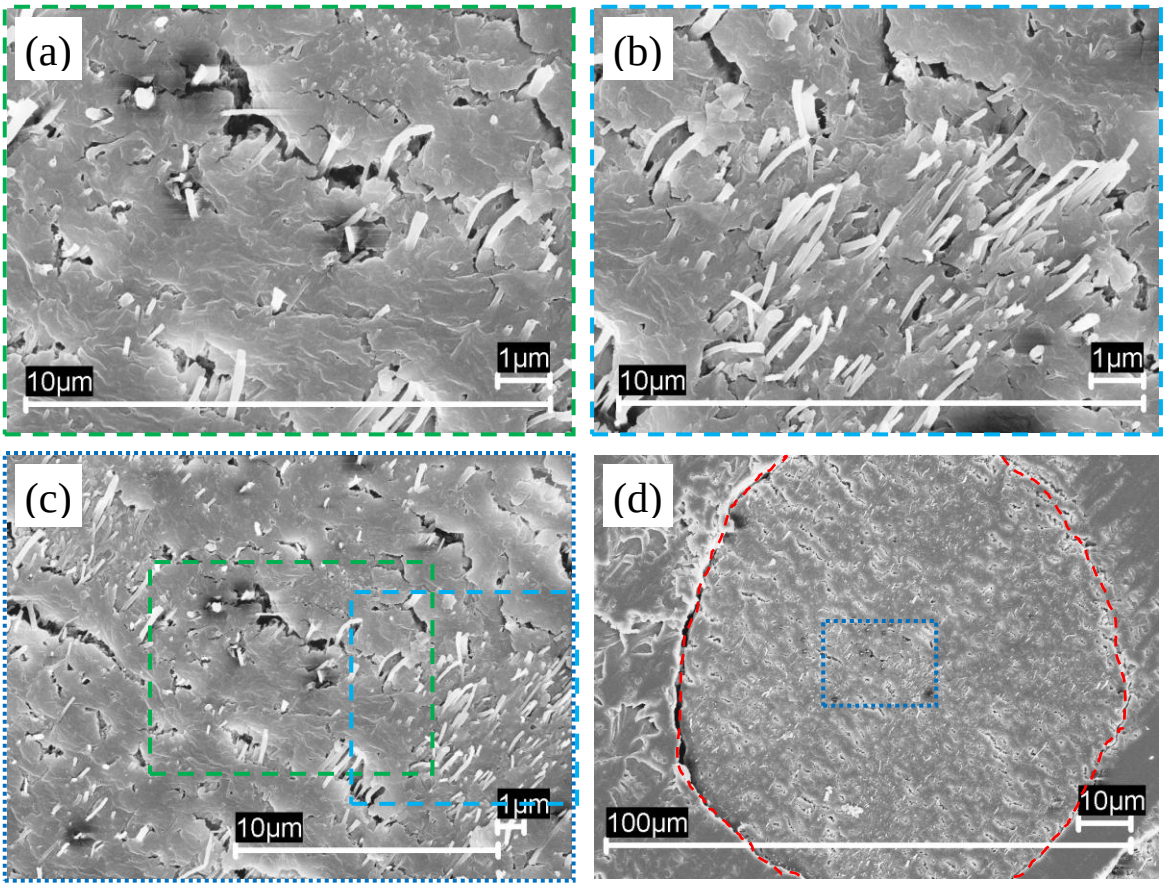

Figure 43. Cross-section images (at different magnifications) of 100K PAN/CNF (80/20) composite fiber (sample C4a). A region is enclosed with red-dashed line to delineate the boundary between the fiber cross-section and embedding medium.

Table 13. Dispersion States of CNFs in Different Composite Fibers

CNF (%)	5	10	15	20	30	40
Scenario I	✓✓	✓✓	✓✓	✓	✓	✓
Scenario II	-	-	✓	✓	✓✓	✓✓

"✓" shows the presence of a particular scenario and "✓✓" shows the dominance of a particular scenario

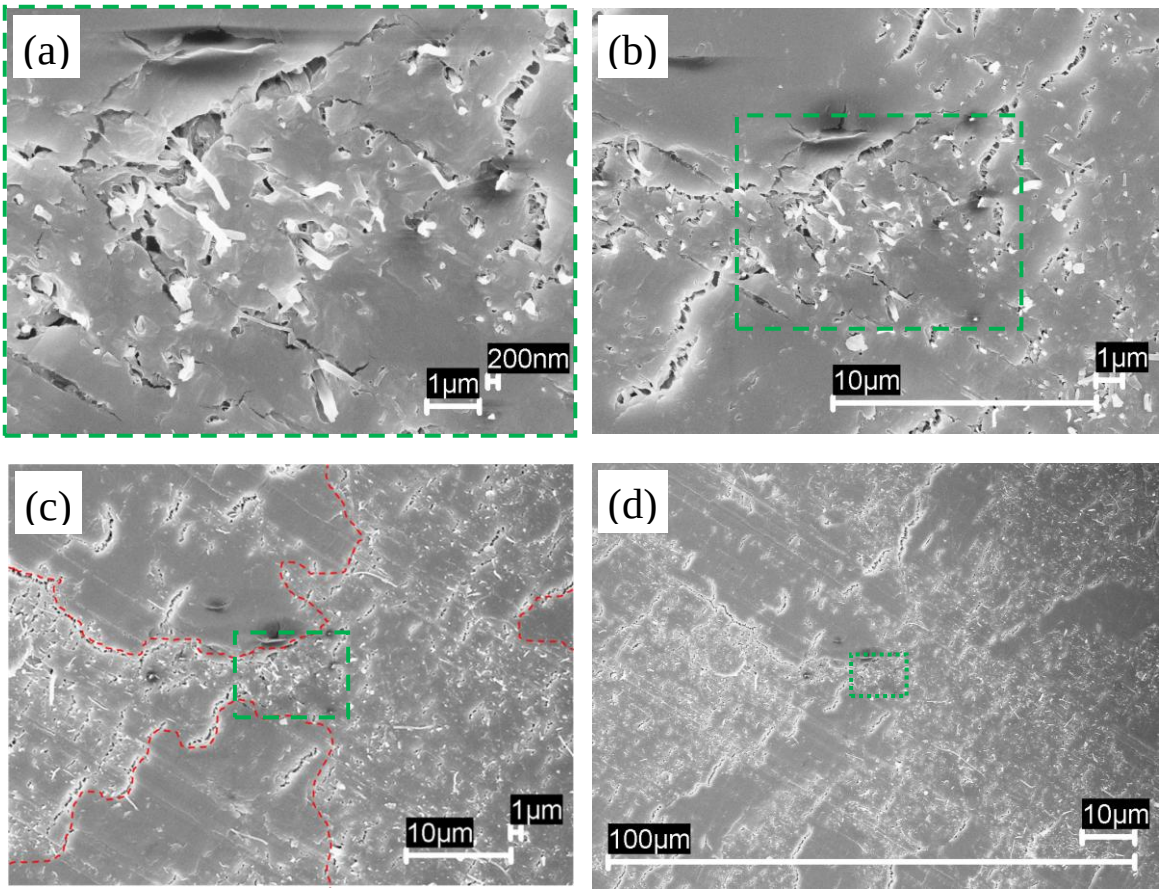

Figure 44. Cross-section images (at different magnifications) of 100K PAN/CNF (70/30) composite fiber (sample C5a). A region is enclosed with red-dashed line to show the phase separated region.

Although a continuous fiber could not be obtained for the 40% CNF concentration, the short fiber segments were obtained. Figure 45 shows the cross-section of 40% CNF composite fiber. The cross-section of 40% CNF containing fiber shows regions of extensive phase separation (Figure 45 f). While one region seems to be compact, the other region seems to be more open and porous. Additionally, both of these regions contain areas of scenario I and scenario II dispersion and overall the scenario II seems to be dominating. The phase separated region contains significantly less polymer

and shows more open/porous structure. Figure 46 shows the images of the phase separated open/porous structure. Figure 47 shows the images of the compact region.

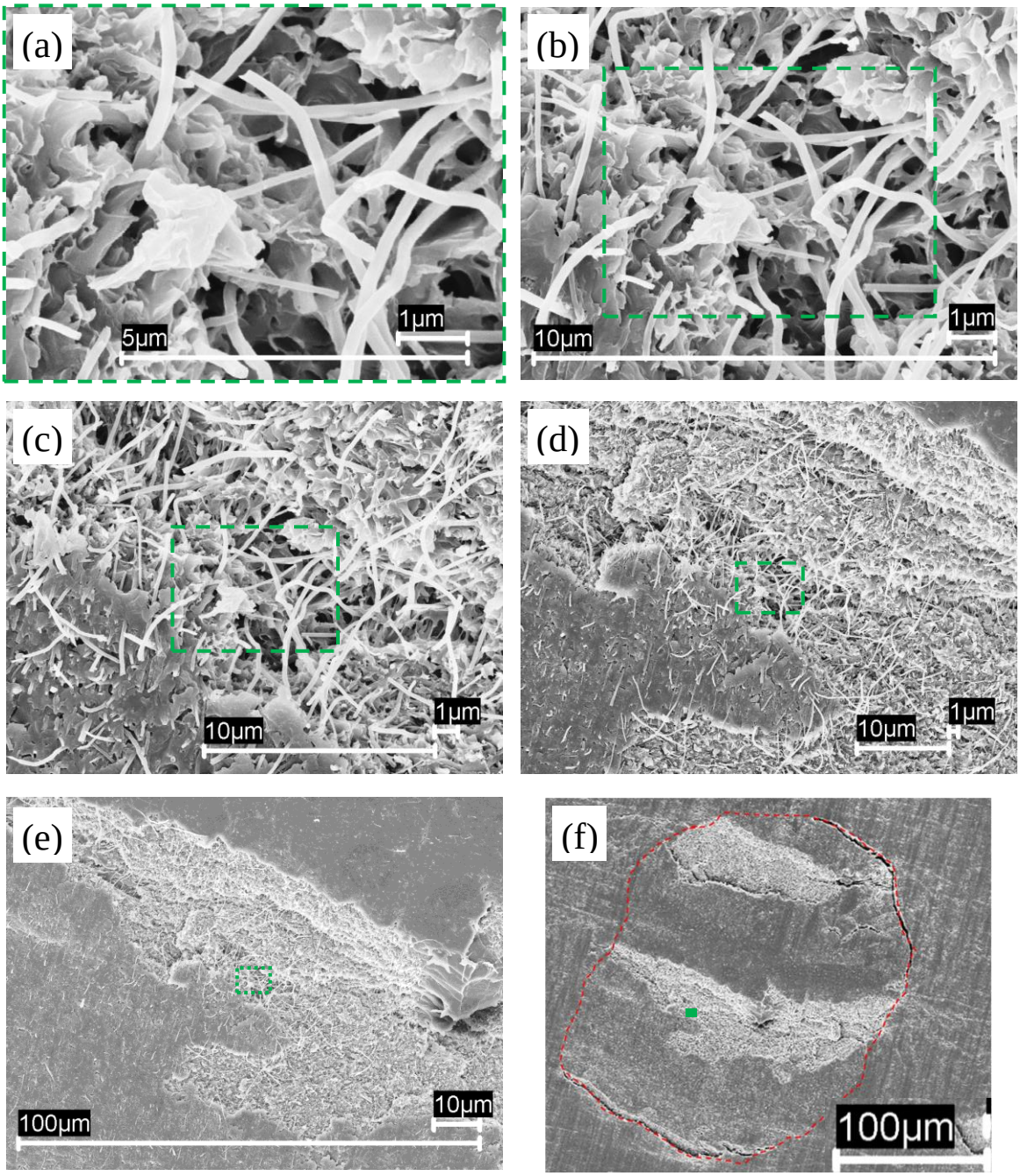

Figure 45. Cross-section images (at different magnifications) of 100K PAN/CNF (60/40) composite fiber. A region is enclosed with red-dashed line to delineate the boundary between the fiber cross-section and the embedding medium.

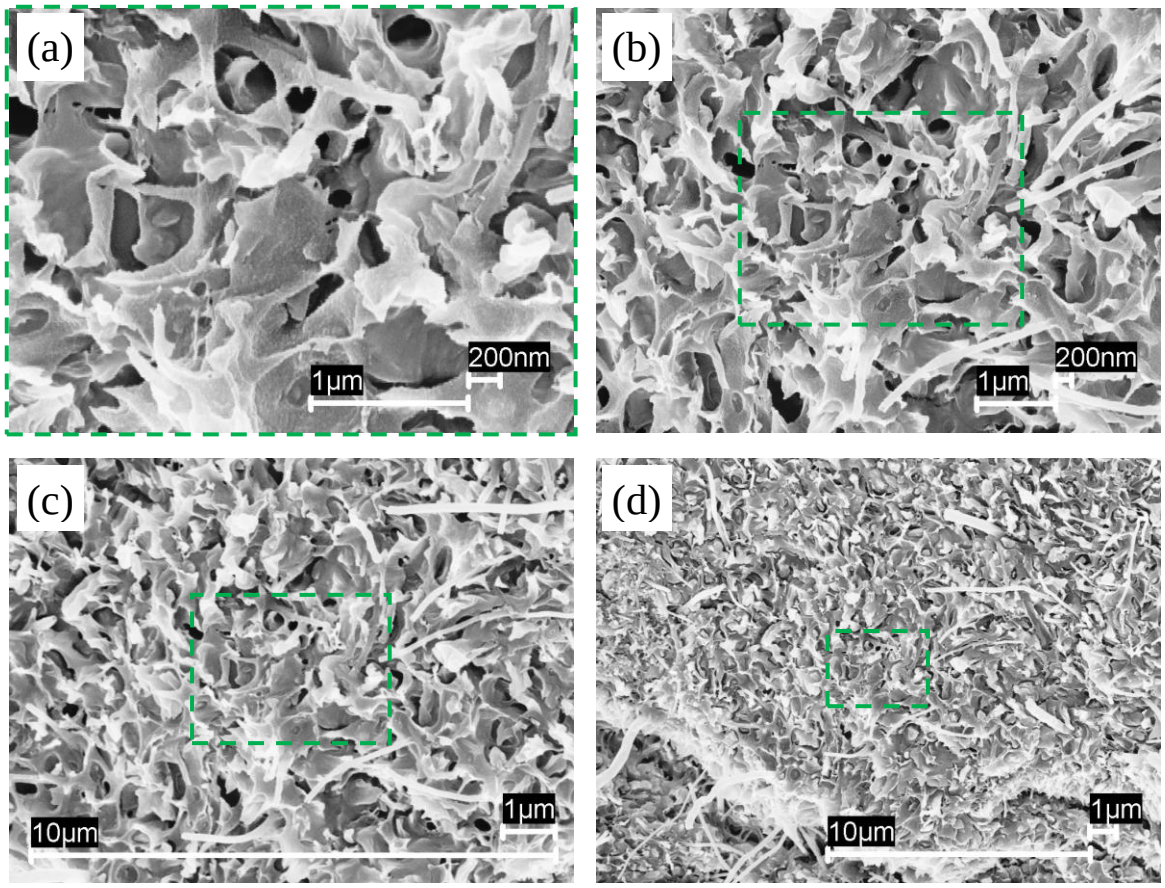

Figure 46. Cross-section images (at different magnifications) of 100K PAN/CNF (60/40) composite fiber showing the phase separated open/porous structure.

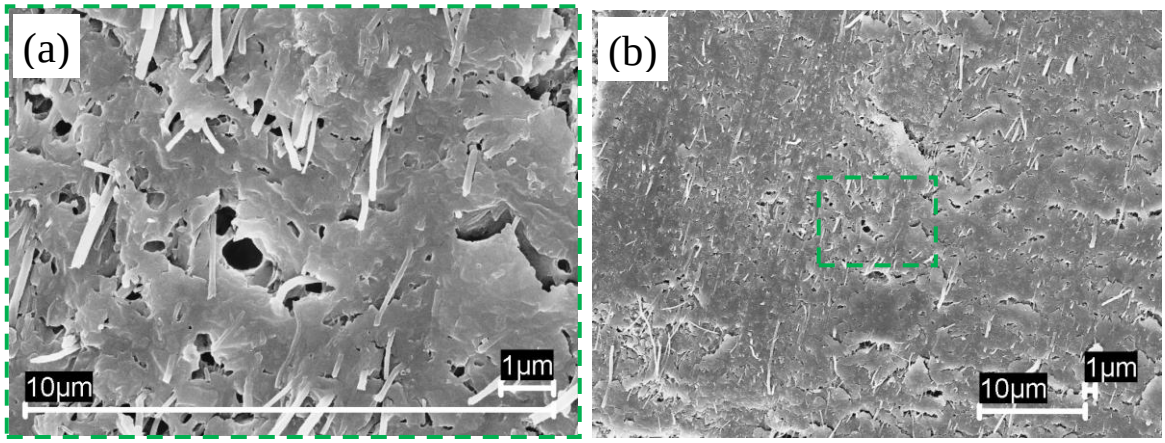

Figure 47. Cross-section images (at different magnifications) of 100K PAN/CNF (60/40) composite fiber showing the compact region.

3.2.3. Fiber Surfaces of Different Composite Fibers

The fiber surfaces of 5, 10, 15, 20, and 30% CNF loaded PAN 100K fibers are shown in Figure 48. As compared to 5% CNF composite fibers, the 10, 15, 20, and 30% CNF composite fibers showed the presence of elongated voids on the surface. The concentration of surface voids and defects increased with an increase in CNF concentration. The probable cause of this increase can be understood from the following hypothesis.

During drawing, the polymer chains are stretched from their coiled state. However, the CNFs are not stretched; they just get oriented/elongated and displaced from their initial position. This creates a void at the two CNF ends. In addition to the incomplete collapse of the polymer chains at CNF ends, the rigidity of the structure also thwarts the polymer collapse along the longitudinal direction. This effect, which occurs both near the ends and edges of CNFs, can be termed as "end-edge effect". The evidence of end-edge effect is shown in the SEM image of the 20% CNF composite fiber (Figure 49).

Since "end-edge" effect occurs due to the presence of CNFs, the concentration of voids increases with increasing concentration of CNFs. This "end-edge effect" combined with "phase separation" (Section 3.2.2) leads to increase in voids with an increase in filler concentration.

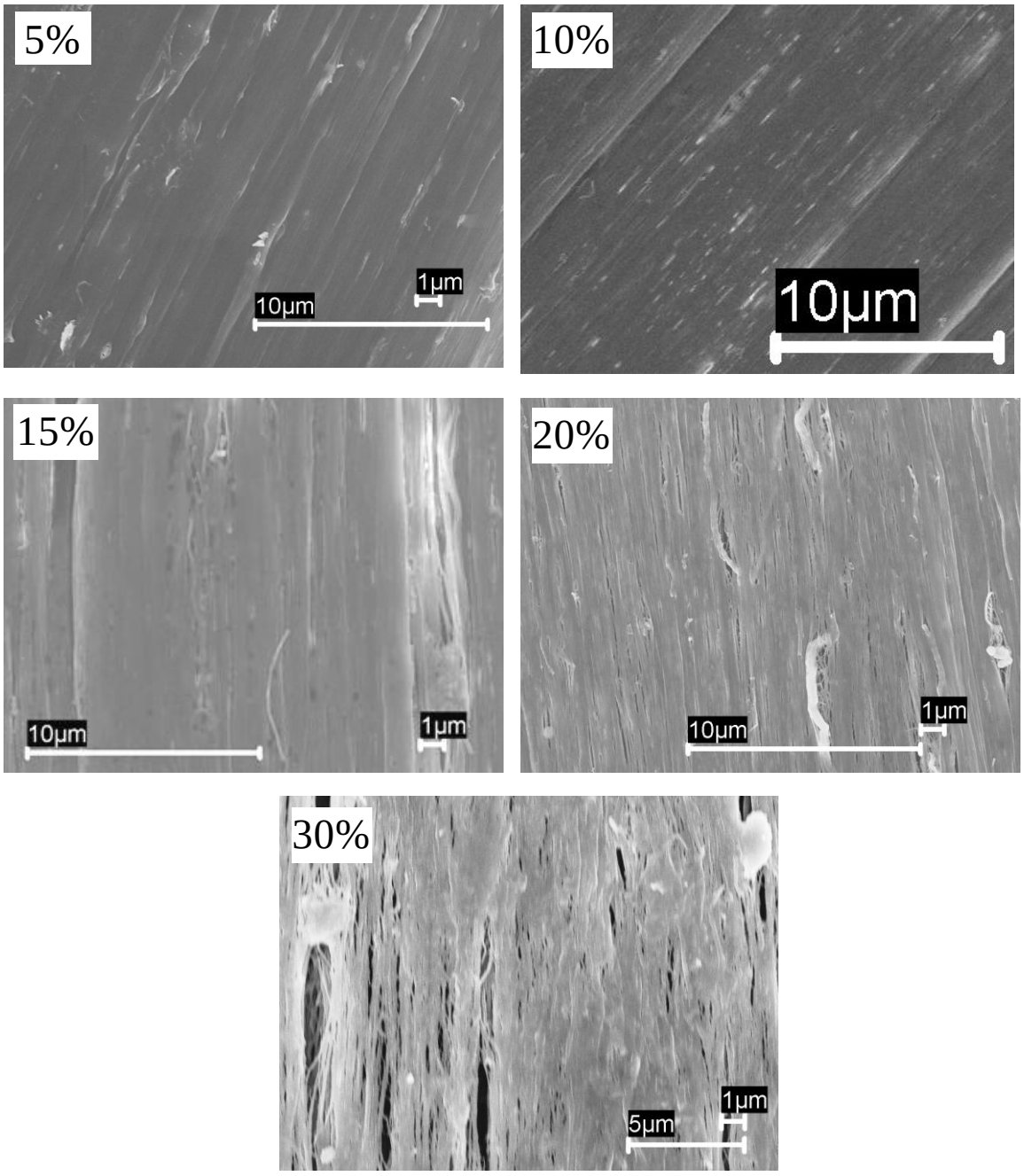

Figure 48. SEM images of the surface of 5, 10, 15, 20, and 30% CNF containing PAN fibers.

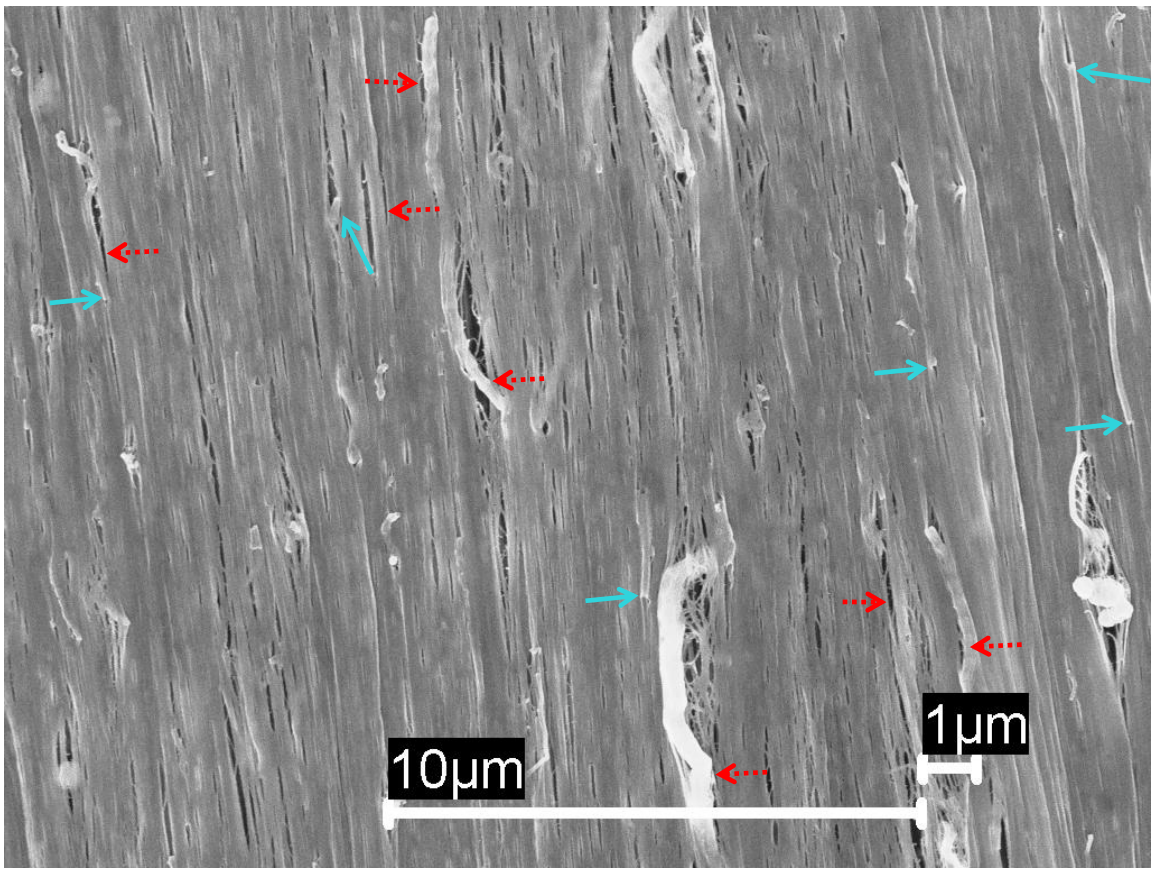

Figure 49. SEM image of the surface of 20% CNF containing PAN fiber. The full arrows (blue color) point towards the "end effect" and dashed arrows (red color) point towards the "edge effect".

3.2.4. Tensile Properties

The tensile properties of various composite fibers are listed in Table 14. Comparison of the tensile properties of the composite fibers with the control PAN fiber (compare Table 2 and 14), for the same DR, showed that only 5% CNF composite fiber showed an improvement in tensile properties. The 5% CNF fiber showed a 30% higher toughness (0.025 ±0.002 N/tex) than control PAN fiber (0.019 ±0.001 N/tex). Among the different composite fibers, 5% CNF composite fibers showed the best tensile properties. The possible reasons for the low tensile properties of high CNF containing fibers are: defects created by the poor dispersion and high entanglement of CNFs (especially at 30%

CNF) and voids created due to end-edge effect. The tensile strength of 5% CNF containing fiber (0.39 N/tex) was even more than 5% MWNT fiber (0.34 N/tex) reported in Chapter 2, 5% SWNT fiber (0.30 N/tex) by Sreekumar *et al.* [4], and 5% SWNT (0.28 N/tex), 5% DWNT (0.26 N/tex), 5% MWNT (0.34 N/tex), and 5% CNF (0.27 N/tex) fibers by Chae *et al.* [1]. Both 15 and 20% CNF fibers showed higher tensile modulus than expected (refer to E_c in Table 14), but 10 and 30% CNF fibers showed lower than expected moduli.

Table 2. Tensile Properties of Control PAN 100K Fibers

Sample	DR	Linear Density (tex)	Tensile Strength (N/tex)	Tensile Modulus (N/tex)	Strain to Failure (%)	Toughness (N/tex)
A1a	3	5.3	0.13 ±0.00	5.5 ±0.2	10.6 ±0.4	--
A1b	4	3.9	0.18 ±0.01	6.7 ±0.2	10.4 ±0.5	0.013 ±0.001
A1c	5	3.2	0.24 ±0.01	7.5 ±0.3	10.8 ±0.6	--
A1d	6	3.0	0.25 ±0.00	8.0 ±0.0	9.3 ±0.0	0.015 ±0.001
A1e	7	3.4	0.34 ±0.01	9.4 ±0.3	9.8 ±0.4	--
A1f	8	2.0	0.36 ±0.01	10.9 ±0.4	7.4 ±0.7	0.017 ±0.002
A1g	9	3.0	0.34 ±0.01	10.0 ±0.3	6.9 ±0.4	--
A1h	10	3.3	0.39 ±0.01	9.7 ±0.2	8.4 ±0.3	0.019 ±0.001

Table 14. Tensile Properties of PAN/CNF Composite Fibers

CNF (%)	DR	Sample	Linear Density (tex)	Tensile Strength (N/tex)	Tensile Modulus (N/tex)	E_{PAN} (N/tex)	$E_{CNT}^{\parallel}$ (N/tex)	E_c (Theoretical) (N/tex)	Strain to Failure (%)
5	6	C1a	1.8	0.39 ±0.02	8.5 ±0.2	--	--	--	12.4 ±0.6
5	9	C1b	3.0	0.45 ±0.02	10.6 ±0.3	10.9	7.4	10.7	9.3 ±0.4
10	10	C2a	1.8	0.23 ±0.00	8.7 ±0.3	10.9	7.8	10.6	9 ±0.3
15	6	C3a	1.9	0.25 ±0.01	9.7 ±0.3	8.0	7.6	7.9	6.5 ±0.3
20	5	C4a	3.3	0.20 ±0.01	8.7 ±0.2	7.5	7.7	7.5	5.7 ±0.3
20	6	C4b	2.4	0.24 ±0.01	9.5 ±0.2	--	--	--	5.8 ±0.3
30	3.5	C5a	5.4	0.09 ±0.01	5.8 ±0.4	6.7	7.4	6.9	2.3 ±0.7

$E_{CNT}^{\parallel}$ and E_c calculated using equations 13-14 and procedure described in Section 2.4.4.

Figures 50 to 54 show the cross-sections of tensile fracture specimens of various PAN/CNF composite fibers. As shown in Figure 50, the 5% CNF composite fiber showed a fibrillar type of failure. The failure became less fibrillar and more brittle with an increase in CNF content (Table 14 and Figures 50 to 54).

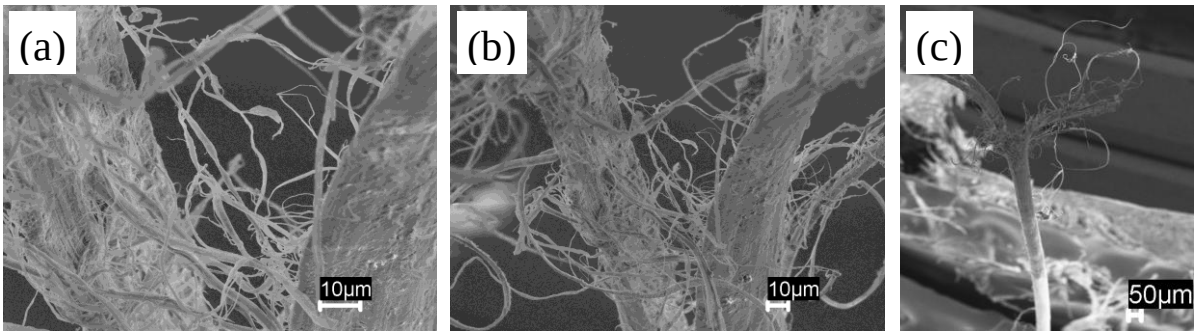

Figure 50. SEM image of tensile fracture of 5% CNF composite fiber.

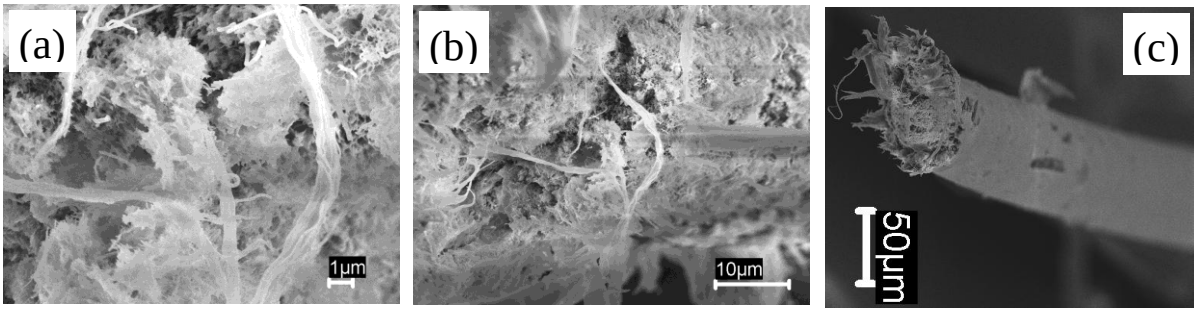

Figure 51. SEM image of tensile fracture of 10% CNF composite fiber.

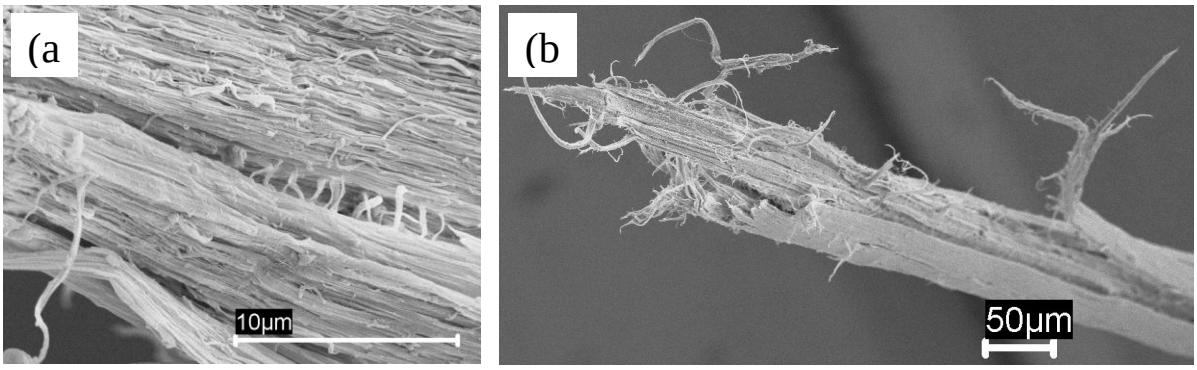

Figure 52. SEM image of tensile fracture of 15% CNF composite fiber.

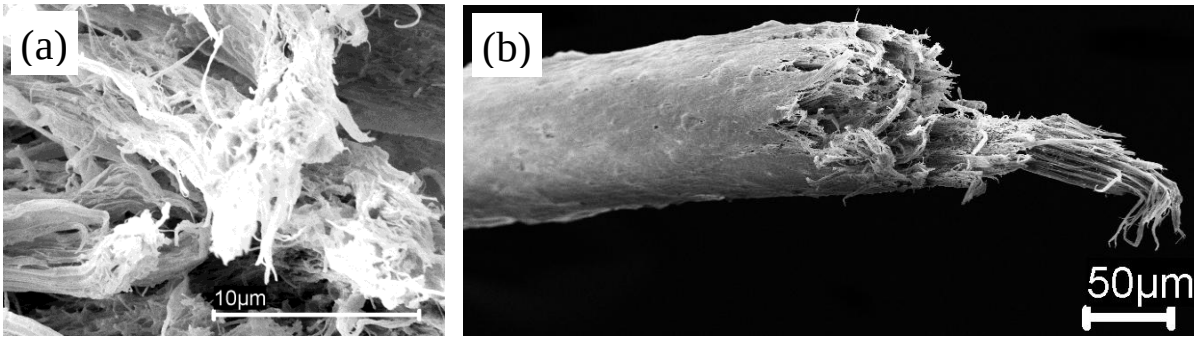

Figure 53. SEM image of tensile fracture of 20% CNF composite fiber.

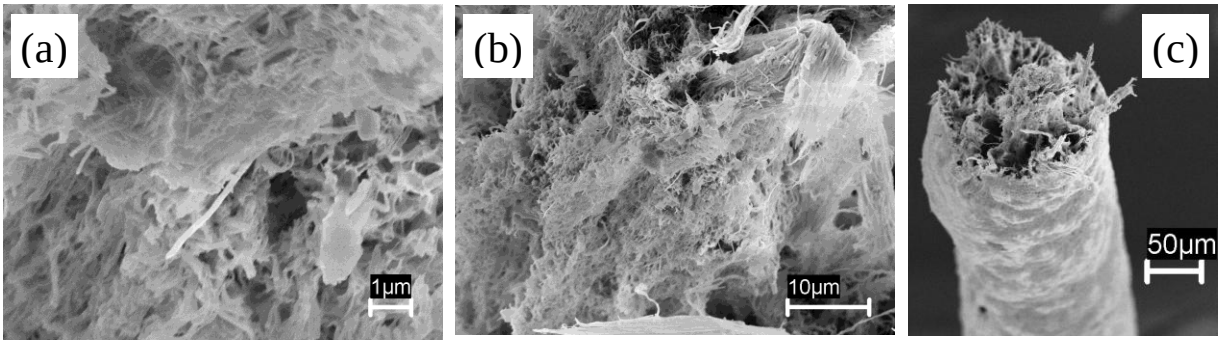

Figure 54. SEM image of tensile fracture of 30% CNF composite fiber.

3.2.5. Dynamic Mechanical Analysis

The storage moduli and tan δ curves for various PAN/CNF fibers are plotted in Figures 55 and 56, respectively. At low temperatures, the storage modulus of various fibers was very close to each other with 15% and 20% CNF containing fibers showing the highest values (Table 15). Same trend continues till room temperature. At temperatures near and above the T_g of PAN (85 ˚C), the storage modulus for CNF containing fibers was higher than that for the control PAN fiber. At 100 ˚C, the storage modulus of 10% and higher CNF containing fibers was three to four times higher than that of the control PAN fiber. However, the 30% CNF containing fibers showed lower

modulus than 15% and 20% CNF containing fibers which could be due to a more defective structure of 30% CNF fibers. As discussed in Section 3.2.3, the 30% CNF containing fibers contained more voids and defects due to both phase separation and end-edge effect. As shown in Figure 56, for 10% and higher CNF loading, the T_g was shifted to higher temperatures.

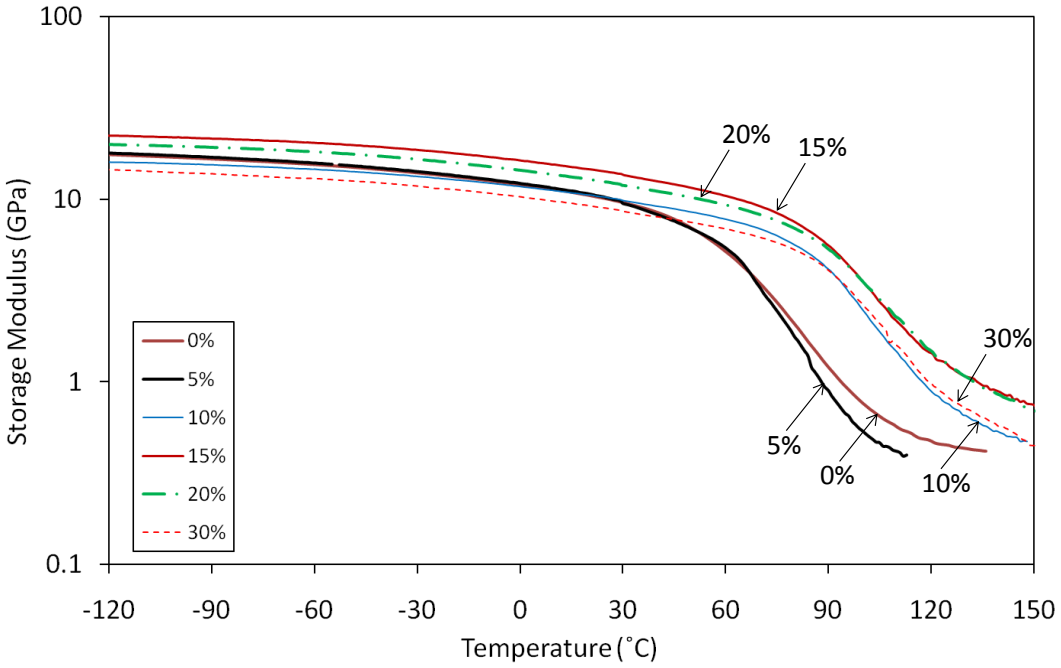

Figure 55. Storage moduli of PAN/CNF composite fibers with different concentrations of CNFs. (0, 5, 10, 15, 20, and 30% correspond to samples A1d, C1a, C2a, C3a, C4a, and C5a, respectively).

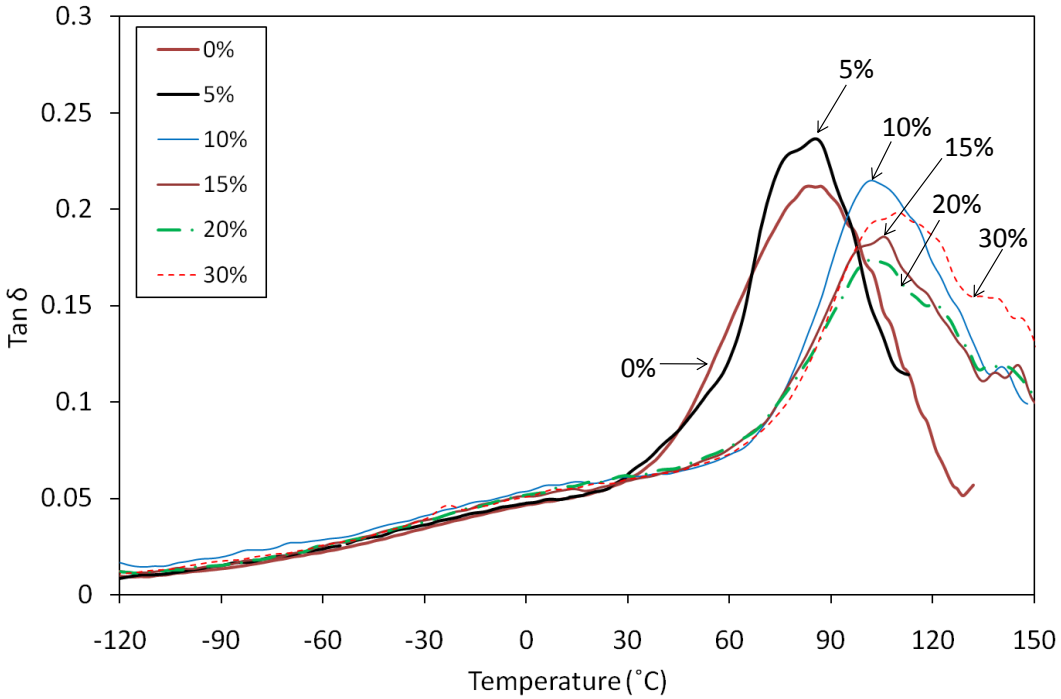

Figure 56. Tan δ of PAN/CNF composite fibers with different concentrations of CNFs. (0, 5, 10, 15, 20, and 30% correspond to samples A1d, C1a, C2a, C3a, C4a, and C5a, respectively).

Table 15. Storage Moduli and T_g of Various PAN/CNF Fibers

CNF (%)	DR	Sample	E' at -120 ˚C (GPa)	E' at 25 ˚C (GPa)	E' at 100 ˚C (GPa)	T_g (˚C)
0	6	A1d	17.6	10.1	0.8	83
5	6	C1a	17.9	10.2	0.5	85
10	10	C2a	15.9	10.2	2.4	102
15	6	C3a	22.3	14.1	3.5	106
20	5	C4a	19.9	12.4	3.5	103
30	3.5	C5a	14.6	9.0	2.7	110

3.2.6. Thermomechanical Analysis

Thermal shrinkage for both control and composite fiber was studied using TMA. For each test, a single fiber filament was heated in nitrogen atmosphere (N_2 flow rate 50 ml/min) from room temperature to 180 ˚C at a heating rate of 5 ˚C/min. Figure 57 shows the shrinkage behavior of control PAN fibers with different draw ratios. The data showed

that draw ratio did not affect the shrinkage of the control PAN fiber significantly. Figure 58 shows the shrinkage behavior of different PAN/CNF composite fibers. In general, the 5% CNF containing fiber showed a higher overall shrinkage as compared to fibers with 10% or more CNF containing fibers. The shrinkage values for both control PAN and PAN/CNF composite fibers are listed in Table 16. In general, the composite fibers showed a lower overall shrinkage than the control PAN fibers. The shrinkage reduced from 19% (for control PAN) to 12-14% for 10% or higher CNF containing fibers. The reduced shrinkage with higher amount of CNF is due to the fact that more and more PAN chains are in the vicinity of CNFs which constraint the movement of PAN chains and reduced thermal shrinkage. The shrinkage of different PAN/CNF fibers is comparable to the shrinkage of different PAN/MWNT fibers reported in Section 2.3.3 (Figure 17).

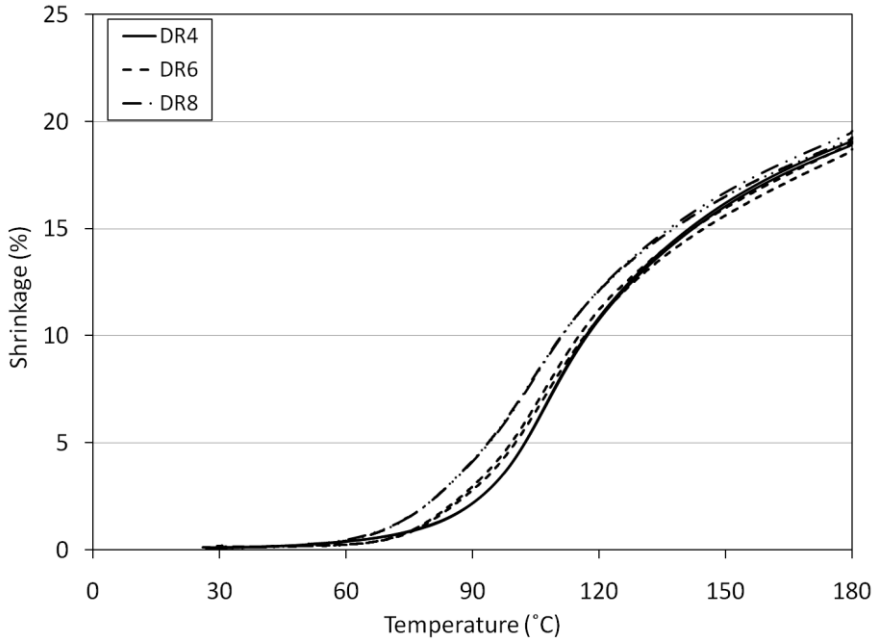

Figure 57. Thermal shrinkage of control PAN fibers as measured using TMA (N_2 flow rate: 50 ml/min; temperature ramp rate: 5 ˚C/min; preload: 0.0002 N/tex). (DR 4, 6, and 8 correspond to samples A1b, A1d, and A1f respectively). Two specimens of each fiber sample were tested and the results were found to be reproducible.

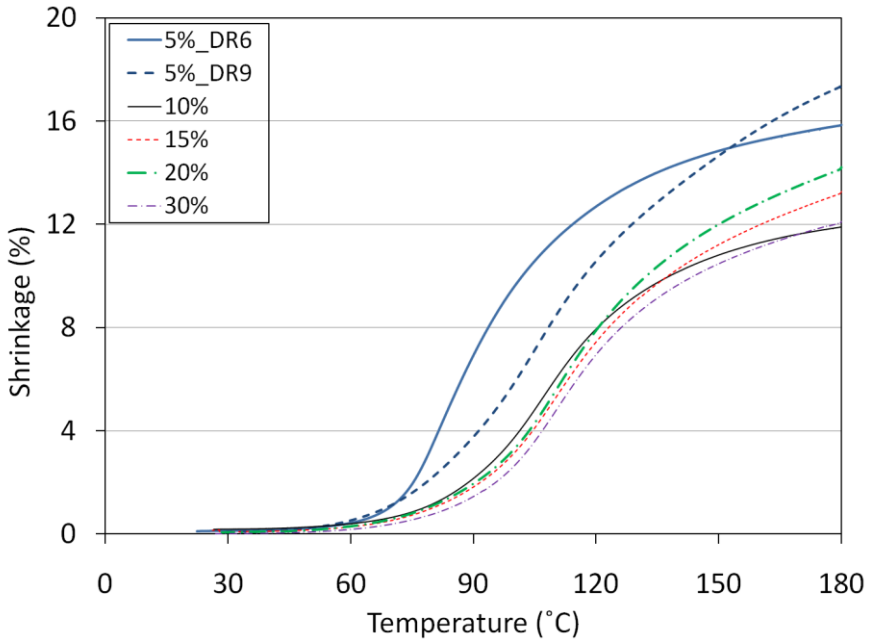

Figure 58. Thermal shrinkage of different PAN/CNF composite fibers as measured using TMA (N_2 flow rate: 50 ml/min; temperature ramp rate: 5 ˚C/min; preload: 0.0002 N/tex). (5%_DR5, 5%_DR9, 10, 15, 20, and 30% correspond to samples C1a, C1b, C2a, C3a, C4a, and C5a, respectively).

Table 16. Shrinkage at 180 ˚C for Various Control and PAN/CNF Composite Fibers (Preload: 0.0002 N/tex)

PAN	CNF (%)	DR	Sample	Shrinkage
100K	0	4	A1b	19
100K	0	6	A1d	19
100K	0	8	A1f	19
100K	5	6	C1a	16
100K	5	9	C1b	18
100K	10	10	C2a	12
100K	15	6	C3a	14
100K	20	5	C4a	14
100K	30	3.5	C5a	12

3.2.7. WAXD Studies

The WAXD patterns for various PAN/CNF composite fibers (5, 10, 15, 20, and 30%) are shown in Figure 59. The corresponding integrated radial and equatorial scans and deconvoluted profiles are shown in Figure 60. The increase in CNF peak (26˚) intensity with increasing CNF concentration is very conspicuous. The measurements for crystallinity, crystal size, and orientation are listed in Table 17. The average crystal size for PAN in different composite fibers was around 6 nm. The different concentrations of CNFs did not have any specific effect on the overall crystallinity, d-spacing, and orientation of PAN. The CNFs alignment was found to be moderate in the range of 0.39 to 0.47. The CNF crystal size in 5% CNF containing fiber was unusually higher than in other fibers, and the values (12-16 nm) reported by Guo *et al.* [5], the reason for which is not quite understood. It was also noted that the ratio of CNT to PAN peak intensity (ratio of intensities at $2\theta = 26^{\circ}$ and 17˚) was higher in PAN/CNF fibers in this study than PAN/CNF films by Guo *et al.* [5]. For example, in PAN/CNF fiber, in the integrated radial scan, the CNF intensity became higher than PAN intensity above 10% CNF loading in the fiber. Whereas in PAN/CNF films by Guo *et al.* [5], the CNF intensity became higher than PAN intensity only above 40% CNF loading. The overall crystallinity, crystal size, and orientation of PAN in PAN/CNF fibers were similar to the values obtained for PAN/MWNT fibers (Table 5). However, as opposed to MWNTs containing fibers that showed lower d-spacing for PAN, the CNFs had no such effect on the d-spacing of PAN for CNF containing fibers. This suggests that planar walls in MWNTs have different effect on the PAN chains in the vicinity than the rough surfaces (due to ridges of graphitic platelets in the stacked-cup geometry) of CNFs.

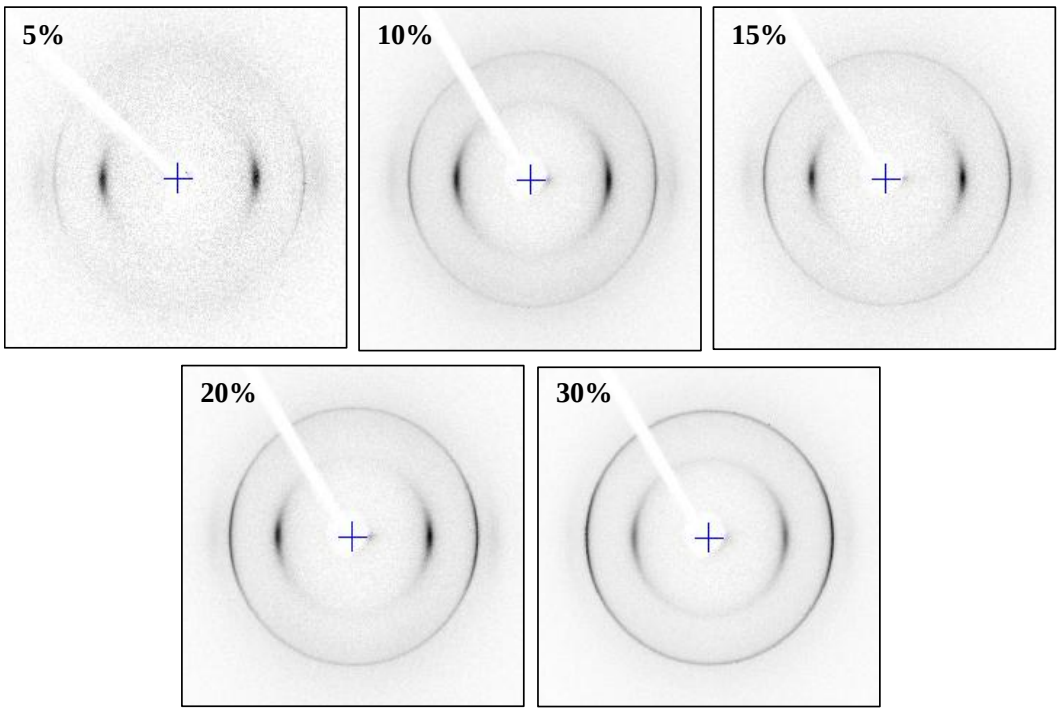

Figure 59. WAXD patterns of different PAN/CNF composite fibers. (5, 10, 15, 20, and 30% corresponds to samples C1b, C2a, C3a, C4a, and C5a, respectively).

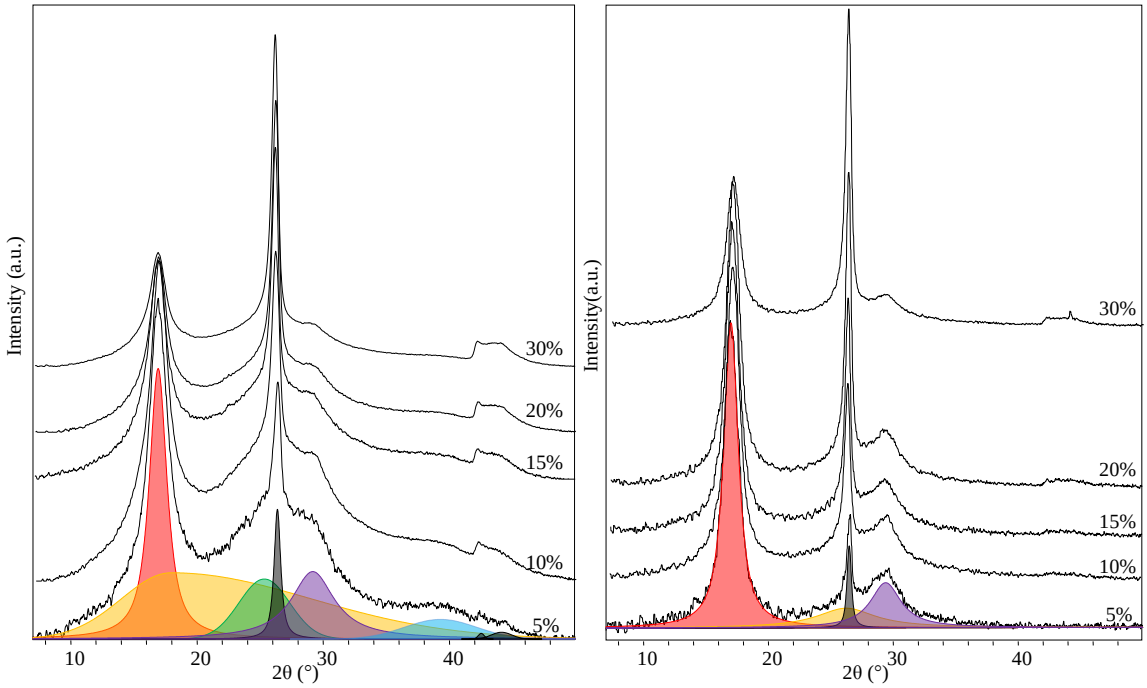

Figure 60. Integrated radial (left) and equatorial (right) scans of different PAN/CNF composite fibers. (5, 10, 15, 20, and 30% corresponds to samples C1b, C2a, C3a, C4a, and C5a, respectively).

Table 17. WAXD Results for Various Control PAN and PAN/CNF Composite Fibers

PAN	CNF (%)	DR	Sample	Crystallinity[1] (%)	d-spacing (PAN 2θ~17°) (Å)	f_{PAN}[2] (2θ~17°)	f_{CNF}[2] (2θ~26°)	L_{PAN}[3] (2θ~17°) (Å)	L_{CNF}[3] (2θ~26.3°) (Å)
100K	**0**	**4**	**A1b**	48	5.25	0.66	---	59	---
100K	**0**	**6**	**A1d**	52	5.24	0.74	---	54	---
100K	**0**	**8**	**A1f**	55	5.25	0.77	---	59	---
100K	**0**	**10**	**A1h**	48	5.26	0.81	---	60	---
100K	**5**	**9**	**C1b**	50	5.21	0.77	0.39	57	192
100K	**10**	**10**	**C2a**	45	5.23	0.68	0.47	60	151
100K	**15**	**6**	**C3a**	57	5.26	0.72	0.43	62	167
100K	**20**	**5**	**C4a**	46	5.26	0.70	0.45	62	157
100K	**30**	**3.5**	**C5a**	47	5.28	0.55	0.39	58	154

[1] Calculated by deconvolution of integrated scan; [2] Herman's orientation factor;
[3] Calculated using Scherrer's equation from equatorial scan

3.2.8. Electrical Conductivity of PAN/CNF Composite Fibers

The electrical conductivities of the composite fibers are listed in Table 18. At 5, 10, and 15% CNF concentration, the PAN/CNF fibers were found to be non-conducting (conductivity below 10^{-6} S/m). The 40% CNF composite fiber showed the highest electrical conductivity, an almost four orders of magnitude higher than that of the 20% CNF containing fiber. At 20% loading, the conductivity for MWNT reinforced fiber was almost four orders of magnitude higher than that of CNF reinforced fiber (compare values in Table 6 and Table 14). The 30% CNF composite fiber showed electrical breakdown (Figure 61) at a current of around 1.26×10^{-4} A.

Table 18. Electrical Conductivity of PAN/CNF Fibers

CNF (%)	DR	Electrical Conductivity (S/m)
20	5	$8.2 \times 10^{-5} \pm 8.7 \times 10^{-6}$
30	3.5	0.9 ± 0.5
40	as spun	42 ± 16

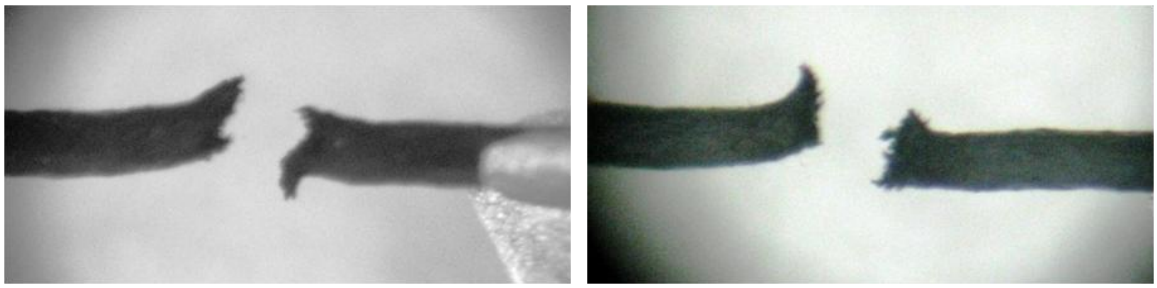
Figure 61. 30%CNF composite fiber after electrical breakdown.

3.2.9. Porous Fiber Structures with Aligned CNFs

CNFs get oriented in the fiber direction during the fiber spinning and drawing process. Both physical and chemical interaction between CNFs and PAN affect the alignment of PAN, alignment of CNF, and coating of PAN onto CNF. To further understand some of these points and to actually see the aligned CNFs on a more global level, the composite fibers were charred in TGA as mentioned in Section 2.2. The SEM images of the charred fibers were taken at different magnifications (high and low) to observe both local and global regions of the fibers. Figure 62 shows the control PAN fiber after charring. The fibers fused resulting in solid mass of charred PAN with compacted regions and voids. Furthermore, the fiber shape was lost in the charred structure.

Figures 63 and 64 show the 5% and 10% CNF loaded PAN/CNF composite fibers, respectively, after charring. Contrary to PAN 100K control fiber, the composite fibers did not fuse and the fiber shape retained in the charred structure. SEM images of the charred fiber show skeleton of the fiber structure and show that aligned CNFs provide porosity to the fibers. Figures 65 and 66 show the 15% and 20% CNF loaded PAN/CNF composite fibers, respectively, after charring. In comparison to the 5% and 10% CNF composite fibers, the porous charred structure seems to be less oriented in case of 15%

and 20% CNF loaded fibers. For the 30% CNF loaded composite fiber (Figure 67), the fiber shape was retained, but the CNFs showed lower alignment. Small bunches of CNFs forming fibrils were evident in the charred structure of 30% CNF composite fiber. This could be due to either poor dispersion or phase separation during solution preparation, or both. This issue of dispersion and bundling at high CNF concentration was discussed in Section 3.2.2.

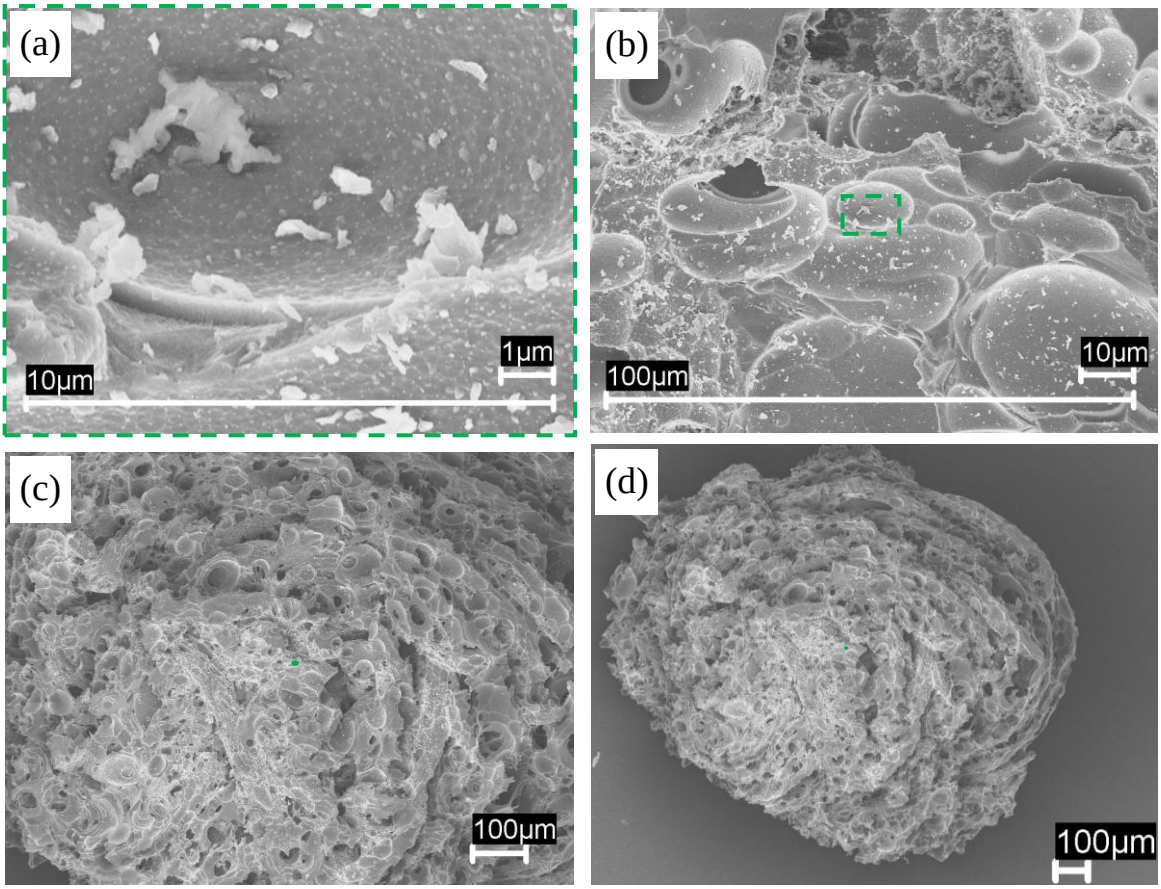

Figure 62. SEM images of the control PAN 100K fiber after charring in TGA at 5 ˚C/min up to 1000 ˚C under N_2.

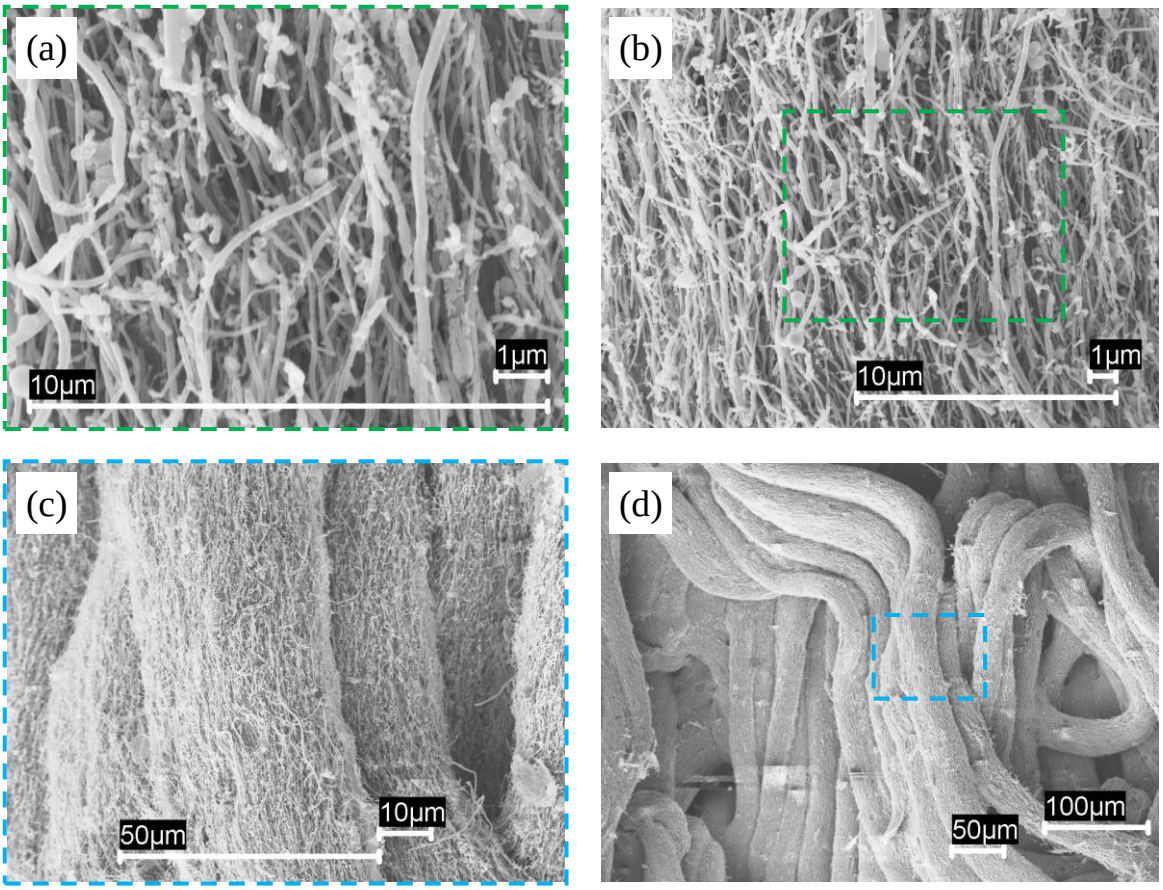

Figure 63. SEM images (at different magnifications) of the 100K PAN/CNF (95/5) composite fiber after charring in TGA at 5 ˚C/min up to 1000 ˚C under N_2.

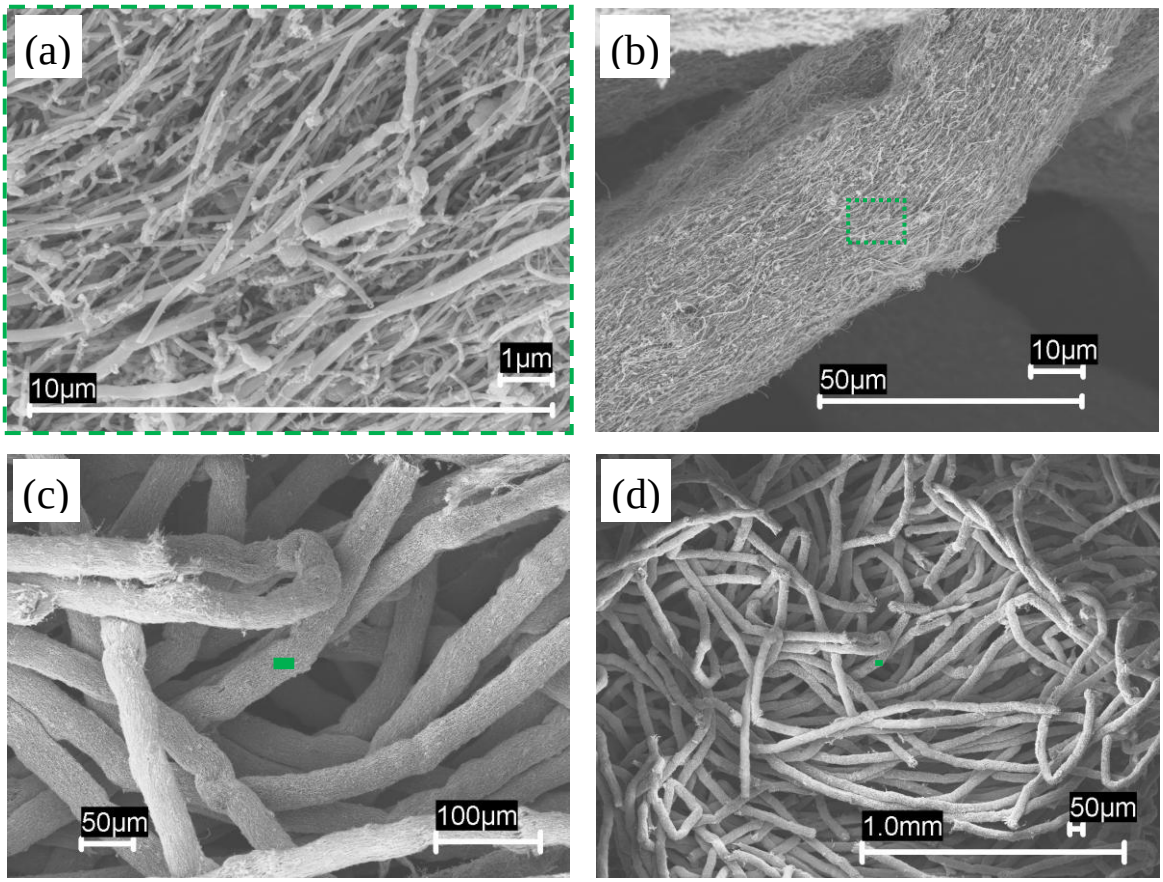

Figure 64. SEM images (at different magnifications) of the 100K PAN/CNF (90/10) composite fiber after charring in TGA at 5 ˚C/min up to 1000 ˚C under N_2.

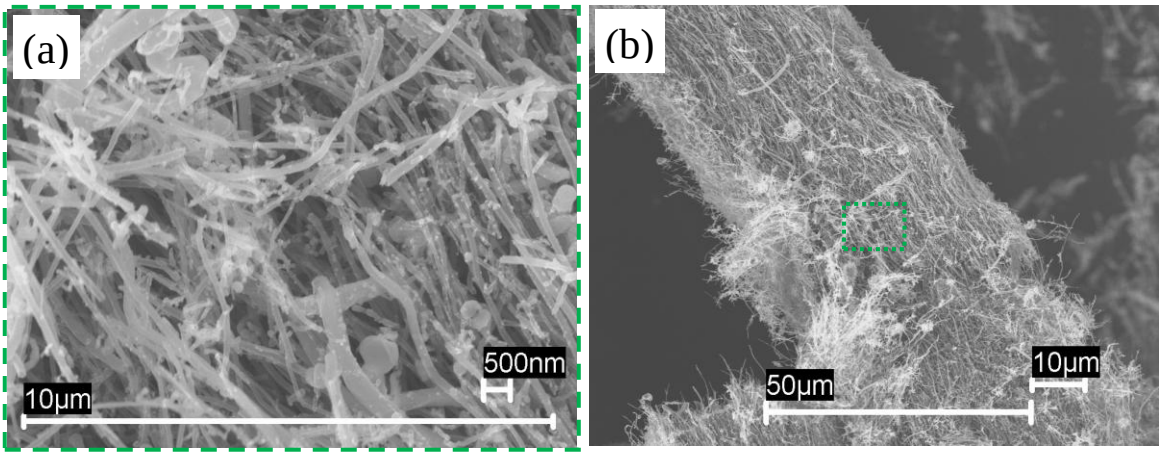

Figure 65. SEM images (at different magnifications) of the 100K PAN/CNF (85/15) composite fiber after charring in TGA at 5 ˚C/min up to 1000 ˚C under N_2.

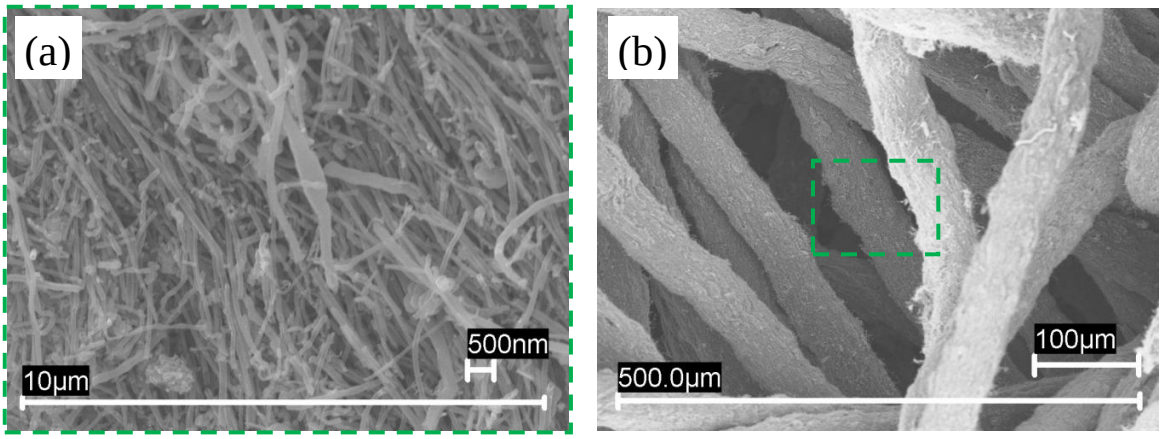

Figure 66. SEM images (at different magnifications) of the 100K PAN/CNF (80/20) composite fiber after charring in TGA at 5 ˚C/min up to 1000 ˚C under N_2.

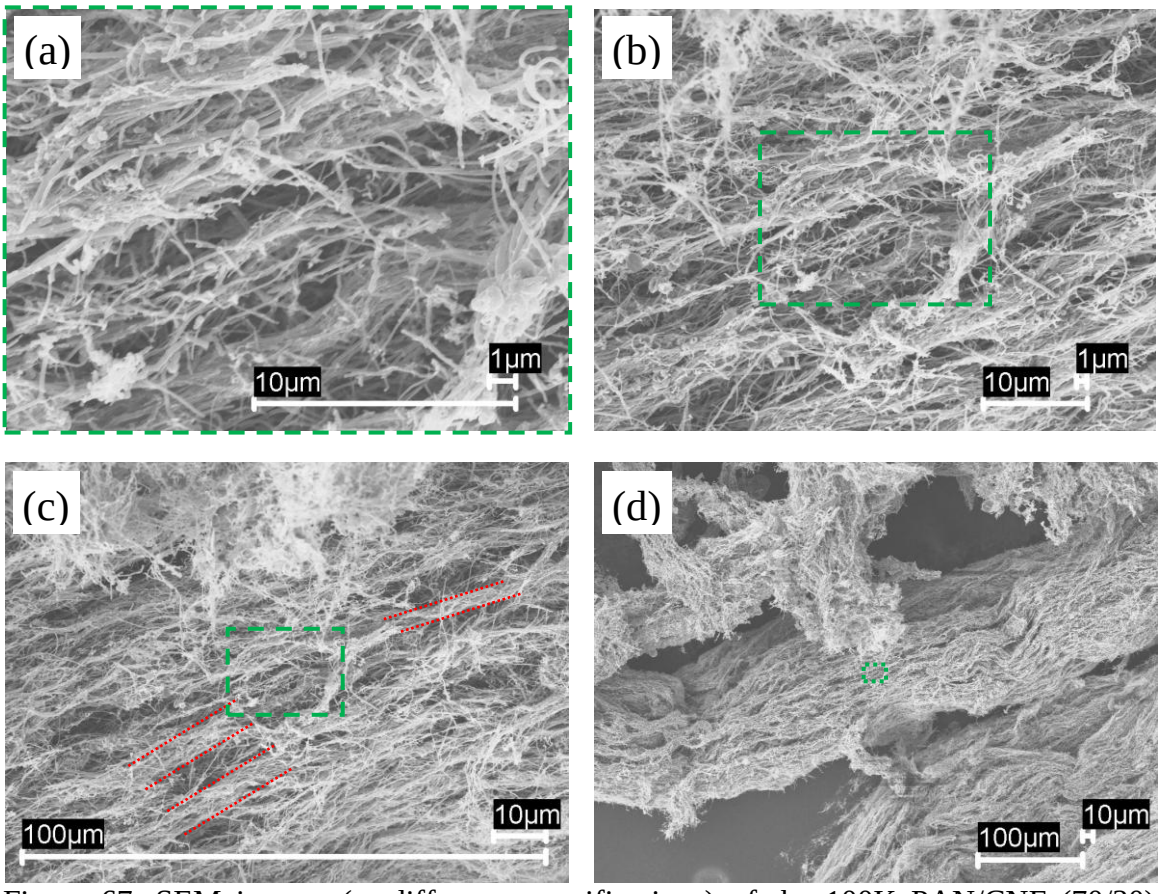

Figure 67. SEM images (at different magnifications) of the 100K PAN/CNF (70/30) composite fiber after charring in TGA at 5 ˚C/min up to 1000 ˚C under N_2. The red dashed-line show the bunches of CNFs forming fibrils.

3.2.10. Effect of CNF Sonication Time on Fiber Structure and Properties

To study the effect of CNF sonication time at two different concentrations of CNFs in the fiber, the solutions were prepared where the CNF sonication times were about 5 and 48 h. For comparing long and short sonication times for CNF dispersion, the 5% CNF composite fibers were made by using two-stage drawing (first drawing in hot water at 85 ˚C and then second drawing in boiling water). The 20% fibers were made by using single-stage drawing (Section 3.1.3). As evident from Figure 68, there was no change in the dispersion state of CNFs in 5% composite fiber when the CNFs were sonicated for 5 and 48 h. In both cases the dispersion state can be described by scenario I. However, for 20% CNF fiber, the dispersion improved after longer sonication time (compare Figure 43 in Section 3.2.2 and Figure 69 in this section). As shown in Appendix B, the length of CNFs decreased with increase in sonication time. The shorter length helps reduce entanglements and improves dispersion. The SEM image of the fiber cross-section for 20% CNFs sonicated for 48 h shows a uniform distribution of CNFs. Under the previous classification scheme of dispersion, this dispersion would fall under scenario I.

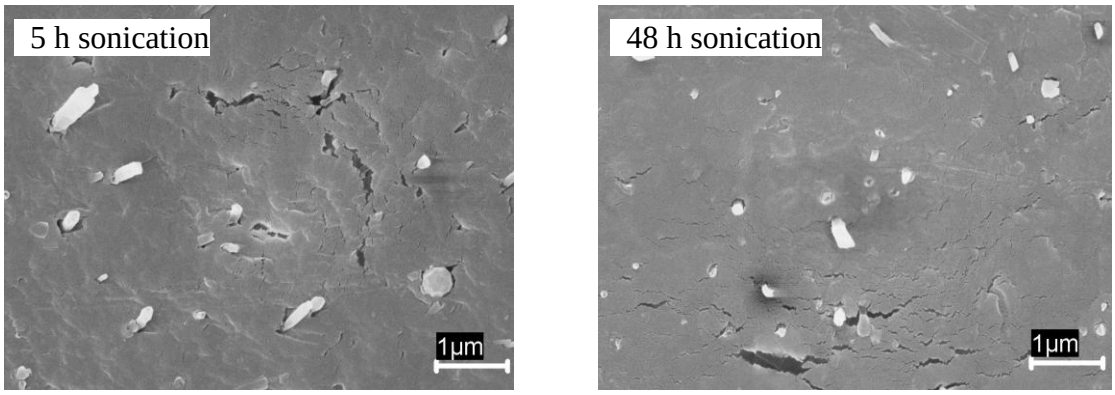

Figure 68. Cross-sections of PAN/CNF (95/5) composite fibers prepared using CNFs sonicated for 5 h and 48 h.

For two different draw ratios, in case of 5% CNF fiber, the tensile strength and modulus increased when the sonication time was changed from 5 h to 48 h. However, for 20% CNF fiber, there was not much change in the tensile properties, but the moduli was high than expected values (7.5 N/tex and 7.6 N/tex for 5 h and 48 h sonication, samples C4a and E3a, respectively) determined using equation 14 and procedure described in Section 2.4.4. Figure 70 shows the shrinkage behavior of these fibers (fibers listed in Table 19) when heated up to 180 ˚C in N_2 atmosphere. The experiment was conducted using TMA. In essence, the sonication time did not have any significant effect on the shrinkage behavior of composite fibers. The shrinkage values for various fibers are listed in Table 19.

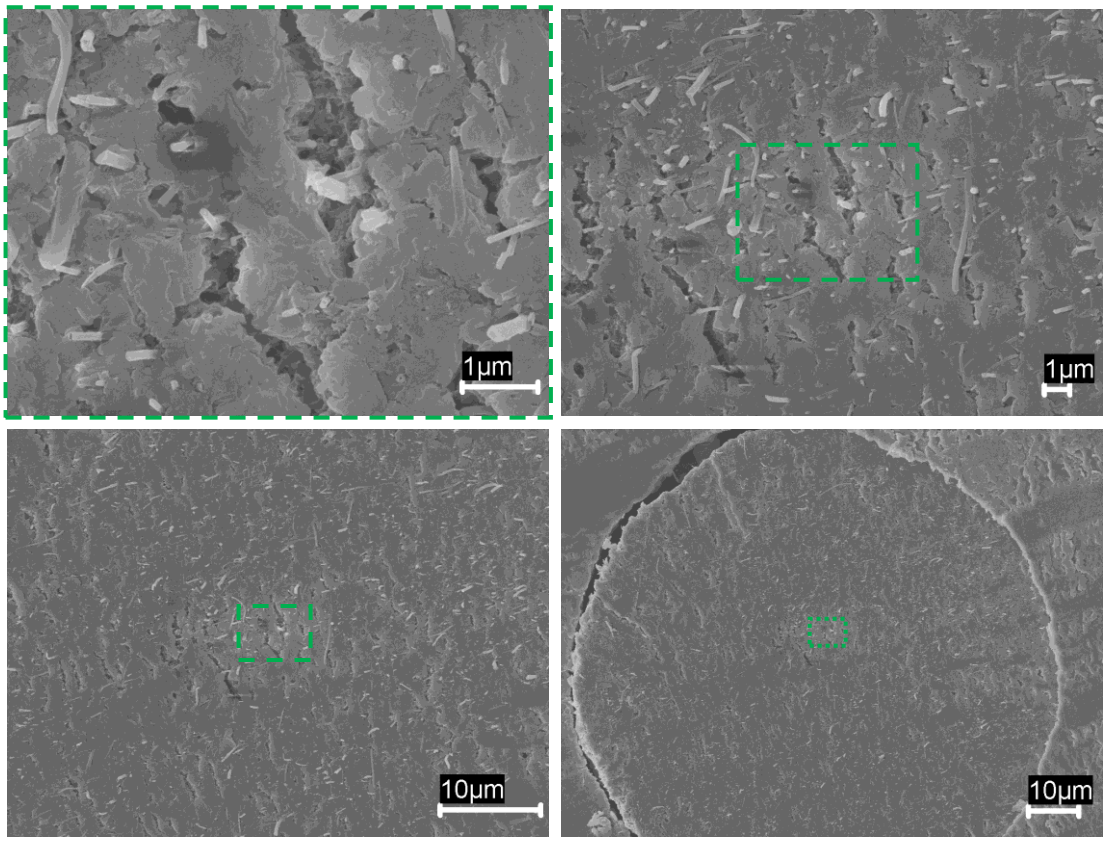

Figure 69. Cross-section (at different magnifications) of PAN/CNF (80/20) composite fiber processed using CNFs sonicated for 48 h.

Table 19. Effect of Sonication Time on the Tensile Properties of the 5% and 20% CNF Composite Fibers

CNF (%)	Sonication Time (h)	Drawing (1 or 2 stage)	DR	Sample	Linear Density (tex)	Tensile Strength (N/tex)	Tensile Modulus (N/tex)	Strain to Failure (%)	Toughness (N/tex)	Shrinkage (%)
5	5	2	9	E1a	3.2	0.28 ±0.01	9.7 ±0.4	11.2 ±0.6	--	19
5	5	2	12	E1b	2.6	0.49 ±0.02	12.8 ±0.5	9.4 ±0.5	0.028 ±0.003	18
5	48	2	9	E2a	3.6	0.41 ±0.04	11 ±0.3	10.8 ±1.1	--	18
5	48	2	12	E2b	2.7	0.52 ±0.02	13.6 ±0.4	9 ±0.7	0.028 ±0.003	16
20	48	1	5	E3a	3.2	0.17 ±0.01	8.4 ±0.4	4.9 ±0.4	--	15
20	5	1	5	C4a	3.3	0.20 ±0.01	8.7 ±0.2	5.7 ±0.3	--	14

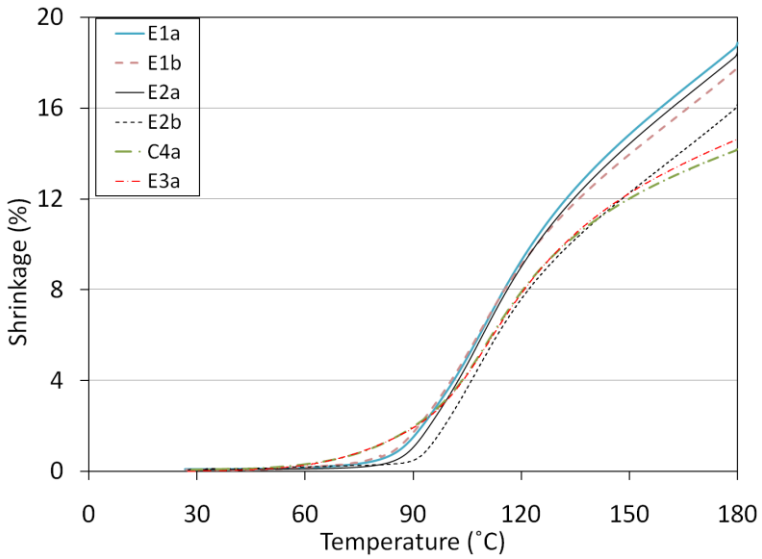

Figure 70. Effect of sonication time (5 h vs. 48 h) on the shrinkage behavior of 5% and 20% CNF reinforced PAN fibers. (N_2 flow rate: 50 ml/min; temperature ramp rate: 5 ˚C/min; preload: 0.0002 N/tex). For sample designation, refer to Table 19.

The improvement in CNF dispersion after sonication for 48 h for 20% CNF loaded fiber contributed to increased electrical conductivity of the composite fiber. As compared to 5 h sonication fiber, which showed a conductivity of 8.21×10^{-5} S/m, the 48 h sonication fiber showed an average conductivity of 1.27×10^{-3} S/m. A better dispersion also resulted in higher orientation of CNFs. The WAXD properties for 20% CNF fibers

with 5 and 48 h sonication time are listed in Table 20 and corresponding patterns and radial profiles are shown in Figures 71 and 72, respectively.

Table 20. WAXD Results for PAN/CNF (80/20) Composite Fibers for 5 h and 48 h Sonication

Sample	DR	Sonication Time (h)	Crystallinity[1] (%)	d-spacing (PAN 2θ~17°) (Å)	f_{PAN}[2] (2θ~17°)	f_{CNF}[2] (2θ~26°)	L_{PAN}[3] (2θ~17°) (Å)	L_{CNF}[3] (2θ~26.3°) (Å)
C4a	**5**	**5**	46	5.26	0.70	0.45	62	157
E3a	**5**	**48**	47	5.26	0.68	0.55	62	156

[1] Calculated by deconvolution of integrated scan; [2] Herman's orientation factor;
[3] Calculated by Scherrer's equation using equatorial scan

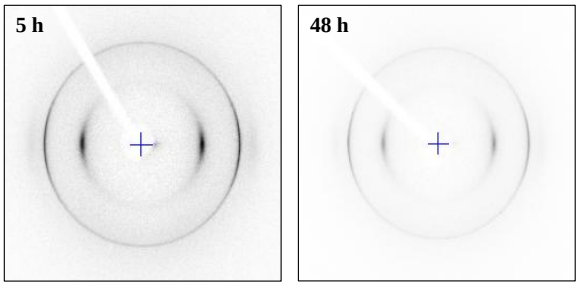

Figure 71. WAXD patterns of PAN/CNF (80/20) composite fibers for 5 h and 48 h sonication times.

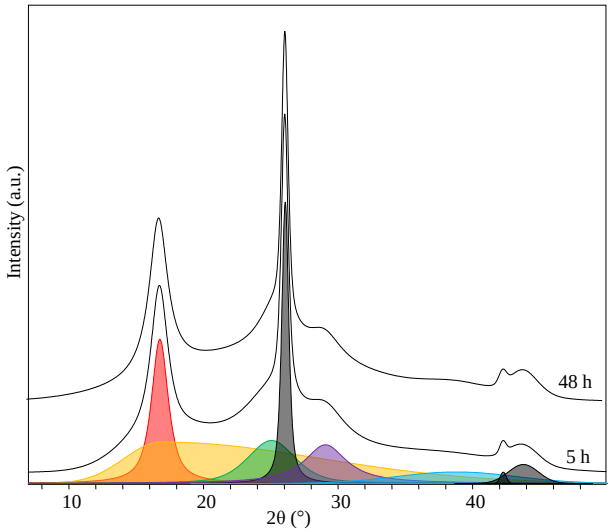

Figure 72. Integrated radial scans of PAN/CNF (80/20) composite fibers for 5 h and 48 h sonication times.

3.2.11. Effect of Drying Temperature on Fiber Properties

The 20% CNF composite fibers were dried at two different temperatures of 50 ˚C and 85 ˚C. The higher drying temperature was used because the literature [6] indicated that if PAN fiber is dried near its wet T_g, then the nano/micro -voids that could have formed during the coagulation or drawing process can collapse during the drying process. As shown in Table 21, the higher drying temperature had no effect on strength and modulus but increased the strain to failure by ~ 25%. The moduli of these fibers were higher than what was expected theoretically. Figure 73 shows the shrinkage behavior of these fibers studied using TMA. The drying temperature did not have any significant effect on the shrinkage behavior of the composite fiber. The shrinkage values for various fibers are also listed in Table 21.

Table 21. Tensile and Shrinkage Properties of 20% CNF Composite Fiber Dried at Two Different Temperatures

Sample	Drying Temp. (˚C)	DR	Linear Density (tex)	Tensile Strength (N/tex)	Tensile Modulus (N/tex)	$E_{CNT}^{\parallel}$ (N/tex)	E_{PAN} (N/tex)	E_c (Theoretical) (N/tex)	Strain to Failure (%)	Shrinkage (%)
E3b	50	6	3.3	0.20 ±0.01	9.7 ±0.5	8.5	8.0	8.1	4.4 ±0.2	14
E3c	85	6	3.3	0.20 ±0.01	9.5 ±0.6	9.4	8.0	8.3	5.4 ±0.3	14

E_c calculated using equations 13-14 and procedure described in Section 2.4.4.

The crystalline properties of the fibers are listed in Table 22. The higher drying temperature resulted into lower d-spacing and orientation for PAN, and a higher orientation for CNF. Since fibers were dried on a spool, any free shrinkage was prevented. But, the molecular motion in the amorphous region was still possible and occurred which reduced PAN orientation. The d-spacing reduced at high temperature because of the thermal stresses generated in the fiber under the constrained heating of the

fiber. It is conceivable that thermal stresses would tend to compact PAN crystals and lead to lower d-spacing. The increase in CNF orientation after drying at high temperature is also due to thermal stresses in the fiber. As opposed to oriented PAN chains which have a tendency to go to random coil configuration in the presence of thermal energy, CNFs are not expected to show any such change in their morphology. Therefore, when the fiber is under higher thermal stress (85 ˚C vs. 50 ˚C), the CNFs tend to orient in the direction of stress, i.e., in the fiber axis direction. An increase in the strain to failure for the fiber dried at high temperature can be attributed to lower PAN orientation, which tends to increase strain to failure.

Table 22. WAXD Results for PAN/CNF (80/20) Composite Fibers Dried at 50 and 85 ˚C

Sample	Drying Temp. (˚C)	DR	Crystallinity (%)	d-spacing (PAN 2θ~17°) (Å)	f_{PAN} (2θ~17°)	f_{CNF} (2θ~26°)	L_{PAN} (2θ~17°) (Å)	L_{CNF} (2θ~26.3°) (Å)
E3b	50	6	49	5.25	0.73	0.58	69	168
E3c	85	6	49	5.21	0.70	0.67	70	167

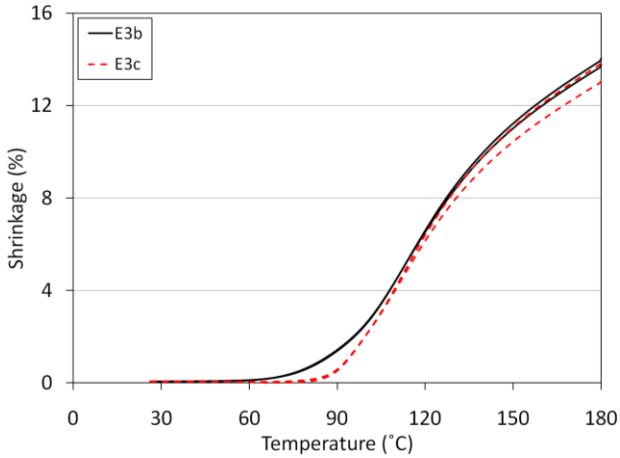

Figure 73. Effect of drying temperature (50 ˚C vs. 85 ˚C) on the shrinkage behavior of 20% CNF reinforced PAN fiber. (N_2 flow rate: 50 ml/min; temperature ramp rate: 5 ˚C/min; preload: 0.0002 N/tex). E3b and E3c correspond to samples in Table 17. Two curves for two specimens of the same sample are shown for reproducibility.

3.2.12. Effect of Two-Stage Drawing on Tensile Properties

The control PAN 100K fibers were made by both one-stage and two-stage drawing. For one-stage drawing, the fibers were drawn in boiling water. For two-stage drawing, the fibers were first drawn in hot water at 85 ˚C and then drawn in boiling water. The tensile properties of fibers are listed in Table 23. The one-stage and two-stage fibers are different in their linear density, because different spinning speeds (plunger and take-up speeds) were used. The fiber in one-stage spinning was taken up very slowly which increased the linear density. For the same draw ratio, the tensile modulus increased when fiber was drawn in two stages, as compared to single stage drawing. There was no clear trend in tensile strength but the strain to failure decreased when the fiber was drawn in two stages.

The effect of relative drawing in two different stages was also studied for 5% CNF case. In case I, the draw ratio was 2 in hot water at 85 ˚C and 3 in boiling water; in case II, the draw ratio was 3 in hot water at 85 ˚C and 2 in boiling water. The total DR for both cases I and II was 6. The tensile properties of the fibers for the two cases are listed in Table 24. The fiber from case I showed better mechanical properties than fiber from case II. Therefore, it can be concluded that, in case of two-stage drawing, for the same total DR 6, the tensile properties are enhanced when the fiber is drawn less in first drawing bath at lower temperature and drawn more in the second bath at higher temperature.

Table 23. Tensile Properties of Control PAN 100K Fibers Drawn in One and Two Stages

Sample	DR	Number of Drawing Stages	Linear Density (tex)	Tensile Strength (N/tex)	Tensile Modulus (N/tex)	Strain to Failure (%)
A1d	6	One	3.0	0.25 ±0.00	8.0 ±0.0	9.3 ±0.0
F1a	6	Two	1.6	0.28 ±0.02	10.5 ±0.9	6.8 ±0.4
A1f	8	One	2.0	0.36 ±0.01	10.9 ±0.4	7.4 ±0.7
F1b	8	Two	1.2	0.34 ±0.01	12.2 ±0.4	6.6 ±0.4

Table 24. Tensile Properties of 5% CNF Composite Fibers Drawn in Two Stages

Case	Sample	DR	Linear Density (tex)	Tensile Strength (N/tex)	Tensile Modulus (N/tex)	Strain to Failure (%)	Shrinkage (%)
I	F1c	6	5.1	0.32 ±0.01	9.8 ±0.2	11.9 ±0.7	16
II	F1d	6	5.1	0.29 ±0.02	9.1 ±0.3	10.7 ±0.7	18

Figure 74 shows the shrinkage behavior of 5% CNF based fiber drawn in two stages (samples corresponding to Table 24) and drawn in single stage. There was not much effect of the relative drawing of fiber in two stages (case I vs. II) on the shrinkage behavior, but as compared to single stage drawing, the temperature for shrinkage inception for the fiber drawn in two stages was increased by almost 20 ˚C.

Interestingly, the 5% CNF composite fibers which were drawn in two stages showed a different tensile failure (Figure 75). The two-stage drawn fiber showed an intermediate region where the stress was constant over a finite strain range, whereas the one-stage drawn fiber showed a typical tensile failure curve (dashed-line) where force/stress increases with strain. It seems that the fiber has core-shell type of structure, where the polymer chains in the very thin shell region are highly oriented and the polymer chains in the core region are not. Therefore, when the forced is applied, the outer

shell breaks after a finite strain and then core region being less oriented sustains the stress and shows increased strain without any appreciable change in stress. Following which, the core region behaves in a typical single stage drawn fiber. The region of finite strain (1-2 %) over a constant stress makes this fracture behavior different and these fibers peculiar. This failure behavior was not observed in control PAN fiber and fibers with 20% CNF loading, which behaved typically.

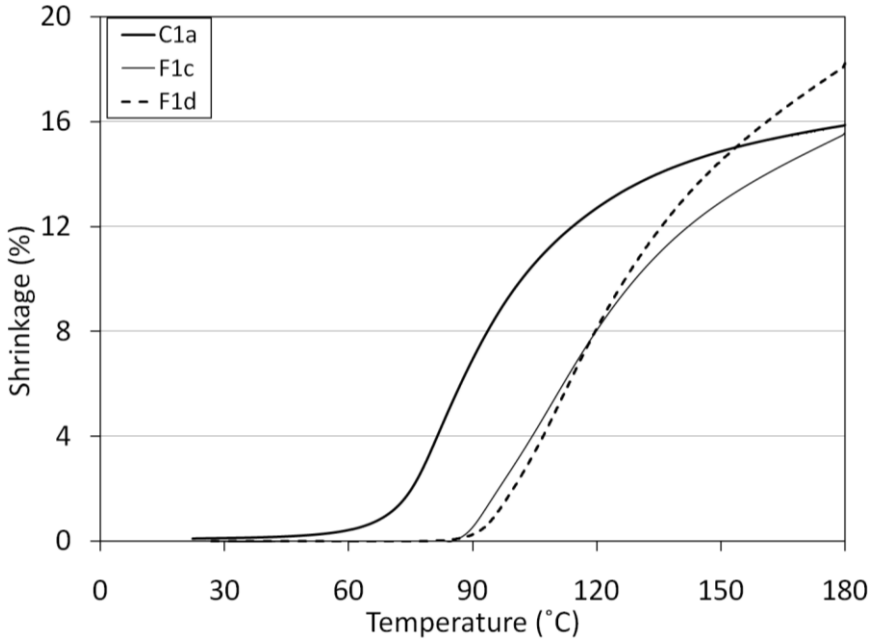

Figure 74. Effect of 1 stage and 2 stage drawing (compare C1a with F1c or F1d) and effect of relative drawing in two stages (compare F1c with F1d) on the shrinkage behavior of 5% CNF reinforced PAN fiber. (N_2 flow rate: 50 ml/min; temperature ramp rate: 5 ˚C/min; preload: 0.0002 N/tex). For sample designation, refer to Tables 14 and 23. The temperature for shrinkage inception for the three fibers (1 stage, I, and II) is around 72 ˚C, 90 ˚C, and 93 ˚C.

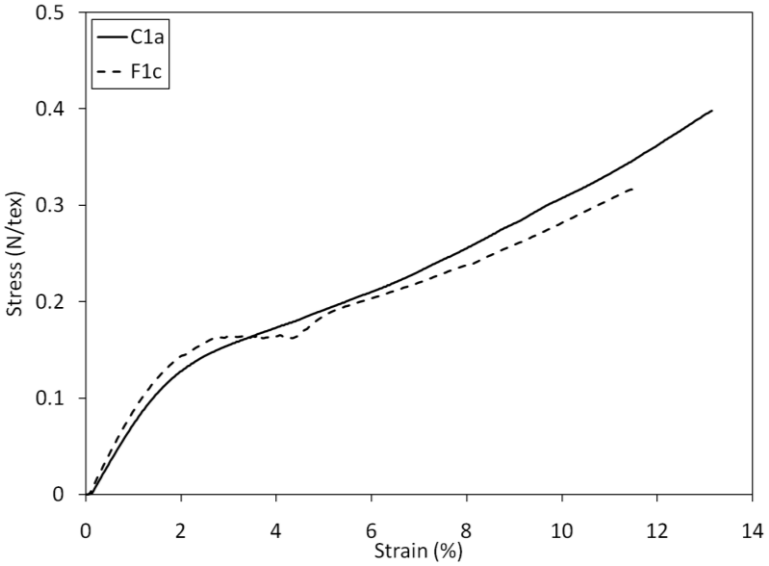

Figure 75. Typical stress strain behaviors of 5% CNF composite fiber drawn in 1 stage (solid line) and drawn in 2 stages (dashed line). For sample designation, refer to Tables 14 and 23.

3.3. Conclusions

- The presence of CNFs helps maintain the composite fiber its form after charring.
- The CNFs increased the overall char yield of the fiber after charring up to 1000 ˚C.
- The combined effect of "end-edge effect" and phase separation leads to an increase in voids and defects with an increase in CNFs concentration.
- Longer sonication time resulted in good CNF dispersion, increased CNF orientation, and increased axial electrical conductivity of the composite fiber.
- The higher drying temperature (85 ˚C as compared to 50 ˚C) increased the composite fiber strain to failure.
- By using high concentration of CNFs in the composite, the conductivity of the fiber could be increased to the level required in applications like electrostatic

dissipation and electromagnetic shielding (more discussion about electrical conductivity of PAN/CNT fibers in Chapter 6).

3.4. References

1. Chae HG, Sreekumar TV, Uchida T, and Kumar S. Polymer 2005;46(24):10925-10935.

2. Uchida T, Anderson DP, Minus ML, and Kumar S. Journal of Materials Science 2006;41(18):5851-5856.

3. Lawrence JG, Berhan LM, and Nadarajah A. ACS Nano 2008;2(6):1230-1236.

4. Sreekumar TV, Liu T, Min BG, Guo H, Kumar S, Hauge RH, and Smalley RE. Advanced Materials 2004;16(1):58-61.

5. Guo H, Rasheed A, Minus ML, and Kumar S. Journal of Materials Science 2008;43(13):4363-4369.

6. Dumbleton JH and Bell JP. Journal of Applied Polymer Science 1970;14(9):2402-2406.

CHAPTER 4

PAN/CNF COMPOSITE FIBERS WITH HIGH MOLECULAR WEIGHT (MW) PAN

PAN/CNF composite fibers with high loading of CNFs (20%) and high MW PAN were spun using dry-jet wet spinning. The composite fibers with high MW PAN showed better tensile properties than with low MW PAN. Though no such increase was observed for 100K based fibers, but after reinforcement with 20% CNFs, the overall crystallinity increased from 44% to 53% for 250K PAN fiber and from 38% to 59% for 700K PAN fiber. The presence of CNFs was found to increase the PAN solution viscosity at lower shear rates and showed a sharp shear thinning behavior with increase in shear rate. CNF increased the storage modulus of the PAN solutions at low frequencies (due to large increase in elastic behavior).

4.1. Experimental

4.1.1. Materials

In addition to PAN with a MW of 100,000 g/mol (100K), PAN with MWs of 250,000 g/mol (250K) and 700,000 g/mol (700K) were also used in this study. All PAN polymers were obtained from Japan Exlan Co. Ltd. All other chemicals/materials were same as mentioned in Sections 2.1.1 and 3.1.1. To ascertain the presence or absence of any copolymer in three different polymers, the infra-red spectroscopy was conducted on dry powders of 100K, 250K, and 700K PAN polymers and control fibers made from them. Figures 76 and 77 show the infra-red spectra of 100K, 250K, and 700K PAN powders and fibers, respectively. The infra-red spectra show that both 250K and 700K

PAN are homopolymers, and the presence of C=O peak at 1740 cm^{-1} in 100K PAN confirmed the presence of MA copolymer. The fiber samples showed the peaks between 1660 and 1680 cm^{-1} corresponding to solvent DMF. To remove the DMF, the 250K PAN fiber was dried in nitrogen at 180 ˚C for 5 minutes. Comparing the spectra of dried fiber with polymer powder and fiber (Figure 78), it seems that some DMF still remains in the fiber.

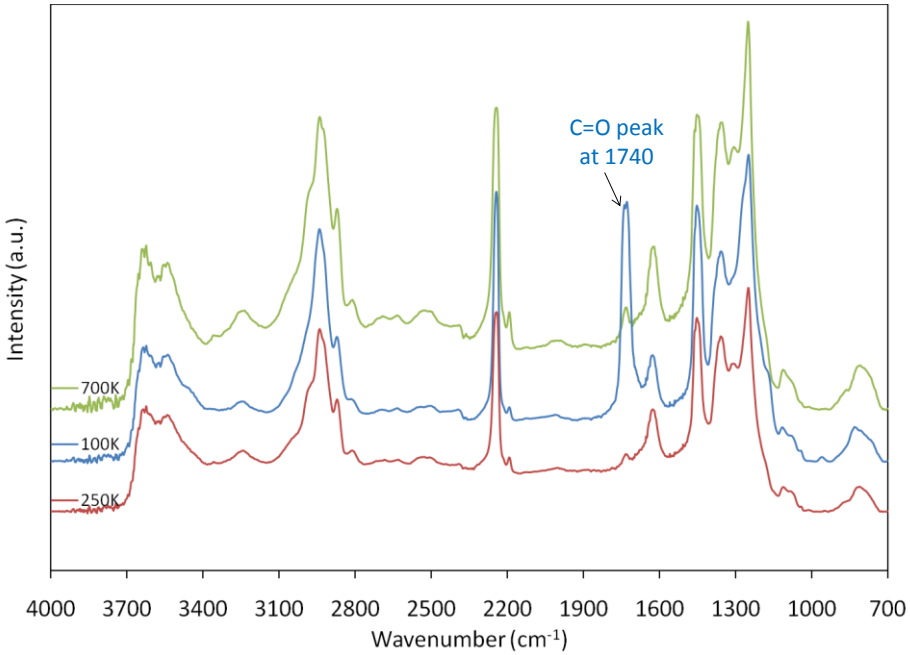

Figure 76. FTIR spectra of 100K, 250K, and 700K PAN powders. The carbonyl peak in 100K is indicated at 1740 cm^{-1}. There are low intensity peaks at 1730 cm^{-1} in 250K and 700K.

4.1.2. PAN/CNF Solution Preparation

For different MW PAN systems, different solid content solutions were prepared for fiber spinning. For PAN with 250K MW and 700K MW, a solid content of around 15 g/100 ml and 8 to 10 g/100 ml, respectively, were used. The rest of the method was similar as mentioned for PAN/CNF systems in Section 3.1.2 and Section 2.1.2.

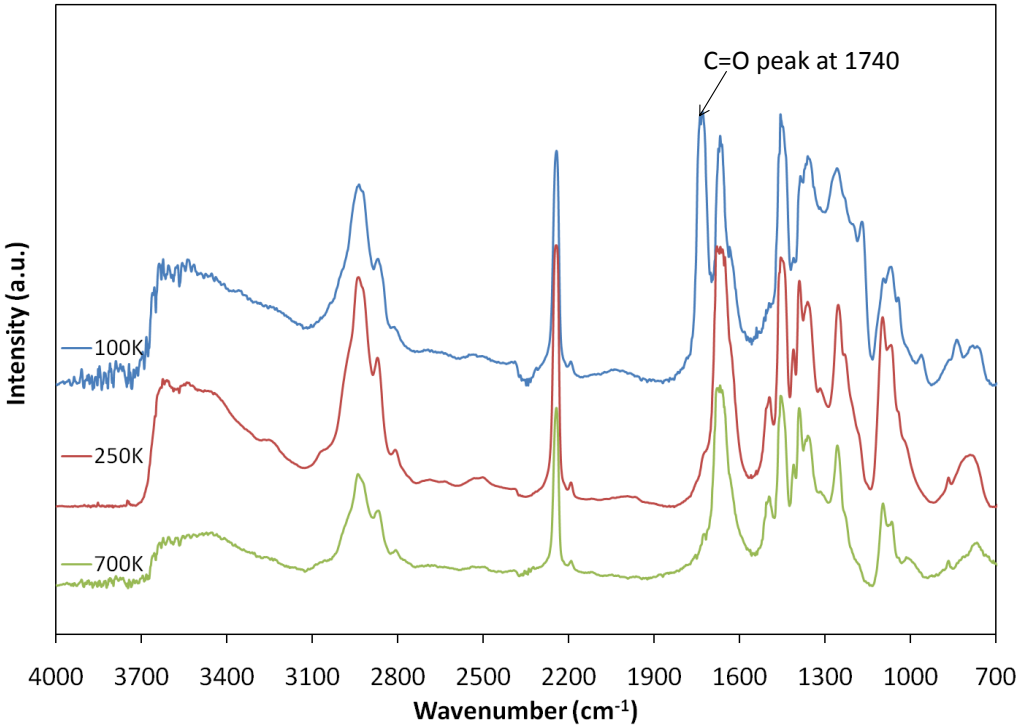

Figure 77. FTIR spectra of 100K, 250K, and 700K fibers. The carbonyl peak in 100K fiber is indicated at 1740 cm^{-1}.

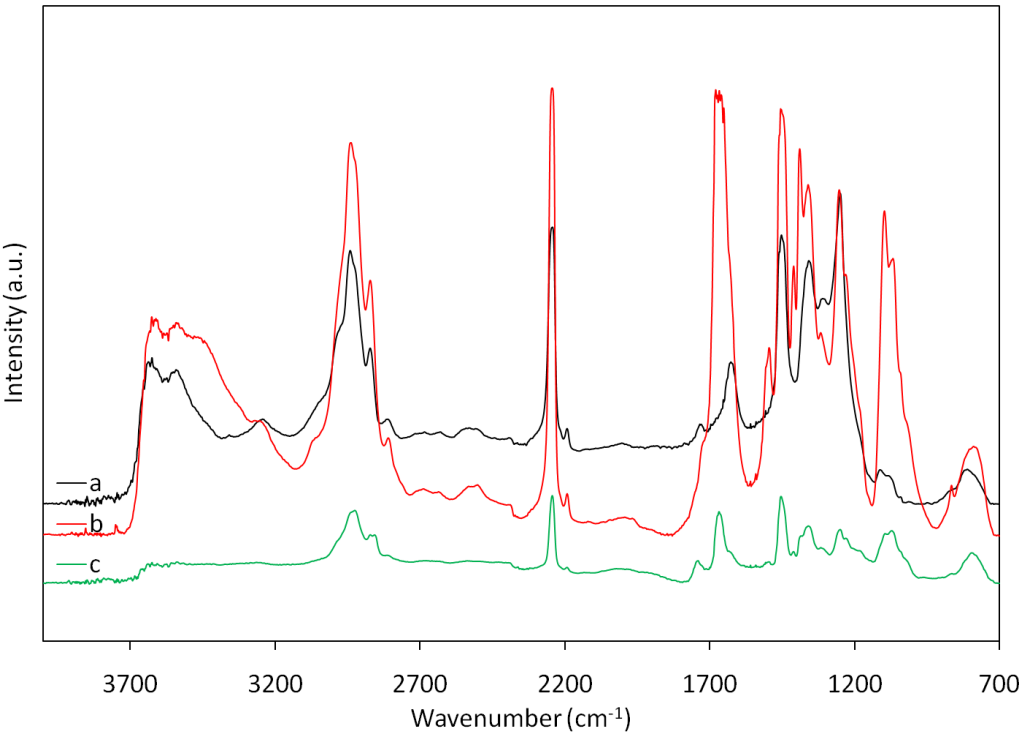

Figure 78. FTIR spectra of PAN 250K (a) powder, (b) fiber, (c) fiber after drying at 180 ˚C for 5 minutes.

4.1.3. PAN/CNF Fiber Spinning

With both 250K and 700K PAN, the composite fibers with 20% CNF loading were spun using dry-jet wet spinning. The PAN/CNF/DMF solution was poured into the barrel (with 28 mm internal diameter). The solution was extruded through a spinneret with a hole diameter of 250 μm. The temperature of the barrel was kept at 110 ˚C for 250K PAN based fibers (15 wt% solid content) and 700K composite fibers (8 wt% solid content), and 20 ˚C for 700K PAN control fibers (9 wt% solid content). Apparently, the 700K PAN control fiber had lower viscosity, which allowed it to be spun at lower temperature than other spinning solutions. The rest of the fiber spinning set-up and procedure (except the heat drawing part) was similar to the ones mentioned in Sections 2.1.3 and 3.1.3. After passing through the second coagulation bath, CB2, Figure 8 (Section 2.1.3), the fibers were kept in a 20/80 DMF/water bath for ~ 24 h before heat drawing. The heat drawing was conducted over a hot-plate set-up at 140 ˚C and 160 ˚C for 250K and 700K based fibers, respectively.

As shown in Figures 79 and 80, the CNFs were found to be uniformly dispersed in both 250K and 700K PAN fibers. According to the scheme mentioned in Section 3.2.2, the scenario I was dominating for both 250K and 700K based composite fibers. At similar 20% CNF loading in PAN 100K, both scenarios I and II were equally present. This suggests that a high MW PAN is more efficient in dispersing CNFs at high concentrations.

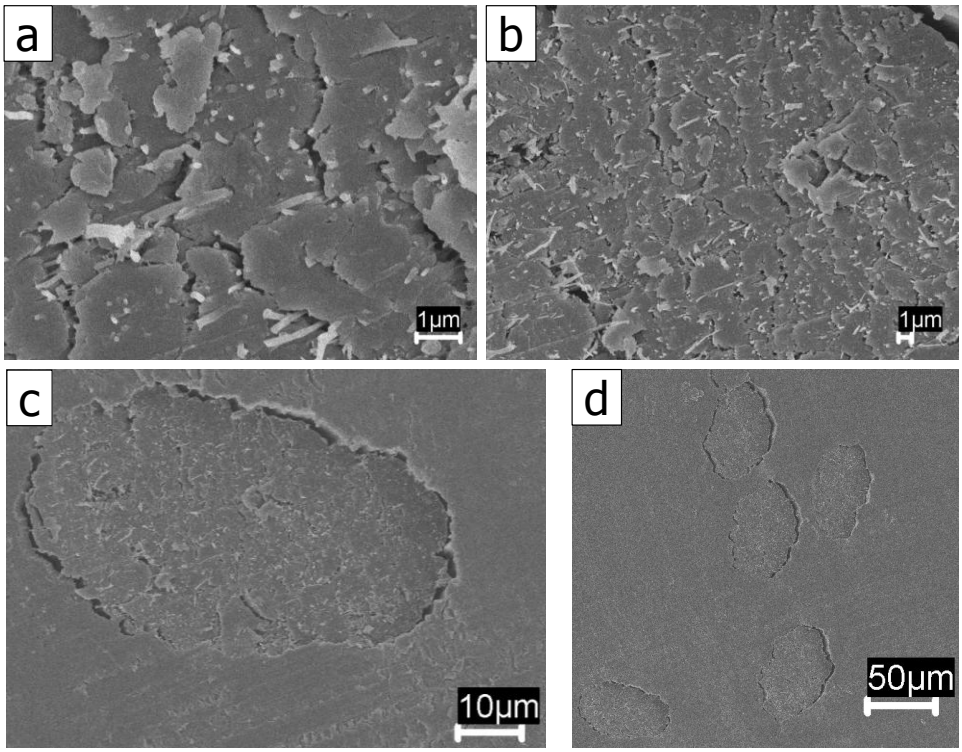

Figure 79. SEM images (at different magnifications) of the cross-section of 20% CNF containing 250K fiber with DR 10.

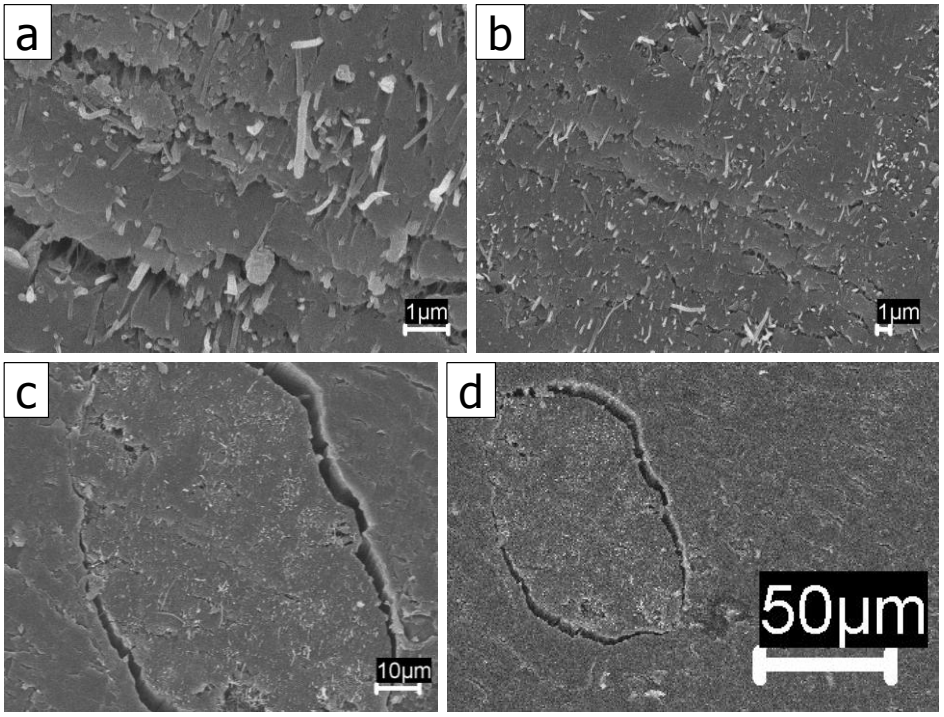

Figure 80. SEM images (at different magnifications) of the cross-section of 20% CNF containing 700K fiber with DR 8.

Figures 81 and 82 show the surface images of 20% CNF containing 250K and 700K fibers. As compared to 20% CNF containing 100K fiber (Figure 43), the 20% CNF containing 250K and 700K fiber surfaces showed less number of voids and cracks. This is despite the fact that both 250K and 700K based composite fibers were drawn to much higher draw ratios than 100K based composite fiber. The higher drawing temperature used for high MW PAN systems may be partly responsible for reduced voids and cracks.

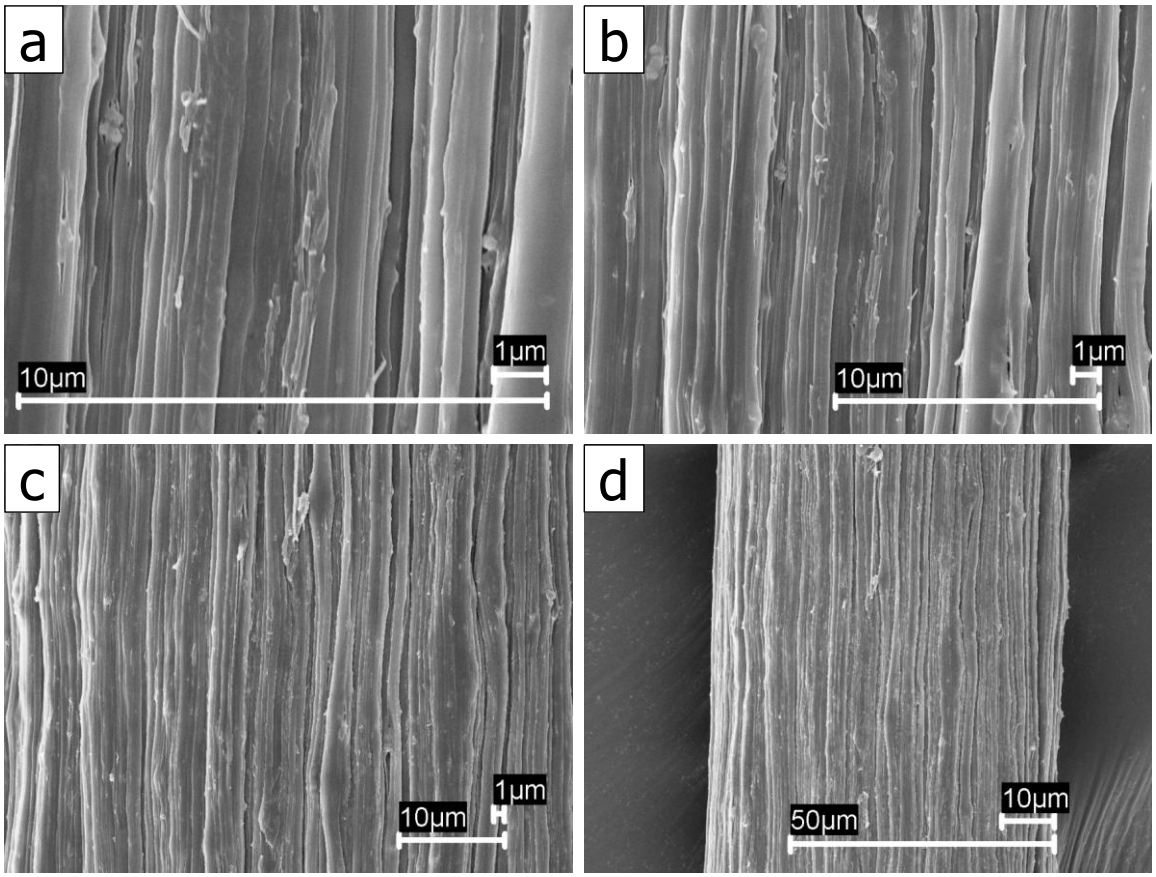

Figure 81. SEM images (at different magnifications) of the fiber surface of 20% CNF containing 250K fiber with DR 10.

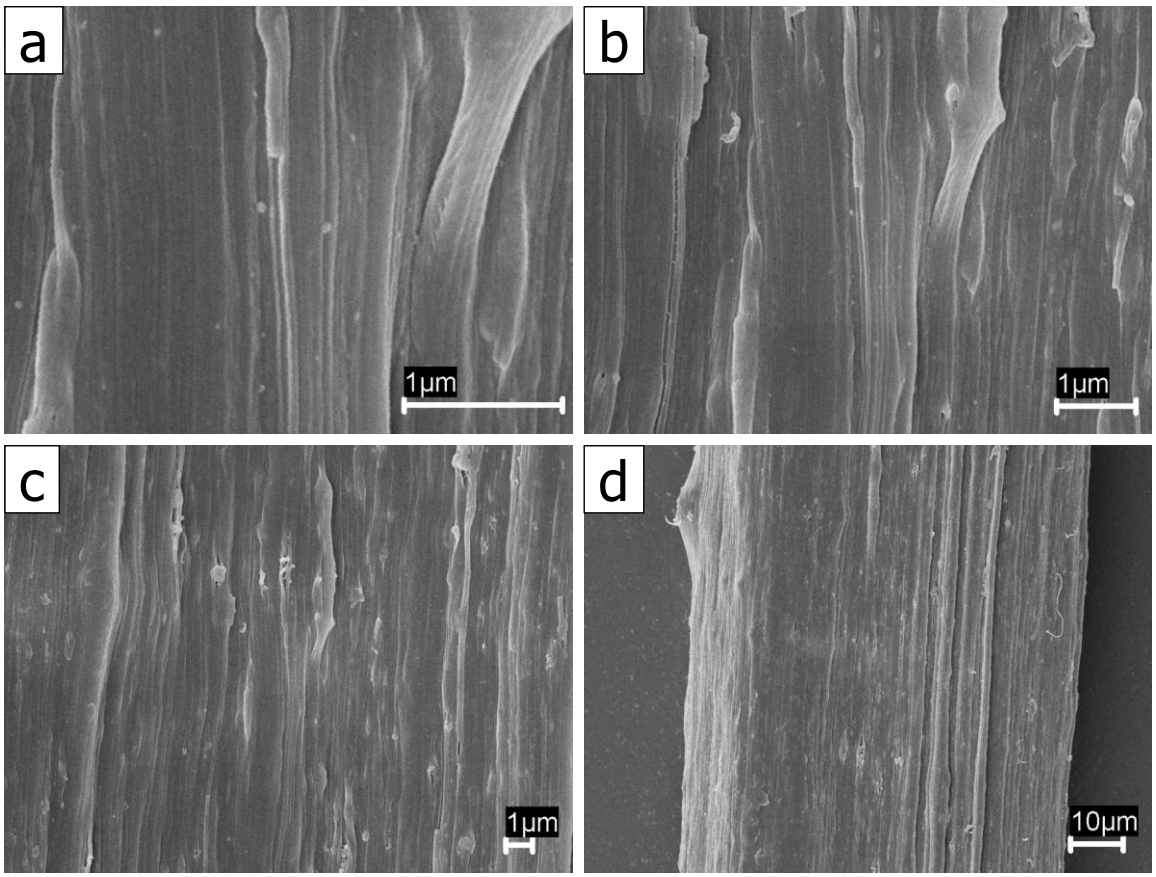

Figure 82. SEM images (at different magnifications) of the fiber surface of 20% CNF containing 700K fiber with DR 8.

4.2. Results and Discussion

4.2.1. Tensile Properties

The tensile properties of the control 250K and 700K PAN fiber are listed in Table 25. For 250K PAN fiber, the tensile strength and modulus increased with an increase in draw ratio up to 10, after which these properties decreased. Therefore, draw ratio 10 seems to be optimum for 250K PAN under these spinning and drawing conditions. Figure 83 shows the images of tensile fracture of control 250K fiber.

There was no significant change in the tensile properties of 700K fiber when the draw ratio was changed from 8 to 10. As shown in Table 26, the tensile properties of the

20% CNF composite fiber with 250K PAN improved with increase in draw ratio. At draw ratio 10, for both 250K and 700K PAN fiber with 20% CNF the moduli were almost 30-40% higher than expected theoretically. The increase in draw ratio became possible by using higher temperature for drawing using hot plate. If compared with the 100K PAN based 20% CNF composite fiber which was drawn using boiling water (Section 3.2.4, Table 14), the tensile properties of 20% CNF composite fiber increased with both 250K and 700K PAN which were drawn to high draw ratios at high temperatures. The SEM images of the tensile fracture of 20% CNF containing 250K PAN composite fiber is shown in Figure 84. Compared to the control PAN 100K fibers, the tensile moduli of both 250K and 700K control PAN fibers were found to be lower (compare values in Tables 14 and 25).

Generally, gel spinning is used to spin high MW polymers where the solution concentration is very low. But, solution spinning requires relatively higher polymer concentration in the solution. High MW PAN chains are more entangled than low MW PAN. A high degree of entanglement may prevent the polymer crystallization and consequently decrease the reinforcing effect of crystals and lead to decreased moduli. As shown later in Section 4.2.4, both 250K and 700K control PAN fibers showed lower crystallinity than 100K fibers discussed in Section 2.3.7. The presence of CNFs and a good interaction between CNF and PAN may decrease the PAN chain entanglement and allow for more efficient crystallization. In fact, as shown later in Section 4.2.4, the CNF containing 250K and 700K based composite fibers showed much higher crystallinity than their control PAN counterparts. This could be the reason for enhanced tensile moduli of 250K and 700K based composite fibers.

Table 25. Tensile Properties of Control High MW PAN Fibers

PAN	DR	Sample	Linear Density (tex)	Tensile Strength (N/tex)	Tensile Modulus (N/tex)	Strain to Failure (%)	Toughness (N/tex)
250K	4	A2a	4.4	0.13 ±0.00	3.3 ±0.4	16.1 ±0.6	--
250K	6	A2b	2.9	0.21 ±0.01	4.7 ±0.3	12.5 ±0.5	--
250K	8	A2c	2.3	0.28 ±0.02	5.8 ±0.6	11.0 ±0.6	--
250K	10	A2d	1.6	0.39 ±0.02	8.1 ±0.3	9.8 ±0.6	0.021 ±0.002
250K	12	A2e	1.5	0.38 ±0.03	7.7 ±0.5	9.0 ±0.7	--
700K	8	A3a	2.3	0.26 ±0.02	6.4 ±0.3	8.5 ±0.9	0.014 ±0.002
700K	10	A3b	1.8	0.25 ±0.01	6.6 ±0.5	7.8 ±0.3	--
700K	12	A3c	1.5	0.32 ±0.02	8.4 ±0.6	6.9 ±0.4	0.013 ±0.002

Table 26. Tensile Properties of 20% CNF Content High MW PAN Composite Fibers

PAN	DR	Sample	Draw Temp. (˚C)	Linear Density (tex)	Tensile Strength (N/tex)	Tensile Modulus (N/tex)	E_{PAN} (N/tex)	$E_{CNT}^{\parallel}$ (N/tex)	E_c (Theoretical) (N/tex)	Strain to Failure (%)	Toughness (N/tex)
250K	5	D1a	boiling water	5.2	0.17 ±0.01	7.1 ±0.4	--	--	--	4.9 ±0.2	--
250K	10	D1b	140	2.5	0.31 ±0.02	10.3 ±0.6	8.1	8.1	8.1	6.3 ±0.5	0.012±0.001
700K	8	D2c	160	2.2	0.34 ±0.04	11.2 ±1.8	--	--	--	8.1 ±0.7	0.016±0.004
700K	10	D2d	160	1.8	0.31 ±0.02	10.9 ±1.7	6.6	8.5	7.0	7.5 ±0.8	0.014±0.002

$E_{CNT}^{\parallel}$ and E_c calculated using equations 13-14 and procedure described in Section 2.4.4.

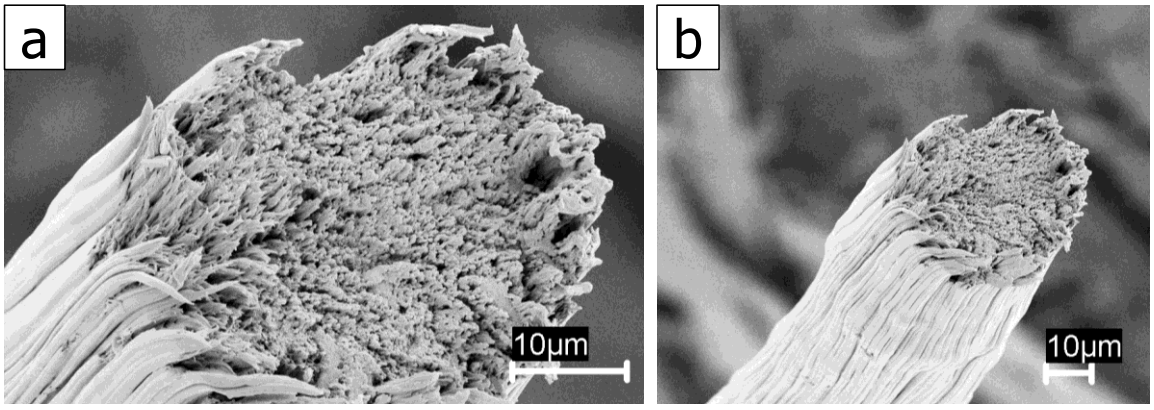

Figure 83. SEM images (at different magnifications) of the tensile fracture of control 250K fiber with DR 12.

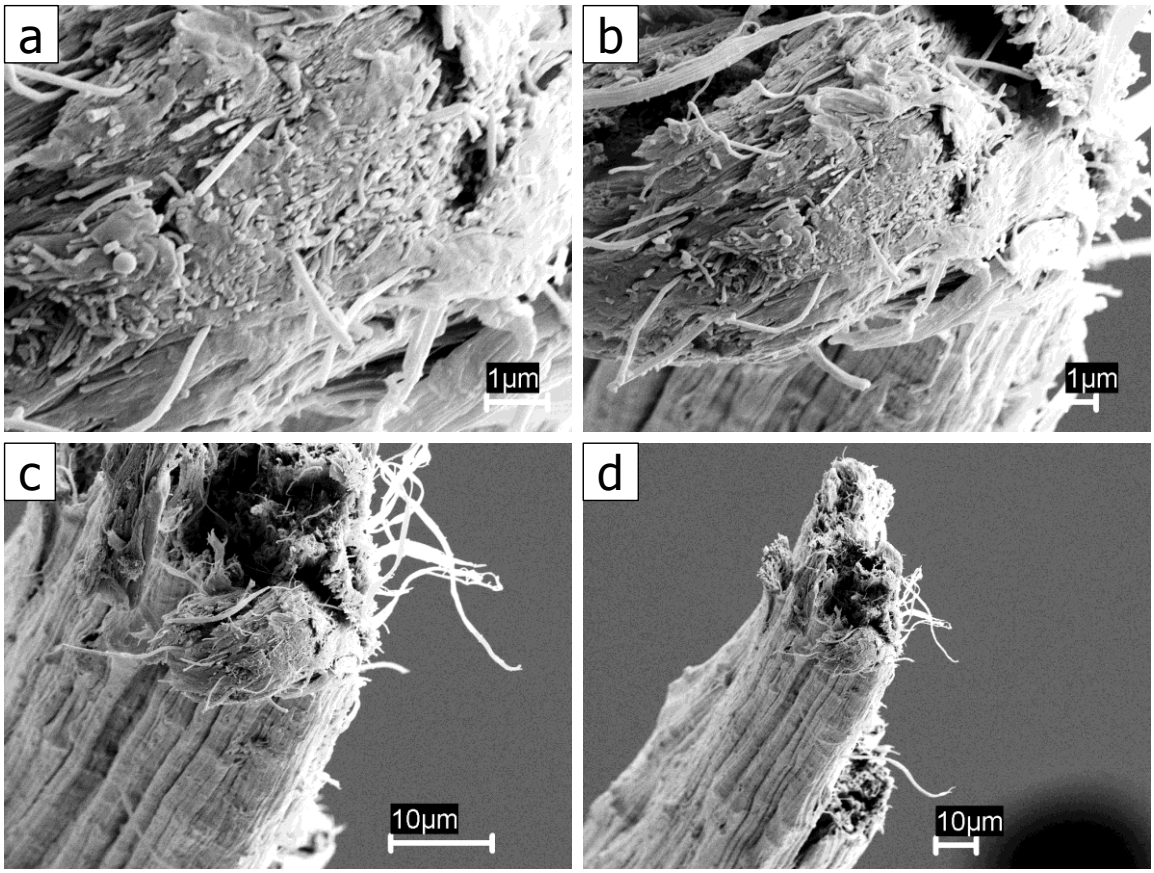

Figure 84. SEM images (at different magnifications) of the tensile fracture of 20% CNF containing 250K fiber with DR 10.

4.2.2. Dynamic Mechanical Analysis

Figures 85 and 86 show the storage moduli and tan δ curves for both 250K and 700K based control and 20% CNF containing composite fibers. The comparisons were made on fibers which were drawn to a draw ratio of 10. The T_g (measured from tan δ peak) and storage modulus values are listed in Table 27. Both 250K and 700K control fibers showed a T_g of around 70 ˚C. T_g of around 71 ˚C for 250K PAN fiber was previously reported by Chae *et al.* [1], but those fibers were spun by gel-spinning. The control 250K PAN showed a higher storage modulus than 700K PAN for most of the temperature range studied. For both 250K and 700K based fibers, the composite fibers

showed higher storage modulus than control fibers. While the 20% CNF reinforcement increased the storage modulus of 250K PAN fiber at room temperature by 19%, the same concentration of CNFs increased the storage modulus of 700K PAN fiber by 71%. The increase in storage modulus after 20% CNF reinforcement was much more significant at the T_g (70 ˚C) of control PAN fibers. At 70 ˚C, the 20% CNF loaded 250K and 700K composite fibers showed the storage modulus values to be increased by almost 90% and 180% over corresponding control fibers. The T_g of the 20% CNF reinforced fibers were found to be increased by 23 ˚C and 17 ˚C for 250K and 700K fibers, respectively. The increase in T_g for the CNF containing fibers is due to both an increase in crystallinity and the presence of CNFs. Polymer crystals and CNFs tend to constrain the movement of PAN chains leading to an increase in T_g.

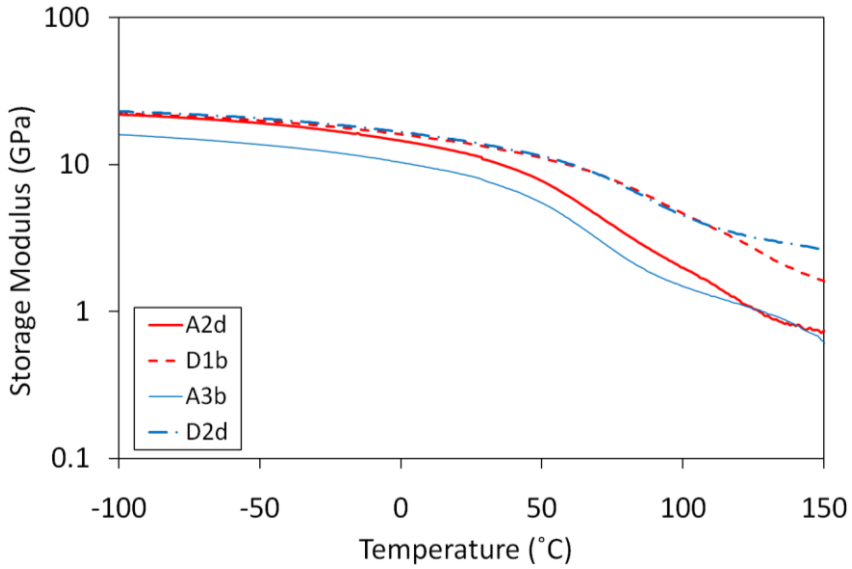

Figure 85. Storage moduli as a function of temperature for 250K control (A2d), 20% CNF containing 250K (D1b), 700K control (A3b), and 20% CNF containing 700K (D2d) fibers listed in Tables 25 and 26.

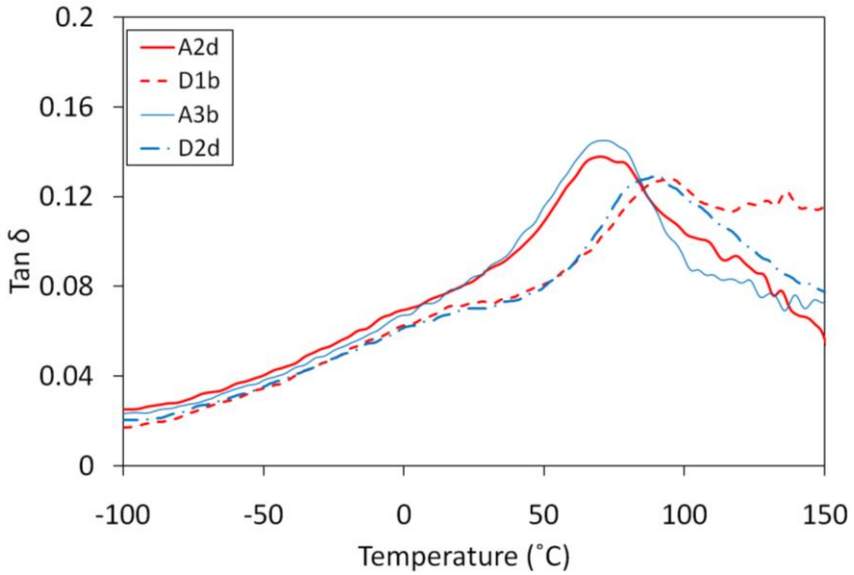

Figure 86. Tangent δ as a function of temperature for 250K control (A2d), 20% CNF containing 250K (D1b), 700K control (A3b), and 20% CNF containing 700K (D2d) fibers listed in Tables 25 and 26.

Table 27. Dynamic Mechanical Properties of 250K and 700K Based Fibers

PAN	DR	CNF (%)	Sample	T_g (˚C)	Storage Modulus at 25 ˚C (GPa)	Storage Modulus at 70 ˚C (GPa)
250K	10	0	A2d	70	11.6	4.5
250K	10	20	D1b	93	13.8	8.5
700K	10	0	A3b	70	8.3	3.1
700K	10	20	D2d	87	14.2	8.6

4.2.3. Thermomechanical Analysis

The thermal shrinkage for both 250K and 700K based control and composite fiber was studied using TMA. Figures 87 and 88 show the shrinkage behavior of control PAN 250K and 700K fibers with different draw ratios. For both types of PAN, the amount of draw ratio did not affect fiber shrinkage. The shrinkage values are listed in Table 28. Comparing the values in Table 16 and 28 indicate that PAN shrinkage decreased with an increase in MW. Figure 89 shows the shrinkage behavior of 20% CNF reinforced 250K

and 700K based fibers. For both PAN, the shrinkage was reduced to half after reinforcement with 20% CNF. Such a large decrease in shrinkage is due to higher crystallinity and presence of CNFs which constrain the movement of PAN chains.

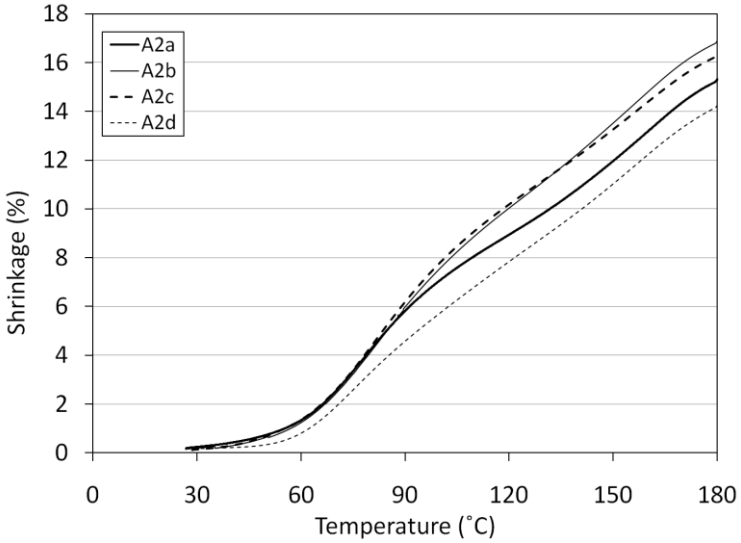

Figure 87. Effect of heat draw ratio on the shrinkage of control PAN 250K fiber (N_2 flow rate: 50 ml/min; temperature ramp rate: 5 ˚C/min; preload: 0.0002 N/tex). Samples A2a, A2b, A2c, and A2d correspond to DR 4, 6, 8, and 10, respectively (Table 28).

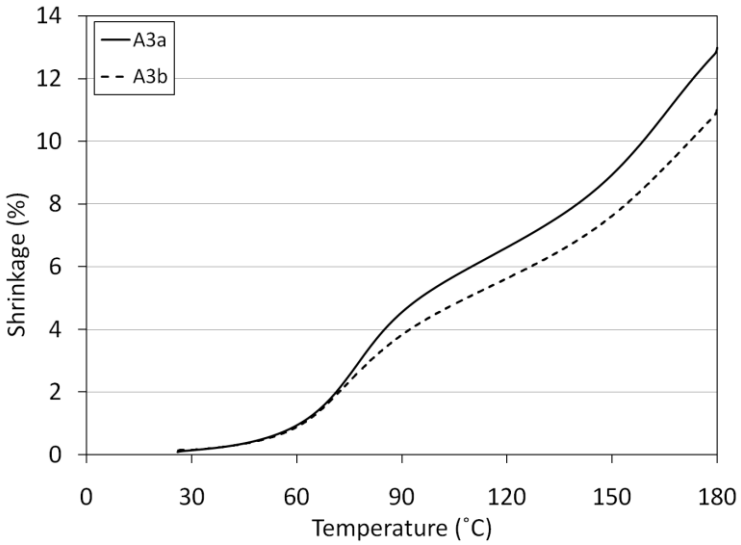

Figure 88. Effect of heat draw ratio on the shrinkage of control PAN 700K fiber (N_2 flow rate: 50 ml/min; temperature ramp rate: 5 ˚C/min; preload: 0.0002 N/tex). Samples A3a and A3b correspond to DR 8 and 10, respectively (Table 28).

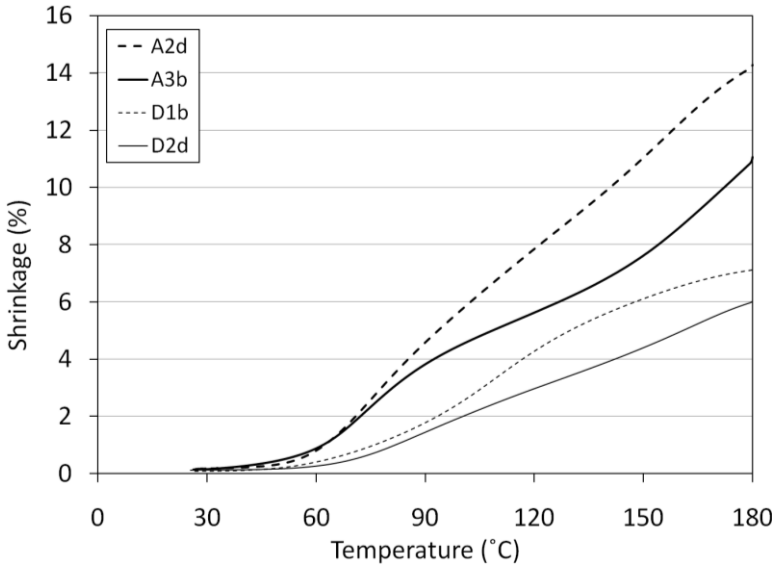

Figure 89. Thermal shrinkage as measured using TMA (N_2 flow rate: 50 ml/min; temperature ramp rate: 5 ˚C/min; preload: 0.0002 N/tex) for 250K control (A2d), 20% CNF containing 250K (D1b), 700K control (A3b), and 20% CNF containing 700K (D2d) fibers listed in Table 28.

Table 28. Shrinkage at 180 ˚C for Various Control and PAN/CNF Composite Fibers

PAN	CNF (%)	DR	Sample	Shrinkage (%)
250K	0	4	A2a	15
250K	0	6	A2b	17
250K	0	8	A2c	16
250K	0	10	A2d	14
700K	0	8	A3a	13
700K	0	10	A3b	11
250K	20	5	D1a	8
250K	20	10	D1b	7
700K	20	10	D2b	6

4.2.4. WAXD Studies

The WAXD patterns for 250K and 700K based fibers are shown in Figure 90. The corresponding integrated radial scans and deconvoluted profiles are shown in Figures C1

to C4 in Appendix C. Crystallinity, crystal size, and orientation values are listed in Table 29. After reinforcement with 20% CNF, the average crystallinity of the control 250K increased from 44% to 53%, and for 700K fiber it increased from 38% to 59%. The average crystal size for PAN in both 250K and 700K based fibers was around 7 nm. The presence of CNFs did not have any specific effect on the d-spacing of 250K PAN fiber, but the d-spacing reduced in case of 700K PAN fiber. In the CNF containing fibers, the PAN orientation decreased in case of 250K fiber and increased in case of 700K fiber. The CNF orientation was found to be higher than what was observed with 100K fiber (0.45 for 100K fiber, 0.53 for 250K, and 0.58 for 700K). The higher orientation for high MW PAN based fibers was obtained due to high draw ratio (DR 10), whereas the low MW 100K PAN was only drawn up to DR 5.

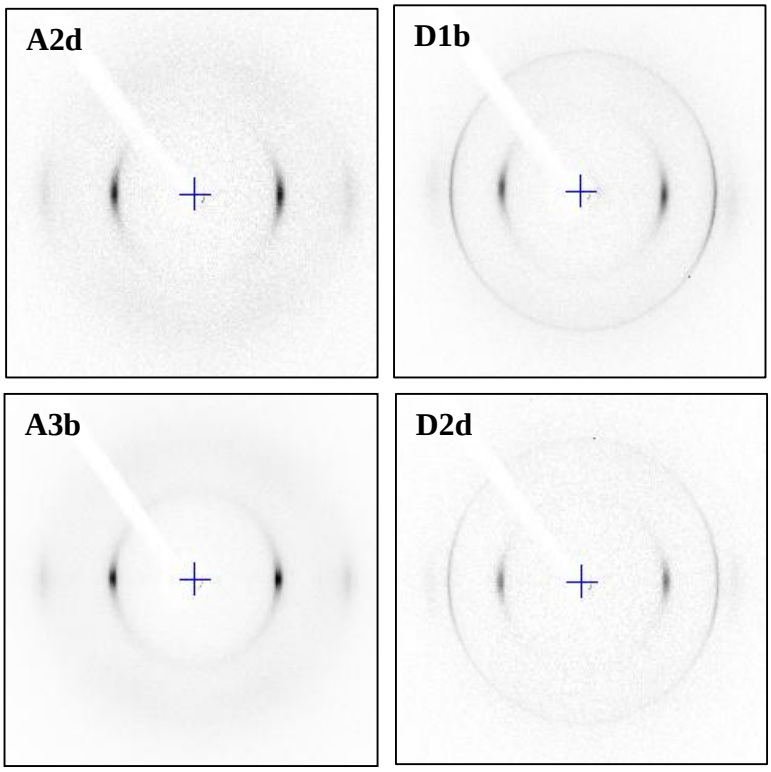

Figure 90. WAXD patterns of 250K and 700K based control and composite fibers with 20% CNF loading and heat draw ratio 10.

Table 29. WAXD Results for Various 250K and 700K Based Fibers

PAN	CNF (%)	DR	Sample	Crystallinity[1] (%)	d-spacing (PAN 2θ~17°) (Å)	f_{PAN}[2] (2θ~17°)	f_{CNF}[2] (2θ~26°)	L_{PAN}[3] (2θ~17°) (Å)	L_{CNF}[3] (2θ~26°) (Å)
250K	**0**	**10**	A2d	44	5.19	0.79	--	66	--
250K	**20**	**10**	D1b	53	5.20	0.77	0.53	68	172
700K	**0**	**10**	A3b	38	5.27	0.72	--	71	--
700K	**20**	**10**	D2d	59	5.24	0.78	0.58	70	175

[1] Calculated by deconvolution of integrated scan; [2] Herman's orientation factor;
[3] Calculated by Scherrer's equation using equatorial scan

4.2.5. Electrical Conductivity of Composite Fibers

The electrical conductivities of the composite fibers are listed in Table 30. At 20% CNF loading, 700K PAN composite fiber showed higher conductivity than 250K PAN composite fiber. These values are almost five orders of magnitude higher than what was obtained for 20%CNF containing PAN 100K fiber (Table 18). The higher conductivity could be a result of higher orientation of CNFs. The conductivity values for 20% CNF loaded 250K and 700K fibers are in the ballpark of values obtained for 20% MWNT loaded 100K PAN fibers (Table 6). This makes the high MW PAN more attractive considering that one can obtain a similarly high conductivity with cheaper CNFs, than by using more expensive MWNTs with low MW PAN. The 20% CNF composite fibers listed in Table 30 showed electrical breakdown at high currents (Figure 91). A more comprehensive discussion, including the effect of orientation on the electrical conductivity of different CNT and CNF reinforced PAN composite fibers is presented in chapter 6.

Table 30. Electrical Conductivity of 20% CNF Composite Fibers

PAN	CNF (%)	DR	Electrical Conductivity (S/m)	Current at Electrical Breakdown of Fiber (A)
250K	20	10	0.1	$2.39x10^{-5}$
700K	20	10	28	$5x10^{-4}$

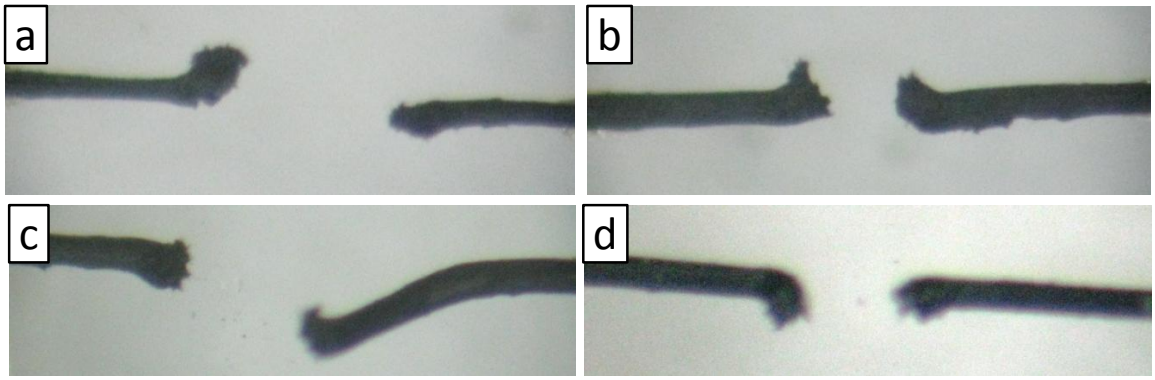

Figure 91. 20%CNF containing 250K (a and b) and 700K (c and d) PAN fibers listed in Table 30.

4.2.6. Rheological Studies

The polymer and polymer/CNT rheology was studied at room temperature using ARES rheometer (Advanced Rheometric Expansion System, TA Instruments Co.). Both steady-state and dynamic tests were conducted using a parallel plate geometry (50 mm diameter) with a separation gap of 1 mm. The elastic nature of the CNFs changed the viscoelasticity of the polymer solutions. As shown in Figure 92, for the same solid content of 15 wt.%, particularly at low frequencies, the storage modulus (G') increased by almost three orders of magnitude for the CNF containing solution. The G' is a direct manifestation of the elasticity of the system, which increased due to the presence of CNFs. For the same concentration of CNFs (20 %), the G' curve was found to be shifted to higher values with overall increase in solid content (20% CNF/250K PAN solution with solid contents of 15 and 18%).

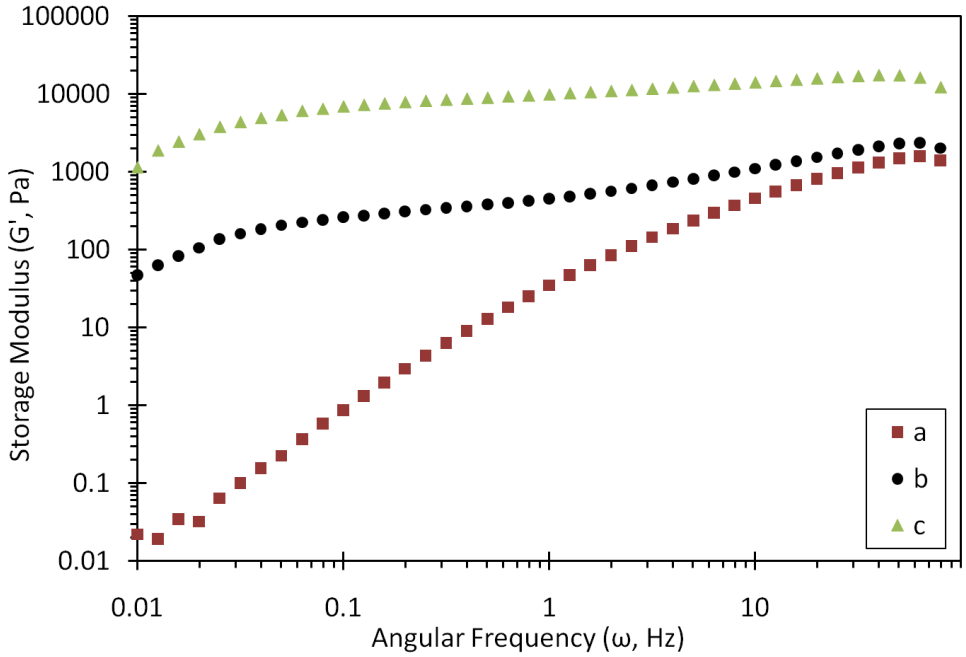

Figure 92. Storage modulus (G') of 250K PAN based solutions as measured in the dynamic frequency sweep test. The total solid content of samples (a) and (b) is 15% and that of (c) is 18%. Both samples (b) and (c) contain 20% CNF.

Figure 93 shows both storage modulus (G') and loss modulus (G") from the same experiment. For the control PAN solution, at low frequencies, G" was almost two orders of magnitude higher than G' and G' crossed-over G" at a high frequency (between 40 and 50 Hz). The cross-over phenomena of G' and G" can be correlated to the viscoelasticity of the system. At low frequency, the polymer behavior is like its behavior at high temperature, and vice-versa. Therefore, polymer behaves more like a liquid at low frequencies and more like a solid at high frequencies. Consequently, G" is high and G' is low at low frequencies, and G' increases faster than G" with increase in frequency. For the 20% CNF containing solution, G' was always higher G", which shows that CNF containing solution was more solid like than liquid like.

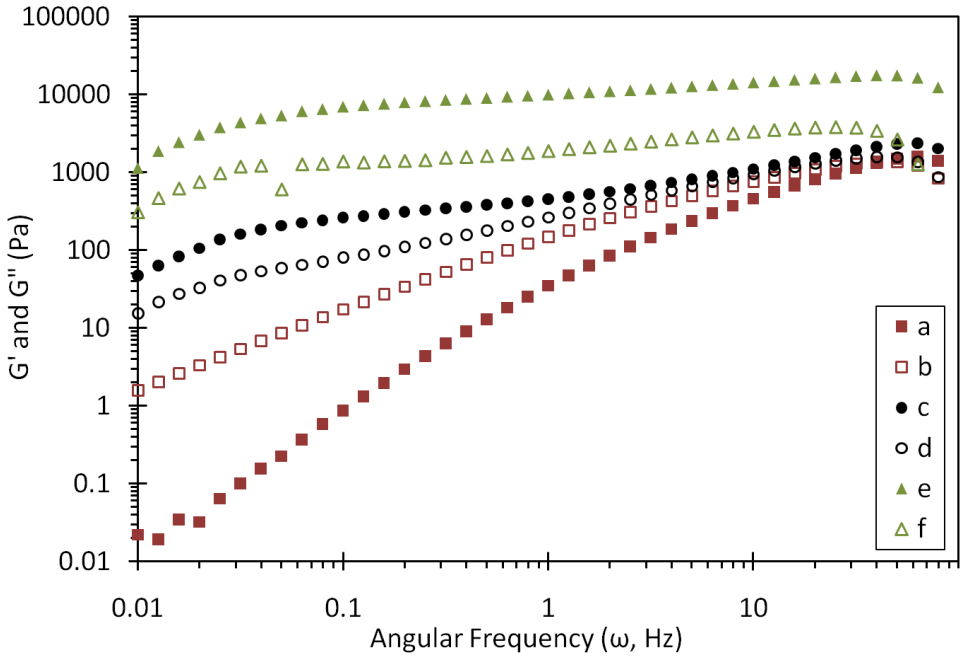

Figure 93. Storage modulus (G') and loss modulus (G") of 250K PAN based solutions as measured in the dynamic frequency sweep test. (a) and (b): G' and G" of control 250K solution with 15% total solid content. (c) and (d): G' and G" of 20% CNF containing 250K PAN solution with 15% total solid content. (e) and (f): G' and G" of 20% CNF containing 250K PAN solution with 18% total solid content.

As shown in Figure 94, the composite solution showed higher viscosity at low shear rate as compared to the viscosity of the control polymer solution at the same solid concentration (15 wt.%). However, at high shear rates it is the composite solution that exhibited lower viscosity. The absence of Newtonian plateau in the composite solution and significant decrease in viscosity with increase in shear rate (shear thinning) has previously been shown with other CNT containing polymer systems [2-6].

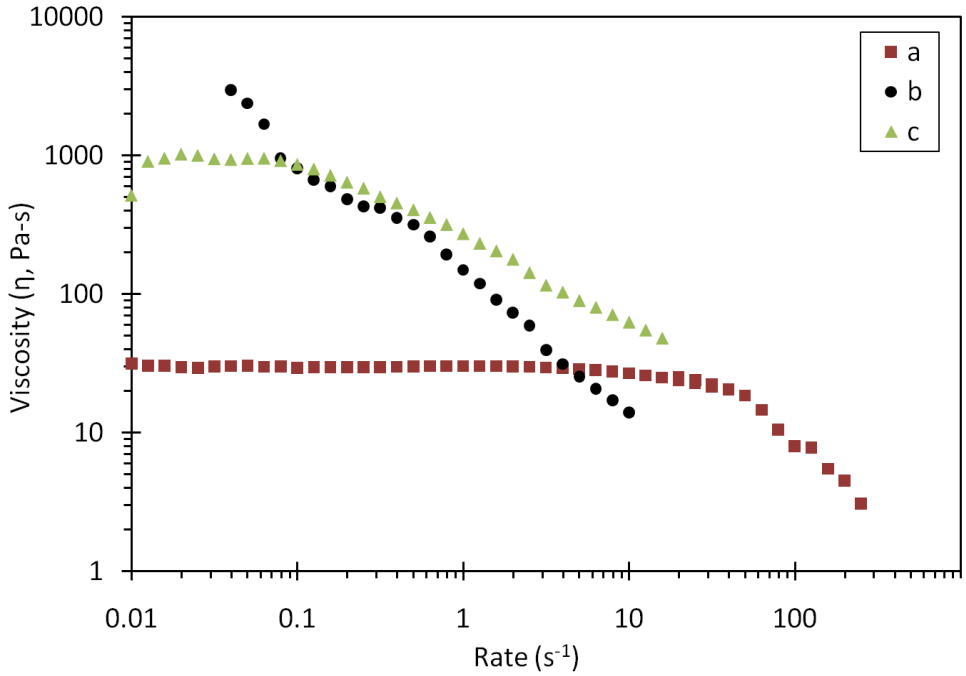

Figure 94. Viscosity of 250K PAN based solutions as measured in the steady rate sweep test. The total solid content of samples (a) and (b) is 15% and that of (c) is 18%. Both samples (b) and (c) contain 20% CNF.

4.3. Conclusions

- For higher loading systems (20% CNF), compared to low MW PAN (PAN 100K) higher MW PAN (250K and 700K) resulted in better mechanical properties. For 20% CNF reinforced fiber, the increase in modulus was almost 27% and 65% over the control 250K and 700K PAN fibers, respectively. For 100K PAN, that increase was only 16%.
- The thermal shrinkage of the 250K and 700K PAN reduced to half after reinforcement with 20% CNFs. For 100K PAN, that decrease was only about 25%.

- Though no such increase was observed for 100K based fibers, but after reinforcement with 20% CNFs, the overall crystallinity increased from 44% to 53% for 250K PAN fiber and from 38% to 59% for 700K PAN fiber.
- Compared to 20%CNF/PAN100K fiber, the 20% CNF reinforced 250K and 700K fibers showed almost five orders of magnitude increase in the electrical conductivity of the composite fiber.
- The aforementioned improvement in fiber properties could be due to the combined effect of several factors including, higher orientation of PAN and CNFs, higher crystallinity for PAN, and better interaction between CNFs and high MW PAN.
- The presence of CNFs was found to increase the PAN solution viscosity at lower shear rates and showed a sharp shear thinning behavior with increase in shear rate.
- CNF increased the storage modulus of the PAN solutions at low frequencies (due to large increase in elastic behavior)

4.4. References

1. Chae HG, Minus ML, and Kumar S. Polymer 2006;47(10):3494-3504.
2. Potschke P, Fornes TD, and Paul DR. Polymer 2002;43(11):3247-3255.
3. Potschke P, Abdel-Goad M, Alig I, Dudkin S, and Lellinger D. Polymer 2004;45(26):8863-8870.
4. Abdel-Goad M and Potschke P. Journal of Non-Newtonian Fluid Mechanics 2005;128(1):2-6.
5. Lin B, Sundararaj U, and Potschke P. Macromolecular Materials and Engineering 2006;291(3):227-238.
6. Defeng W, Liang W, and Zhang M. Journal of Polymer Science Part B: Polymer Physics 2007;45(16):2239-2251.

CHAPTER 5

EFFECT OF CNT DIAMETER AND CONCENTRATION ON COMPOSITE FIBER SPINNABILITY

The theoretical calculations are presented to show the maximum possible limit of carbon nanotubes (CNTs) in PAN/CNT composite fiber. Different type of CNTs including single-wall carbon nanotube (SWNT), multi-wall carbon nanotube (MWNT), and carbon nanofiber (CNF) show a different limit for their loading. The experimental observations with different composite fibers (PAN/SWNT, PAN/MWNT, and PAN/CNF) are compared with the theoretical calculations. This work suggests that CNT diameter is the most important factor in controlling the concentration of CNT in a composite fiber.

5.1. Experimental

Four different types of composite fibers were considered for this study: PAN/SWNT composite fibers spun using dry-jet wet spinning and gel spinning, and PAN/MWNT and PAN/CNF composite fibers spun using dry-jet wet spinning (described in Chapter 2 and 3). The materials and methods of PAN/SWNT composite fibers have been described elsewhere [1, 2].

5.2. Results and Discussion

The carbon nanotube and nanofiber reinforced polymeric fibers have been researched by many groups in a quest to make a unique or next generation high performance fibers [3]. Tables 31 and 32 summarize PAN/CNT and other polymer/CNT

composite fiber studies, respectively. The reasons for using CNTs have been to increase the mechanical strength of the fiber, to increase its electrical and thermal conductivity, or to enhance other properties. The question arises, "What is the maximum possible limit of CNT inclusion in a composite fiber?". The answer to this question will depend on several factors including polymer/CNT interaction, polymer molecular weight (MW), CNT diameter, and dispersion and exfoliation state of CNTs. All these factors along with the processing method and conditions used to make a fiber control the ultimate composite fiber properties.

Depending on the type of polymer, a variety of fiber spinning techniques can be used to make CNT reinforced polymer fiber. Conventionally, the polymer fibers are spun by either melt spinning or solution spinning. Solution spinning can be further divided into dry spinning, wet spinning, dry-jet wet spinning, and gel spinning. A CNT reinforced polymer composite can be spun into fiber using any of the aforementioned technologies. Alternatively, first only-CNT fiber can be spun, which can be later infiltrated with polymer to make a CNT/polymer composite fiber [4-6]. Using the latter approach, fibers with high CNT concentrations have been processed. However, from the commercial point of view, the conventional approaches are most desirable.

Table 31. Summary of the Studies on PAN/CNT Composite Fibers (Continued on Next Page)

Publication	Polymer	CNT Type and %	Spinning Method	Major Findings
Sreekumar [1]	PAN	5%, 10% SWNT	Dry-jet wet spinning	• 10% SWNT fiber - showed 100% increase in tensile modulus - 40 ˚C increase in T_g - 50% decrease in thermal shrinkage • Composite fibers showed higher chemical stability than control fiber
Chae [7]	PAN	5% SWNT, DWNT, MWNT, CNF	Dry-jet wet spinning	• SWNT reinforced fiber showed increase in the low strain properties - 75% increase in modulus - 50% reduction in thermal shrinkage • MWNT reinforced fiber showed improvements in high strain properties - 75% increase in tensile strength - 110% increase in strain to failure - 230% improvement in work of rupture • Increase in crystal size and orientation and decrease in crystallinity of PAN in composite fibers
Jain [Chapter 2]	PAN	5, 10, 15, 20% MWNT	Dry-jet wet spinning	• PAN was found to be coating the MWNTs • Increased T_g and reduced thermal shrinkage • 15% MWNT fiber showed electrical conductivity four orders of magnitude higher than 10% MWNT fiber
Jain [Chapter 3]	PAN	5, 10, 15, 20, 30% CNF	Dry-jet wet spinning	• Presence of CNF maintained the structural form after charring at 1000 ˚C • CNF increased the char yield • High concentration (≥ 20%) of CNFs increased the conductivity of the fiber to the level required in applications like electrostatic dissipation and electromagnetic shielding
Jain [Chapter 4]	High molecular weight PAN	20% CNF	Dry-jet wet spinning	• CNF increased the tensile modulus by 20 to 80% • Thermal shrinkage reduced to half • Crystallinity increased by 20 to 50% • CNF containing solutions showed high storage modulus, shear-thinning viscosity behavior and a higher initial viscosity than control PAN solutions

Liu [8]	PAN	SWNT	Electrospinning	• Exhibits SWNT core and PAN shell structure
Ko [9]	PAN	4% SWNT	Electrospinning	• Good distribution and alignment of SWNT in composite fibers (no quantification)
Ge [10]	PAN	2, 3, 5, 10, 20% MWNT	Electrospinning	• MWNTs orientation (f_{MWNT} = 0.90) was much higher than the PAN (f_{PAN} = 0.62) orientation in the 10 wt% MWNT/PAN • Tensile strength and modulus increased with the increasing percentage of MWNTs • Degradation temperature was found to be shifted from 268 ˚C for the neat PAN to 292 ˚C for the 5 wt% MWNT composite • Coefficient of thermal expansion (CTE) was reported to be decreased by more than an order of magnitude for 10 and 20% MWNTs nanofiber sheets (18×10^{-5} to 17×10^{-6}/˚C)
Ye [11]	PAN	1% SWNT, MWNT	Electrospinning	• The polymer crazing was hindered by the presence of CNTs which reduced the stress concentration and ultimately CNTs helped in the higher energy dissipation through the pull-out mechanism [Though higher toughness was suggested for composite nanofibers, but no quantitative studies were conducted to support the same point]
Hou [12]	PAN	2, 3, 5, 10, 20, 35 % MWNT	Electrospinning	• TEM showed the orientation of MWNTs in the fiber axis direction • Modulus increased with MWNT %
Chae [2]	PAN	0.5, 1% SWNT	Gel spinning	• Composite fibers showed higher electron beam radiation and chemical stability than control fiber • SWNTs exfoliation was successfully achieved

Table 32. Summary of the Studies on Polymer/CNT Composite Fibers (Continued on Next Page)

Publication	Polymer	CNT Type and %	Spinning Method	Major Findings
Rahatekar [13]	Cellulose	1, 3, 5, 7, 10% MWNT	Dry-jet wet spinning	• Lower thermal shrinkage than control cellulose fiber • High electrical conductivity (~3000 S/m)
Ma [14]	PET	5% CNF	Melt spinning	• 10 to 50% increase in compressive strength and 20- 50% increase in torsional modulus • Low shear rate viscosity increased by 1-2 orders of magnitude
Zeng [15]	PMMA	5, 10% CNF	Melt spinning	• At 5% CNF, tensile modulus increased by ~ 50% • Composite fibers showed higher thermal stability, reduced thermal shrinkage, and higher compressive strength than the control PMMA fiber
Kumar [16]	PP	5% CNF	Melt spinning	• Tensile modulus and compressive strength increased by 50% and 100%, respectively
Fornes [17]	Polycarbonate	1, 3, 5% SWNT, MWNT	Melt spinning	• MWNTs were found to be easier to disperse than SWNTs, and provided greater improvement in strength and stiffness
Kumar [18]	PBO	5, 10% SWNT	Dry-jet wet spinning	• Tensile strength improved by ~ 50% with 10% SWNT
Sennett [19]	Polycarbonate	5% SWNT, MWNT	Melt spinning	• MWNTs were found to be easier to disperse • MWNT alignment improved with draw rate
Haggenmueller [20]	PMMA	1 – 8% SWNT	Melt spinning	• The elastic modulus and yield strength increased with nanotube loading and draw ratio
Miaudet [21]	PVA	MWNT	MWNT dispersion co-injection with aqueous solution of PVA , followed by coagulation	• Resistivity decreased when fiber heated to near T_g (76 ˚C)

Gao [22]	Nylon 6	0.5 % SWNT	Melt Spinning	• Tensile strength and modulus increase with carboxylic acid functionality on to SWNTs (due to better SWNT-nylon interaction)
Chen [23]	Fluoro-ethylene-propylene copolymer	0.5, 1, 5% MWNT	Melt Spinning	• Yield strength and modulus increased, strain to failure decreased with increasing MWNT %
Li [24]	PBO	2, 8% MWNT	Dry-jet wet spinning	• With 2% MWNT, tensile strength improved by 20-50%. SEM and WAXD showed lower orientation for MWNT than PBO.
Sandler [25]	Polyamide 12	5, 10, 15%CNF 1.25, 2, 5, 10% MWNT	Melt spinning	• CNTs acted as nucleation sites for polymer crystallization under slow cooling
Dupire [26]	PP	3% CNT	Melt spinning	• ~ 4 fold increase in tensile strength and modulus
Kitagawa [27]	Polybenzazole	1-15% CNT (dia < 20 nm)	Solution spinning	• ~ 4 fold increase in compressive strength
Ruan [28]	UHMWPE	5% MWNT	Gel spinning	• ~ 19% increase in tensile strength, 15.4% increase in ductility, 44.2% increase in fracture energy
Zhang [29]	PVA	3% SWNT	Gel spinning	• 40% increase in modulus • T_g increased from 62 to 75 ˚C
Pötschke [30]	PC	2% MWNT	Melt spinning	• Tensile modulus increased but strength decreased • The fibers were not found to be conductive
Haggenmueller [31]	PE	1, 5, 10, 20 % SWNT	Melt spinning	• Degree of alignment increased with decrease in fiber diameter and decreased with increasing nanotube loading • 20% SWNT fiber showed 450% increase in tensile modulus
Muñoz [32]	Polyethyleneimine	~ 75% SWNT	Injection-coagulation spinning	• Low strength and modulus but very high electrical conductivity ~ 10000 S/m

The following calculations show the maximum content of CNTs that is possible in a polymer matrix in a fiber (in this case PAN, but similar calculations can be done for another polymer), where CNTs are perfectly aligned in the fiber direction, and no two NTs are touching each other (i.e. bridged/separated by at least one polymer chain). It is known that CNTs exist in different diameters and this diameter can range from 0.4 nm to 4 nm for SWNTs, 5 nm to 70 nm for MWNTs (depending on number of walls), and > 50 nm for CNFs. The diameter of a fully extended PAN chain is around 0.6 nm and in case of perfect alignment and packing they arrange themselves in a hexagonal pattern (same as for SWNTs).

Figure 95 shows two extreme cases, where in one case polymer chains are entangled and are surrounding a CNT in a random coil configuration, and in the other case, a polymer chain is fully extended (zig-zag conformation) while sandwiched between two CNTs. The latter case represents an ideal composite fiber, where both polymer and CNTs are fully extended and oriented in the fiber direction, and the nanotube fraction is maximum while in the fully exfoliated state. A top-view of this ideal composite fiber, where any two NTs are separated from each other by just one polymer chain, is shown in Figure 96.

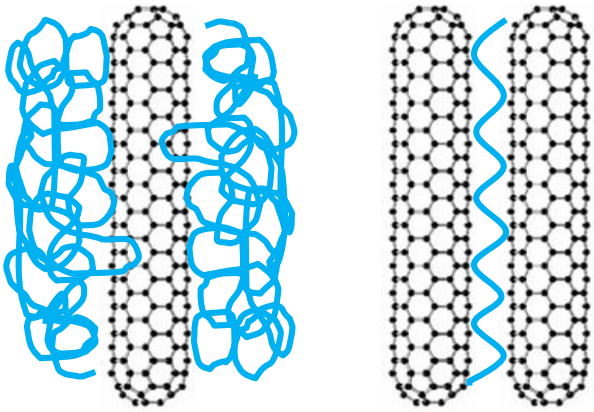

Figure 95. Left: polymer random coil adsorbed/wrapped around a CNT; Right: a fully extended polymer chain separating two CNTs (this case is shown in top-view in Figure 96).

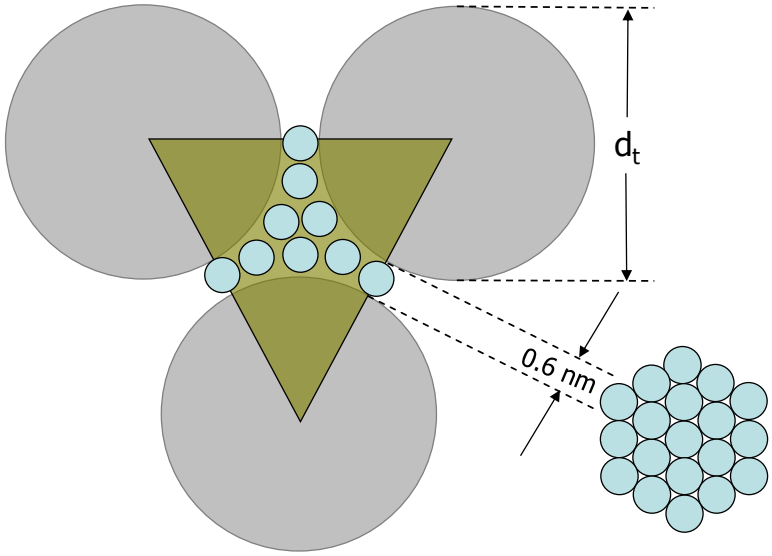

Figure 96. Ideal arrangement of CNTs and PAN chains in a composite fiber. CNTs (big circles) are separated by PAN chains (small circles). The triangle shows a unit cell for calculation purposes and shows the area occupied by CNTs and area that is available for PAN chains to occupy.

In Figure 96, for each NT of diameter d_t, the available free area (A_{PAN}) for PAN to occupy is given by equation 16. The volume fraction, F_{PAN}, (represented by fractional area) of PAN in the unit cell (Figure 96) can be represented by equation 17. This equation can be used to find the volume fraction of PAN (or volume fraction of CNT, or volume

fraction of any cylindrical filler) that is required to make an ideal composite. Figure 97 shows the different scenarios of PAN volume fraction with different kinds of CNTs (depending on diameter). As evident, the volume fraction of NT increases with increase in their diameter. The volume fraction for a NT of 100 nm diameter can be as much as 90%, while for the 1 nm diameter NT, the NT volume fraction cannot exceed 36%.

$$A_{free} = A_{PAN} = \frac{\sqrt{3}}{2}(d_t + 0.6)^2 - \frac{\pi d_t^2}{4} \tag{16}$$

$$F_{PAN} = \frac{\frac{\sqrt{3}}{2}(d_t + 0.6)^2 - \frac{\pi d_t^2}{4}}{\frac{\sqrt{3}}{2}(d_t + 0.6)^2} = 1 - \frac{\pi d_t^2}{2\sqrt{3}(d_t + 0.6)^2} \tag{17}$$

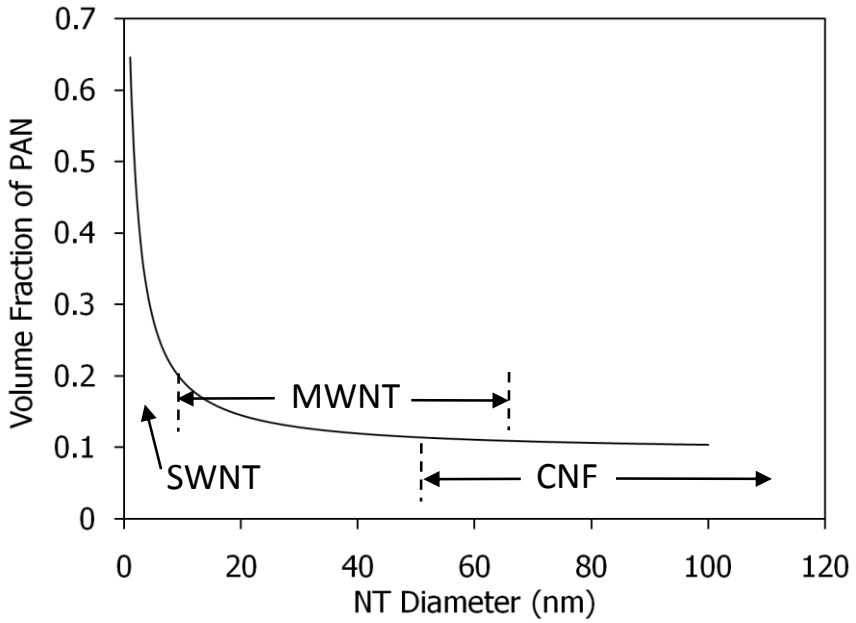

Figure 97. Volume fraction of PAN vs. NT diameter in an ideal composite fiber.

Though the limitation from above calculations is shown to be 90% loading for largest diameter NTs, but a higher CNT content is possible by blending in the small

diameter NTs with larger diameter NTs where the small diameter NTs may occupy the central region enclosed by three larger diameter NTs and still all the NTs can be separated from each other by one polymer chain.

The above case represented when only one PAN chain is separating the nanotubes. However, in reality there is more than one PAN chain separating two nanotubes. The number of PAN chains separating the NTs in a composite fiber will depend on several factors including the type and degree of PAN-CNT interaction, CNT diameter and surface morphology (planer wall in case of SWNT and MWNT, and numerous edges in case of CNFs), molecular weight and composition of PAN, method of solution preparation and fiber processing. Obviously an increase in the number of PAN chains separating the CNTs will reduce the loading of CNTs in the fiber. These factors will limit the fraction of NT filler that can be practically achieved in a composite fiber.

The volume fraction of PAN, F_{PAN}, in the composite fiber can be calculated using equation 18, where n is the number of PAN chains between any two CNTs. The plot in Figure 98 shows the variation in volume fraction of PAN with different number of PAN chains separating the NTs for different diameter NTs.

$$F_{PAN} = 1 - \frac{\pi d_t^2}{2\sqrt{3}\left[d_t + (0.6 \times n)\right]^2} \tag{18}$$

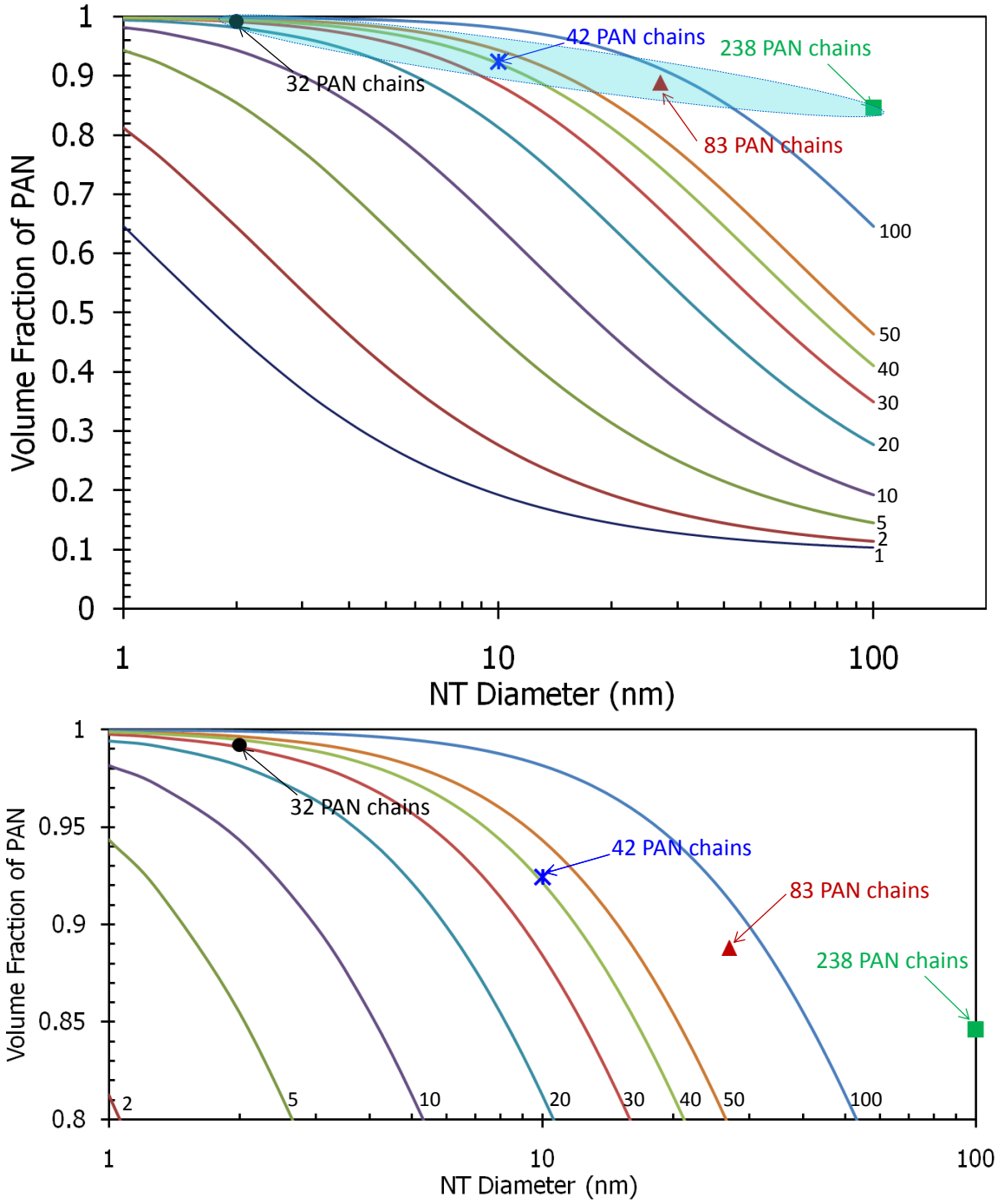

Figure 98. Volume fraction of PAN vs. NT diameter when NTs are separated from each other by a different number of PAN chains. The number of PAN chains (1, 2, 5, 10, 20, 30, 40, 50, and 100 PAN chains) separating any two NTs are listed right next to the corresponding curve. The four data points showing 32, 42, 83, and 238 PAN chains correspond to 2 nm diameter SWNT, 10 nm diameter SWNT bundle, 27 nm diameter MWNT, and 100 nm diameter CNF reinforced fibers, respectively. A part of image at top is shown is shown in image at bottom.

It is interesting to see that for a SWNT of 2 nm diameter, when the SWNTs are separated by ~ 32 PAN chains (or a coating of 10 nm associated with each SWNT) the theoretical possible limit of SWNTs in the fiber is less than one volume percent. Chae *et al.* [2] spun the 1 wt% (0.8 vol%) SWNT (average diameter 2 nm) containing PAN/SWNT fiber using gel-spinning and showed good dispersion, exfoliation, and orientation of SWNTs in the composite fiber. Therefore, it can be assumed that the present model would be applicable in their case. In fact, it was difficult to spin PAN/SWNT fiber containing 2 wt% (1.5 vol%) SWNT under typical gel spinning conditions.

Sreekumar *et al.* [1] observed that SWNTs existed in bundles in the dry-jet wet spun PAN/SWNT composite fibers. The diameter of SWNT bundles was evaluated to be around 10 nm [33]. The authors experienced difficulty in spinning a SWNT/PAN composite fiber with a SWNT loading of 15 wt% (11.5 vol%). Assuming that 10 wt% (8 vol%) was the upper limit for SWNT loading in their PAN/SWNT composite fiber, Figure 96 suggests that SWNT bundles were separated by ~ 42 PAN chains. We think that the degree of interaction between a CNT and PAN decreases with increase in CNT diameter. This is due to the fact that a larger fraction of PAN was influenced in case of 1 wt % SWNT gel spun fiber, which limited the SWNT fraction to only 1 wt %. However, a lower fraction of PAN was influenced in case of 10 wt% SWNT dry-jet wet spun fiber (where the effective SWNT bundle diameter was 10 nm), which allowed the SWNT fraction to be increased up to 10 wt%.

In this work, the MWNT reinforced PAN fiber could be spun up to 20 wt.% (11.1 vol%) MWNT loading, which corresponds to CNT-CNT separation of 50 nm. PAN/CNF

composite fibers spun in this work showed an upper limit of 30 wt.% (15.4 vol%) CNF loading. Correlating this limit with the average diameter of 100 nm for CNFs suggest that CNFs are separated from each other by ~ 238 PAN chains. This again supports the fact that the degree of physical interaction between a CNT and PAN decreases with increase in CNT diameter, which allows a higher fraction of CNTs to be included in the composite fiber as CNT diameter increases.

The aforementioned four cases (marked with data points in Figure 98) are illustrated in Figure 99 where NT diameter and volume fraction in the PAN matrix are drawn to scale. The dimensional characteristics of cases shown in Figure 99 are listed in Table 33.

It is noteworthy here (from experimental data points) that even at large concentrations (~ 15.4 vol.%), the CNFs are separated from each other by almost 143 nm, but the SWNTs at lower concentration (~ 0.8 vol. %) are separated by just 19 nm. We think that if we could increase the SWNT loading to a concentration (~ 3-4 vol. %) such that they are separated by just 9 PAN chains (or less), we will be able to make a composite fiber which is not just mechanically strong, thermally and chemically stable, but also have good electrical conductivity. This idea comes from the fact that electrons can hop between electrically conducting SWNTs when the separation is around 5 nm or less [34]. The electrical conductivity of various CNT-polymer fibers is discussed in Chapter 6.

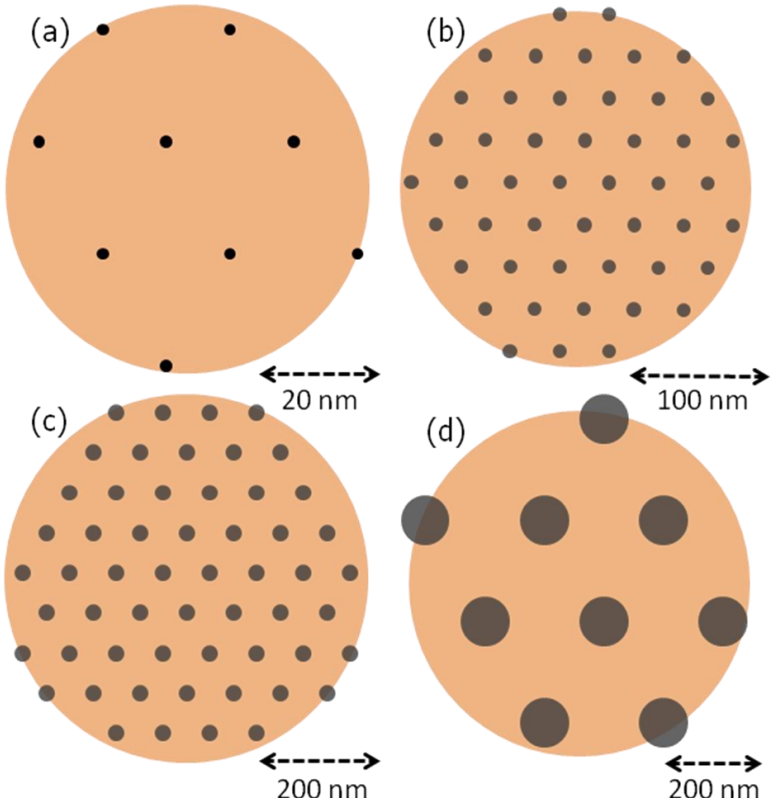

Figure 99. Illustrations showing the part of the cross-sections of different PAN/CNT composite fibers. (a) PAN reinforced with 0.8 vol.% SWNT; (b) PAN reinforced with 7.7 vol.% SWNT; (c) PAN reinforced with 11.1 vol.% MWNT; (d) PAN reinforced with 15.4 vol.% CNF. The dimensional characteristics of these composite fibers are listed in Table 33.

Table 33. Characteristics of the Composite Fibers Illustrated in Figure 97.

CNT type	CNT Dia. (nm)	Loading (vol. %)	Loading (wt.%)	CNT-CNT separation (nm)
SWNT	2	0.77	1	19
SWNT bundle	10*	7.7	10	25
MWNT	27	11.1	20	50
CNF	100	15.4	30	143

* SWNT existed in a bundle where the bundle diameter was nearly 10 nm

From Table 33, it is conceivable that if a SWNT based PAN fiber is spun, where all the SWNTs are exfoliated, the SWNTs can augment the PAN crystals orientation during the heat drawing process, whereas the same may not be true with CNFs. This is

due to the fact that even at low volume concentration the separation between two SWNTs is much smaller than separation between two CNFs at high volume concentration. This means that polymer crystals will have less room for relaxation or mis-orientation during or after the heat-drawing. Hence a higher crystalline orientation structure can be retained. This can also help in providing high crystallinity to the fiber (or a more chain extended morphology similar to UHMWPE chains in Spectra®). This particular fact has further implication in the long-term performance of the SWNT based composite fiber. This is due to the fact that a more perfect and crystalline structure will be more resistant to environmental factors like thermo-oxidation, UV induced degradation, and other chemical attacks which mainly attack the amorphous structure.

The key observations from this work are that the CNT diameter affects the CNT-polymer interaction and controls the amount of CNTs that can be loaded into a system. Though it is generally desired to have the strongest possible interaction between CNT and polymer, the strong interaction may limit the amount of CNTs that can be loaded into a system. Furthermore, it is conceivable that the presence of CNTs affects the interchain interaction of polymer. The shaded region enclosing the four data points in Figure 98 shows the limit of CNT inclusion that we have achieved in our group so-far. The next challenge for us and others who are making CNT-polymer composite fibers is to be able to generate experimental data points below the shaded region. As mentioned before, the polymer-CNT interaction is affected by several factors, and this may be advantageous for designing composite materials with wide varieties of structures and properties.

Though not directly measured here in this study, the fiber spinnability of a material can be correlated to the physically measured rheological parameters. For

example, a sufficiently high viscosity is necessary to spin a fiber from polymer solutions. As discussed in Section 4.2.6, the CNT inclusions increase the solution elasticity and the composite solutions show higher storage modulus. If the solution becomes too elastic, the tendency of drop formation increases and it becomes difficult to spin a continuous fiber. Ziabicki [35] correlated the viscosity (η) and surface tension (α) to the fiber spinning of different materials (Table 34).

Table 34. Physical Characteristics Controlling Capillary Break-Up in Various Fiber Spinning Procedures [35]

Material	Spinning	η (Pa-s)	α (N/m)	η/α (s/m)	Capillary break-up probability
Metals	Melt	0.01-0.1	0.2-1	0.05-0.1	+++
Inorganic glasses	Melt	100-1000	0.2-0.5	500-2000	+
Condensation polymers	Melt	100-500	0.03-0.08	3000-6000	+
Polyolefins	Melt	200-1500	0.03-0.05	6000-30000	-
Polymer	Solution dry-spinning	20-100	0.03-0.08	600-1200	++
Polymer	Semi-melt spinning	30-200	0.03-0.08	1000-2500	-
Polymer	Wet-spinning	5-50	0.001-0.01*	5000	-

* Interface tension 'solution-coagulation bath'
+, ++, +++ increasing probability of capillary break-up
- no break-up noted in technical conditions

The higher is the η/α ratio of a material, higher is the probability of continuous fiber formation. For polymer solutions that are spun using solution spinning, in addition to the surface tension of spinning solution, the interfacial tension between coagulation bath and polymer solution also become important. It is conceivable that, in the presence

of CNTs, not only is the surface tension of polymer solution affected, but the interfacial tension between polymer solution and coagulation bath is affected also. For dry-jet wet spinning, if the fiber breaks in the air-gap that means surface tension of the solution should be adjusted, (e.g., by changing spinning temperature, polymer/CNT solid content) but if the fiber breaks in the coagulation bath that means interfacial tension should be adjusted (e.g., by changing polymer/CNT solid content, coagulation bath concentration and temperature).

5.3. Conclusions

The theoretical maximum concentration of SWNT in an ideal PAN fiber where all the SWNTs are exfoliated and unidirectionally aligned is 35%. CNT diameter affects the CNT-polymer physical interaction and controls the maximum possible concentration of CNTs in a composite fiber. SWNTs at smaller concentration may prove to be better than MWNTs and CNFs at higher concentration for achieving high electrical conductivity.

5.4. References

1. Sreekumar TV, Liu T, Min BG, Guo H, Kumar S, Hauge RH, and Smalley RE. Advanced Materials 2004;16(1):58-61.
2. Chae HG, Minus ML, and Kumar S. Polymer 2006;47(10):3494-3504.
3. Chae HG and Kumar S. Science 2008;319(5865):908-909.
4. Li Y-L, Kinloch IA, and Windle AH. Science 2004;304(5668):276-278.
5. Vigolo B, Penicaud A, Coulon C, Sauder C, Pailler R, Journet C, Bernier P, and Poulin P. Science 2000;290(5495):1331-1334.
6. Zhang M, Atkinson KR, and Baughman RH. Science 2004;306(5700):1358-1361.

7. Chae HG, Sreekumar TV, Uchida T, and Kumar S. Polymer 2005;46(24):10925-10935.

8. Liu J, Wang T, Uchida T, and Kumar S. Journal of Applied Polymer Science 2005;96(5):1992-1995.

9. Ko F, Gogotsi Y, Ali A, Naguib N, Ye H, Yang GL, Li C, and Willis P. Advanced Materials 2003;15(14):1161-1165.

10. Ge JJ, Hou H, Li Q, Graham MJ, Greiner A, Reneker DH, Harris FW, and Cheng SZD. J. Am. Chem. Soc. 2004;126(48):15754-15761.

11. Ye H, Lam H, Titchenal N, Gogotsi Y, and Ko F. Applied Physics Letters 2004;85(10):1775-1777.

12. Hou H, Ge JJ, Zeng J, Li Q, Reneker DH, Greiner A, and Cheng SZD. Chem. Mater. 2005;17(5):967-973.

13. Rahatekar SS, Rasheed A, Jain R, Zammarano M, Koziol KK, Windle AH, Gilman JW, and Kumar S. Composite Science and Technology 2009:submitted.

14. Ma H, Zeng J, Realff ML, Kumar S, and Schiraldi DA. Composites Science and Technology 2003;63(11):1617-1628.

15. Zeng J, Saltysiak B, Johnson WS, Schiraldi DA, and Kumar S. Composites Part B: Engineering 2004;35(2):173-178.

16. Kumar S, Doshi H, Srinivasarao M, Park JO, and Schiraldi DA. Polymer 2002;43(5):1701-1703.

17. Fornes TD, Baur JW, Sabba Y, and Thomas EL. Polymer 2006;47(5):1704-1714.

18. Kumar S, Dang TD, Arnold FE, Bhattacharyya AR, Min BG, Zhang X, Vaia RA, Park C, Adams WW, Hauge RH, Smalley RE, Ramesh S, and Willis PA. Macromolecules 2002;35(24):9039-9043.

19. Sennett M, Welsh E, Wright JB, Li WZ, Wen JG, and Ren ZF. Applied Physics A: Materials Science & Processing 2003;76(1):111-113.

20. Haggenmueller R, Gommans HH, Rinzler AG, Fischer JE, and Winey KI. Chemical Physics Letters 2000;330(3-4):219-225.

21. Miaudet P, Bartholome C, Derré A, Maugey M, Sigaud G, Zakri C, and Poulin P. Polymer 2007;48(14):4068-4074.

22. Gao J, Zhao B, Itkis ME, Bekyarova E, Hu H, Kranak V, Yu A, and Haddon RC. J. Am. Chem. Soc. 2006;128(23):7492-7496.

23. Chen X, Burger C, Fang D, Sics I, Wang X, He W, Somani RH, Yoon K, Hsiao BS, and Chu B. Macromolecules 2006;39(16):5427-5437.

24. Li J, Chen X, Li X, Cao H, Yu H, and Huang Y. Polymer International 2006;55(4):456-465.

25. Sandler JKW, Pegel S, Cadek M, Gojny F, van Es M, Lohmar J, Blau WJ, Schulte K, Windle AH, and Shaffer MSP. Polymer 2004;45(6):2001-2015.

26. Dupire M and Michel J. Reinforced Polymers. USPatent 6331265 B1: Atofina Research, 2001.

27. Kitagawa T. Polybenzazole Fiber. US Patent 6884506 B2: Toyo Boseki Kabushiki Kaisha, 2005.

28. Ruan S, Gao P, and Yu TX. Polymer 2006;47(5):1604-1611.

29. Zhang X, Liu T, Sreekumar TV, Kumar S, Hu X, and Smith K. Polymer 2004;45(26):8801-8807.

30. Pötschke P, Brünig H, Janke A, Fischer D, and Jehnichen D. Polymer 2005;46(23):10355-10363.

31. Haggenmueller R, Zhou W, Fischer JE, and Winey KI. Journal of Nanoscience and Nanotechnology 2003;3:105-110.

32. Muñoz E, Suh D-S, Collins S, Selvidge M, Dalton AB, Kim BG, Razal JM, Ussery G, Rinzler AG, Martínez MT, and Baughman RH. Advanced Materials 2005;17(8):1064-1067.

33. Uchida T and Kumar S. Journal of Applied Polymer Science 2005;98(3):985-989.

34. Hu G, Zhao C, Zhang S, Yang M, and Wang Z. Polymer 2006;47(1):480-488.

35. Ziabicki A. "Fundamentals of Fiber Formation". John Wiley & Sons, New York 1976:28.

CHAPTER 6

CARBON NANOTUBE REINFORCED ELECTRICALLY CONDUCTING POLYMER FIBERS

Different types of carbon nanotubes (CNTs), single-wall carbon nanotube (SWNT), multi-wall carbon nanotube (MWNT), and carbon nanofiber (CNF), were used to reinforce polyacrylonitrile (PAN) and polyvinyl alcohol (PVA) fibers. The effects of CNT type, CNT concentration, CNT length, fiber draw ratio, and polymer molecular weight on electrical conductivity of composite fibers were studied. For a particular CNT, as expected, the electrical conductivity increased with increase in CNT concentration. The electrical conductivity also increased with increase in draw ratio. For a particular CNT concentration, the high MW PAN based composite fibers showed higher electrical conductivity. The results show that by properly choosing the type of CNT, length of CNTs, dispersion of CNTs, fiber spinning method, fiber draw ratio or orientation of CNTs, and type of polymer, one can get electrically conducting fibers with wide range of conductivities for different applications.

6.1. Experimental

PAN/CNT and PVA/CNT composite fibers were considered for this study. PAN/SWNT and PAN/MWNT composite fibers were spun using dry-jet wet spinning and gel spinning, and PAN/CNF composite fibers were spun using dry-jet wet spinning. PVA/SWNT and PVA/MWNT fibers were spun using gel spinning. The materials and methods of PAN/SWNT and PVA/SWNT has been described elsewhere [1-3]. The PAN/MWNT and PAN/CNF composite fibers spun using dry-jet wet spinning has been

described in Chapter 2, 3 and 4. The ac electrical conductivity of the composite fibers was measured using the procedure described in section 2.2.

6.2. Results and Discussion

The electrical conductivities of various fibers reported in this study are listed in Tables 35 and 36. The typical voltage-current (V-I) curves for some of the fiber samples are shown in Figure 100. These curves could be fitted with a linear equation (with more than 90% confidence in most of the samples and more than 80% confidence in all the samples). In some cases, there was an abrupt increase in voltage above a particular current. This abrupt increase in voltage could be due to the break-up of CNT-CNT junctions and consequent loss of certain conducting channels.

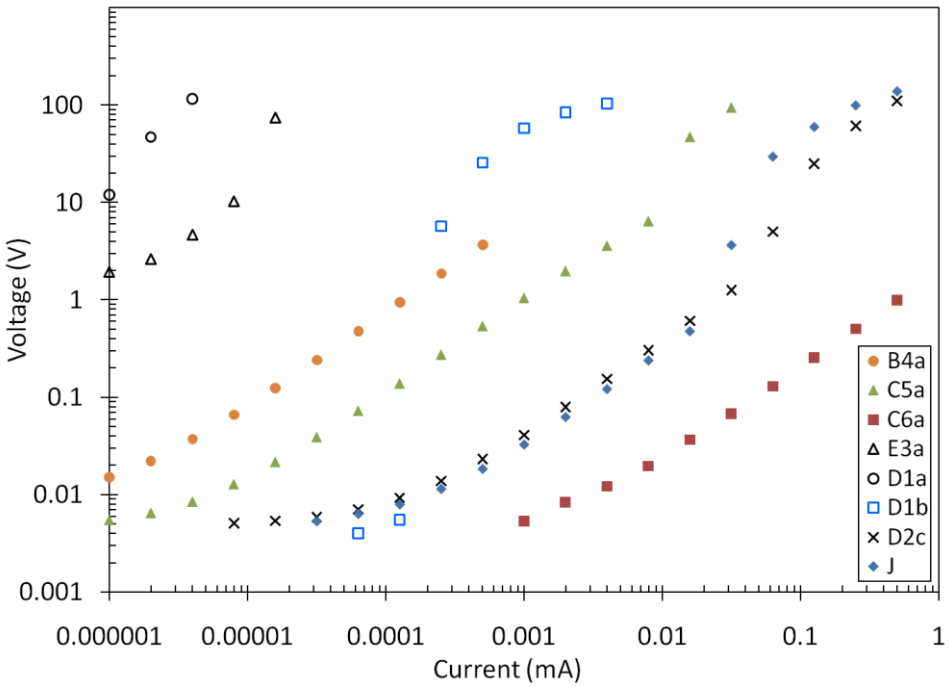

Figure 100. Typical voltage-current (V-I) curves for dry-jet wet spun PAN/CNT fibers listed in Table 35.

Table 35. Electrical Conductivity and Structural Parameters for Various PAN/CNT and PAN/CNF Fibers Spun Using Dry-Jet Wet Solution Spinning

Sample	PAN	CNT	CNT Dia. (nm)	CNT (wt%)	Impurity (wt%)	Draw Ratio	Fiber Diameter (μm)	f_{PAN} [1] (2θ~17°)	f_{CNT} [1] (2θ~26°)	Electrical Conductivity (S/m)
B2a	100K	MWNT	27	10	5	5	46.2	0.73	0.60	1.04×10^{-4} $\pm4.22\times10^{-6}$
B3a	100K	MWNT	27	15	5	4	59.9	0.64	0.40	1.24 ±1.01
B4a	100K	MWNT	27	20	5	2.5	44.1	0.55	0.32	0.61 ±0.80
C4a	100K	CNF	100	20	2	5	55.7	0.70	0.45	8.2×10^{-5} $\pm8.7\times10^{-6}$
C5a	100K	CNF	100	30	2	3.5	69.8	0.55	0.39	0.9 ±0.5
C6a	100K	CNF	100	40	2	as spun	210	---	---	42 ±16
E3a	100K	CNF	100	20*	2	5	55.6	0.68	0.55	1.27×10^{-3} $\pm1.8\times10^{-3}$
D1a	250K	CNF	100	20	2	5	70.8	0.38	0.42	4.35×10^{-5} $\pm9.1\times10^{-7}$
D1b	250K	CNF	100	20	2	10	48.6	0.77	0.53	0.14 ±0.33
D2a	700K	CNF	100	20	2	4	67.9	---	---	7.4 ±3.3
D2b	700K	CNF	100	20	2	6	58.3	---	---	6.3 ±2.3
D2c	700K	CNF	100	20	2	8	45.6	---	---	15 ±6.8
D2d	700K	CNF	100	20	2	10	42.0	0.78	0.58	28 ±12
J	100K	SWNT	10**	10	5	3	39.5	---	---	4 ±0.6
K#	250K	FWNT	5-10	1	1	6	12.0	0.81	---	$0.01\pm4.52\times10^{-3}$

[1] Herman's orientation factor; * CNF sonicated for 48 h (as opposed to 5 h for other CNF based fibers); ** SWNT existed in an average bundle diameter of 10 nm, and the fiber was drawn less than reported in [1]; # Coagulation bath contained only de-ionized water

Table 36. Electrical Conductivity and Structural Parameters for Various PAN/CNT and PVA/CNT Composite Fibers Spun Using Gel Spinning [2, 3]

Sample	PAN	CNT	CNT Dia. (nm)	CNT (wt%)	Impurity (wt%)	Draw Ratio	Fiber Diameter (μm)	f_{PAN} [1] (2θ~17°)	f_{CNT} [1] (2θ~26°)	Electrical Conductivity (S/m)
L	250K	FWNT	5-10	1	1	13.5	11.1	0.89	0.93	$1.05\times10^{-2} \pm 3.75\times10^{-4}$
M	250K	FWNT	5-10	1	4	13.5	10.2	0.89	0.94	$1.61\times10^{-2} \pm 5.03\times10^{-3}$
N	250K	FWNT	2-5	1	1.6	16.5	13.3	---	---	$9.59\times10^{-3} \pm 8.81\times10^{-3}$
O	250K	SWNT	1.3	1	1.1	48	12.8	---	---	$1.55\times10^{-2} \pm 2.49\times10^{-3}$
P	250K	SWNT	2	1	1	51	18.7	---	---	$9.60\times10^{-3} \pm 1.78\times10^{-3}$
Q1	250K	MWNT	20	1	5	25	15.5	0.86	---	$1.10\times10^{-3} \pm 4.3\times10^{-5}$
Q2	250K	MWNT	20	1	5	35	13.1	0.88	---	$1.38\times10^{-3} \pm 2.04\times10^{-5}$
Q3	250K	MWNT	20	1	5	45	11.7	0.89	---	$1.65\times10^{-3} \pm 1.26\times10^{-5}$
Q4	250K	MWNT	20	1	5	55	10.4	0.90	---	$4.06\times10^{-3} \pm 3.4\times10^{-4}$
R	250K	MWNT	20	2	5	73.5	14.2	---	---	$2.57\times10^{-2} \pm 5.32\times10^{-3}$
S1	240K	FWNT	2-5	0.5	1.6	14.0	18.2	---	---	$6.50\times10^{-4} \pm 1.02\times10^{-5}$
S2	240K	FWNT	2-5	0.5	1.6	17.3	16.4	---	---	$8.18\times10^{-4} \pm 1.48\times10^{-5}$
T	240K	FWNT	2-5	0.1	1.6	14.9	17.7	---	---	$6.90\times10^{-4} \pm 1.11\times10^{-5}$
U	PVA	MWNT	27	1	5	130	9.5	---	---	$4.02\times10^{-2} \pm 7.72\times10^{-3}$
V1	PVA	SWNT		1		8	49.4	---	---	$1.52\times10^{-4} \pm 8.55\times10^{-6}$
V2	PVA	SWNT		1		13	34.3	---	---	$3.44\times10^{-4} \pm 3.15\times10^{-5}$
V3	PVA	SWNT		1		21	38.1	---	---	$2.79\times10^{-4} \pm 1.36\times10^{-5}$
V4	PVA	SWNT		1		42	22.6	---	---	$6.13\times10^{-3} \pm 8.89\times10^{-4}$
W	PVA	SWNT		1		80	11.5	---	---	$3.33\times10^{-3} \pm 1.9\times10^{-4}$
X	PVA	FWNT	2-5	1	1.6		12.2	---	---	$1.43\times10^{-3} \pm 2.09\times10^{-5}$

[1] Herman's orientation factor

Figure 101 shows the electrical conductivity of various PAN/CNT composite fibers (listed in Tables 35 and 36) as a function of CNT %. As mentioned before, the conductivity of a composite fiber is a function of CNT %, state of dispersion, aspect ratio, purity, defects, type and degree of interaction with polymer, orientation of nanotubes, and tunneling distance between nanotubes.

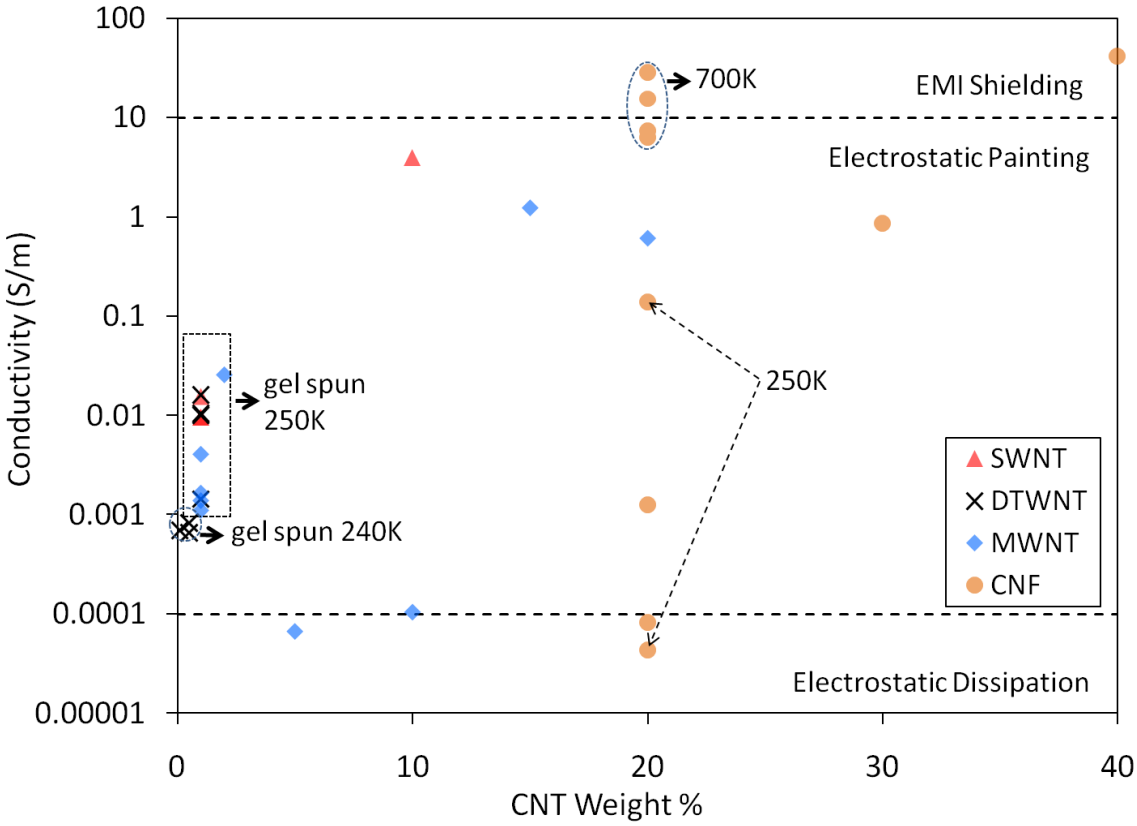

Figure 101. Electrical conductivity of PAN based composite fibers with different types of CNTs as a function of CNT concentration. The low CNT containing (≤ 2 wt.% CNT) fibers were spun using gel spinning and higher CNT containing fibers (≥ 5 wt.%) were spun using dry-jet wet spinning. PAN with four different molecular weights of 100K, 240K, 250K, and 700K was used. Fibers based on 240K, 250K and 700K PAN are marked and the rest of the unmarked fibers are based on 100K PAN. Note: PVA based composite fibers with 1% SWNT or 1% MWNT showed electrical conductivity in the range of 0.001 to 0.1 S/m (PVA /CNT data are not included in this Figure). All data points were taken from Tables 35 and 36.

6.2.1. Effect of Fiber Draw Ratio

Fibers with different draw ratios were spun to achieve different degrees of CNT orientation in the fiber. A higher draw ratio results into a fiber with higher degree of CNT orientation. The 20% CNF containing 700K PAN fiber was spun using dry-jet wet spinning and subsequently heat drawn to four different draw ratios of 4, 6, 8, and 10. The 1% MWNT containing 250K PAN fiber was spun using gel spinning and drawn to four different draw ratios of 25, 35, 45, and 55. The 1% SWNT containing PVA fiber was spun using gel spinning and drawn to four different draw ratios of 8, 13, 21, and 42. The 20% CNF containing 250K fiber was spun using dry-jet wet spinning and subsequently heat drawn to two different draw ratios of 5 and 10.

The data for the aforementioned four cases are shown in Figure 102. In general, the electrical conductivity increased with increase in draw ratio. A greater increase of nearly 4 orders of magnitude in electrical conductivity was observed in the case of 20% CNF containing 250K PAN fiber. Two models illustrating the effect of drawing on fibers containing SWNTs and MWNTs (or CNFs) are shown in Figure 103. The drawing affects the composite fiber morphology in three ways which may increase the fiber conductivity: (i) the effective aspect ratio of CNTs increases (a SWNT bundle has lower aspect ratio than individual SWNT and a MWNT agglomerate has lower aspect ratio than a non-agglomerated MWNT), (ii) orientation of CNTs increases in the fiber direction, and (iii) separation (tunneling distance) between CNTs decreases. Zhang *et al.* [4] blended conductive polyaniline with polyamide-11 and showed one order of magnitude increase in the conductivity of the fiber when the draw ratio was increased from 1.52 to 3.57.

They attributed this to the formation of more perfect conductive channels with increase in draw ratio.

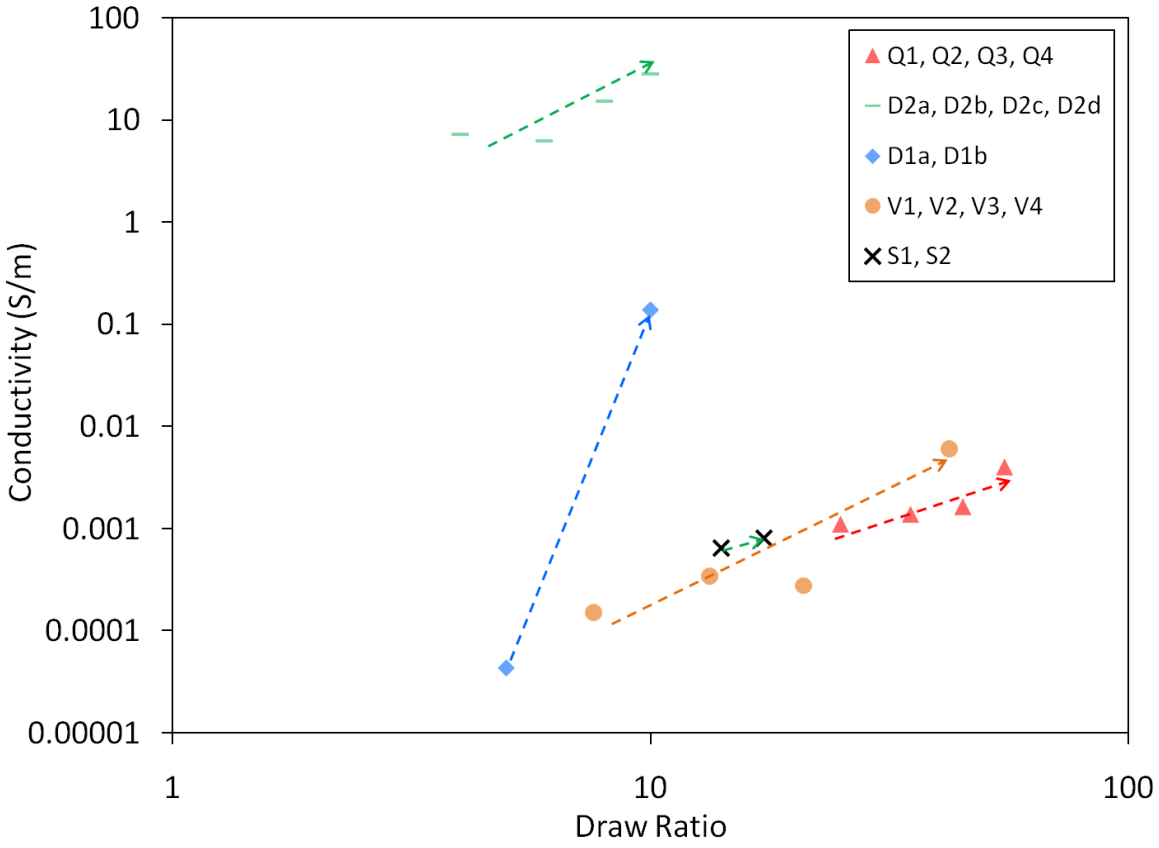

Figure 102. Effect of draw ratio on conductivity for different fibers. The arrows are not fitted to the data points but are drawn as an aid to the eye to show dominating trend. Q series: 1% MWNT containing 250K PAN fiber, D2 series: 20%CNF containing 700K PAN fiber, D1 series: 20%CNF containing 250K PAN fiber, V series: 1% SWNT containing PVA fiber, S series: 0.5% FWNT containing 240K PAN fiber. For more sample information, refer Tables 35 and 36.

Equation 19 has conventionally been used to successfully describe the percolation and conductivity in isotropic composite systems [5].

$$\sigma_c = \sigma_o \left(f - f^*\right)^t \qquad for \quad f > f^* \tag{19}$$

where σ_c is the conductivity of the composite, σ_o is a scaling factor, f is the fraction of the filler, f* is the fraction of the filler at percolation threshold, and t is the percolation exponent.

(a)

(b)

(c)

(d)

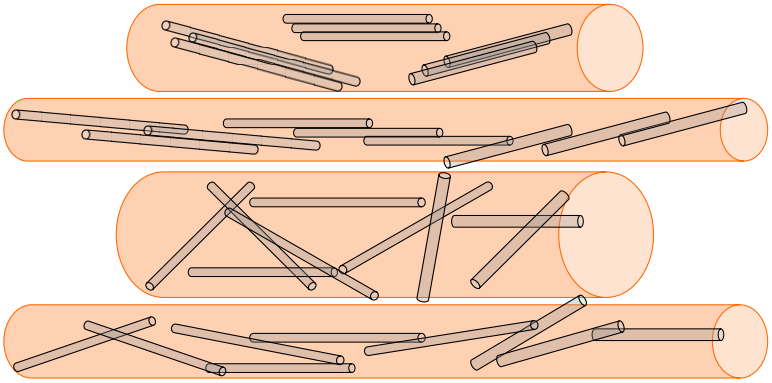

Figure 103. Illustration showing the effect of drawing and orientation. (a) and (b): composite fiber containing SWNT bundle before drawing, and oriented and exfoliated tubes after drawing. (c) and (d): composite fiber containing randomly oriented MWNTs (or CNFs) before drawing and oriented MWNTs (or CNFs) after drawing. Drawing induced exfoliation and orientation leads to the formation of a continuous conducting path which increases conductivity.

The situation of filler dispersion and percolation is very simplistic in conventional filler based composite systems where the filler size/diameter is in the range of microns. Compared to nanoscale fillers (CNTs), it is relatively easy to uniformly disperse the macro scale fillers in a matrix. Furthermore, as shown in Figure 104, at a given volume fraction, the separation distance between one micron size fillers is very large as compared to the separation distance for the nanoscale fillers. Even at 50 vol% concentration, the one micron size fillers would be separated from each other by almost 350 nm. Equation 20 was used to calculate the separation distance *s* between cylindrical fillers of diameter d_t for a particular volume fraction of filler $(1-F_{polymer})$ and assumes that filler particles are all uniaxially oriented.

$$F_{polymer} = 1 - \frac{\pi d_t^2}{2\sqrt{3}(d_t + s)^2} \quad (20)$$

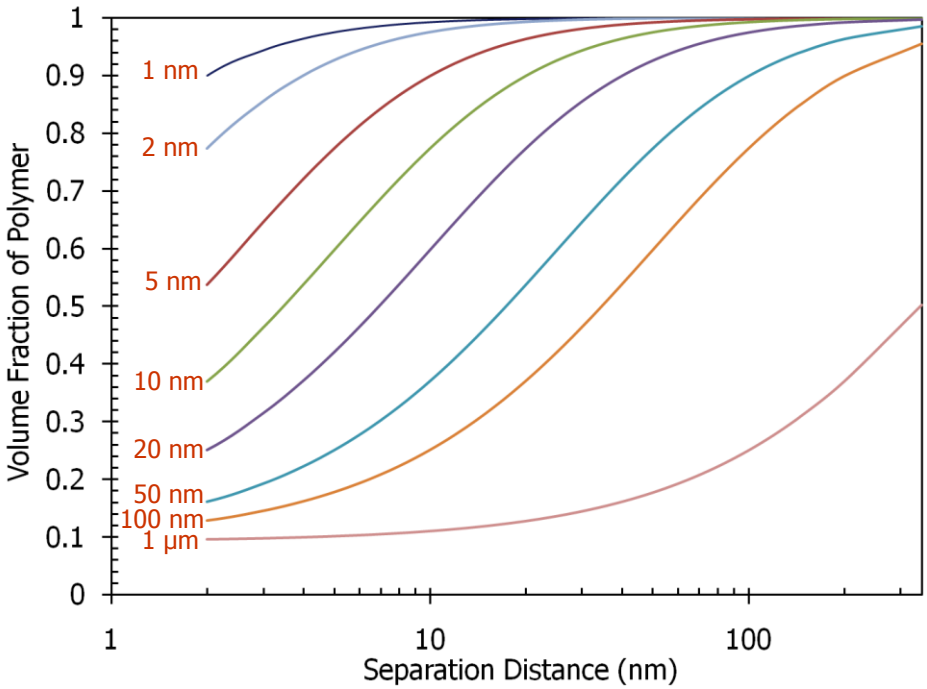

Figure 104. Volume fraction of polymer vs. separation distance between CNTs of different diameters. CNT diameters are as indicated in the Figure. It is assumed that CNTs are uniformly dispersed and uniaxially oriented along the fiber axis.

The situation of filler dispersion and percolation is quite complex in case of nanoscale fillers. CNTs have a tendency to agglomerate which makes it difficult to uniformly disperse them in the matrix. There are several factors that limit the use of equation 16 to fairly describe or predict the conductivity and percolation of CNT containing composites, especially fibers. The processing of nanocomposites has a huge influence on the morphology and microstructure of the composite. For example, drawing/stretching may increase the effective aspect ratio of SWNT or MWNT (by de-bundling or de-agglomeration) and decrease the separation distance between CNTs.

Furthermore, the effects of electron hopping and tunneling become more important when the separation distance decreases to tens of nanometers or less. For example, even at just 1 vol%, SWNTs of 1 nm diameter have a separation distance of just 9 nm. The separation distance can be correlated to the CNT-CNT contact resistance. A larger separation means higher tunneling resistance. Li *et al.* [6] calculated that three orders of magnitude decrease in contact resistance can increase the conductivity by almost similar magnitude.

6.2.2. Effect of CNT Length or State of Dispersion

The CNFs were sonicated for two different periods of 5 h and 48 h. The 48 h sonicated CNFs were much shorter in lengths than CNFs sonicated for 5 h. The SEM images showing the effect of sonication time on the CNF length are shown in Appendix C. The 5 h and 48 h sonicated CNFs were used to spin 20%CNF containing 100K PAN fibers using dry-jet wet spinning which were drawn to a draw ratio of 5. The 48 h fiber showed higher conductivity than 5 h fiber (1.27×10^{-3} vs. 8.21×10^{-5} S/m). For the 48 h sample, the CNFs dispersion in the fiber was found to be much better than 5 h fiber (Compare Figures 43 and 69 in Chapter 3). The increase in conductivity could be due to better dispersion or lower agglomeration and higher degree of CNF orientation (Herman's orientation factor 0.55 and 0.45 for 48 h and 5 h samples, respectively). As mentioned in the previous section, a better dispersion may increase the effective aspect ratio and decrease the separation distance between CNFs (decreasing tunneling distance or contact resistance).

6.2.3. Effect of CNT Concentration

The effect of CNT concentration was studied from the dry-jet wet spun fibers of 100K PAN with different concentration of MWNTs (10, 15, and 20 wt%) and CNFs (20, 30, and 40 wt%). In general, the electrical conductivity increased with increase in CNT concentration. Since the fibers with different concentration of CNTs could not be drawn to the same degree, the trend of increasing conductivity was not linear. For solution spun PAN/MWNT fibers, the percolation threshold is between 10 and 15 % loading (conductivity increased by nearly four orders of magnitude from 10 to 15% MWNT). For solution spun PAN/CNF fibers, the percolation threshold is observed between 20 and 30 % loading (conductivity increased by nearly four orders of magnitude from 20 to 30% CNF). The effect of concentration is very complex in case of CNT type nanoscale fillers as compared to conventional micron scale fillers. For example, at higher concentrations, the chances of CNT agglomeration increases, which may lead to poor dispersion and decrease the effective aspect ratio and hence increase the separation distance. Therefore, to fully utilize the effect of higher concentration of CNT type fillers, it becomes very important to achieve a uniform dispersion of CNTs in the matrix.

6.2.4. Effect of CNT Type

The 100K PAN fibers containing different types of CNTs (SWNTs, MWNTs, and CNFs) were spun using dry-jet wet spinning. At 10% loading, the SWNT containing fiber was 10,000 times more conductive than MWNT containing fiber. At that loading the CNF containing fiber was not even conducting enough to be measured by our instrument. Only at 20% CNF (not even at 15% loading) did CNF containing fiber showed a

conductivity value which was still lower than 10% SWNT containing fiber by almost five orders of magnitude. In general, the conductivity showed this trend: SWNT>MWNT>CNF. This trend could be a result of the fact that the inherent conductivity of these fillers follows the same trend [7-9]. In fact, as shown in Figure 104, for a particular CNT concentration, the tunneling distance also increases with increase in CNT diameter. Therefore, for a particular volume fraction of CNTs, the nanotube-nanotube separation would be maximum for CNFs and minimum for SWNTs. A lower tunneling distance would result in lower percolation threshold and higher conductivity.

6.2.5. Effect of Polymer Molecular Weight

PAN with three different molecular weights of 100K, 250K, and 700K was used to spin 20% CNF composite fibers. The 20% CNF containing 100K PAN fiber could only be drawn up to 5 times (draw ratio 5) and showed an electrical conductivity value of 8.21×10^{-5} S/m. On the other hand, both 20% CNF containing 250K and 700K PAN fibers could be drawn up to 10 times. Comparing the conductivity values at draw ratio 5, the 20% CNF containing 100K and 250K PAN fibers showed similar electrical conductivity. However, the 20% CNF containing 700K PAN fiber at draw ratio 4 showed an electrical conductivity which was nearly five orders of magnitude higher than both 20% CNF containing 100K and 250K PAN fibers at draw ratio 5. Comparing the conductivity values at draw ratio 10, 20% CNF containing 700K PAN fiber showed an electrical conductivity which was two orders of magnitude larger than that of the 250K PAN fiber. Wide angle X-ray diffraction analyses showed that 20% CNF containing 250K and 700K based composite fibers had higher crystallinity and larger PAN crystals than 100K based

composite fiber. The 20% CNF containing PAN 100K, 250K and 700K fibers showed a crystallinity of 46, 53, and 59% respectively, and crystal sizes of 6.2, 6.8, and 7.0 nm, respectively. Though uncertain, these factors may affect the flow of electrons in the composite fibers and ultimately change the electrical conductivity of the fibers.

6.2.6. Controlling Multiple Variables to Get Desired Conductivity

As shown in Figure 101 and Tables 35 and 36, by properly choosing the spinning method, type of CNT, fiber draw ratio, and controlling the CNT dispersion, one can get fibers with wide range of electrical conductivity. The low SWNT and MWNT containing fibers spun using gel spinning drawn to very high draw ratios provided electrical conductivity which even surpassed many of the solution spun fibers with much higher loading of MWNTs and CNFs. The data suggests that even in highly oriented systems, the electrical percolation can be obtained at just 1% CNT loading.

The effect of processing on the percolation and conductivity for a composite fiber can be described as follows. In the undrawn fiber, the alignment of both polymer and CNT is low and CNTs are more bundled (SWNTs) and/or entangled (SWNTs, MWNTs, CNFs) together and the polymer is mostly in a random coil state. At this stage, the percolation for conductivity results from the random orientation of CNTs. During drawing, both polymer and CNTs get oriented and the degree of overlap among CNTs decreases. But the separation distance among CNTs also decrease. Drawing may also result in debundling and disentanglement of nanotube agglomerates, which increase the effective aspect ratio of CNTs. Consequently, while on the one hand the degree of overlap between CNTs decrease (which tends to increase percolation threshold and

decrease conductivity), on the other hand the separation and debundling/disentanglement decrease and aspect ratio increase (which tend to decrease percolation threshold and increase conductivity). In some cases, both of these phenomena may compete leaving the resulting percolation and conductivity unchanged. This suggests that for a particular CNT/polymer system, both percolation and value of conductivity can be tailored by tailoring the processing method.

6.3. Conclusions

The electrical conductivity of the fibers increased with increase in fiber draw ratio and CNT concentration. The fiber conductivity was found to depend on the CNT type and diameter. The conductivity followed the trend of SWNT>MWNT>CNF. We showed that a smaller diameter CNT would provide shorter tunneling distance and hence would prove to be more useful for increasing the electrical conductivity and lowering the percolation threshold. The uniform CNT dispersion and de-agglomeration were found to be critical factors to increase fiber conductivity. We showed that the composite fibers with different conductivities can be made by choosing different CNTs in different concentrations and lengths and by controlling CNT dispersion and fiber synthesis parameters.

6.4. References

1. Sreekumar TV, Liu T, Min BG, Guo H, Kumar S, Hauge RH, and Smalley RE. Advanced Materials 2004;16(1):58-61.
2. Chae HG, Minus ML, and Kumar S. Polymer 2006;47(10):3494-3504.
3. Minus M. Ph.D. Thesis. Georgia Institute of Technology 2008.

4. Zhang Q, Jin H, Wang X, and Jing X. Synthetic Metals 2001;123(3):481-485.

5. Taya M, Kim WJ, and Ono K. Mechanics of Materials 1998;28(1-4):53-59.

6. Li C, Thostenson ET, and Chou T-W. Applied Physics Letters 2007;91(22):223114-223113.

7. McEuen PL, Fuhrer MS, and Hongkun P. Nanotechnology, IEEE Transactions on 2002;1(1):78-85.

8. Kasumov AY, Khodos II, Ajayan PM, and Colliex C. Europhysics Letters 1996;34:429-434.

9. Stokes KL, Tritt TM, Fuller-Mora WW, Ehrlich AC, and Jacobsen RL. Electronic transport properties of highly conducting vapor-grown carbon fiber composites. Thermoelectrics, 1996., Fifteenth International Conference on, 1996. pp. 164-167.

CHAPTER 7

CARBON NANOTUBE REINFORCED POLY(ETHERKETONE) FIBERS

Different types of carbon nanotubes (CNTs), e.g. single-wall carbon nanotubes (SWNTs), few-wall carbon nanotubes (FWNTs), and multi-wall carbon nanotubes (MWNTs) were used to reinforce poly(etherketone) (PEK) fibers. PEK was grafted on to CNT walls during the in-situ polymerization of PEK. The effects of CNT type and CNT concentration on the fiber morphology and structure have been studied. The fibers were also tested for their electrical conductivity, tensile properties, thermal properties, thermomechanical, and dynamic mechanical properties. The PEK based fibers were found to have the most unique combination of properties with toughness surpassing that of the Kevlar® (~ 30-45 J/g) [1-3], Zylon® (~ 50 J/g) [1, 4, 5] and other high-performance fibers, and approaching values closer to that of the spider silk (~ 165 J/g) [3]. PEK has high thermal stability with degradation beginning only above 500 ˚C and possess high char yield.

7.1. Experimental

7.1.1. Materials

All reagents and solvents were purchased from Aldrich Chemical Inc. and used as received, unless otherwise mentioned. The monomer, 4-phenoxybenzoic acid (4-PBA), was purified by recrystallization from toluene/heptane. MWNT (<5% impurity) was obtained from Cheaptubes.com. SWNT (R0 238, ~35% impurity) and FWNT (XO437VA, 4 wt% catalytic impurity) were obtained from Unidym Inc. (Houston, USA).

CNTs were characterized using Raman spectroscopy and SEM imaging. Figure 105 shows the Raman spectra of SWNT, FWNT, and MWNT used for making PEK-g-CNT fibers. The Raman spectra were recorded by using a Witek (Alpha 300 R) confocal Raman microscope with Nikon 20x objective (NA = 0.4) in back-scattered configuration. The excitation laser was an Ar+ ion laser (514.5 nm) and the power delivered to the sample was 1-3 mW. The spectra were recorded using a 600 grooves/mm grating with a spectral resolution of about 2 cm^{-1}. A brief review of the Raman spectroscopy of CNTs is given in Appendix D. The G/D band intensity ratios for SWNT, FWNT, and MWNT are around 10, 6, and 0.8, respectively. This means that SWNTs contain few defects on the tube walls and MWNTs contain the most. Figures 106 and 107 show the SEM images of as-received FWNT and MWNT powders.

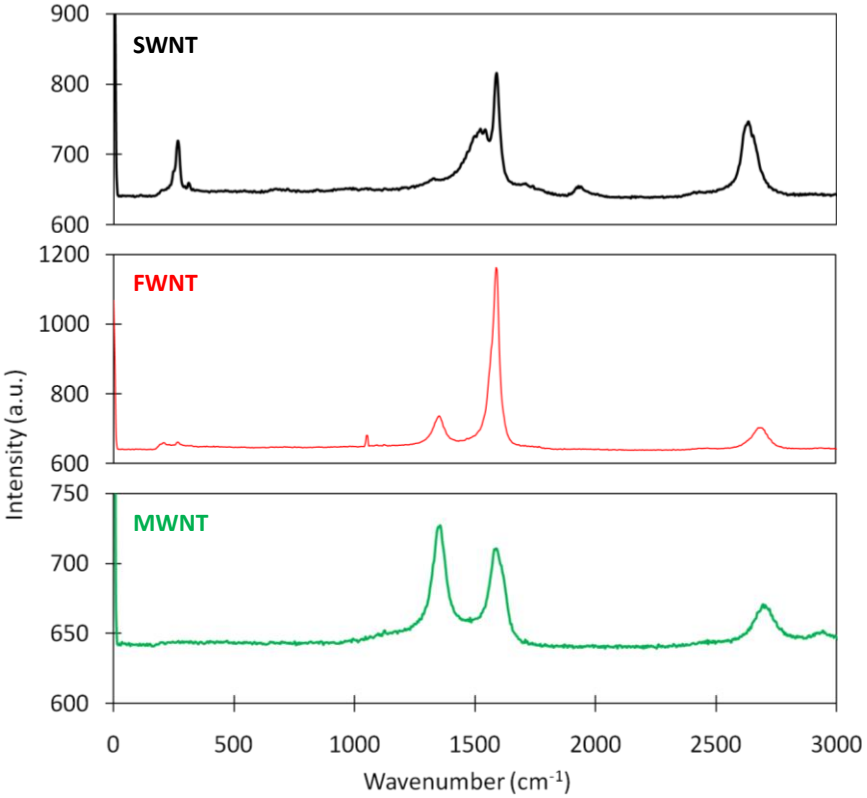

Figure 105. Raman spectra of SWNT, FWNT, and MWNT.

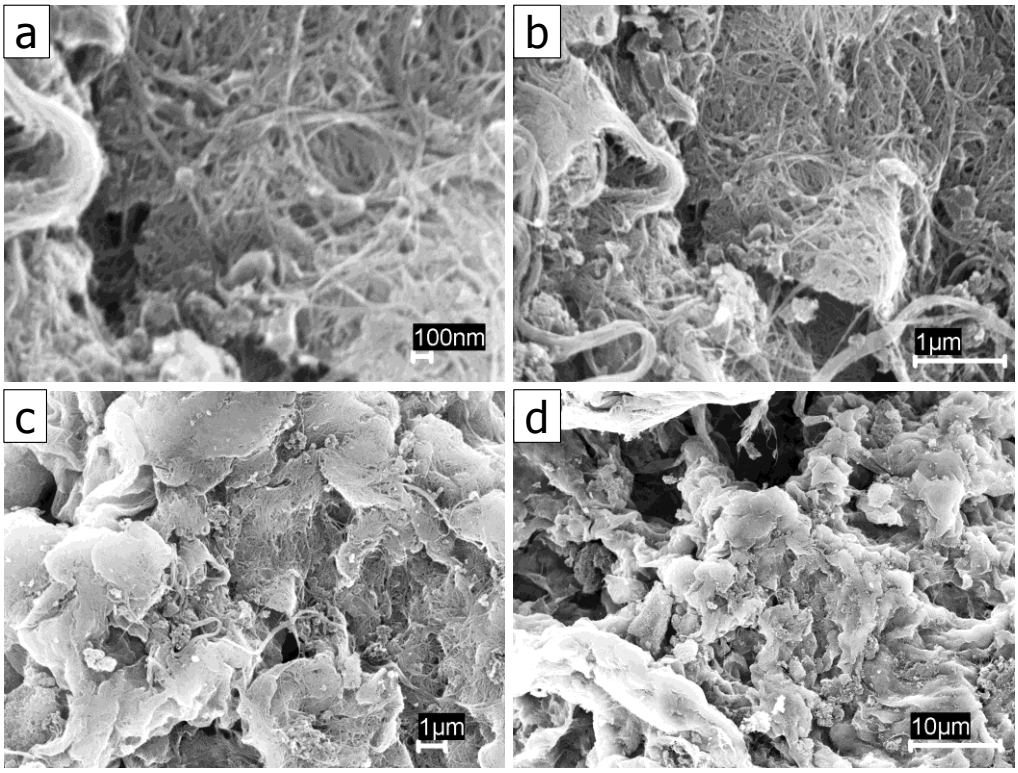

Figure 106. SEM images (at different magnifications) of as-received FWNTs.

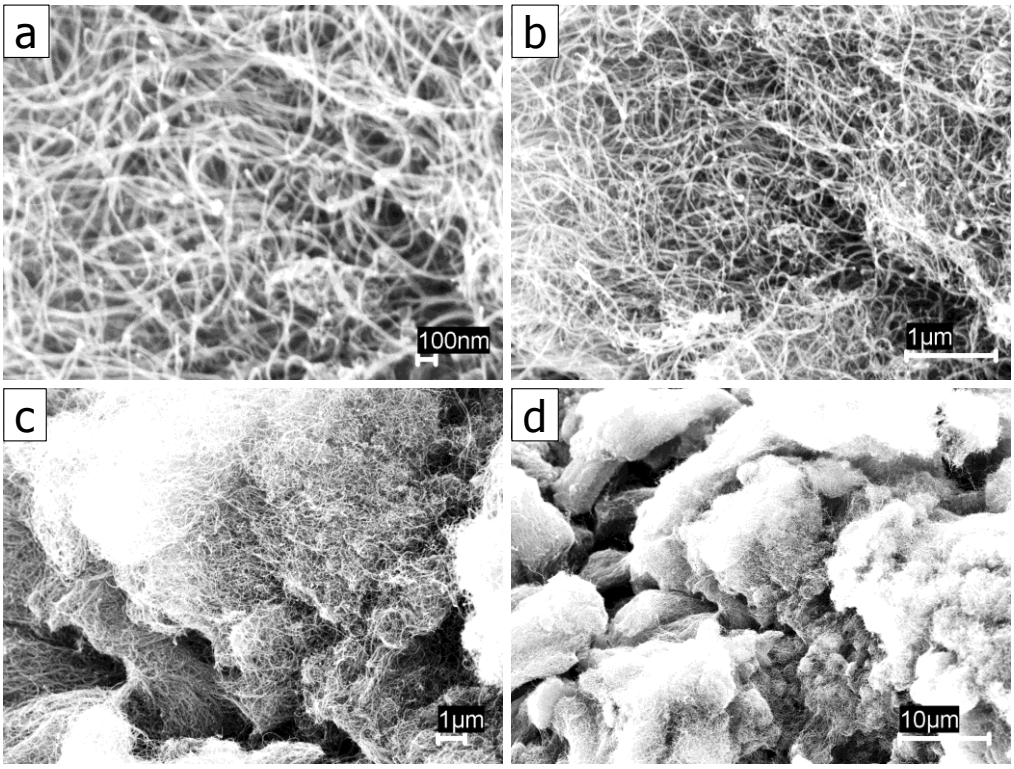

Figure 107. SEM images (at different magnifications) of as-received MWNTs.

7.1.2. In-situ Polymerization of 4-Phenoxybenzoic Acid in the Presence of CNT

For PEK and PEK-g-CNT synthesis, a 250 ml flask equipped with a high torque mechanical stirrer, nitrogen inlet and outlet, and a solid-addition port was used. For 1% FWNT containing PEK-g-FWNT, 4-phenoxybenzoic acid (4.95 g, 23.1 mmol), FWNT (0.05 g), P_2O_5 (25.0 g), and polyphosphoric acid (PPA) (100 g; 83% P_2O_5 assay) were mixed under dry nitrogen purge at 130 ˚C for 72 h. The resultant product was referred to as PEK-g-FWNT. The same basic procedure was used to synthesize the PEK-g-SWNT and PEK-g-MWNT with different concentrations of SWNT or MWNT. All the monomer purification and polymer synthesis work was developed and conducted by Dr. Jong-Beom Baek [6-8]. The representative procedure of "direct" Friedel-Crafts acylation reaction in a mild reaction medium of PPA with additional phosphorous pentoxide (P_2O_5) has been described previously [6-8].

Para-PEK (PEK) was selected as the matrix polymer because 4-phenoxybenzoic acid is commercially available, and high molecular weight PEK can be synthesized in PPA with an optimized P_2O_5 content. The in-situ polycondensation of 4-phenoxybenzoic acid in the presence of dispersed CNT is depicted in Figure 108. The different solid content and feed ratio are summarized in Table 37. As the reaction progressed at the polymerization temperature, the dope stuck to the stirring rod at 130 ºC within 72 h and could not be mixed further.

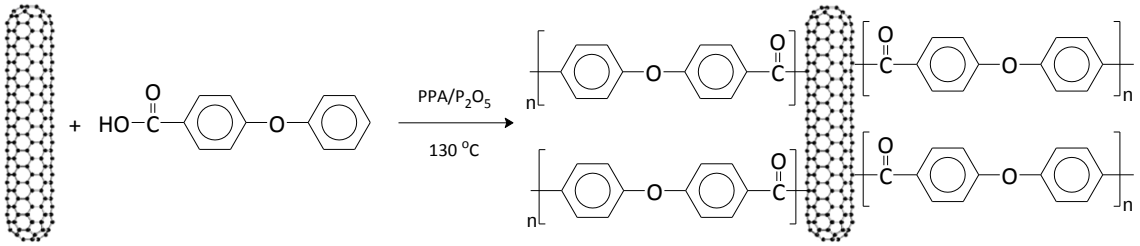

Figure 108. In-situ polymerization of 4-phenoxybenzoic acid with CNT.

Table 37. Feed Ratios of Monomer and CNT, and Solid Contents for Various PEK/CNT Samples

Sample	CNT (%)	Composition	monomer + CNT (g)	PPA (g)	P_2O_5 (g)	Solid Content (wt.%)
J1a	0	PEK	5.0 + 0	100	25	3.7
J2a	0	PEK	5.0 + 0	50	12.5	7.3
K1a	1	PEK-g-SWNT	4.95 + 0.05	50	12.5	7.3
K2a	5	PEK-g-SWNT	4.75 + 0.25	50	12.5	7.3
L1a	1	PEK-g-FWNT	4.95 + 0.05	100	25	3.7
L2a	1	PEK-g-FWNT	4.95 + 0.05	50	12.5	7.3
L3a	5	PEK-g-FWNT	4.75 + 0.25	50	12.5	7.3
L4a	10	PEK-g-FWNT	4.50 + 0.50	50	12.5	7.3
L5a	20	PEK-g-FWNT	4.00 + 1.00	50	12.5	7.3
M1a	1	PEK-g-MWNT	4.95 + 0.05	50	12.5	7.3
M2a	10	PEK-g-MWNT	4.50 + 0.50	50	12.5	7.3

7.1.3. Fiber Spinning

PEK and PEK/CNT fibers were spun using dry-jet wet-spinning. The PEK-g-CNT+PPA solution was placed into the barrel (with 28 mm internal diameter). The solution was extruded through a spinneret of 120 μm diameter and passed through distilled water coagulation bath (~1.5 m long) maintained at room temperature. The as-spun fibers were kept in water for several days to remove the residual PPA. The low solid content fibers were drawn in two stages at 120 ˚C and 180 ˚C. The high solid content fibers were drawn in one stage at 200 ˚C. The SEM images of the fiber surfaces and

cross-sections of PEK and 1% FWNT containing PEK fibers are shown in Figures 109 and 110 respectively. The fibers appeared to be smooth, uniform, and circular in cross-section. All other fibers with and without different CNTs had similar appearances. However, some fibers appeared to be cracked in the cross-section (Figure 111). This could be a result of compression stresses generated during the microtomy of cross-sections. This suggests that these PEK/CNT fibers possess poor compression properties in the transverse direction.

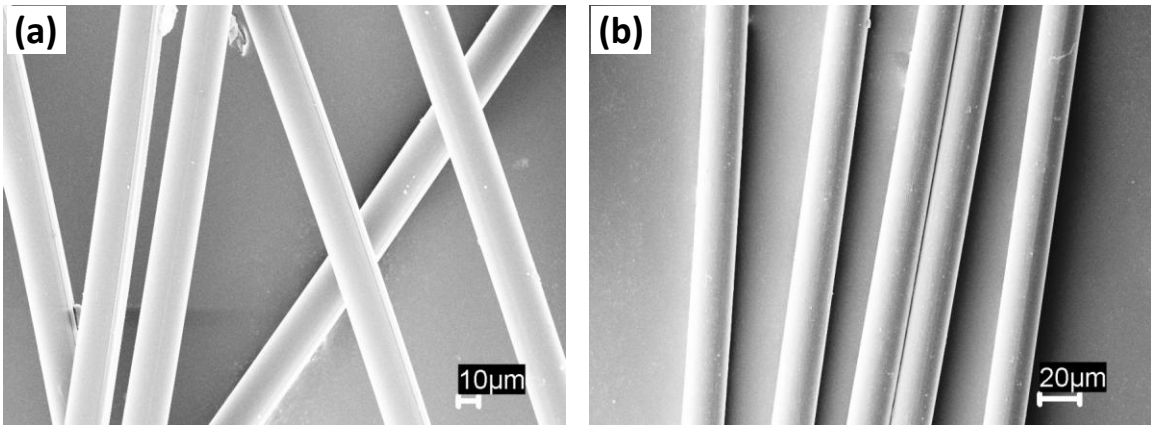

Figure 109. SEM images of the surfaces of (a) PEK and (b) PEK-g-1%FWNT fibers spun from high solid content solutions.

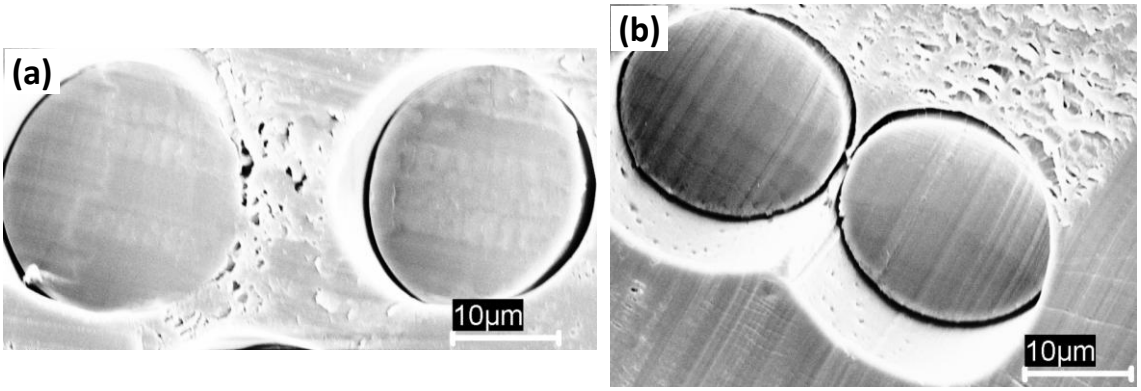

Figure 110. SEM images of the cross-sections of (a) PEK and (b) PEK-g-1%FWNT fibers spun from high solid content solutions.

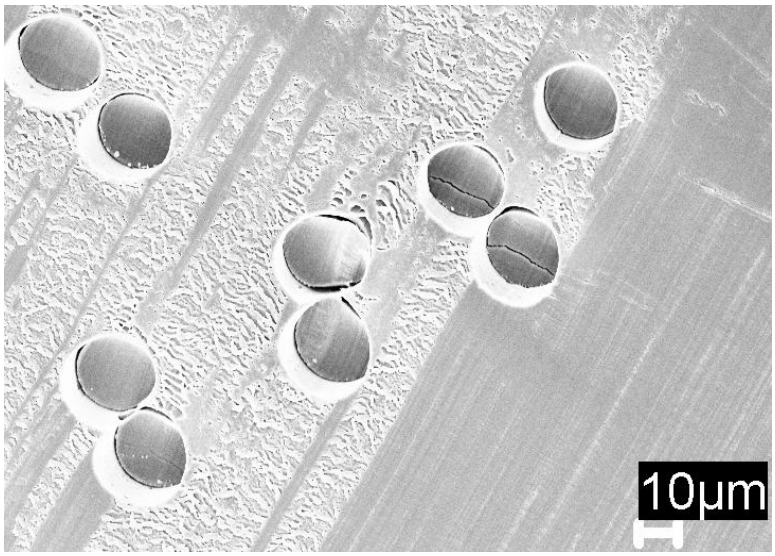

Figure 111. SEM images of the cross-sections of PEK-g-1%FWNT fibers. Some fibers appeared to be cracked in the direction perpendicular to the cutting direction.

7.2. Results and Discussion

The fibers were characterized using wide-angle X-ray diffraction (WAXD) to measure the crystallinity, crystal size, and orientation of PEK and CNTs. The CNT dispersion in the PEK matrix was studied using SEM. The composite fibers were evaluated for their tensile, thermal, thermo-mechanical, and electrical properties.

7.2.1. Thermogravimetric Analysis

PEK based fibers showed very high thermal stability and char yield. Figure 112 shows the PEK fibers with 1% CNT loading. The fibers showed very small degradation up to 550 ˚C and 55% char yield at 700 ˚C. The high thermal stability and char yield are important for high temperature applications. The high char yield makes PEK and PEK-CNT fibers an attractive candidate for precursor fiber for carbon fiber.

At higher CNT concentrations, the char yield was found to be affected by the CNT type and concentration. Figure 113 shows the TGA of 5% SWNT and 5, 10, and

20% FWNT containing PEK-g-CNT fibers. The PEK-g-5%SWNT fiber showed higher char yield than PEK and PEK-g-1%CNT fibers (61% vs. 55%). At 5% loading, the FWNT containing fibers showed a similar char yield (~54%) as control PEK and PEK-g-1%CNT fibers, but at higher loadings of 10 and 20%, the char yield reduced to 42 and 24%, respectively. Such a drastic decrease in char yield at 10 and 20% FWNT loading could be due to the defective fiber structure at such a high FWNT loading. As mentioned later, the defective structure at such high FWNT loadings also led to the decrease in mechanical properties of the fiber.

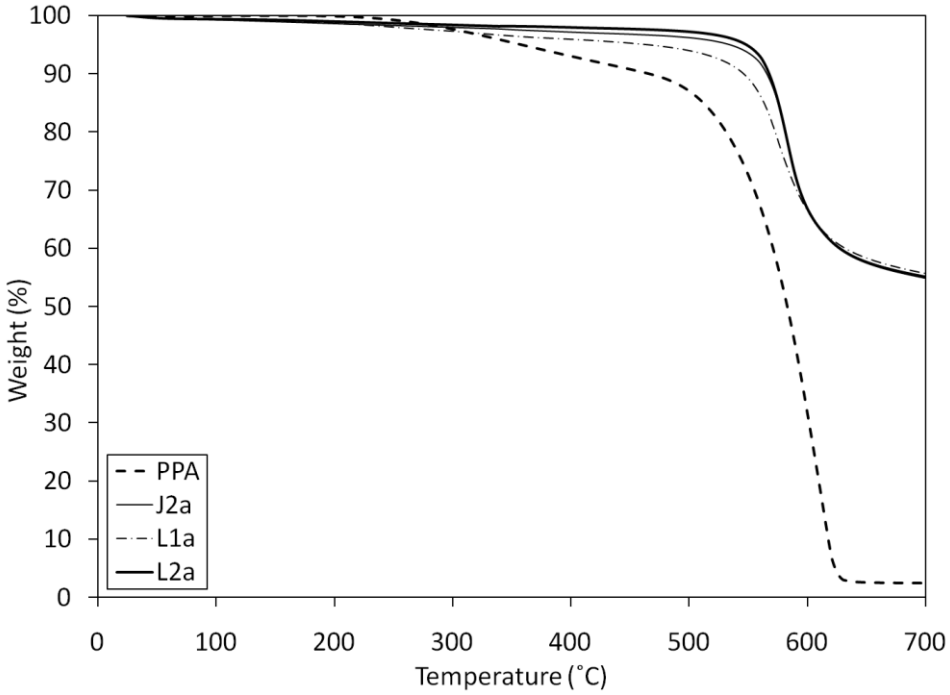

Figure 112. TGA (in nitrogen at a heating rate of 10 ˚C/min) of some of the PEK and PEK-g-1%CNT fibers listed in Table 32. TGA of PPA is also shown for comparison. The solvent PPA also shows very high thermal stability with almost no degradation up to 230 ˚C.

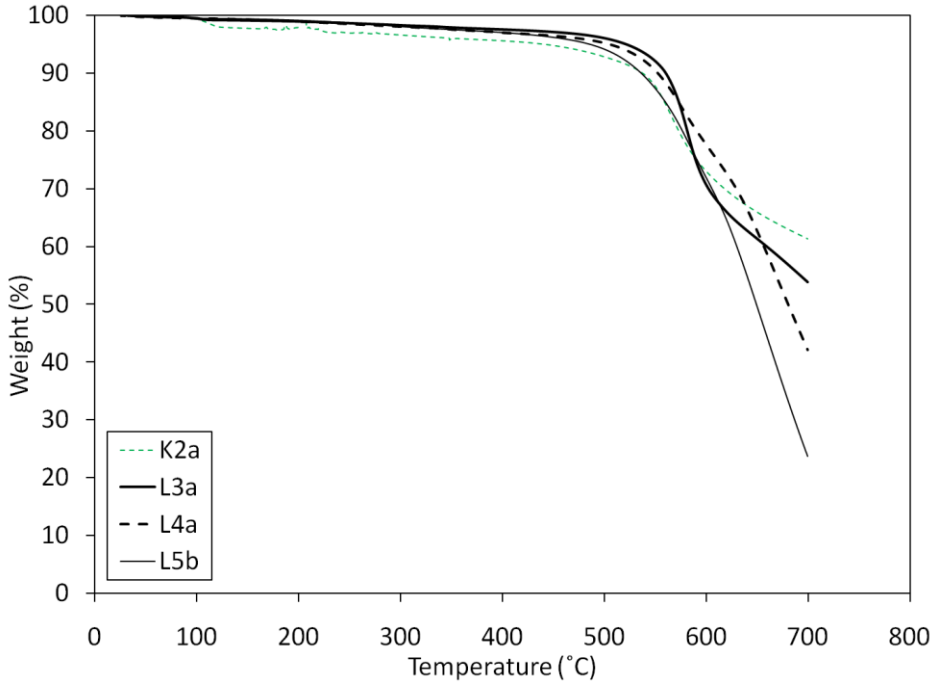

Figure 113. TGA (in nitrogen at a heating rate of 10 ˚C/min) of PEK-g-5%SWNT (K2a), PEK-g-5%FWNT (L3a), PEK-g-10%FWNT (L4a), and PEK-g-20%FWNT (L5b) fibers.

7.2.2. Differential Scanning Calorimetry

Figure 114 shows the DSC thermograms for PEK-g-5%FWNT fiber in both air and N_2 atmosphere. Similar curves were obtained for all other samples with and without different CNTs, the only difference being the little shift in position of peaks and amount of heat involved in exotherm and endotherm. The melting temperature and heat of endotherm and exotherm are listed in Table 38. In N_2, only an endothermic peak (melting) was observed at around 350-355 ˚C during first heating and a small endothermic peak during second heating. In air, a large exothermic peak was observed at around 290 ˚C followed by an endothermic peak at around 350-355 ˚C during first heating and a small endothermic peak during second heating. In air, for more than 5% CNT containing fibers, the exothermic peak became so strong and broad that it became difficult to separate the exotherm from melting endotherm at high temperature. DSC

curves for other PEK-g-CNT fibers are included in Appendix E. Takahashi *et al.* [9] observed the sharp crystallization exotherm at ~ 180 ˚C for the melt quenched PEK films. But they did not report whether DSC was conducted in N_2 or air and what heating rate they used. Since their films were melt-quenched, it is possible that it was purely recrystallization. The T_g for both control PEK and PEK-g-CNT fibers was observed at around 165 ˚C during first cooling and second heating in both N_2 and air. The T_g value reported by Takahashi *et al.* [9] (150 ˚C) was also lower than observed in our fibers and values reported by others (165 ˚C) [10].

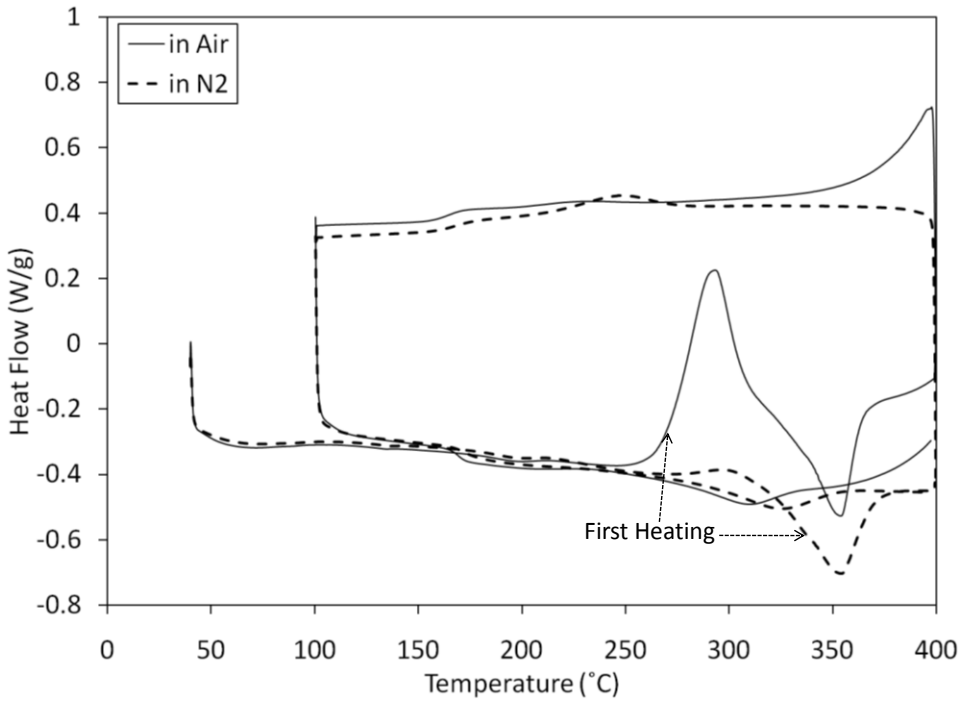

Figure 114. DSC thermograms (in nitrogen and air at a heating rate of 10 ˚C/min) of PEK-g-5%FWNT fiber (sample L3a in Table 38) for heat-cool-heat cycles. A positive heat flow (upwards) represents exotherm and a negative heat flow (downwards) represents endotherm. For all samples, the straight-line baseline was drawn between 250 ˚C and 380 ˚C.

Table 38. Physical, Thermal, and Mechanical Properties, and Structural Parameters of Various PEK-g-CNT Fibers

Sample	CNT (%)	CNT Type	Solid Content (%)	DR	Crystallinity (%)		FWHM (2θ~23°) (˚)	L_{PEK} (Å)			Tensile Strength (N/tex)	Tensile Modulus (N/tex)	Strain to Failure (%)	Toughness (J/g)	T_g (1Hz) (˚C)	Exotherm Heat (J/g)	Endotherm Heat (J/g)	T_m (˚C)	Electrical Conductivity (S/m)
					I	II		(16°)	(19°)	(23°)									
J1a	0	--	3.7	1.6	41	50	9.9	53	47	35	0.28±0.01	7.2±0.3	11±2	45±14	--	--	--	--	--
J2a	0	--	7.3	2.3	38	48	10.3	55	52	36	0.32±0.01	7.0±0.2	30±4	77±15	213	73	48	350	--
J2b	0	--	7.3	As spun	--	--	--	--	--	--	0.10±0.01	2.9±0.1	163±37	130±37	--	--	--	--	--
K1a	1	SWNT	7.3	2.3	45	54	8.9	57	51	35	0.35±0.01	8.9±0.3	9±2	23±8	221	80	24	343	$2.1x10^{-4}$
K2a	5	SWNT	7.3	2.1	34	46	11.0	75	53	35	0.29±0.01	8.6±0.5	25±3	60±9	--	85	24	355	$3.0x10^{-4}$
K2b	5	SWNT	7.3	As spun	--	--	--	--	--	--	0.13±0.02	4.7±0.4	122±30	122±19	--	--	--	--	--
L1a	1	FWNT	3.7	3	49	56	8.4	59	49	33	0.28±0.04	9.1±1.3	5±1	9±4	223	--	--	--	--
L2a	1	FWNT	7.3	2.7	42	51	10.6	50	50	37	0.33±0.01	7.3±0.3	30±4	79±12	210	93	41	347	--
L3a	5	FWNT	7.3	1.8	44	52	13.3	60	55	35	0.26±0.01	6.8±0.5	53±8	116±22	--	92	32 *(51)**	350	$2.1x10^{-4}$
L3b	5	FWNT	7.3	As spun	--	--	--	--	--	--	0.10±0.01	3.7±0.4	137±19	109±23	--	--	--	--	--
L4a	10	FWNT	7.3	3.7	42	--	12.3	44	54	39	0.25±0.01	9.4±0.7	18±3	37±8	--	--	--	--	25 ± 7
L5a	20	FWNT	7.3	1.1	--	--	--	--	--	--	0.08±0.01	11.3±0.9	3±1	2±1	--	--	--	--	240 ± 88
L5b	20	FWNT	7.3	As spun	--	--	--	--	--	--	--	--	--	--	--	--	--	--	--
M1a	1	MWNT	7.3	2	38	48	9.8	58	49	33	0.32±0.02	7.5±0.1	29±8	76±15	213	70	52 *(56)**	354	--
M2a	10	MWNT	7.3	2	26	--	15.5	43	50	38	0.13±0.01	5.2±0.3	24±8	27±11	--	--	--	--	$2.8x10^{-4}$

Crystallinity I and II were calculated from the WAXD integrated radial scans peaks between 2θ = 7 to 32˚ and 7 to 55˚, respectively. Except the one broadest peak between 2θ = 7 to 32˚ (which was considered as an amorphous peak), all other peaks were considered crystalline. FWHM was calculated from the azimuthal scan of the peak at 2θ = 23˚. The crystal size (L_{PEK}) was calculated using the peaks in equatorial scans at 2θ = 16˚, 19˚, and 23˚. The toughness was calculated from the area under the stress-strain curve in tensile test. T_g was measured from the peak position of tangent delta from DMA test. The standard deviation for electrical conductivity of K1a, K2a, L3a, and M2a are $6.4x10^{-6}$, $9.3x10^{-6}$, $5.9x10^{-6}$, and $1.3x10^{-5}$, respectively.

* *(values in parenthesis were obtained from experiments conducted in N_2 atmosphere)*

The exothermic peak could have originated due to secondary chain extension (polymerization) of PEK in air. The possibility of crystallization is ruled-out because such an exotherm was not observed in N_2 atmosphere. The observed exotherm could be due to cross-linking in the polymer, but it could not be verified. In another experiment, the PEK and PEK-g-CNT samples were only heated to 310 ˚C in both N_2 and air and retrieved for WAXD studies. The samples were heated only up to 310 ˚C because melting endotherm started above that temperature (Figure 114). Samples from both N_2 and air showed no significant change in crystallinity but showed larger crystal size. The WAXD and FTIR studies of DSC retrieved samples are discussed in later sections.

7.2.3. WAXD Studies

PEK has an orthorhombic crystal structure with lattice parameters a = 7.63 Å, b = 5.96 Å, and c = 10 Å [10-12]. All PEK based fibers were studied for PEK crystallinity, orientation and crystal size. Figure 115 shows the WAXD patterns of PEK-g-CNT fibers with different CNTs at 1% loading. Figure 116 shows the corresponding integrated radial and equatorial scans. Figure 117 shows the WAXD patterns of PEK-g-CNT fibers with high CNT loading. Figure 118 shows the corresponding integrated radial and equatorial scans. The fibers made from low and high solid containing solutions of control PEK and PEK-g-1%FWNT were also compared. Their respective integrated radial and equatorial scans are shown in Figure 119. The crystallinity, crystal size, and orientation (FWHM) of PEK for these different fibers are listed in Table 38.

In general, the fibers spun from low solid content (3.7%) showed higher PEK orientation (lower FWHM), than fibers spun from high solid content. In general, for a

particular CNT, the PEK orientation was found to be decreased with increased CNT loading. Different types of CNTs at different loadings did not have any particular effect on the crystal size of PEK. In general, for a particular CNT, the crystallinity was found to be decreased with increased amount of CNTs in the PEK-g-CNT fibers. This could be due to the fact that, in high CNT content fibers, a larger number of shorter PEK chains are grafted on to CNTs, which reduces the number of free PEK chains for crystallization.

CNT peak (from 002 plane) was not observed for any CNT at 1% loading in the fiber. At higher loadings (≥5%), the CNT peak was visible at $2\theta \sim 26^{\circ}$, but still was difficult to resolve from the overlapping PEK intensity in that region. Therefore, the CNT orientation in PEK-g-CNT fibers was evaluated from the Raman G-band intensity ratio. As described in Appendix D, the G-band intensity decreases as the CNT alignment deviates from the polarization of the incident light. Therefore, the CNT alignment in fiber can be evaluated by comparing the G-band intensity when the fiber is parallel (I_0) to the polarization direction of incident light and when it is perpendicular (I_{90}). The higher the I_0/I_{90} ratio, higher is the degree of CNT alignment in fiber axis direction. At 1% loading, no Raman intensity was observed for the CNT containing fibers. It appeared that PEK suppressed the CNT resonance enhanced Raman intensity.

For PEK-g-5%SWNT, PEK-g-5%FWNT, PEK-g-10%FWNT, and PEK-g-20%FWNT fibers, the I_0/I_{90} were ~ 7, 4, 5, and 4 respectively. These values are in the same trend as with the PEK orientation (FWHM) determined from the WAXD. The PEK orientation in PEK-g-5%SWNT was higher than in PEK-g-5%FWNT, PEK-g-10%FWNT. Also, the PEK orientation in PEK-g-10%FWNT (DR 3.7) was higher than in PEK-g-5%FWNT (DR 1.8).

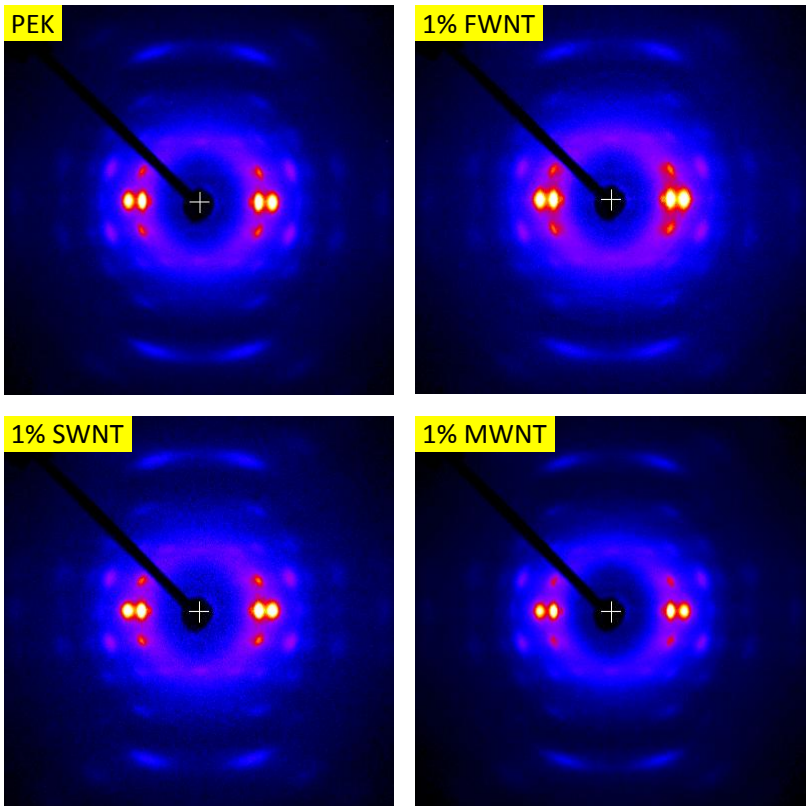

Figure 115. WAXD patterns of PEK (J2a), PEK-g-1%FWNT (L2a), PEK-g-1%SWNT (K1a), and PEK-g-1%MWNT (M1a) fibers.

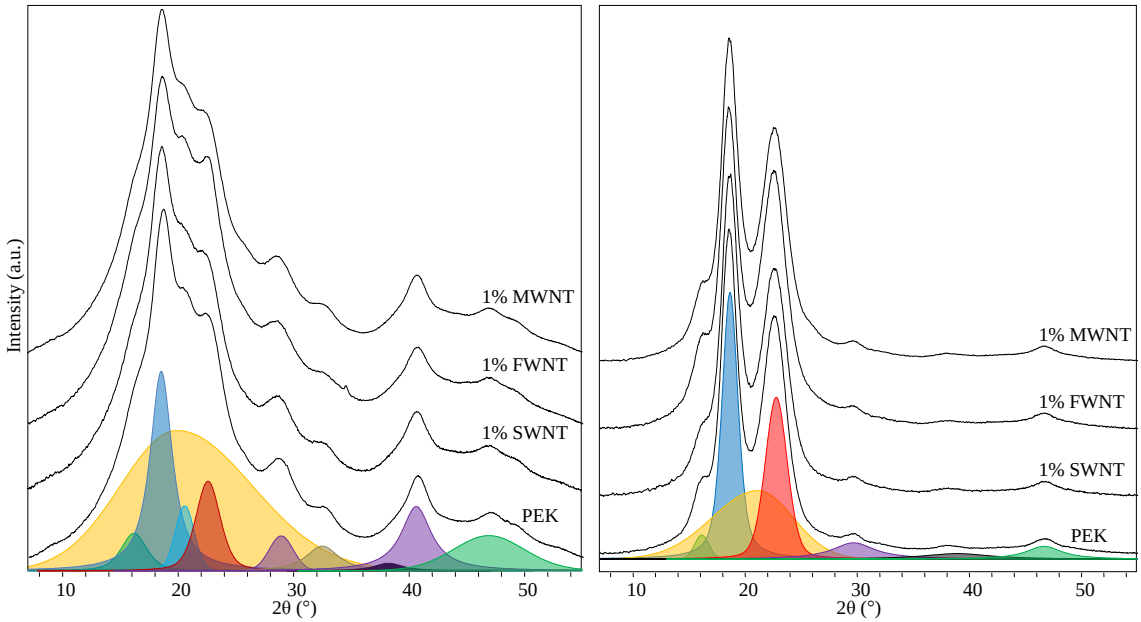

Figure 116. Integrated radial (left) and equatorial (right) scans of PEK (J2a), PEK-g-1%FWNT (L2a), PEK-g-1%SWNT (K1a), and PEK-g-1%MWNT (M1a) fibers. The representative deconvoluted profiles are also shown.

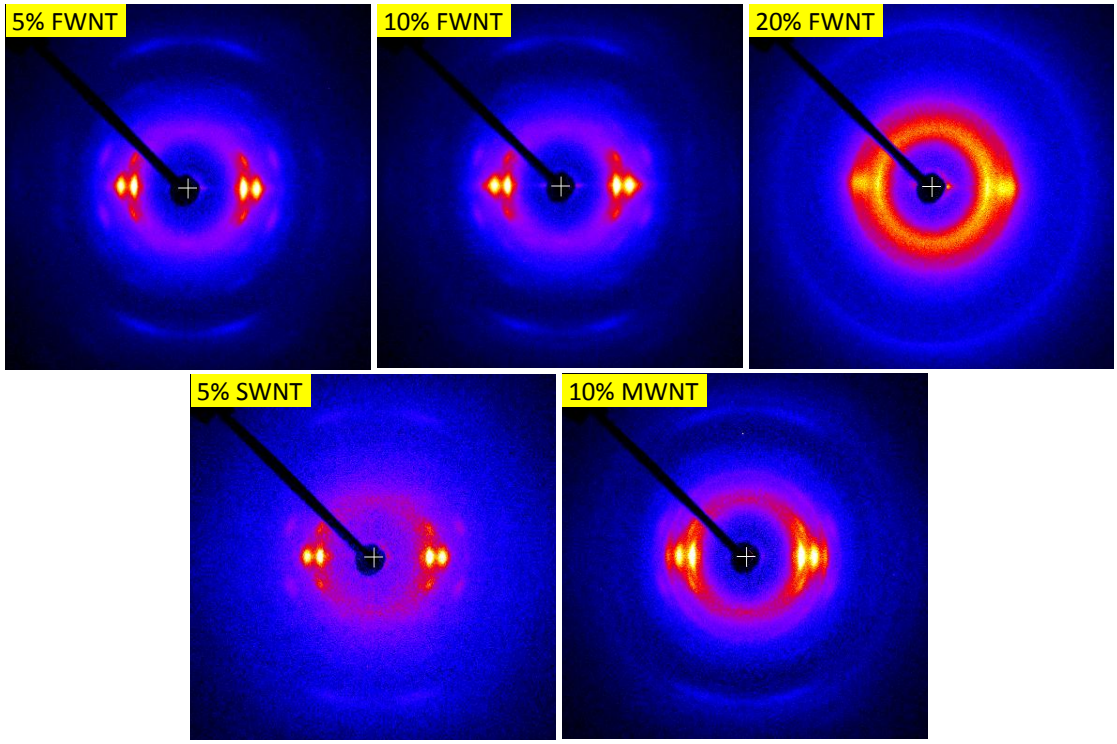

Figure 117. WAXD patterns of PEK-g-5%FWNT (L3a), PEK-g-10%FWNT (L4a), PEK-g-20%FWNT (L5a), PEK-g-5%SWNT (K2a), and PEK-g-10%MWNT (M2a) fibers.

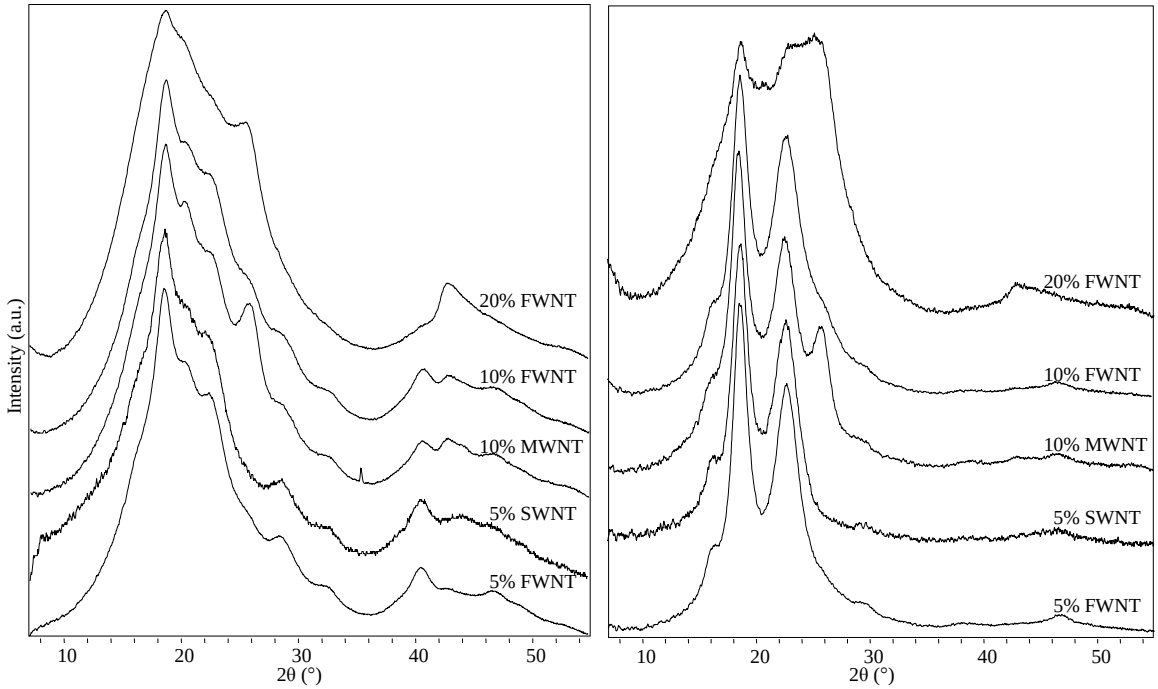

Figure 118. Integrated radial (left) and equatorial (right) scans of PEK-g-5%FWNT (L3a), PEK-g-10%FWNT (L4a), PEK-g-20%FWNT (L5a), PEK-g-5%SWNT (K2a), and PEK-g-10%MWNT (M2a) fibers.

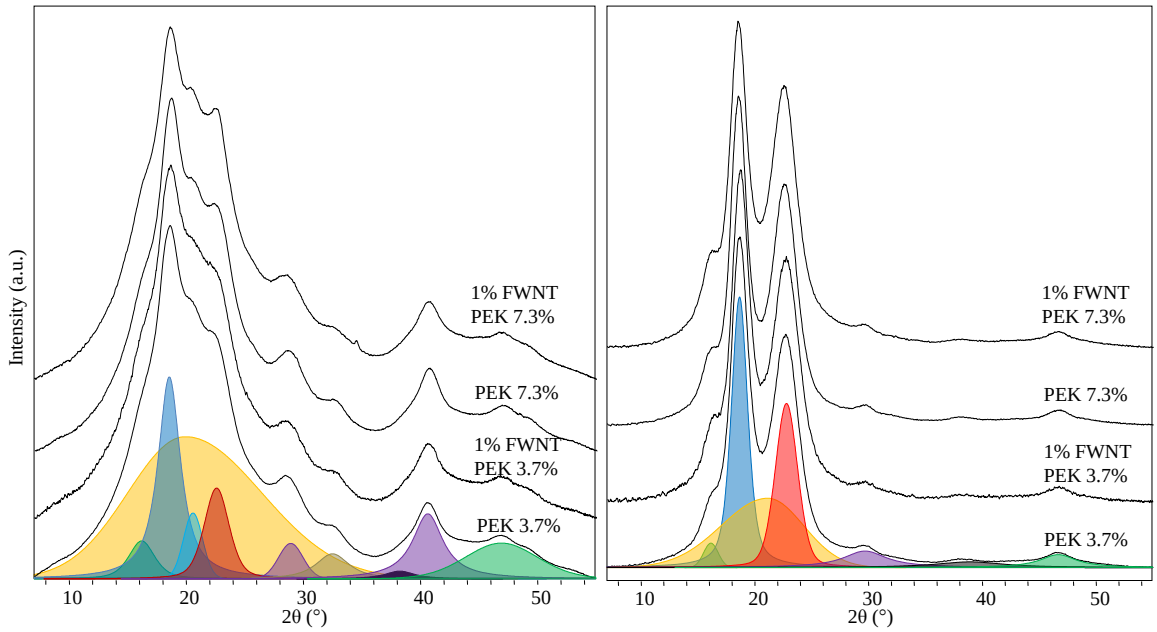

Figure 119. Integrated radial (left) and equatorial (right) scans of PEK (J1a and J2a) and PEK-g-1%FWNT (L1a and L2a) fibers spun from low (3.7%) and high (7.3%) solid solutions. The representative deconvoluted profiles are also shown.

7.2.4. Tensile Properties

The tensile properties of all the fibers are listed in Table 38. For fibers spun from high solid content solutions (7.3%), both PEK and PEK-g-1%CNT fibers showed similar tensile strength, modulus and strain to failure. The 1% SWNT containing fibers showed high tensile strength and modulus and lower strain to failure than other fibers. Compared to fibers spun from high solid content, fibers spun from low solid content showed lower strain to failure. Among various heat-drawn fibers, the 5% FWNT containing fiber showed the highest strain to failure of about 53%. The typical stress-strain curves of some of the fibers listed in Table 38 are shown in Figure 120. The PEK fibers turned out to be very tough and showed toughness values (up to ~ 130 J/g) that surpassed other high performance fibers including Kevlar® (~ 30-45 J/g) [1-3] and Zylon® (~ 50 J/g) [1, 4, 5]. The toughness values of PEK and PEK-g-CNT fibers are also listed in Table 38. The

tensile fractures of control PEK and PEK-g-1%FWNT are shown in Figure 121. In general, other PEK-g-CNT fibers showed a similar failure as PEK-g-1%FWNT fiber. Figure 122 shows the FWNTs in the tensile fracture surface of the PEK-g-10%FWNT fiber.

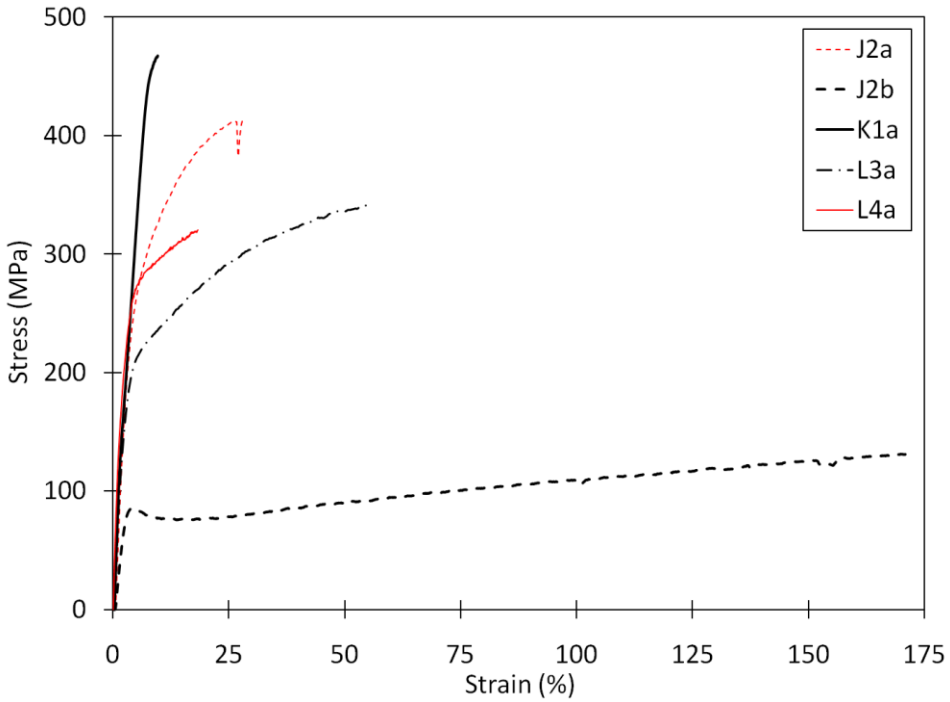

Figure 120. Typical stress-strain curve of some of the PEK and PEK-g-CNT fibers listed in Table 38.

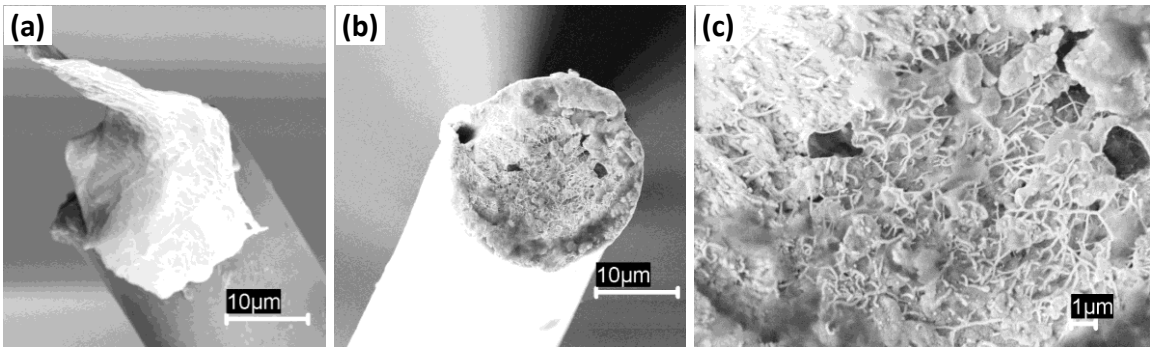

Figure 121. SEM images of the tensile fracture surfaces of (a) PEK (J2a) and (b) PEK-g-1%FWNT (L2a) fibers spun from high solid content solutions. High magnification image (c) shows the FWNTs at the fracture surface of PEK-g-1%FWNT (L2a).

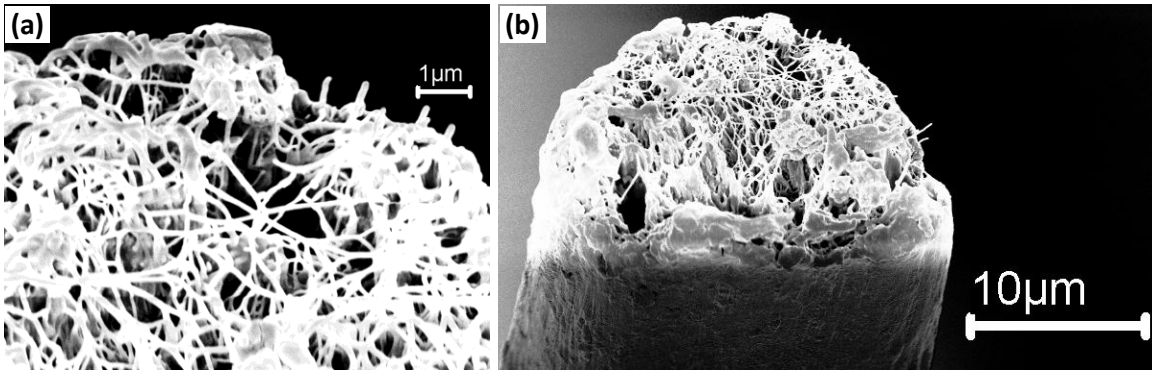

Figure 122. SEM images of the tensile fracture surfaces of PEK-g-10%FWNT (L4a) fibers.

7.2.5. Dynamic Mechanical Analysis

The storage modulus and tan δ curves of different PEK-g-CNT fibers are shown in Figures 123 and 124, respectively. The T_g values measured from the tan δ peak are listed in Table 38. The PEK based fibers showed high modulus retention even above T_g. The storage moduli and tan δ of various PEK and PEK-g-CNT fibers showed similar behavior. However, the fibers containing 5% or more CNT showed tan δ curve with no clear peak for T_g (Figure 124). For example, the tan δ for PEK-g-5%SWNT increased at around T_g of PEK, but it never decreased after that and for PEK-g-10%FWNT, it kept increasing with increasing temperature. The similar behavior was observed by Sreekumar *et al.* [13] in PAN/SWNT fibers containing 10 wt.% SWNT.

The PEK-g-5%FWNT sample showed unusual decrease in storage modulus at around 100 ˚C (Figure 125), but it again increased after 140 ˚C. There could be several reasons for this behavior. For example, there could be moisture in the fiber that got removed between 100-130 ˚C, or there could be crystallization at 130 ˚C, which could cause the modulus to increase. Actually, both of these possibilities are ruled-out because no mass loss (corresponding to moisture) was observed in TGA study and no

crystallization exotherm was observed in that temperature range in DSC study. It is possible though that there could be stress-induced crystallization, which could occur while the sample is under tension in DMA and would not occur in DSC.

When second DMA run was conducted on the same sample (Figure 125), it did not show any decrease in storage modulus and showed a usual behavior as shown by other PEK-g-CNT samples. The tan δ curve was found to be shifted to the right, which suggests that elastic component of the viscoelastic fiber increased after first DMA run. This sample after DMA test was further investigated using WAXD. Figures 126, 127, and 128 show the WAXD patterns, integrated radial and equatorial scans, and azimuthal scans of PEK-g-5%FWNT fiber before and after DMA test. Though the overall crystallinity was found to be the same, the crystal size was found to be increased by nearly 40% (Table 39) after the DMA test. The PEK orientation was also found to be improved after DMA test (Figure 128 and Table 39).

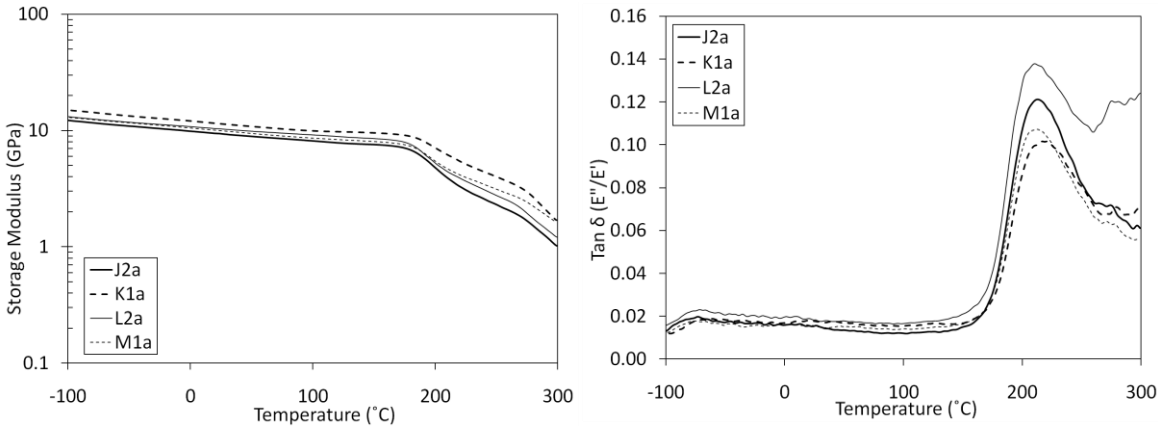

Figure 123. Storage moduli and tan δ of PEK and PEK-g-1%CNT fibers at 1 Hz.

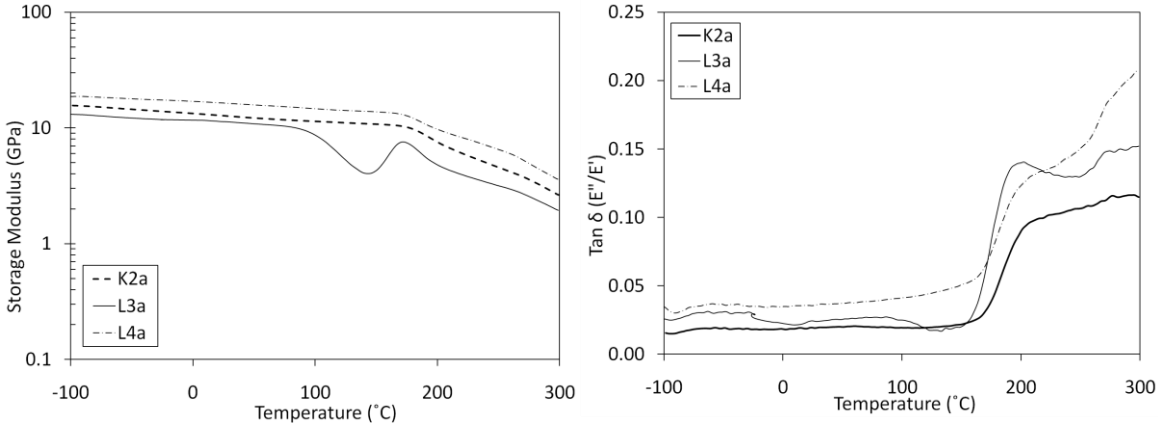

Figure 124. Storage moduli and tan δ of PEKg-5%SWNT (K2a), PEK-g-5%FWNT (L3a), and PEK-g-10%FWNT (L4a) fibers at 1 Hz.

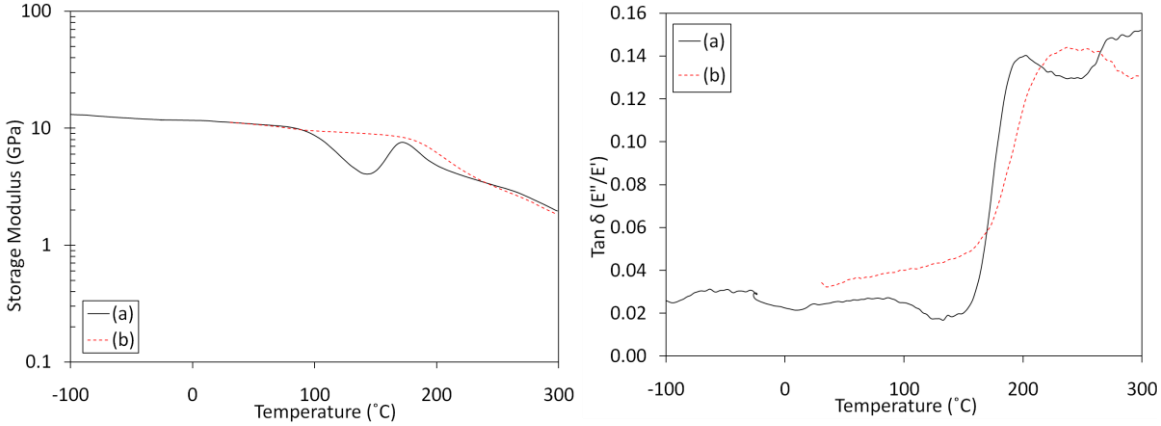

Figure 125. Storage moduli and tan δ of PEK-g-5%FWNT fiber (L3a) at 1 Hz. The curve represented by dashed line (b) was for the second DMA run on the same sample (a).

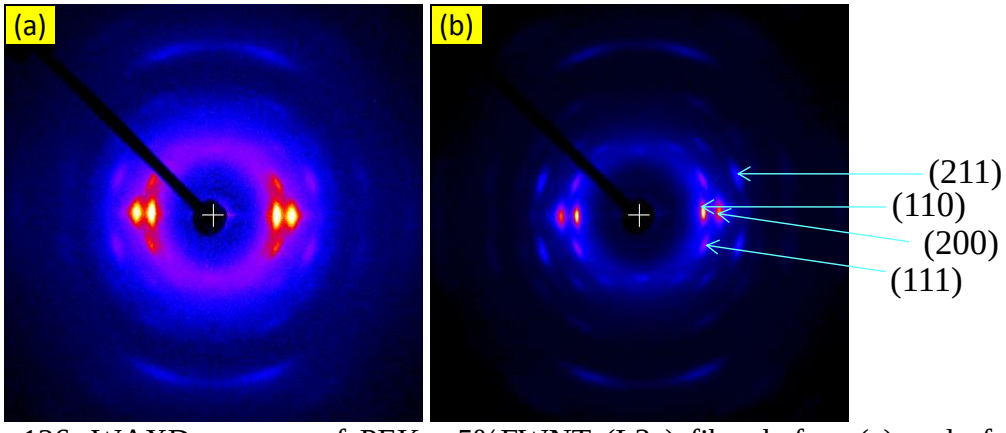

Figure 126. WAXD patterns of PEK-g-5%FWNT (L3a) fiber before (a) and after (b) DMA test.

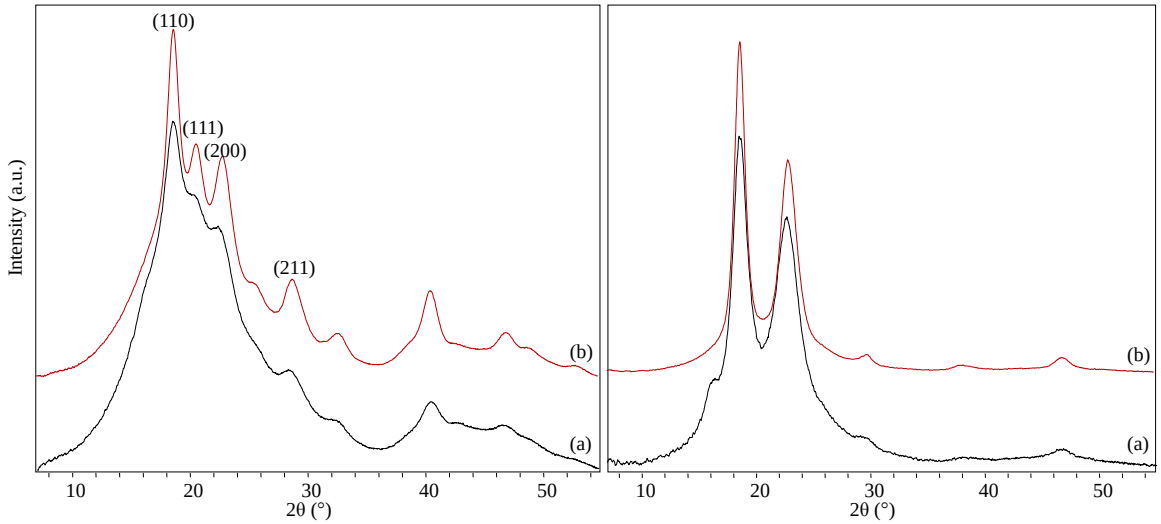

Figure 127. Integrated radial (left) and equatorial (right) scans of PEK-g-5%FWNT (L3a) fiber before (a) and after (b) DMA test.

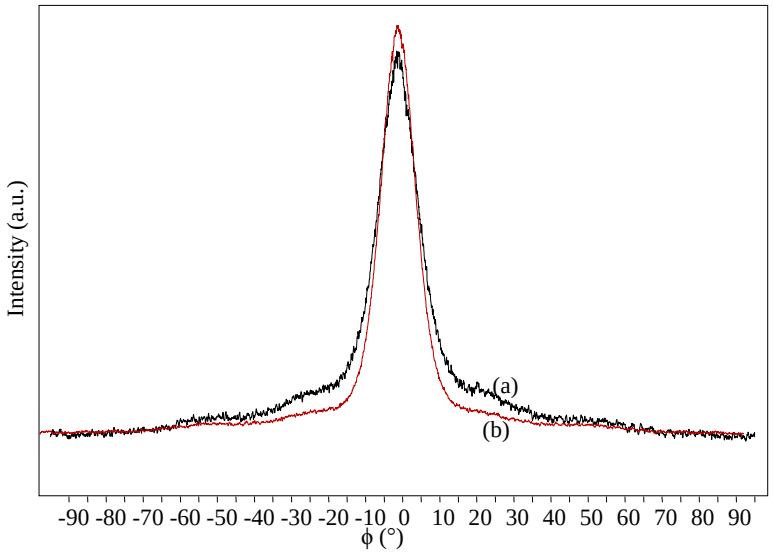

Figure 128. Azimuthal scans of 2θ = 23˚ peak of PEK-g-5%FWNT (L3a) fiber before (a) and after (b) DMA test.

Table 39. Crystalline Information of PEK-g-5%FWNT (L3a) Fibers before (a) and after (b) DMA Test

Sample	Crystallinity (I) (%)	Crystallinity (II) (%)	FWHM (2θ~23°) (˚)	L_{PEK} (2θ~16°) (Å)	L_{PEK} (2θ~19°) (Å)	L_{PEK} (2θ~23°) (Å)
(a)	44	52	13.3	60	55	35
(b)	44	53	11.1	--	74	50

Crystallinity I and II were calculated from the WAXD integrated radial scans peaks between 2θ = 7 to 32˚ and 7 to 55˚, respectively. FWHM was calculated from the azimuthal scan of the peak at 2θ = 23˚. The crystal size (L_{PEK}) was calculated using the peaks in equatorial scans at 2θ = 16˚, 19˚, and 23˚.

7.2.6. Thermomechanical Analysis

The thermal shrinkage of PEK fiber was studied using TMA under very low load in both air and N_2 atmosphere. The fiber showed almost no shrinkage up to 200 ˚C and shrank almost 6% up to 340 ˚C (Figure 129). A large shrinkage (of about 30%) was observed around the melting peak of PEK (after 350 ˚C), during which the PEK chain molecules go from an oriented state to an unoriented state. No meaningful data could be collected beyond 380 ˚C.

The thermal shrinkage of PEK-g-CNT fibers was studied using TMA in N_2 atmosphere. The fibers showed almost no shrinkage up to 180 ˚C and shrank less than 5% (Figure 130). Due to relatively higher tension during testing, the fibers showed expansion above the melting point of PEK (~ 350 ˚C). The PEK-g-5%FWNT fiber showed almost no shrinkage and expansion up to almost 300 ˚C. The PEK-g-20%FWNT fiber showed no shrinkage or expansion up to 190 ˚C, above which it showed a large expansion. This could be due to the fact that PEK-g-20%FWNT fiber had lower draw ratio and consequently there were no internal forces for entropic thermal shrinkage. An initial lower draw ratio (DR ~ 1.1) can also be the reason for large expansion observed for PEK-

g-20%FWNT fiber. In case of high CNT content in the fiber, the polymer chain entanglement is expected to reduce with increase in CNT content. However, this is true only when there is a good interaction between polymer and CNT or when the polymer is grafted on to CNT walls. In the PEK-g-20%FWNT, the polymer chain entanglements are relatively lower; this can induce polymer chain slippage above the T_g of PEK, which could be another reason for higher expansion observed for PEK-g-20%FWNT fiber (Figure 130).

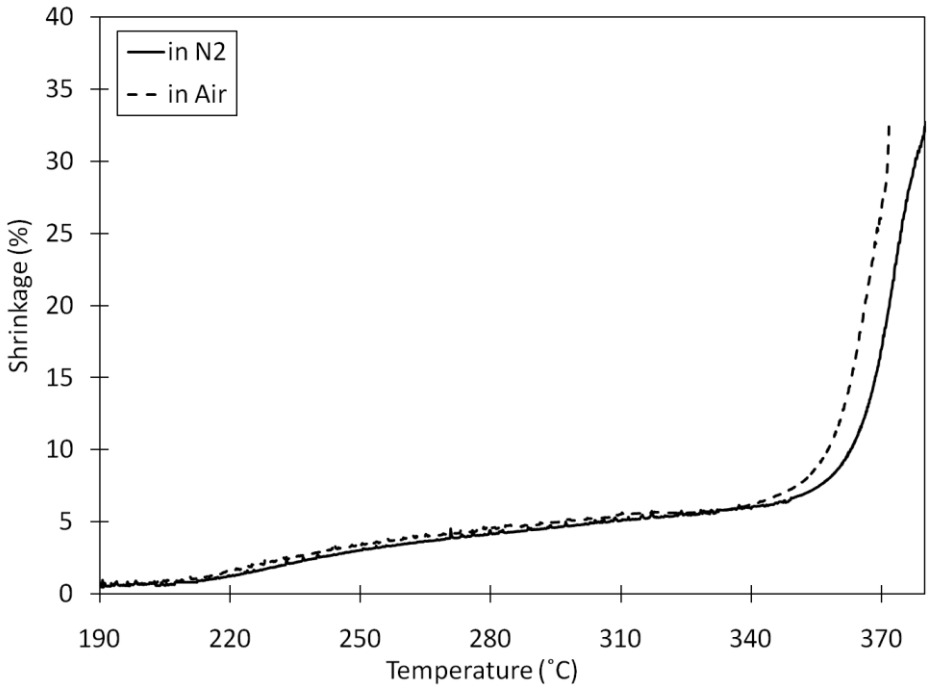

Figure 129. Thermal shrinkage of PEK fiber (J2a) in air and N_2 measured using TMA (air/N_2 flow rate: 50 ml/min; temperature ramp rate: 10 ˚C/min; preload: 0.0008 N/tex).

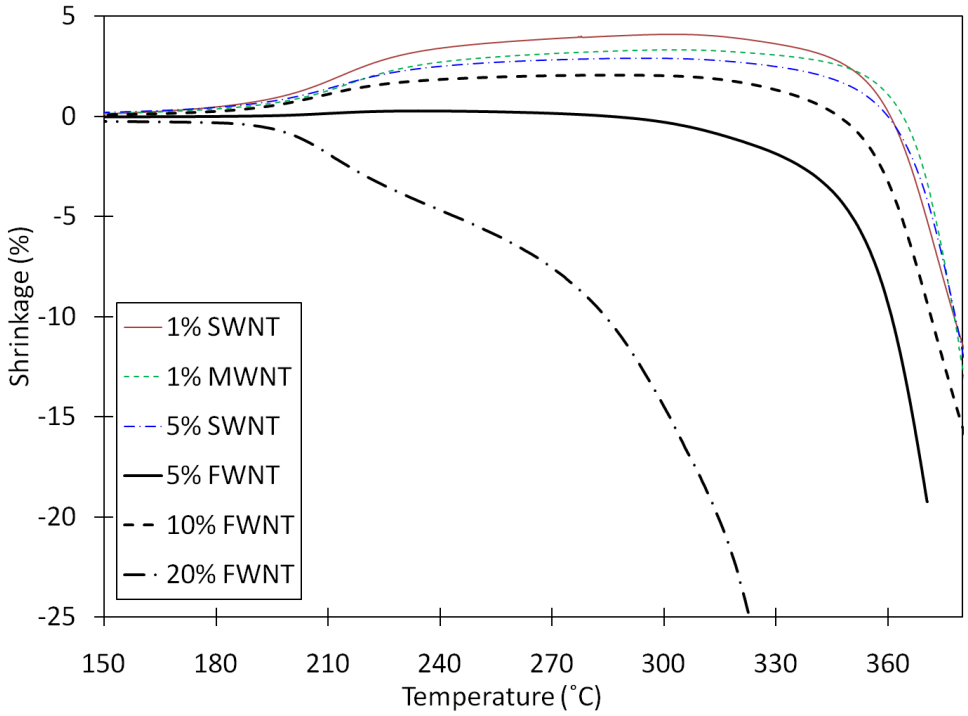

Figure 130. Thermal shrinkage of PEK-g-CNT fibers in N_2 measured using TMA (N_2 flow rate: 50 ml/min; temperature ramp rate: 10 ˚C/min; preload: 0.0094 N/tex). 1%SWNT: (K1a), 1%MWNT: (M1a), 5%SWNT: (K2a), 5%FWNT: (L3a), 10%FWNT: (L4a), 20%FWNT: (L5a). A negative shrinkage represents thermal expansion.

To find the conditions for fiber annealing or stabilization and to see if, during heating, the fiber will generate so much thermal stress that it might break, the thermal stresses were also studied in both air and N_2 using TMA. Figure 131 shows the thermal stresses as a function of temperature for PEK-g-CNT fibers. Among the studied fibers, in both air and N_2, PEK and PEK-g-1%FWNT showed little or no stress generation during heating and PEK-g-1%SWNT and PEK-g-1%MWNT showed significant stress generation of up to 60-70 MPa. The thermal stresses peaked at around the T_g of PEK between 200 and 240 ˚C. Due to softening near the melting of PEK, no meaningful data could be obtained after 320 ˚C.

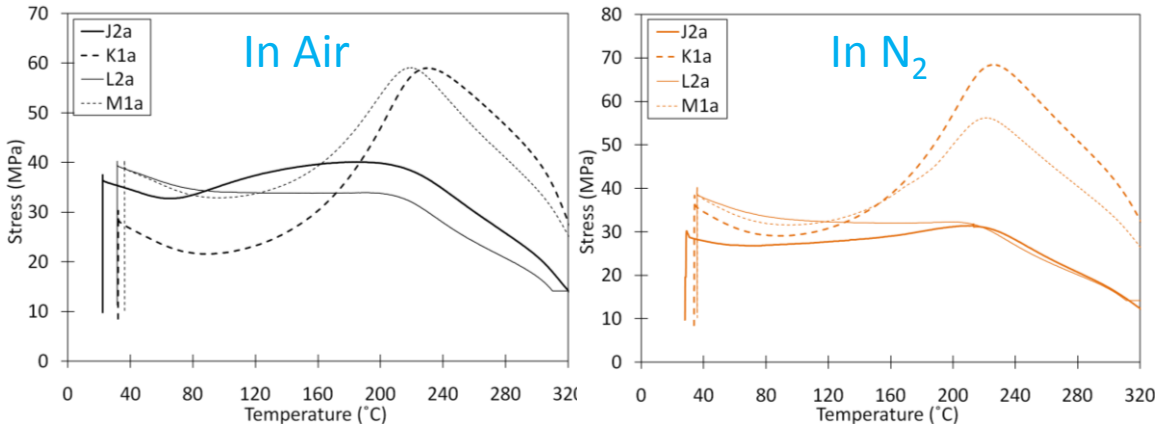

Figure 131. Thermal stress generation in PEK and PEK-g-1%CNT fibers (Table 37) as a function of temperature. The initial stress (of about 30-40 MPa) corresponds to the initially applied isostrain. This stress is relaxed up to around 80 ˚C and the further increase in this stress is the thermal stress of interest. (gas flow rate: 50 ml/min; temperature ramp rate: 10 ˚C/min; isostrain: 0.3%).

7.2.7. Electrical Conductivity of PEK-g-CNT Fibers

The electrical conductivity of various PEK-g-CNT fibers is listed in Table 37. Even at 5% loading, both SWNT and FWNT containing fibers showed very low electrical conductivity of the order of 2-3x10^{-4} S/m. Similar level of conductivity was observed with 10% MWNT containing PEK fibers. The electrical conductivity of 10% FWNT containing fiber was around 25 S/m, which further increased to 240 S/m at 20% FWNT loading. A 5 order magnitude increase in electrical conductivity with an increase in FWNT concentration from 5 to 10% suggests that percolation threshold for FWNT in PEK-g-FWNT fibers is somewhere between 5 and 10%. To our knowledge, there is no other fiber which has an electrical conductivity of 25 S/m and a toughness of around 37 J/g. This makes the PEK-g-10%FWNT fiber with unique combination of properties.

7.2.8. Charring of PEK and PEK-g-FWNT Fibers

The PEK based fibers were charred to ascertain the stability of PEK fibers and to see if the fibers retain their shape after charring. These factors are important from the point of view of evaluating PEK as a potential precursor for carbon fiber. The PEK and PEK-g-1%FWNT fibers were placed in a crucible in a box furnace and heated up to 700 ˚C in argon at a heating rate of 10 ˚C/min. Figures 132 and 133 show the fiber surfaces and Figures 134 and 135 show the cross-sections of PEK and PEK-g-1%FWNT fibers after charring. The fibers surfaces appeared to be smooth and fiber cross-sections retained their circularity. The fibers were found to shrink in the longitudinal direction and expand in the lateral direction. The longitudinal shrinkage was almost 60% and 50% for PEK and PEK-g-1%FWNT fibers, respectively. Such a large shrinkage is due to the fact that fibers were not constrained and were allowed to shrink freely. The PEK and PEK-g-1%FWNT fibers expanded laterally by almost 65% and 44%, respectively.

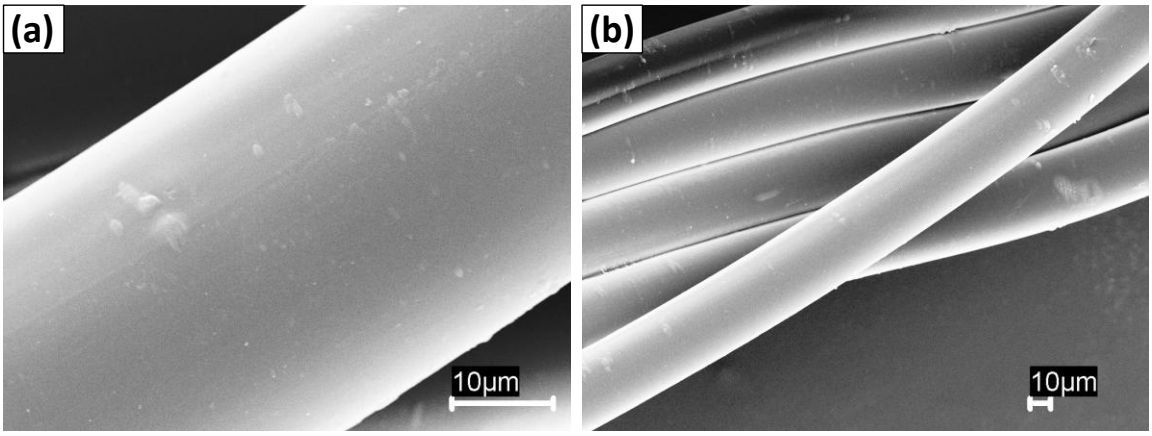

Figure 132. SEM images of the PEK fiber (J2a) surface after charring in argon at 700 ˚C.

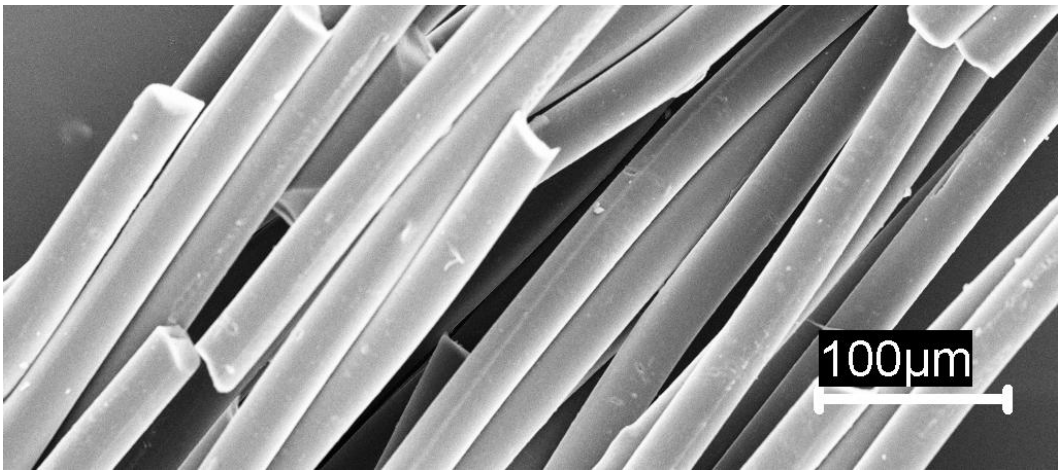

Figure 133. SEM image of the PEK-g-1%FWNT fiber (L2a) surface after charring in argon at 700 ˚C.

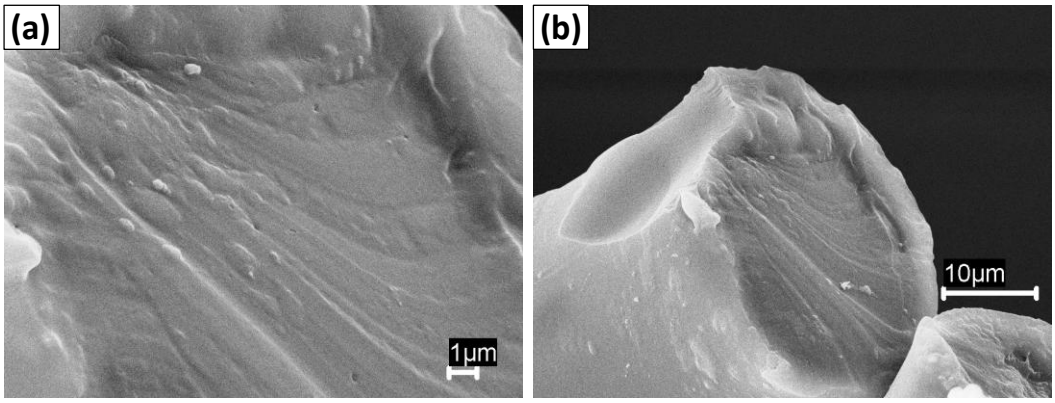

Figure 134. SEM images of the PEK fiber (J2a) cross-section after charring in argon at 700 ˚C.

From the volume calculations of the fibers before and after charring, it was found that fiber volume increased by almost 9% and 4% for PEK and PEK-g-1%FWNT fibers, respectively. This is despite the fact that TGA showed almost 45% weight loss for both PEK and PEK-g-1%FWNT fibers. This increase in volume with accompanied weight loss suggests that both PEK and PEK-g-1%FWNT fibers became porous after charring. Since the increase in volume was higher for control PEK fiber, the control PEK fiber is more porous than PEK-g-1%FWNT composite fiber.

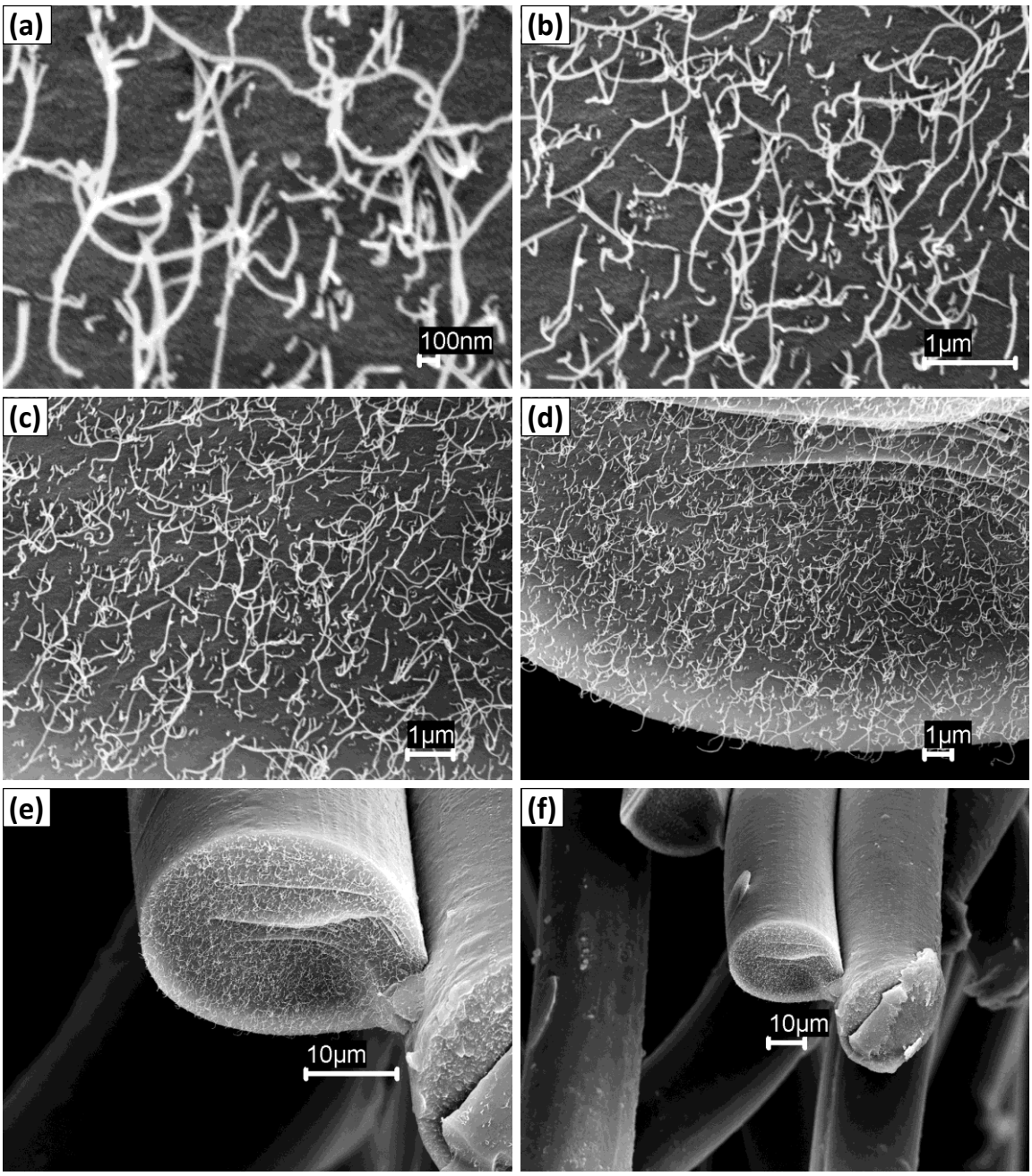

Figure 135. SEM images of the PEK-g-1%FWNT fiber (L2a) cross-section after charring in argon at 700 ˚C.

7.2.9. State of CNT Dispersion in PEK-g-CNT Fibers

The SEM images of cross-sections of charred PEK-g-1%FWNT fiber can also be used to study the dispersion of FWNTs in composite fiber. Figure 135 shows that

FWNTs are fairly uniformly dispersed. The PEK-g-FWNT fibrils showed diameters ranging from 20-40 nm, which is much higher than the original FWNT diameter of around 2-4 nm. This suggests that PEK was successfully grafted on to the CNT walls and in this case, created a coating of around 8-19 nm thickness.

The CNT dispersion in different PEK-g-CNT fibers was also studied from the SEM images of the microtomed fiber cross-sections. Figure 136 shows the fiber cross-sections of 1 and 5% SWNT and FWNT containing fibers. Though no SWNTs could be observed in the SEM images, a uniform dispersion of FWNTs was observed in both 1 and 5% FWNT containing fibers. Generally, SWNT agglomerates (if there are any) can be observed in SEM images at the magnifications shown here. Since no SWNT agglomerates were observed in the SEM images, it seems that SWNTs are uniformly dispersed in the PEK matrix. The PEK-g-5%SWNT and PEK-g-5%FWNT fibers cross-sections also showed uniformly distributed voids of the order of <50 nm.

It was noted that PEK/CNT fibers when exposed to the electron beam in SEM for even few seconds at a voltage around 5 kV showed degradation (arrows pointing toward dark square regions in Figures 136 and 137). No such degradation was observed in case of PAN based fibers under similar imaging conditions. This suggests that the radiation resistance of PEK polymer is significantly lower (or radiation sensitivity is higher) than that of PAN.

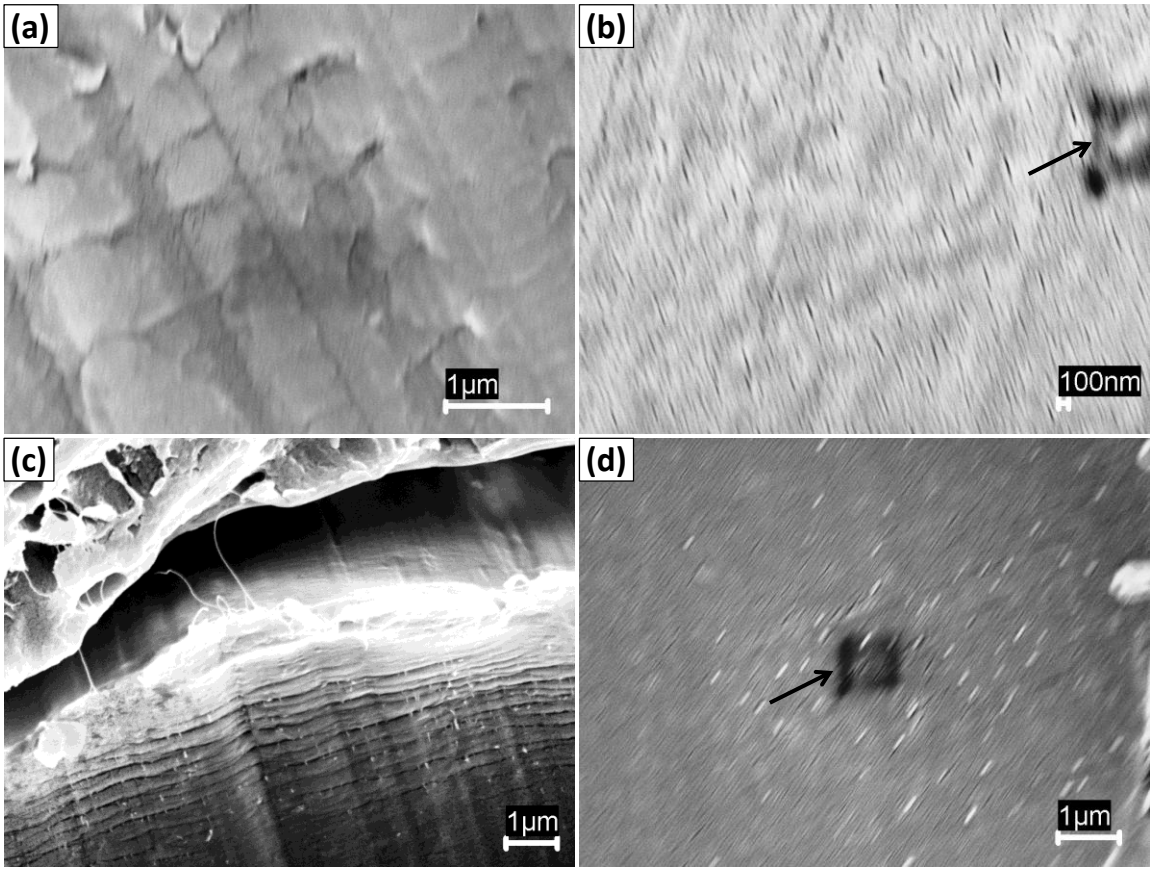

Figure 136. SEM images of the cross-sections of (a) PEK-g-1%SWNT (K1a), (b) PEK-g-5%SWNT (K2a), (c) PEK-g-1%FWNT (L2a), and (d) PEK-g-5%FWNT (L3a) fibers. The arrows point toward degraded PEK.

Figure 137 shows the fiber cross-sections of 1 and 10% MWNT containing fibers. At 1% loading, the MWNTs appeared to be uniformly dispersed. However, at 10% loading, some of the MWNT agglomerated regions could be observed in the SEM images of fiber cross-sections. For different types of CNTs, at 5% loading and higher, the fiber cross-sections also showed the presence of small voids. These voids are detrimental to the mechanical properties of the fibers, but a uniformly porous structure may be advantageous for other applications.

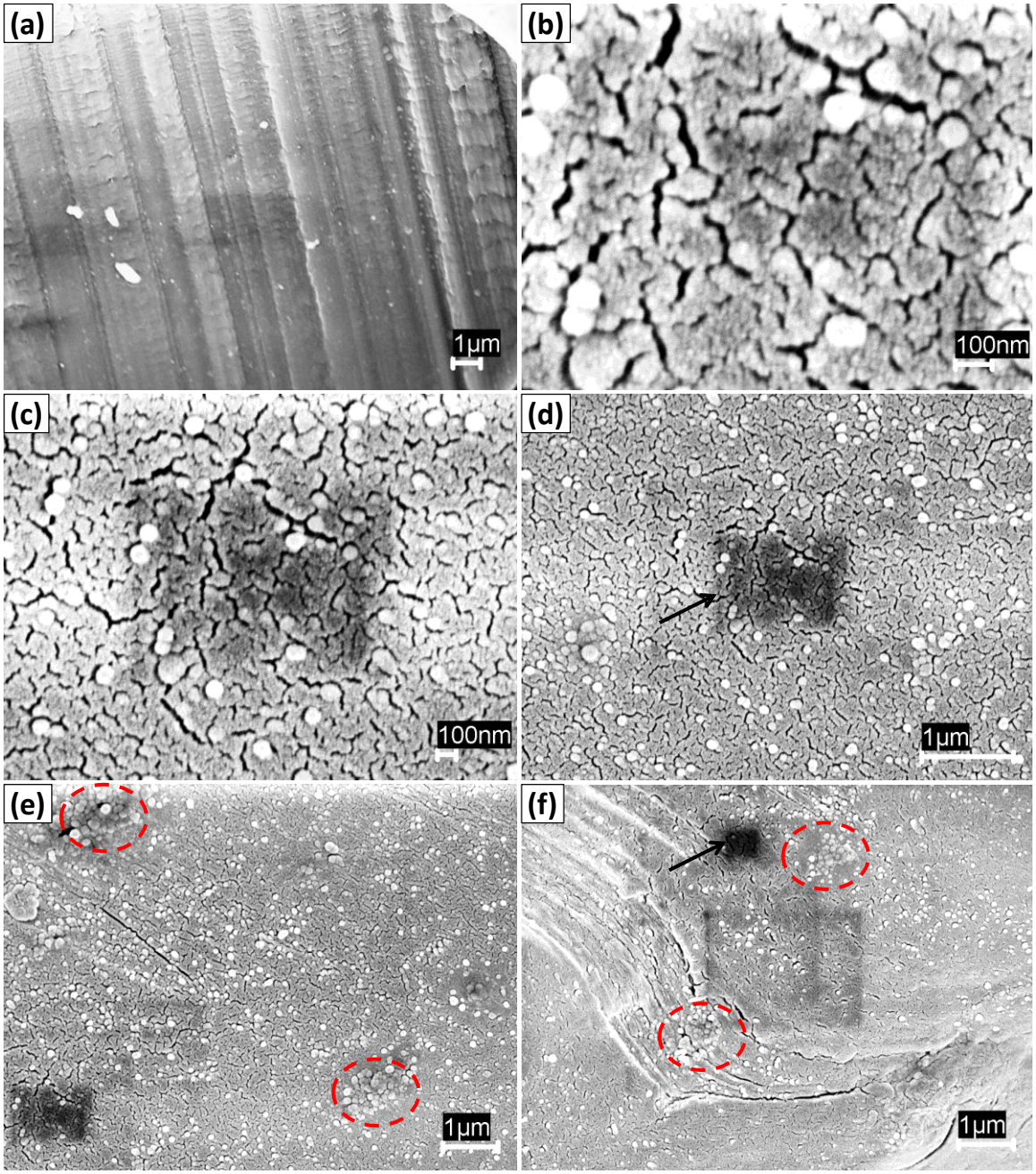

Figure 137. SEM images of the cross-section of (a) PEK-g-1%MWNT (M1a) and (b-f) PEK-g-10%MWNT (M2a) fibers. The dashed circles show the agglomerated MWNT regions and arrows point toward degraded PEK.

The CNT dispersion in PEK-g-CNT fibers could also be studied from the SEM images of the fiber cross-sections after charring in TGA at 700 ˚C under N_2 atmosphere. Figures 138, 139, 140, and 141 show the cross-sections of PEK-g-5%SWNT, PEK-g-

5%FWNT, PEK-g-10%FWNT, and PEK-g-20%FWNT fibers, respectively, after charring. The CNTs appear to be uniformly dispersed in the fiber.

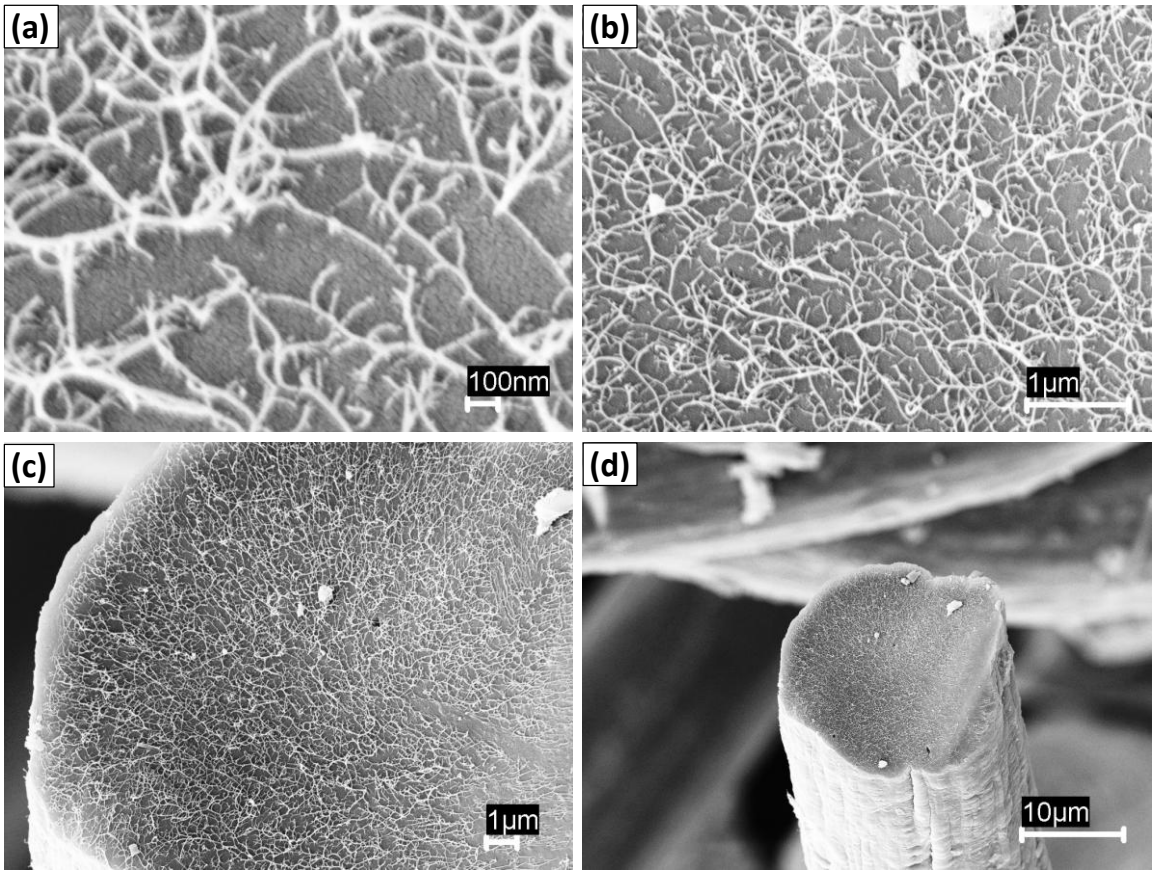

Figure 138. SEM images of the PEK-g-5%SWNT fiber (K2a) cross-section after charring in N_2 at 700 ˚C.

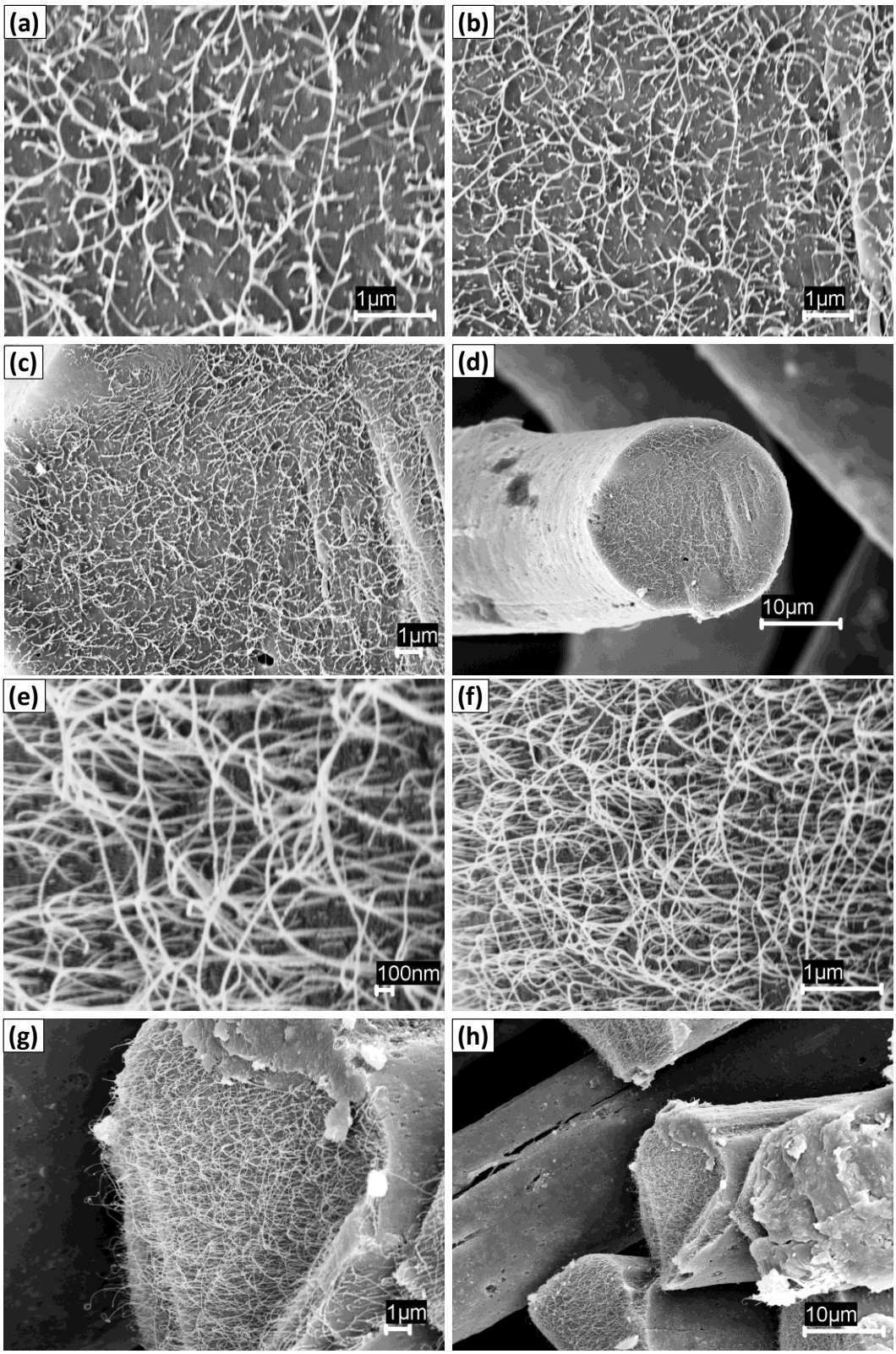

Figure 139. SEM images of the PEK-g-5%FWNT fiber (L3a) cross-section after charring in N_2 at 700 ˚C. Images a, b, c, and d belong to one cross-section. Images e, f, g, and h belong to another cross-section.

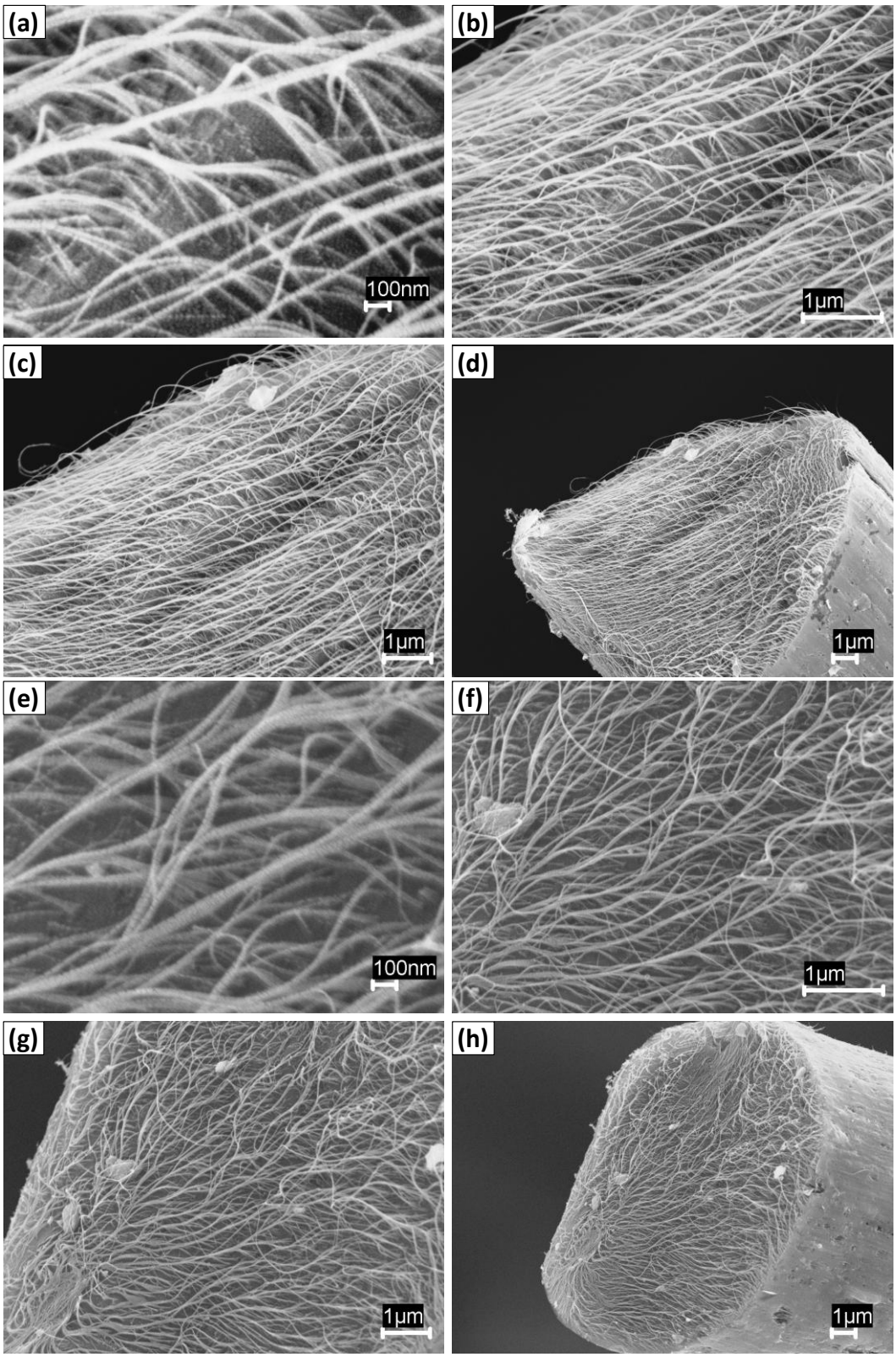

Figure 140. SEM images of the PEK-g-10%FWNT fiber (L4a) cross-section after charring in N_2 at 700 ˚C. Images a, b, c, and d belong to one cross-section. Images e, f, g, and h belong to another cross-section.

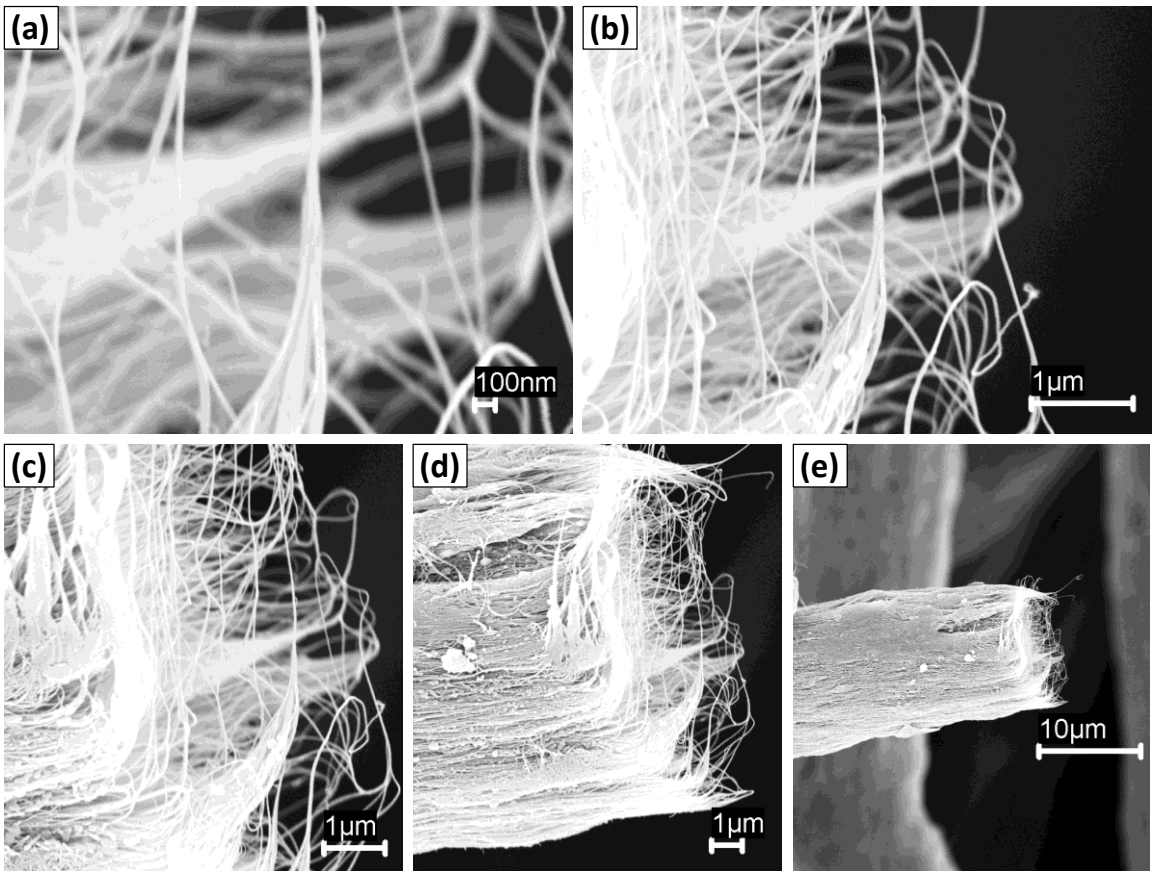

Figure 141. SEM images of the PEK-g-20%FWNT fiber (L5a) cross-section after charring in N_2 at 700 ˚C.

7.2.10. WAXD and FTIR of DSC Retrieved Samples

To further investigate as to what might be happening during the heating in air (corresponding to exotherm in air during first heating in DSC), the PEK and PEK-g-1%FWNT fiber samples were heated in both air and N_2 up to 310 ˚C (at 10 ˚C/min) and retrieved for further investigation. As mentioned before, the exotherm was only observed in samples heated in air and not N_2 (Figure 142).

Figure 143 shows the integrated radial scans of PEK fiber before heating and PEK fiber after heating in both air and N_2. After heating, the crystalline peaks for PEK became sharper and no distinction was found between samples heated in air and N_2. Similar

observations were made for the PEK-g-1%FWNT fiber. The crystallinity and crystal sizes of these fibers are listed in Table 40. In the heat treated samples, not much change in overall crystallinity was observed, but the crystal sizes increased by 10-40%.

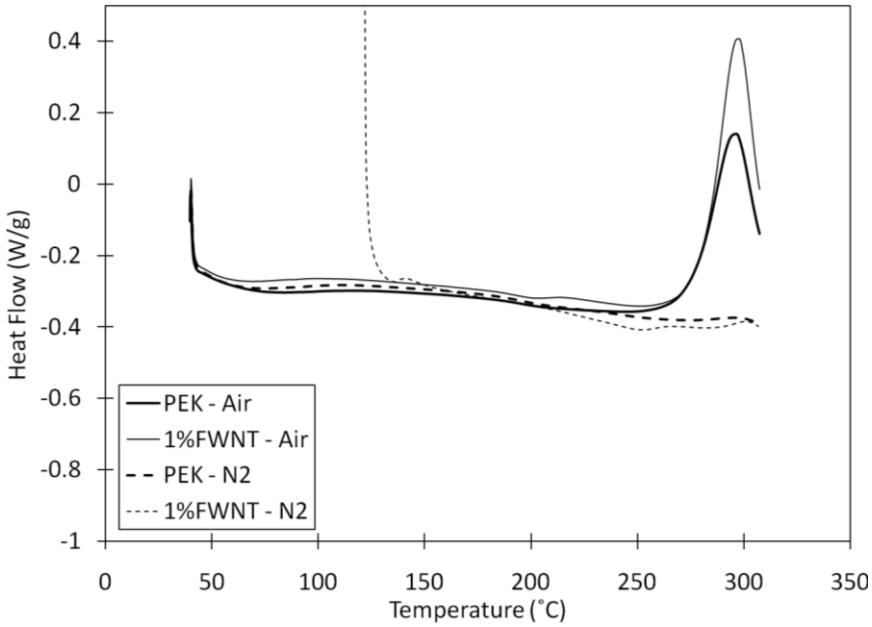

Figure 142. DSC scans of PEK (J2a) and PEK-g-1%FWNT (L2a) fibers when heated in air and N_2 up to 310 ˚C (at 10 ˚C/min).

Figure 144 shows the FTIR spectra of PEK and PEK-g-1%FWNT fibers. Since both spectra appeared to be same (no missing or extra peaks in PEK-g-1%FWNT), we only studied the PEK fiber for other FTIR studies. Figure 145 shows the FTIR spectra of PEK fibers before and after heating in DSC in air and N_2. From these results, no distinction could be made between the fibers before and after heating. This suggests that, the exotherm observed in air during heating in DSC could not be an oxidation process. It is possible that some of the small PEK chains participated in a secondary chain extension (polymerization), which only occurred in presence of air or O_2 in air (to be more specific).

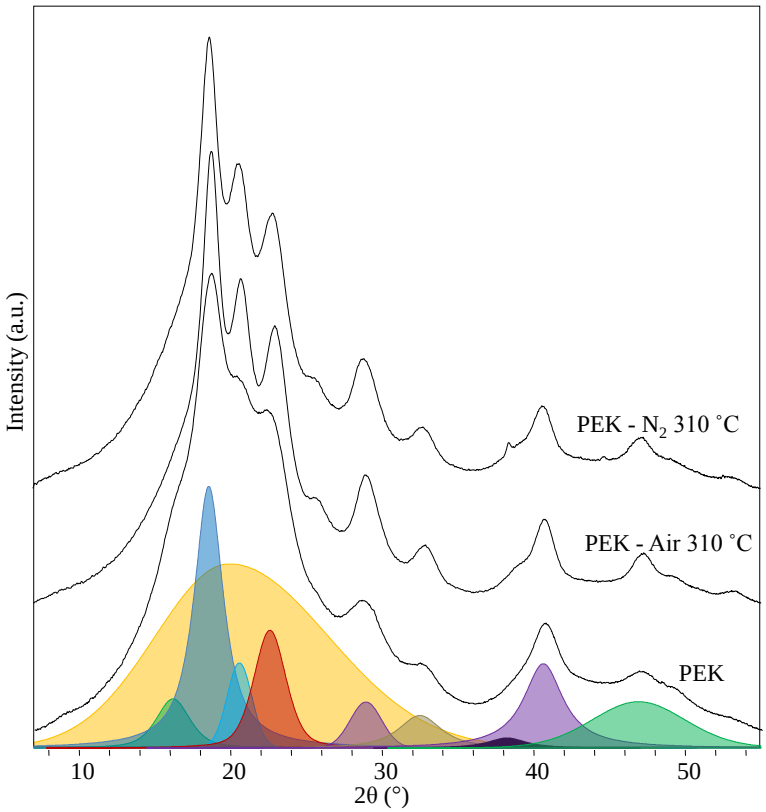

Figure 143. Integrated radial scans of PEK (with no DSC heating) and PEK fibers (J2a) retrieved from DSC after heating in air and N_2 up to 310 ˚C.

Table 40. Crystalline Information of PEK (J2a) and PEK-g-1%FWNT (L2a) Fibers Before and After Heating in DSC in Air and N_2 up to 310 ˚C

CNT (%)	DSC @ 310 ˚C in	Crystallinity (I) (%)	Crystallinity (II) (%)	FWHM (2θ~23°) (˚)	L_{PEK} (2θ~16°) (Å)	L_{PEK} (2θ~19°) (Å)	L_{PEK} (2θ~23°) (Å)
0	No treatment	38	48	10.3	55	52	36
0	Air	37	45	--	--	69	58
0	N_2	44	52	--	--	64	42
1% FWNT	No treatment	42	51	10.6	50	50	37
1% FWNT	Air	37	42	--	--	70	52
1% FWNT	N_2	39	47	--	--	61	46

Crystallinity I and II were calculated from the WAXD integrated radial scans peaks between 2θ = 7 to 32˚ and 7 to 55˚, respectively. FWHM was calculated from the azimuthal scan of the peak at 2θ = 23˚. The crystal size (L_{PEK}) was calculated using the peaks in equatorial scans at 2θ = 16˚, 19˚, and 23˚.

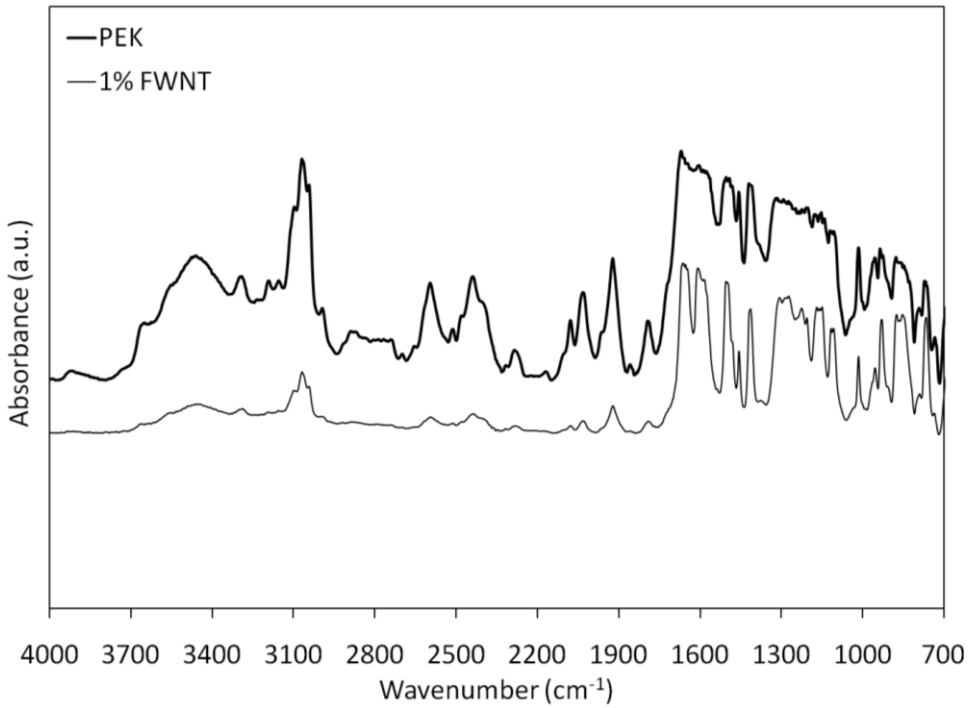

Figure 144. FTIR spectra of PEK (J2a) and PEK-g-1%FWNT (L2a) fibers.

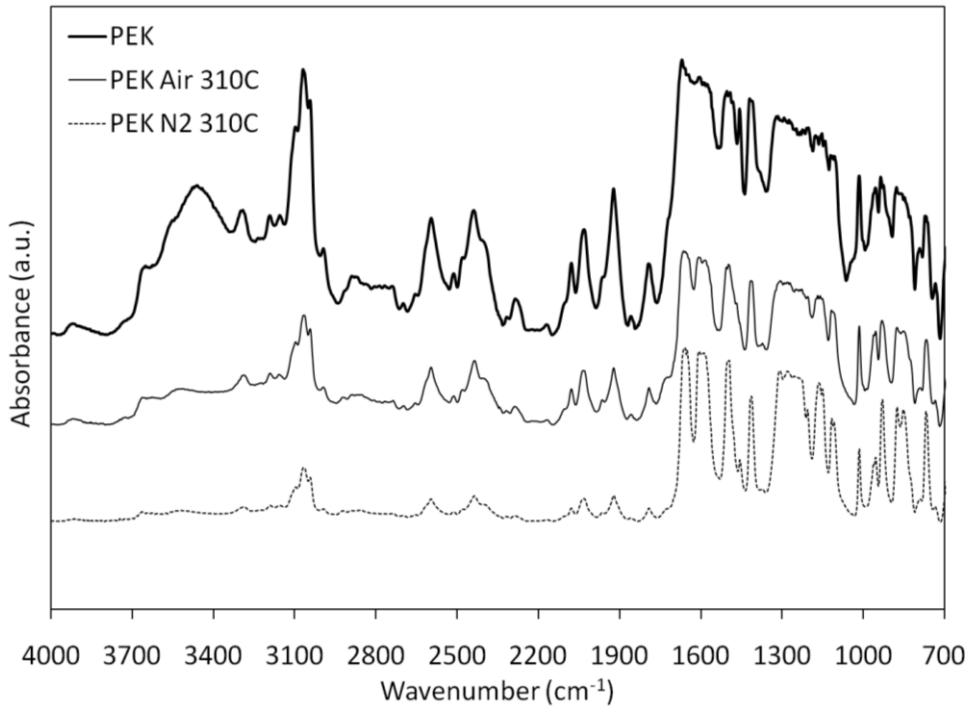

Figure 145. FTIR spectra of PEK fibers (J2a) before and after heating in DSC in air and N_2 up to 310 ˚C.

7.3. Conclusions

The PEK and PEK-g-CNT fibers could be successfully spun with different types of CNTs in different concentrations. At low concentrations, CNTs were found to be uniformly distributed and dispersed in the composite fibers. The PEK and PEK-g-CNT fibers were fairly circular in cross-section. The PEK based control and composite fibers possess high thermal stability with almost no weight loss up to 500 ˚C. PEK and PEK-g-CNT fibers showed a strong exotherm in air at around 290 ˚C, which was absent in N_2. At low CNT concentrations, no significant effect was observed, in the presence of different CNTs, in the crystallinity and crystal size of PEK. However, the tensile modulus and dynamic modulus of the fibers improved in the presence of CNTs. The PEK based fibers showed high toughness which surpassed many of the high performance fibers like Kevlar® and Zylon®. The energy dissipation behavior of high CNT (≥ 5 wt.%) containing fibers changed above the T_g of the fiber, which was evident from the tan δ curves obtained from DMA experiments. PEK fibers showed negligible thermal shrinkage up to 200 ˚C and a little shrinkage of about 6 % up to 340 ˚C. PEK-g SWNT and PEK-g-MWNT fibers showed larger thermal stresses than PEK and PEK-g-FWNT fibers. The 10% FWNT containing fibers were unique in terms of high electrical conductivity and high toughness.

7.4. References

1. Rajan S. Stress-Strain Curves of Kevlar and Zylon: http://www.coe.faa.gov/Combined_Folders/4thMeeting/SRajan.pdf (accessed on 01/02/2009).

2. Cheng M, Chen W, and Weerasooriya T. Journal of Engineering Materials and Technology 2005;127(2):197-203.

3. Vollrath F and Knight DP. Nature 2001;410(6828):541-548.

4. Zylon stress-strain curve: http://www.sri.com/psd/fracture/material_properties.html (accessed on 02/04/2009).

5. Toyobo. Zylon Brochure: http://www.toyobo.co.jp/e/seihin/kc/pbo/Technical_Information_2005.pdf (accessed on 02/18/2009).

6. Baek JB and Tan LS. Polymer 2003;44(15):4135-4147.

7. Baek JB, Lyons CB, and Tan LS. Journal of Materials Chemistry 2004;14(13):2052-2056.

8. Baek JB, Lyons CB, and Tan LS. Macromolecules 2004;37(22):8278-8285.

9. Takahashi T, Hii S-H, and Sakurai K. Journal of Macromolecular Science, Part B 1998;37(1):59 - 71.

10. Harris JE and Robeson LM. Journal of Polymer Science Part B: Polymer Physics 1987;25(2):311-323.

11. Waddon AJ, Hill MJ, Keller A, and Blundell DJ. Journal of Materials Science 1987;22(5):1773-1784.

12. Dawson PC and Blundell DJ. Polymer 1980;21(5):577-578.

13. Sreekumar TV, Liu T, Min BG, Guo H, Kumar S, Hauge RH, and Smalley RE. Advanced Materials 2004;16(1):58-61.

CHAPTER 8

CONCLUSIONS AND RECOMMENDATIONS FOR FUTURE WORK

The objectives of this study were to spin the PAN and PEK fibers with various carbon nanotubes at different concentrations. More specifically, the interest was in processing composite fibers containing high concentration (≥ 20%) CNTs and CNFs. To the best of our knowledge, the high MWNT and CNF containing fibers spun using conventional spinning technology have not been previously reported. The PAN/CNT and PEK/CNT fibers were processed using dry-jet wet solution spinning. The fibers were characterized to evaluate their structure and morphology and tested for their thermal stability, tensile properties, dynamic mechanical properties, thermo-mechanical properties, and electrical conductivity. The main conclusions from this study are given below.

8.1. PAN/MWNT Composite Fibers Using Low MW PAN (~ 100,000 g/mole) and Different Concentrations of MWNTs (5, 10, 15, and 20 wt.%)

- The thermomechanical properties of the PAN fiber, particularly above T_g, were improved after the addition of MWNTs. The presence of MWNTs constrained the movement of PAN chains, which increased the T_g and reduced the thermal shrinkage in PAN fiber.
- Among all the composite fibers, the 5% MWNT fiber showed the maximum modulus and strength (at the heat drawn stage). After stabilization, the modulus of the composite fibers increased with increasing percentage of MWNTs.

- Though the absolute mechanical properties of the composite fibers decreased as the draw ratio decreased with an increase in MWNT content. However, the moduli values in each case were still higher than theoretically expected.
- The possible factors which seem to be detrimental to the mechanical properties of the composite fibers include MWNTs entanglements at high concentrations (> 5%) and void formation in the fiber.
- The MWNTs were found to be very well coated/wetted with PAN polymer, which suggests good interaction between PAN polymer and MWNT. The presence of MWNTs showed no particular affect on the crystallinity, crystal size, and orientation of PAN. In general, the PAN orientation increased with increase in draw-ratio.
- The 15% MWNT fiber showed electrical conductivity which was four orders of magnitude higher than that of the 10% MWNT fiber.
- The improvement in tensile modulus of the control PAN and 5% MWNT fibers after second spinning trial suggests that properties can be further improved by optimizing the solution preparation and fiber spinning conditions.

8.2. PAN/CNF Composite Fibers using Low MW PAN (~ 100,000 g/mole) and Different Concentrations of CNFs (5, 10, 15, 20, and 30 wt.%)

- The presence of CNFs helps maintain the composite fiber structural form after charring.

- The charred porous fibers may find applications in biomedical implants (bone, nerve, and cell growth), filtration/adsorption-desorption media, and electrodes for electrochemical capacitors.
- The CNFs increased the overall char yield of the fiber after charring up to 1000 ˚C.
- The combined effect of "end-edge effect" and "phase separation" led to increase in voids and defects with increase in CNFs concentration. This also presented challenges for fiber spinnability.
- Longer sonication time provided good CNF dispersion in PAN matrix, which improved the CNF orientation and electrical conductivity.
- The higher drying temperature (85 ˚C as compared to 50 ˚C) increased the composite fiber strain to failure.
- By using high concentration of CNFs, the conductivity of the fiber could be increased to the level required in applications like electrostatic dissipation and electromagnetic interference shielding.

8.3. PAN/CNF Composite Fibers from High MW PAN (~ 250,000 and 700,000 g/mole) with 20 wt.% CNFs

- For higher loading systems (20% CNF), compared to low MW PAN (PAN 100K) higher MW PAN (250K and 700K) provided better mechanical properties. For 20% CNF reinforced fiber, the increase in modulus was almost 20% and 80% over the control 250K and 700K PAN fibers, respectively.

- The thermal shrinkage of the 250K and 700K PAN was reduced to half after reinforcement with 20% CNFs.
- Though no such increase was observed for 100K based fibers, but after reinforcement with 20% CNFs, the overall crystallinity increased from 44% to 53% for 250K PAN fiber and from 38% to 59% for 700K PAN fiber.
- The presence of CNFs was found to increase the PAN solution viscosity at lower shear rates and show a sharp shear thinning behavior with increase in shear rate.
- CNF increased the storage modulus of the PAN solutions at low frequencies (due to large increase in elastic behavior). Even at low frequencies of 0.01 Hz, G' became higher than G" in CNF containing PAN/CNF composite solutions.

8.4. Effect of CNT Diameter and Concentration on Fiber Spinnability and Electrical Conductivity of the PAN/CNT Composite Fiber

- The composite fiber spinnability, at a particular CNT concentration, was found to be strongly dependent on the CNT diameter.
- The ultrasonication studies in this work showed that the dispersion of CNFs in the PAN matrix can be improved by using longer sonication times, which decreased the CNF length.
- The better dispersion proved to be helpful for increasing the CNF orientation.
- For a particular CNT, as expected, the electrical conductivity increased with increase in CNT concentration.
- The electrical conductivity also increased with increase in fiber draw ratio.

- For a particular CNT concentration, the high MW PAN based composite fibers showed higher electrical conductivity.
- The results show that by properly choosing the type of CNT, length of CNTs, dispersion of CNTs, fiber spinning method, fiber draw ratio or orientation of CNTs, and type of polymer, one can get electrically conducting fibers with wide range of conductivities for different applications.

8.5. CNT Reinforced Poly(etherketone) Fibers

- The PEK/CNT fibers could be successfully spun with different types of CNTs at different concentrations.
- The CNTs were found to be uniformly distributed and dispersed in the composite fibers.
- The PEK based control and composite fibers possess high thermal stability with almost no weight loss up to 500 ˚C.
- The PEK based fibers showed high toughness which surpassed many of the high performance fibers like Kevlar® and Zylon®.
- The energy dissipation behavior of high CNT (≥ 5 wt.%) containing fibers changed above the T_g of the fiber, which was evident from the tan δ curves obtained from DMA experiments.
- PEK fibers showed negligible thermal shrinkage up to 200 ˚C and a little shrinkage of about 6 % up to 340 ˚C.
- The 10% FWNT containing fibers were unique in terms of high electrical conductivity (25 S/m) and high toughness (50 MPa).

8.6. Recommendations for Future Work

Since the PAN/CNF properties including tensile strength and electrical conductivity were found to be improved with high MW PAN, the SWNT and MWNT should also be spun using high MW PAN, which might further enhance the PAN/SWNT and PAN/MWNT composite fiber properties. To further evaluate the applicability of these fibers for structural applications, the fatigue properties of these fibers should be studied. The effects of different types of CNTs, different concentrations of CNTs, and different MW PAN, on the fiber stabilization should be studied, if the fibers were to be considered for fire barrier and fire protection applications.

In case of PEK/CNT fibers, the CNFs can also be used as reinforcement. Since, the CNF surface is very different than SWNT and MWNT, this might lead to a tougher fiber than obtained with SWNT, FWNT, and MWNT. The stacked-cup geometry of the CNF may add to the already high strain to failure of the PEK based fibers. The higher thermal stability of CNFs than other types of CNTs can be another reason for making PEK/CNF fibers, which may have higher thermal stability than other PEK/CNT fibers. The origin of exotherm (and the mechanism of possible reaction) in the DSC run in air needs further investigation.

APPENDIX A

Sample Name	Linear Density (tex)	PAN MW	Type of CNT	CNT %	Draw Ratio
A1a	5.3	100K	NO CNT		3
A1b	3.9				4
A1c	3.2				5
A1d	3.0				6
A1e	3.4				7
A1f	2.0				8
A1g	3.0				9
A1h	3.3				10
A2a	4.4	250K			4
A2b	2.9				6
A2c	2.3				8
A2d	1.6				10
A2e	1.5				12
A3a	2.3	700K			8
A3b	1.8				10
A3c	1.5				12
B1a	1.5	100K	MWNT	5	6
B2a	2.1			10	5
B3a	3.6			15	4
B4a	2.0			20	2.5
C1a	1.8	100K	CNF	5	6
C1b	3.0				9
C2a	1.8			10	10
C3a	1.9			15	6
C4a	3.3			20	5
C4b	2.4				6
C5a	5.4			30	3.5
D1a	5.2	250K		20	5
D1b	2.5				10
D2a	--	700K			4
D2b	--				6
D2c	2.2				8
D2d	--				10
E1a	3.2	100K		5[#]	9
E1b	2.6				12
E2a	3.6			5[#*]	9
E2b	2.7				12
E3a	3.2			20[*]	5
E3b[$$]	3.3			20[*#]	6
E3c[$$]	3.3			20[*#+]	6
F1a	1.6	100K	NO CNT[#]		6
F1b	1.2				8
F1c[$]	5.1		CNF	5	6
F1d[$$]					

1 tex = g/1000 m, [#] two-stage drawing, [*] 48 h sonication

[$]draw ratio 2 in hot water at 85 ˚C and 3 in boiling water; total draw ratio 6

[$$]draw ratio 3 in hot water at 85 ˚C and 2 in boiling water; total draw ratio 6

[+]dried at 85 ˚C

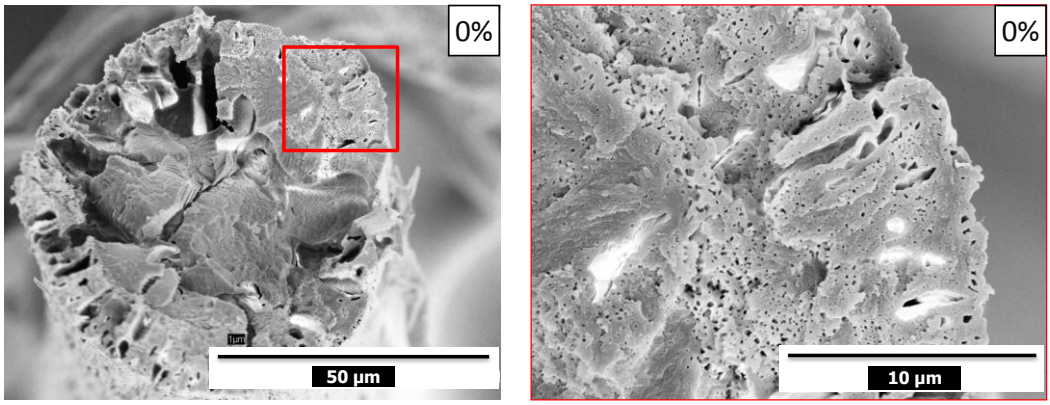

Figure A1. Cross-sections of the tensile fracture specimens of control PAN fiber (A1d) after stabilization (a section of the image on left is shown at high magnification on right image)

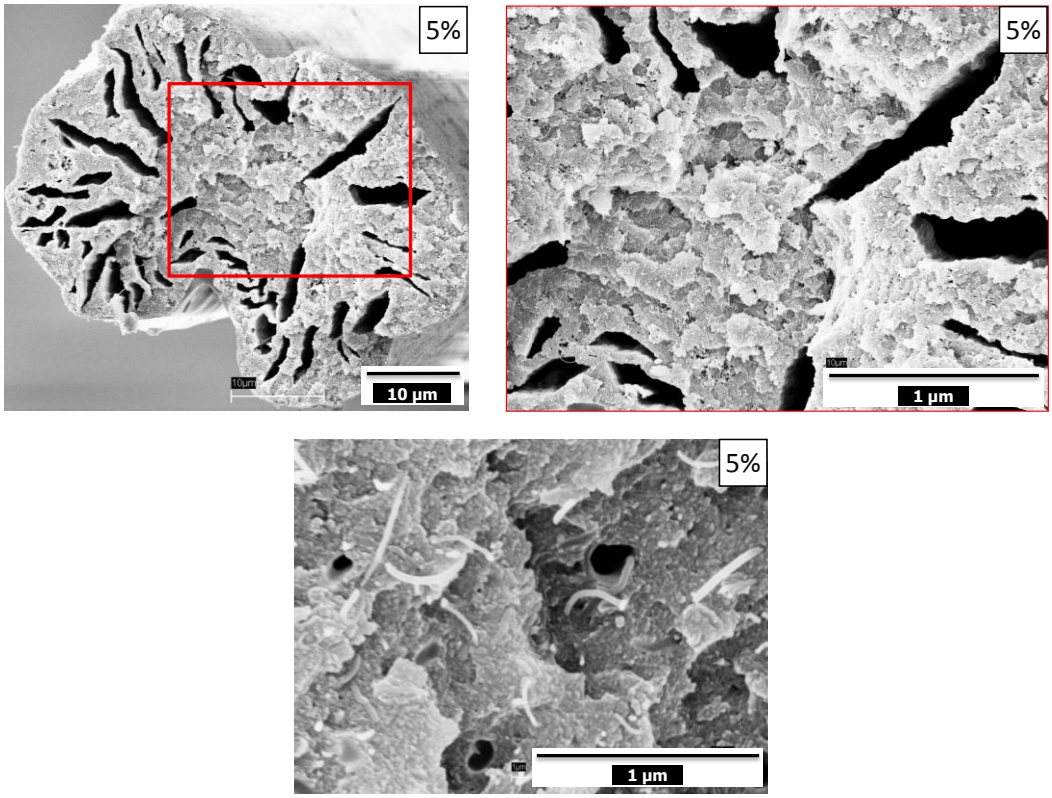

Figure A2. Cross-sections of the tensile fracture specimens of PAN/MWNT (95/5) composite fiber (B1a) after stabilization (a section of the image on top-left is shown at high magnification on top-right image and high magnification image at the bottom shows the MWNTs embedded in the PAN matrix)

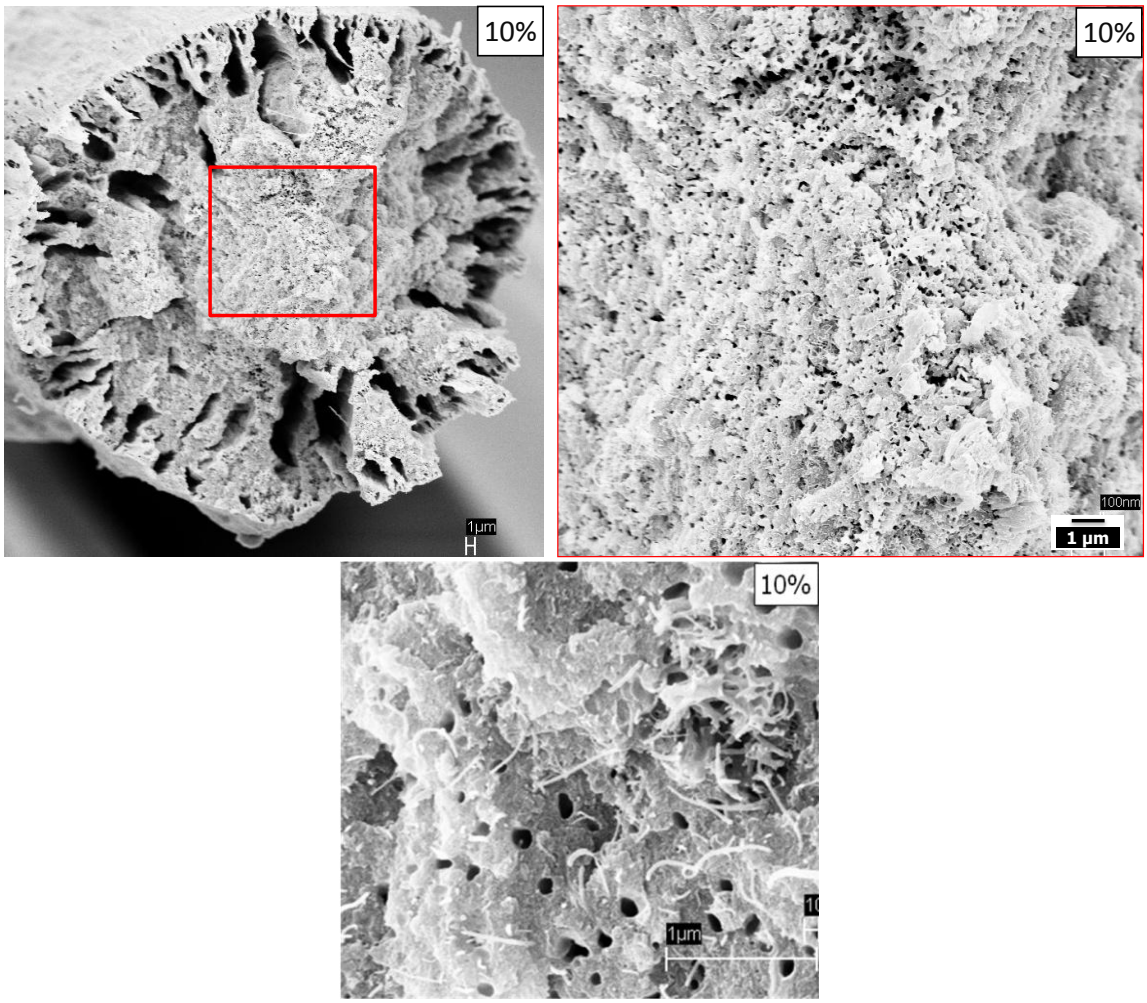

Figure A3. Cross-sections of the tensile fracture specimens of PAN/MWNT (90/10) composite fiber (B2a) after stabilization (a section of the image on left is shown at high magnification on right image)

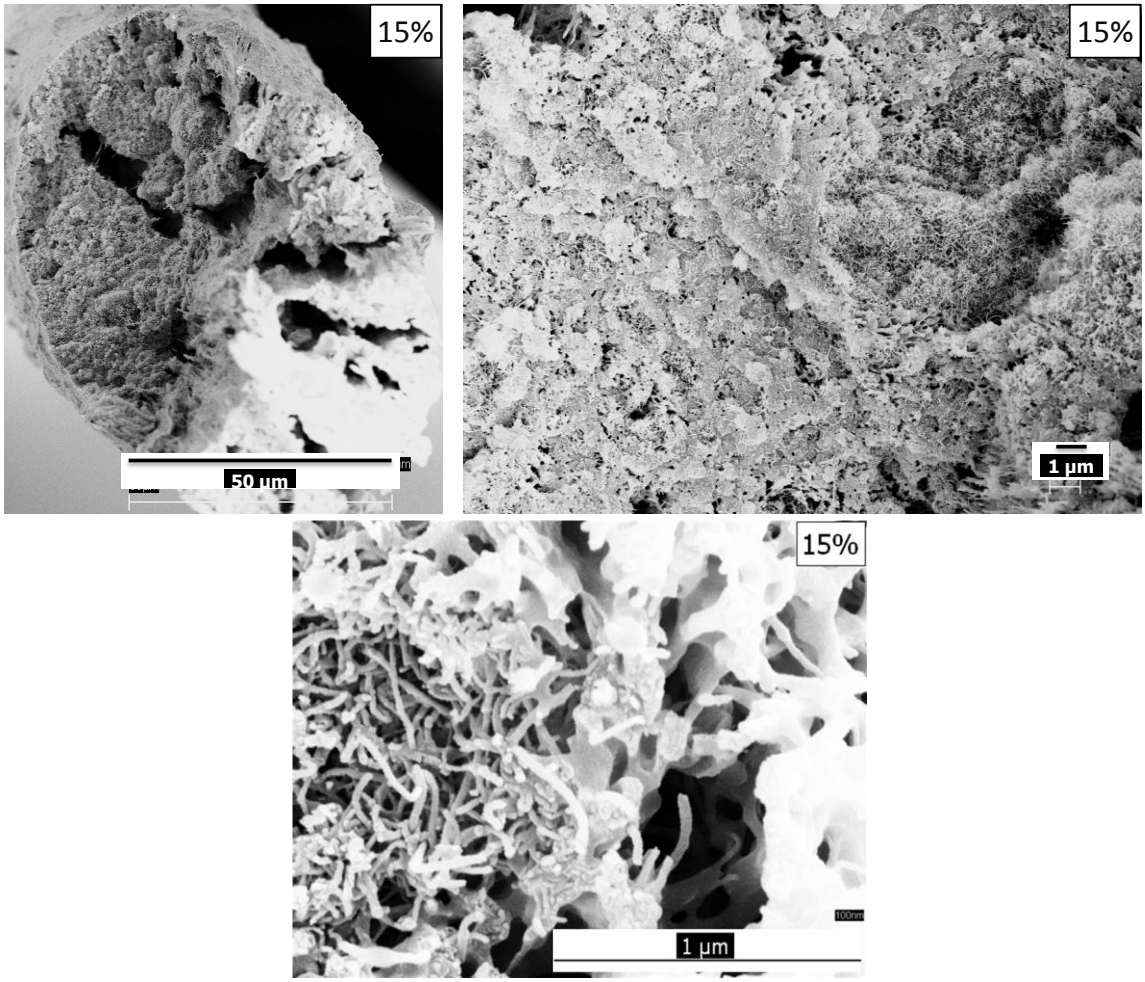

Figure A4. Cross-sections of the tensile fracture specimens of PAN/MWNT (85/15) composite fiber (B3a) after stabilization (a section of the image on left is shown at high magnification on right image)

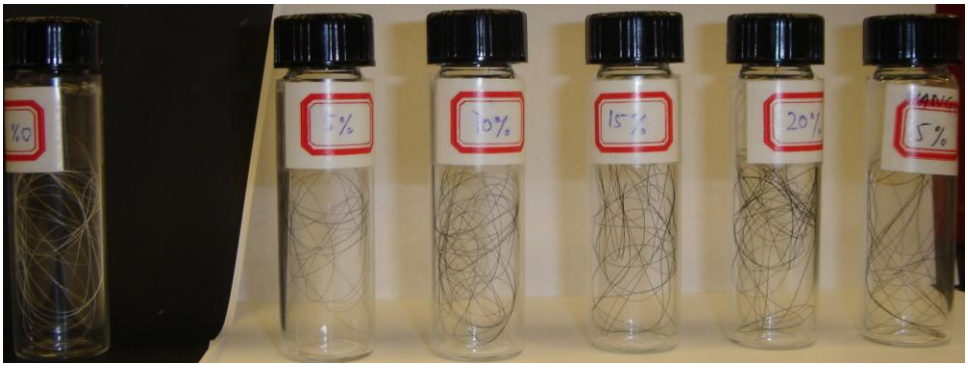

Figure A5. PAN/MWNT composite fibers with different concentrations of MWNTs (0, 5, 10, 15, 20%) in glass vials. The right-most vial contains the 5%MWNT/PAN composite fiber spun by Chae *et al.* [1].

Figure A6. PAN/MWNT composite fibers after 1 minute after pouring DMF in vials. All composite fibers disintegrated into small fragments. Chae's fiber surface slowly dissolves but does not disintegrate into fibrils. Control PAN fiber (not shown in this image) was intact.

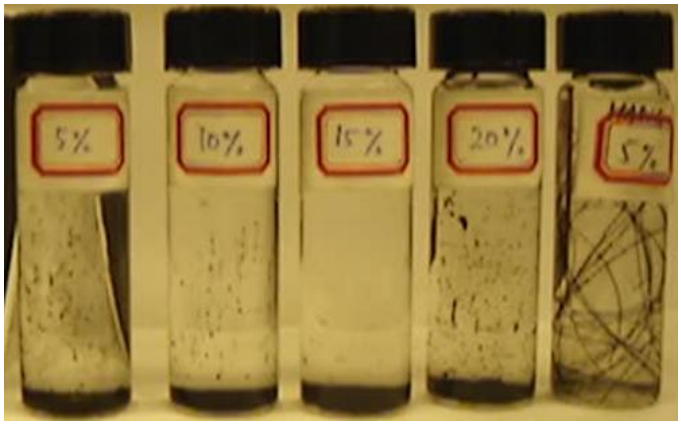

Figure A7. PAN/MWNT composite fibers after 3 minutes after pouring DMF in vials. The disintegrated fragments settled at the bottom in the vials. Chae's fiber starts to disintegrate. Control PAN fiber (not shown in this image) was intact.

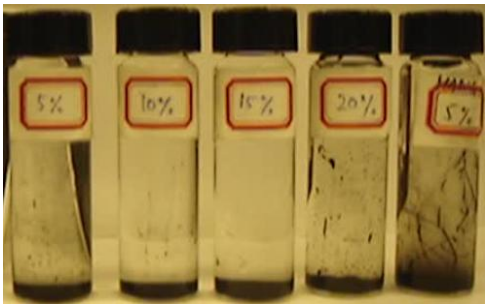

Figure A8. PAN/MWNT composite fibers after 5 minutes after pouring DMF in vials. The disintegrated fragments settled at the bottom in the vials. Control PAN fiber (not shown in this image) was intact in its form but started to dissolve.

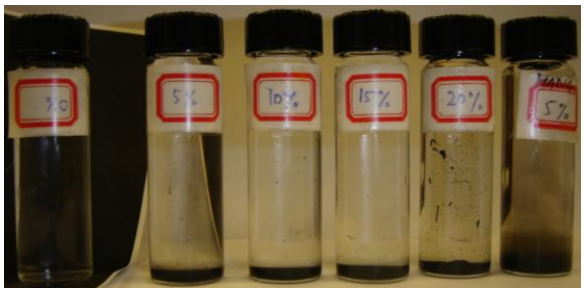

Figure A9. PAN/MWNT composite fibers after 13 minutes after pouring DMF in vials. The disintegrated fragments settled at the bottom in the vials. Control PAN fiber was fully dissolved.

Figure A10. PAN/MWNT composite fibers after 13 minutes after pouring DMF in vials. The vials were shaken to see the disintegrated fibrils. The disintegrated fragments settled at the bottom in the vials.

References

1. Chae HG, Sreekumar TV, Uchida T, and Kumar S. Polymer 2005;46(24):10925-10935.

APPENDIX B

Effect of Sonication Time on the Length of CNFs

The CNFs were sonicated in DMF at a concentration of 1 g per 200 ml at about 46 ˚C. A drop of dispersion (CNFs in DMF) was taken out after 0.5, 1, 2, 3, 4, 5, 8, 24, 48, and 72 hours and dried on SEM stub. The dispersion was imaged using SEM. Figure B1 shows the SEM images of as-received CNFs, where the CNFs are at least few microns in length and show extensive bundling. Figures B2 and B3 show the images for CNFs dispersion after 30 min and 1 h sonication, respectively. Though the bundles of CNFs remain, they still seem to be loosened a little bit. After 2 h sonication (Figure B4), the CNF bundles seem to be loosened to large extent and the CNFs seem to be shortened in length. After 3 h of sonication (Figure B5), no bundles were conspicuous, but the CNFs length continued to decrease with increase in time (Figures B6 through B11). Very small fragments of CNFs can be easily seen in the images for 24, 48, and 72 h sonication dispersion.

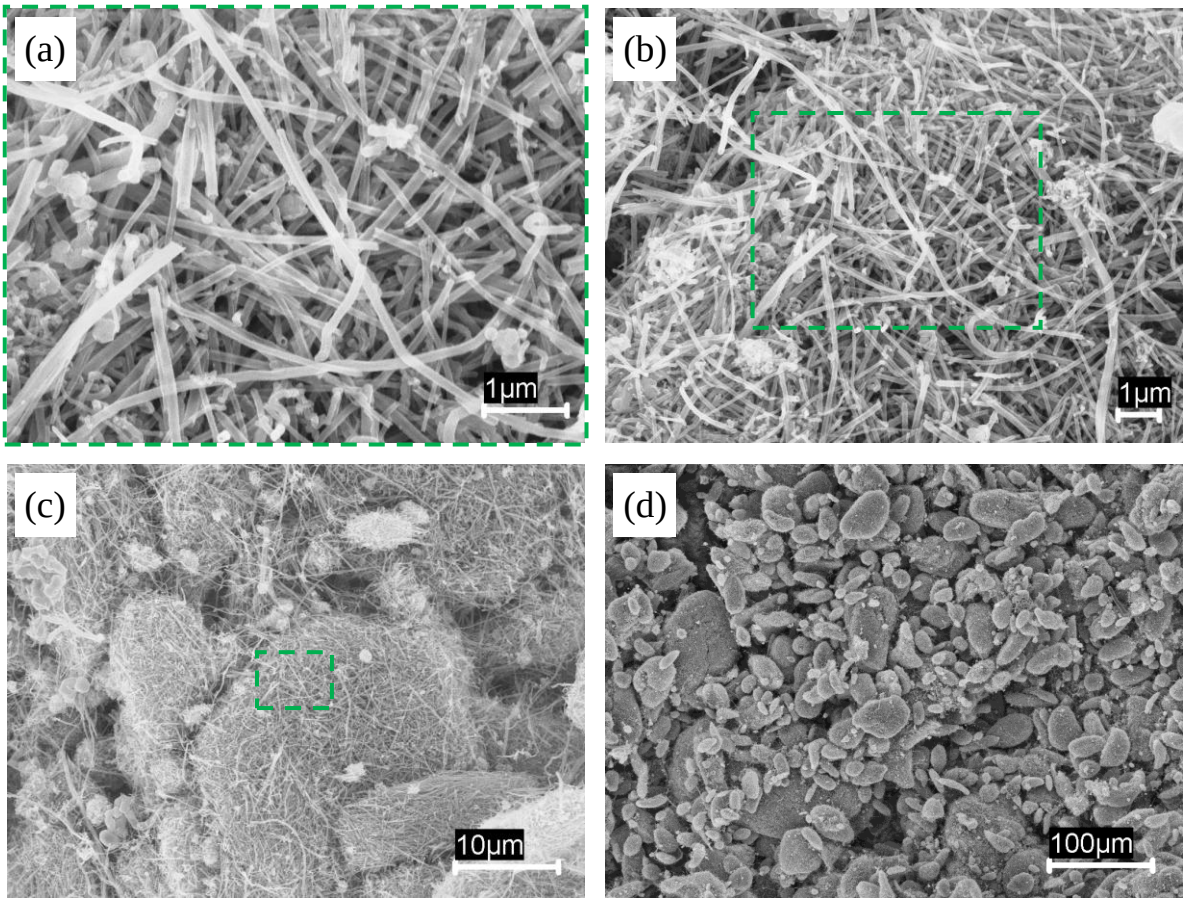

Figure B1. As received CNF powder at different magnifications.

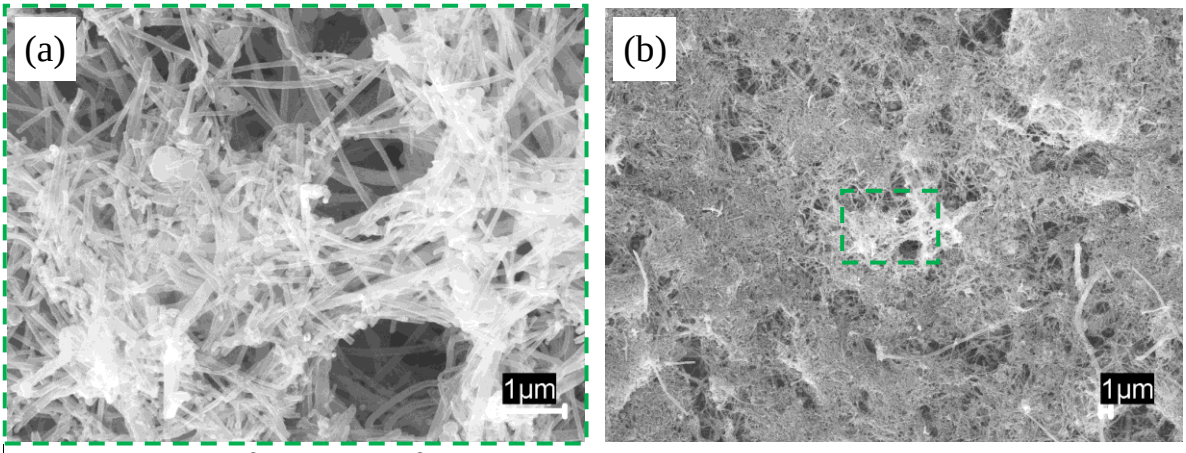

Figure B2. CNFs after 30 min of sonication in DMF

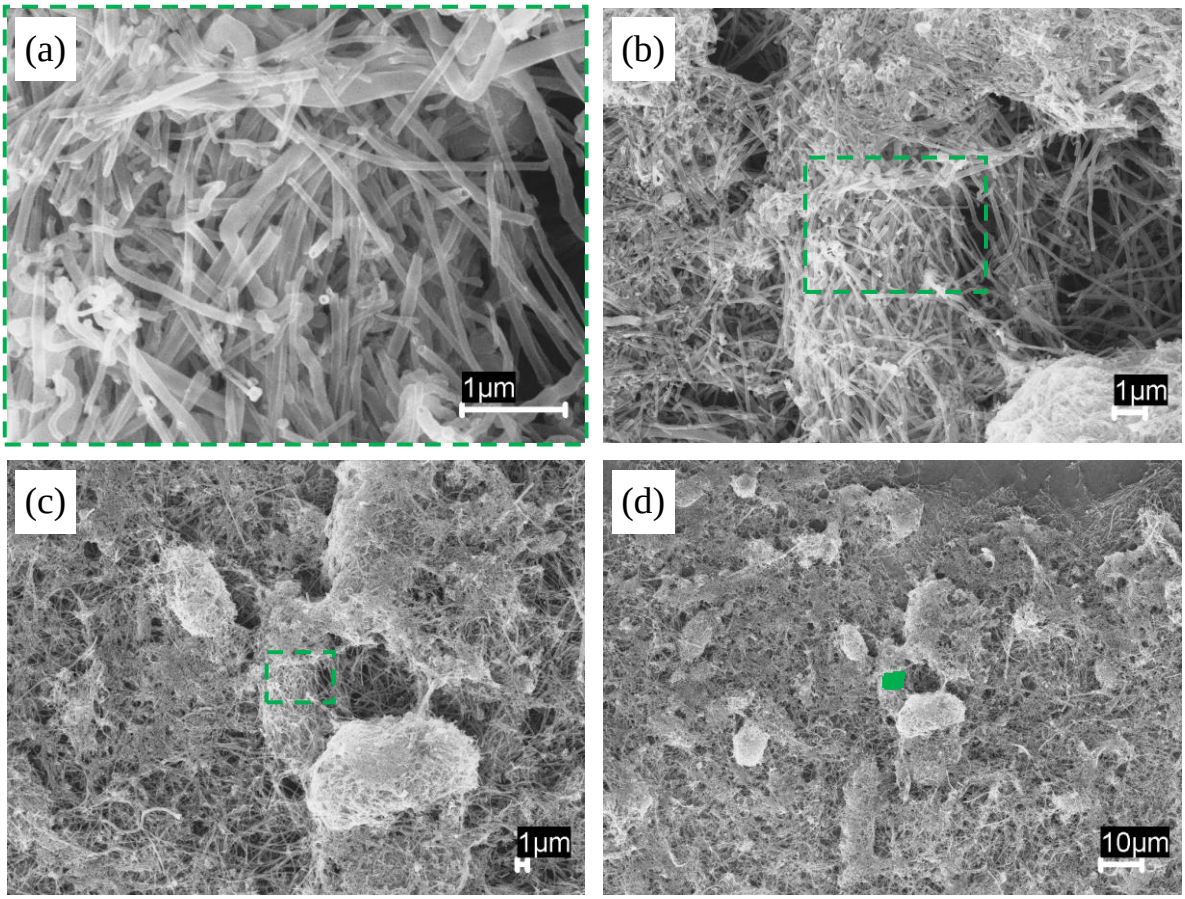

Figure B3. CNFs after 1 h of sonication in DMF

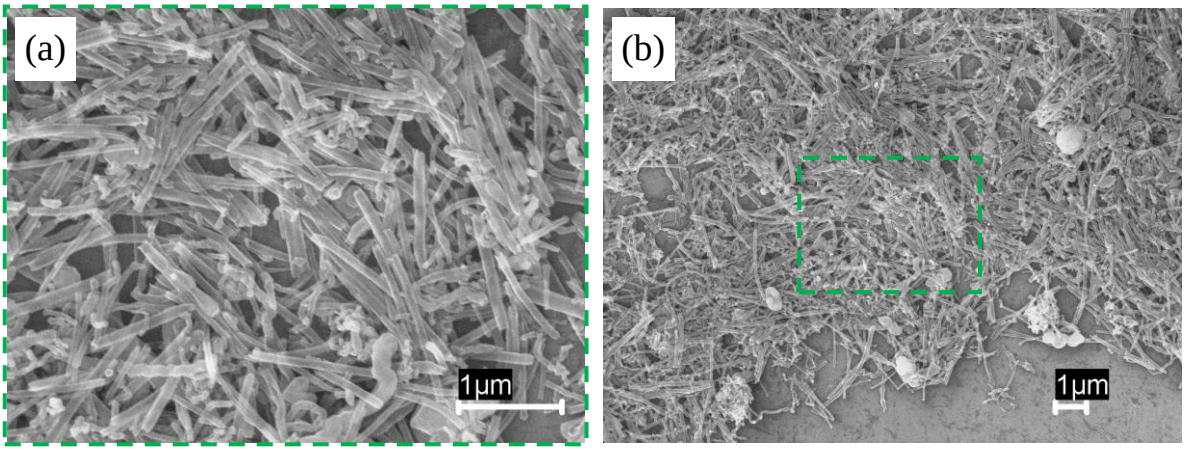

Figure B4. CNFs after 2 h of sonication in DMF

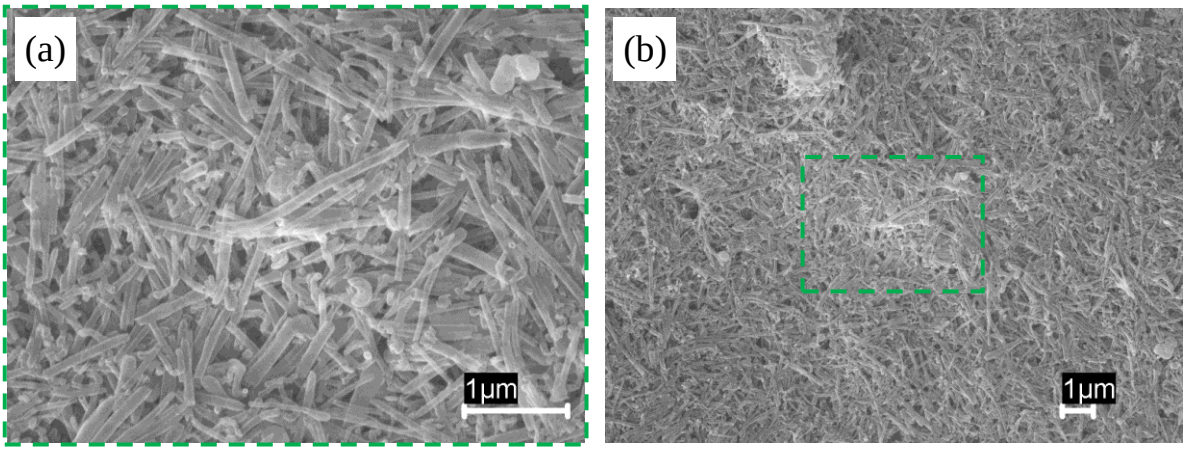

Figure B5. CNFs after 3 h of sonication in DMF

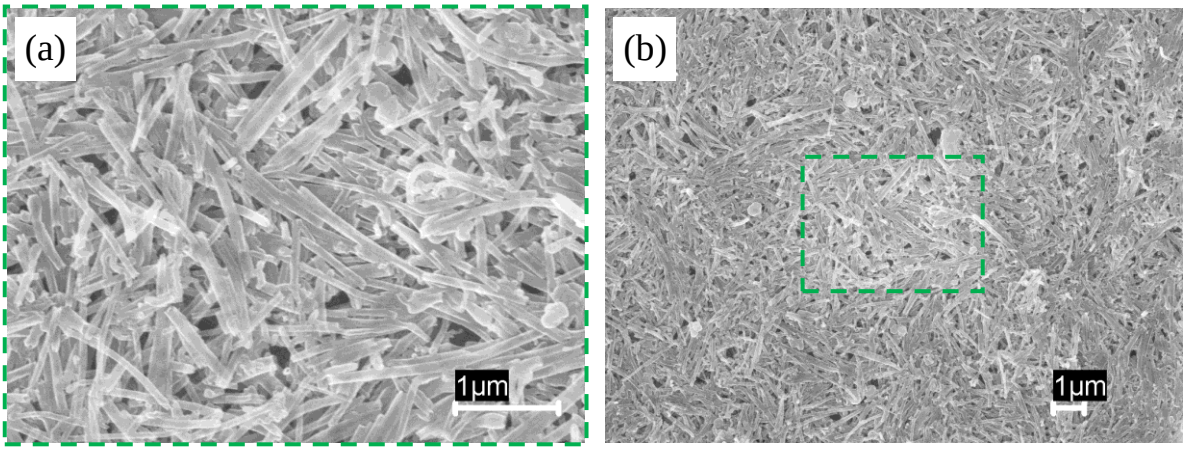

Figure B6. CNFs after 4 h of sonication in DMF

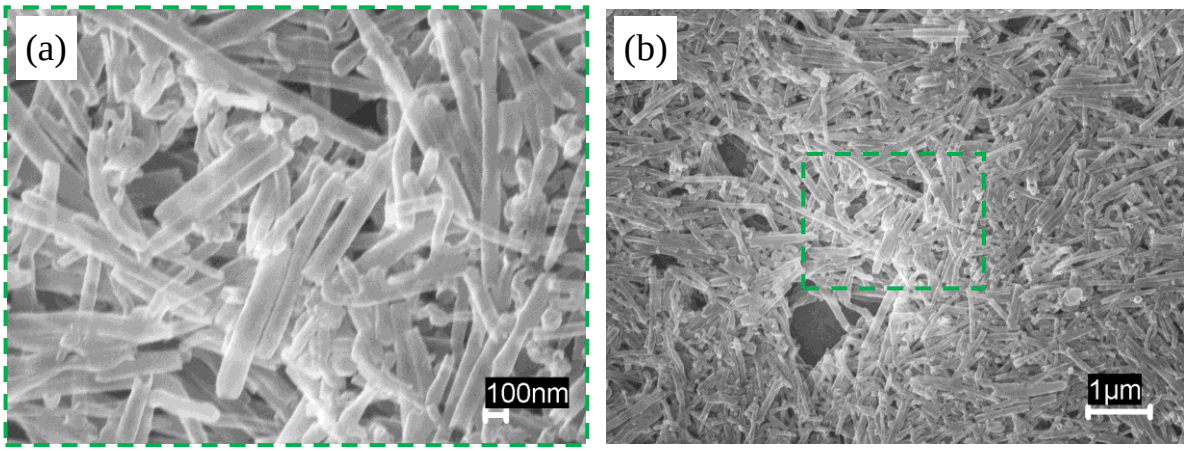

Figure B7. CNFs after 5 h of sonication in DMF

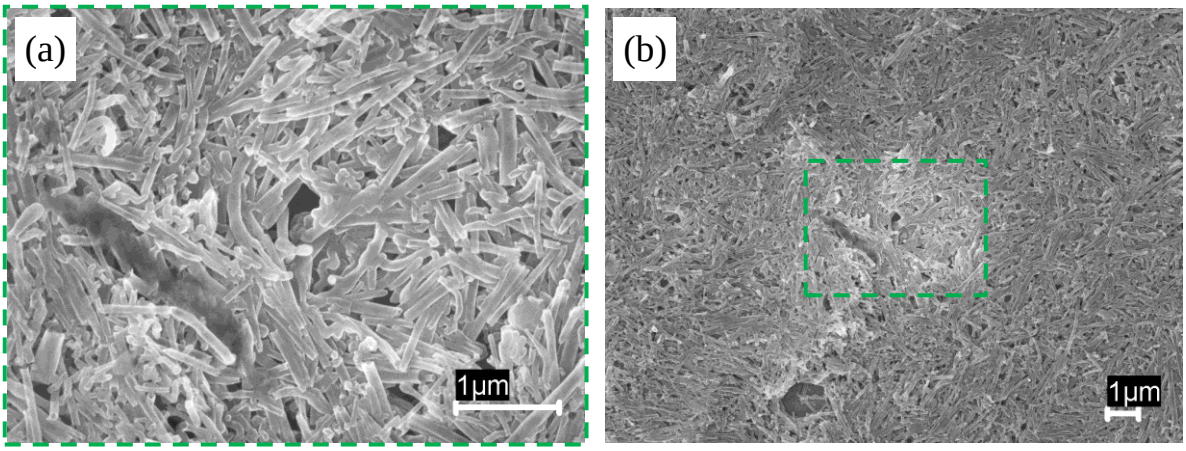

Figure B8. CNFs after 8 h of sonication in DMF

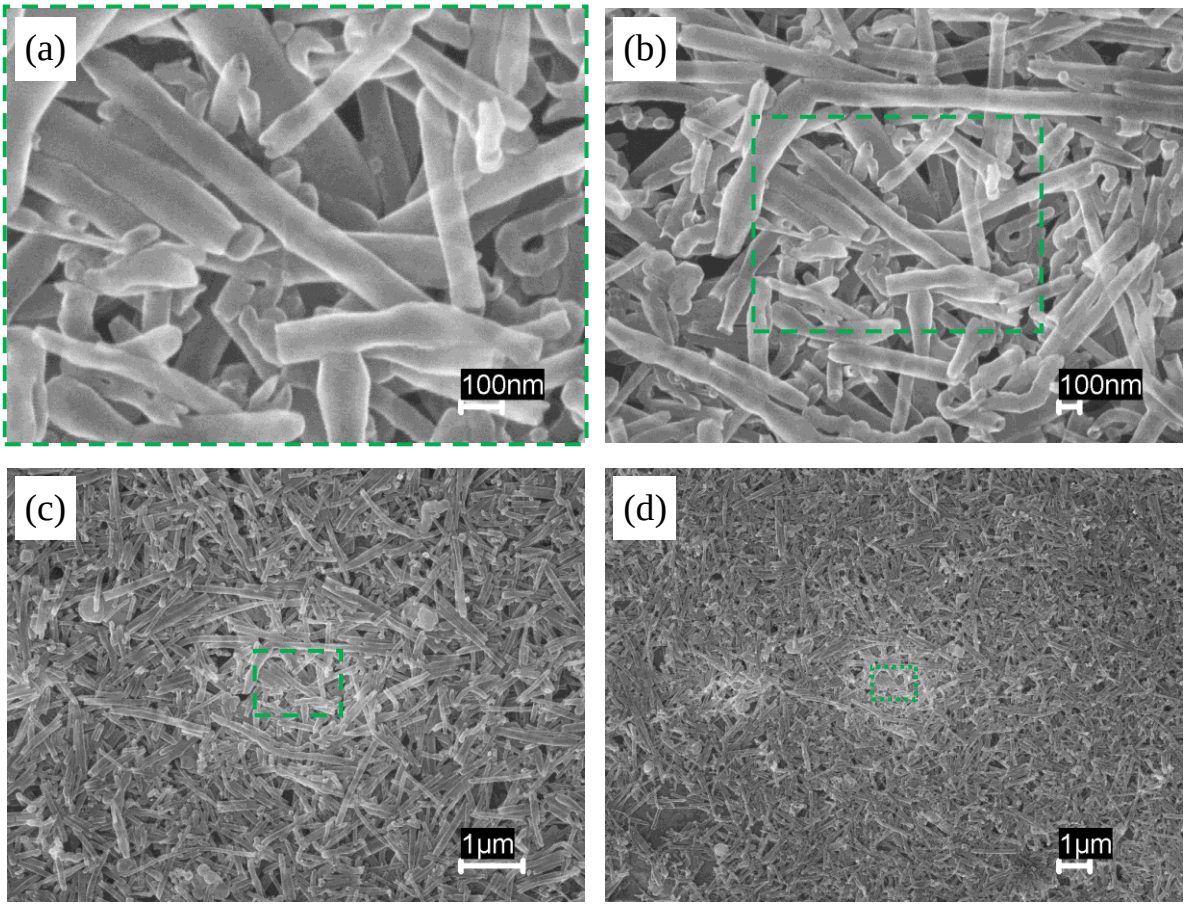

Figure B9. CNFs after 24 h of sonication in DMF

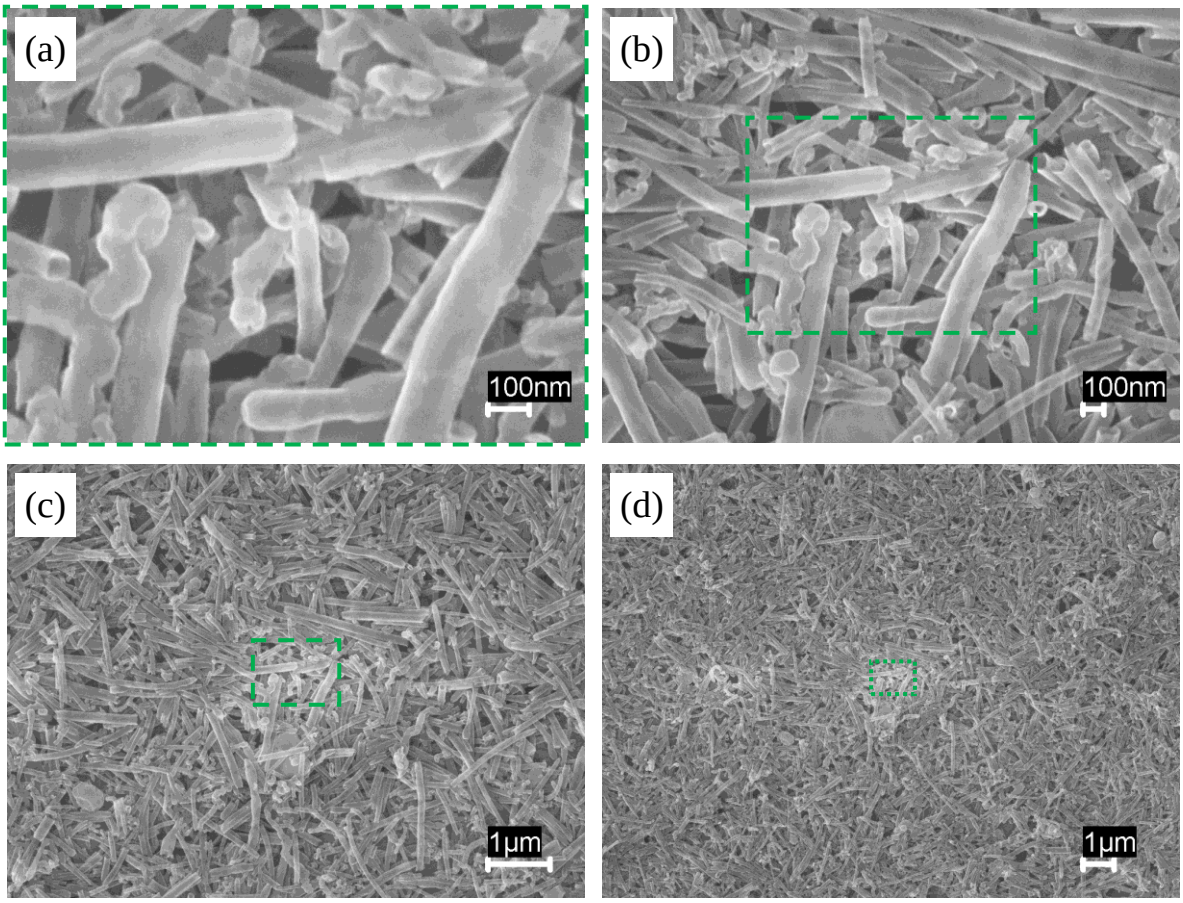

Figure B10. CNFs after 48 h of sonication in DMF

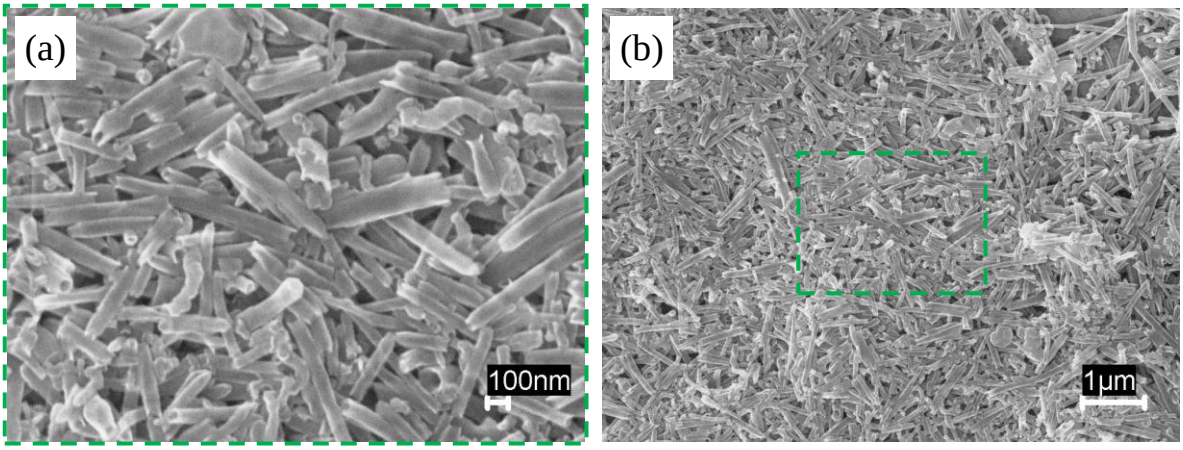

Figure B11. CNFs after 72 h of sonication in DMF

APPENDIX C

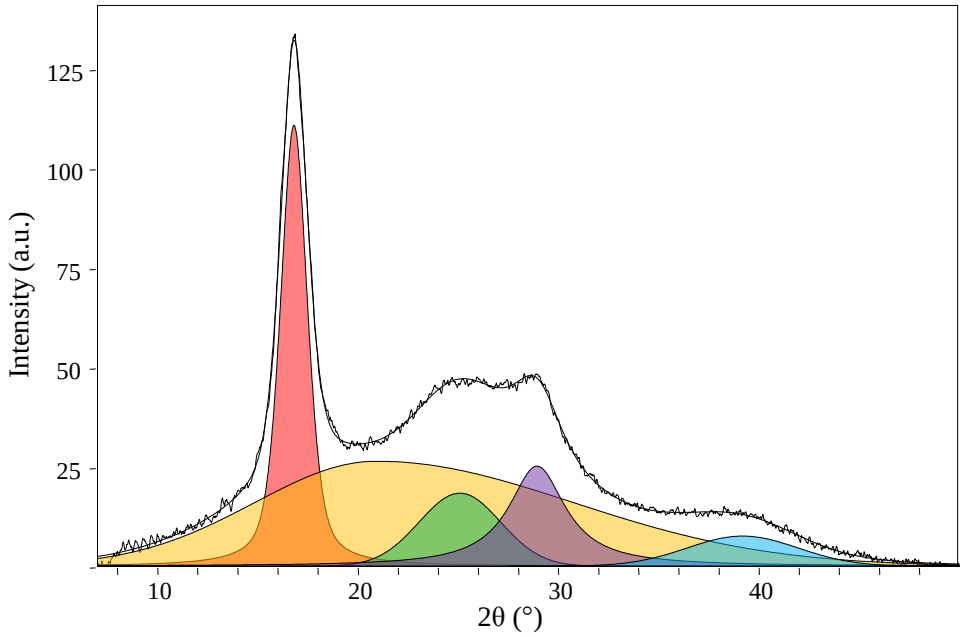

Figure C1. Integrated radial scan and deconvoluted profile for control PAN 250K fiber with DR 10 (Sample A2d). The different peaks are same as identified for PAN 100K fiber in Figure 25.

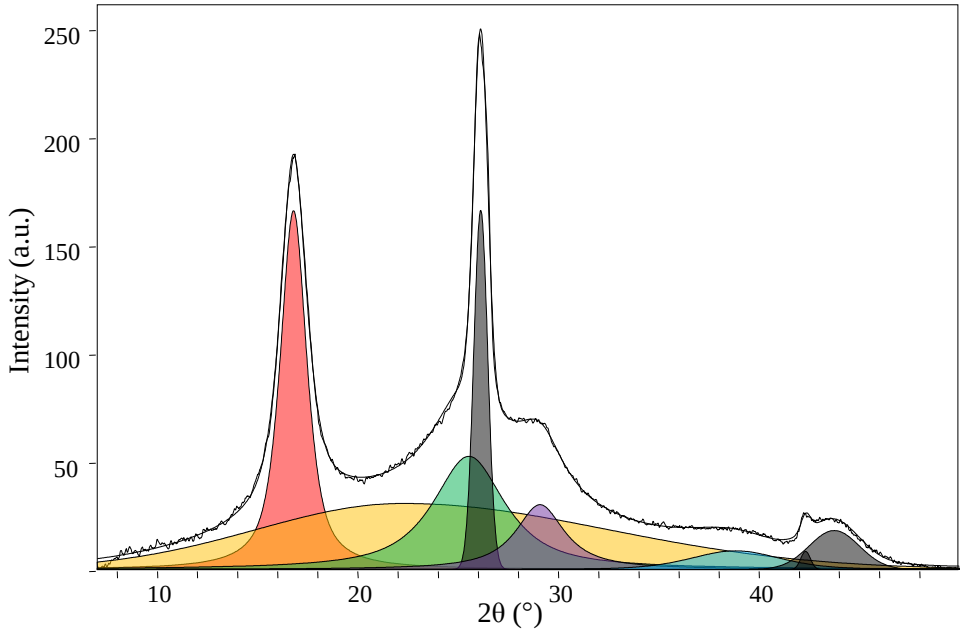

Figure C2. Integrated radial scan and deconvoluted profile for 20% CNF PAN 250K fiber with DR 10 (Sample D1b).

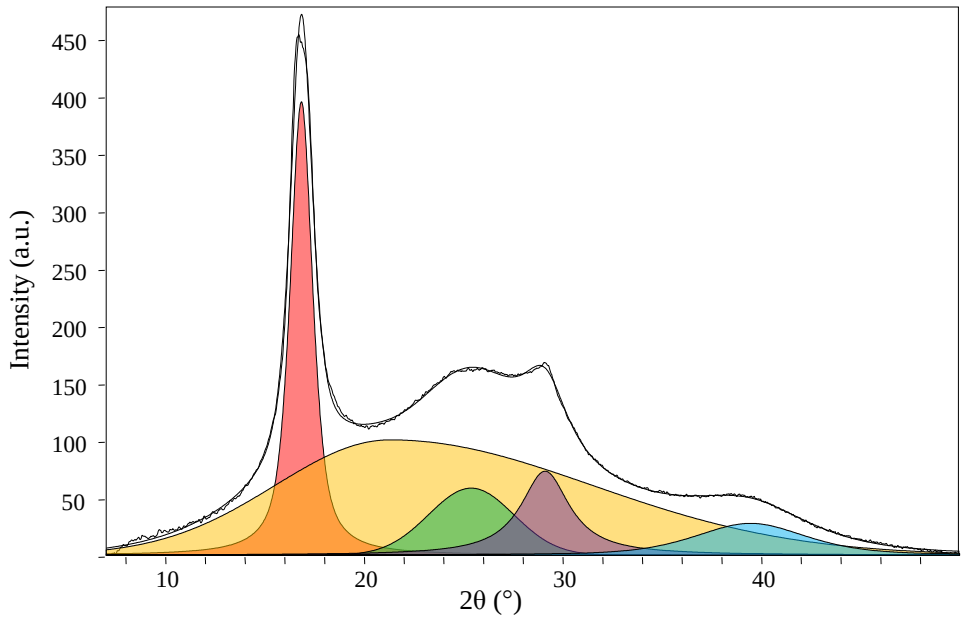

Figure C3. Integrated radial scan and deconvoluted profile for control PAN 700K fiber with DR 10 (Sample A3b). The different peaks are same as identified for PAN 100K fiber in Figure 25.

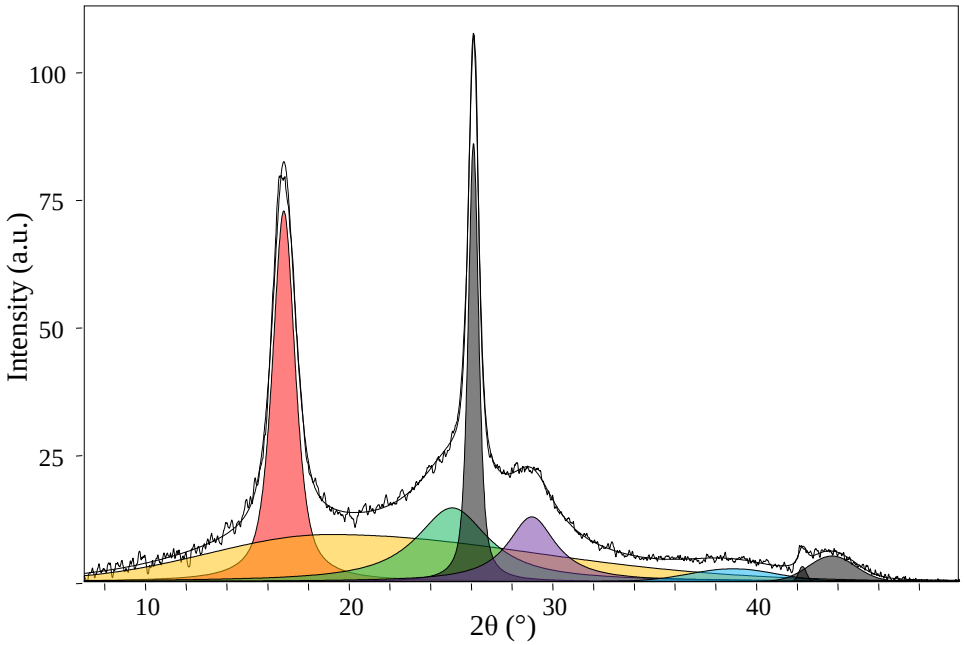

Figure C4. Integrated radial scan and deconvoluted profile for 20% CNF PAN 700K fiber with DR 10 (Sample D2b).

APPENDIX D

Raman Spectroscopy of Carbon Nanotubes

Upon interaction with matter, the incident light can be scattered elastically (i.e. no energy/frequency change after scattering) or inelastically (i.e. a finite change in energy/frequency after scattering). The elastic scattering is termed Rayleigh scattering and inelastic scattering is termed Raman scattering. Figure D1 shows both the scattering processes and the corresponding energy transitions between the ground and virtual vibrational states of the molecules. As a matter of fact, only a very small fraction of light is scattered inelastically hence Raman scattering is like detecting one photon out of a billion!

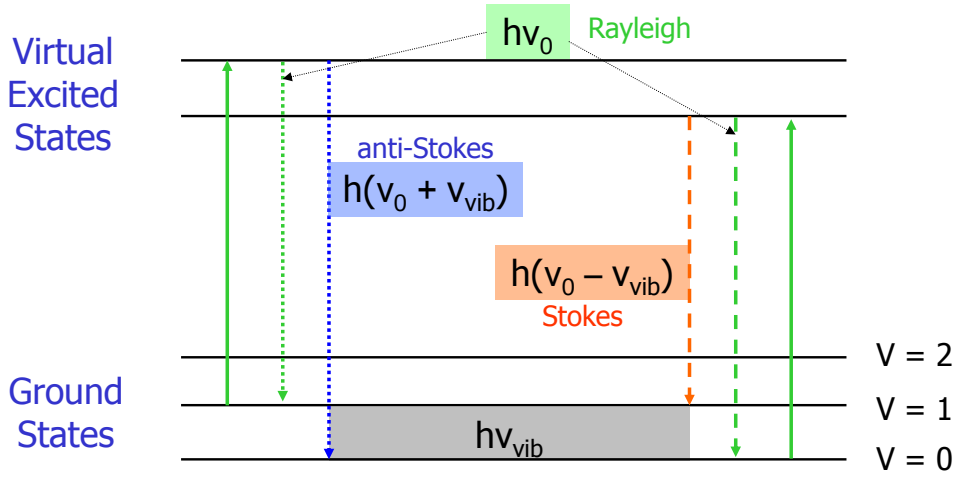

Figure D1. Elastic (Rayleigh) and inelastic (Raman) scattering of light. Solid green lines represent the incident light, dotted and dashed green lines represent elastically scattered light, dotted blue line represents inelastic scattering where the energy/frequency is increased after scattering (anti-Stokes shift), and dashed orange line represents elastic scattering where the energy/frequency is decreased after scattering (Stokes shift). (figure adapted from Campbell *et al.* [1])

A typical Raman spectrum of CNTs is shown in Figure D2. Details of the origin of various features that are seen in the spectrum are described elsewhere [2]. Figure D3 shows the G-band characteristics for semi-conducting and metallic type of SWNTs. Figure D4 shows the dependence of tangential vibrational energy on the tube diameter.

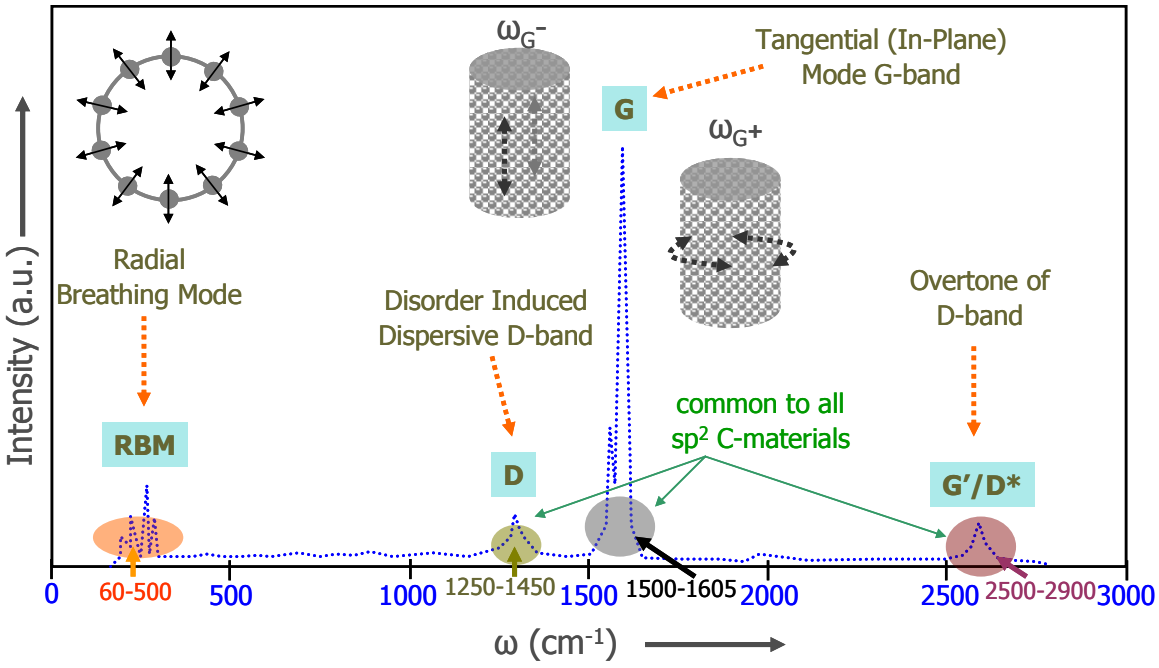

Figure D2. A typical Raman spectrum of CNTs (except that RBM is not observed in MWNTs). The four common bands that appear in a Raman spectrum of a SWNT are RBM-band, D-band, G-band, and D*-band. The appearance of D-band (between 1250 and 1450 cm^{-1}) in the spectrum originates from the presence of symmetry-breaking defects in any sp^2 hybridized C-material. (figure adapted from [2])

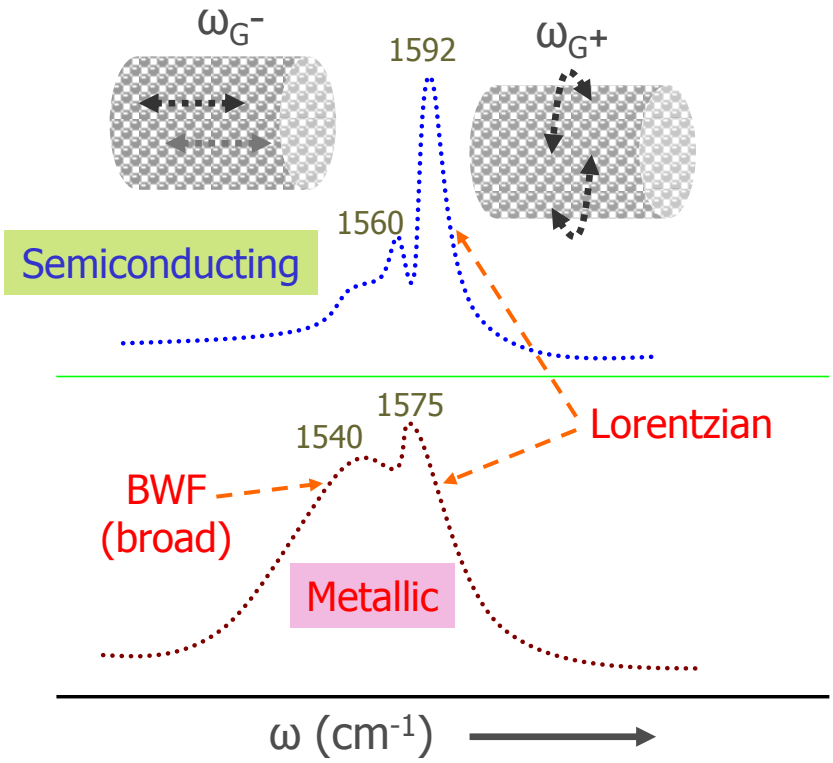

Figure D3. Longitudinal (lower energy) and circumferential (higher energy) type tangential vibrations corresponding to semi-conducting and metallic type of SWNTs. The peak coming from a metallic type of SWNT corresponding to longitudinal vibrations is generally broad and is described by Breit-Weigner-Fano (BWF) type of shape. (figure adapted from [2])

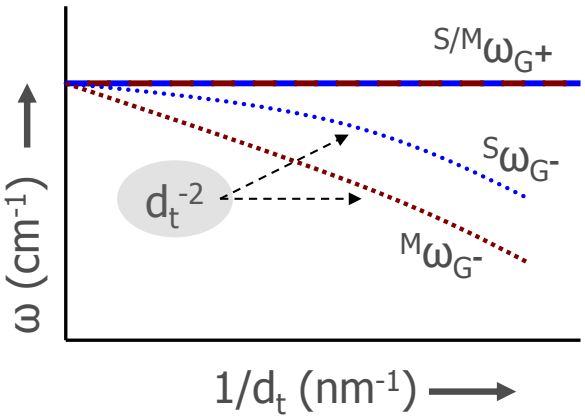

Figure D4. Dependence of circumferential and longitudinal vibrations energy on the diameter of the tubes. For both metallic and semi-conducting SWNT, the energy for circumferential vibration is independent of tube diameter, whereas the energy for longitudinal vibrations decreases by inverse square relationship with diameter. (figure adapted from [2])

The strength (intensity) of various Raman bands has been shown to be dependent on the orientation of CNTs. When the orientation is parallel to the polarization of light, then a strong spectrum is resulted. However, the features in Raman spectrum can be totally quenched if the CNTs are aligned perpendicular to the direction of polarization (of incident light) [3]. Such a kind of polarization effect is shown in Figure D5. Therefore, it is intuitive that alignment of nanotubes in different domains can be studied using polarized Raman spectroscopy.

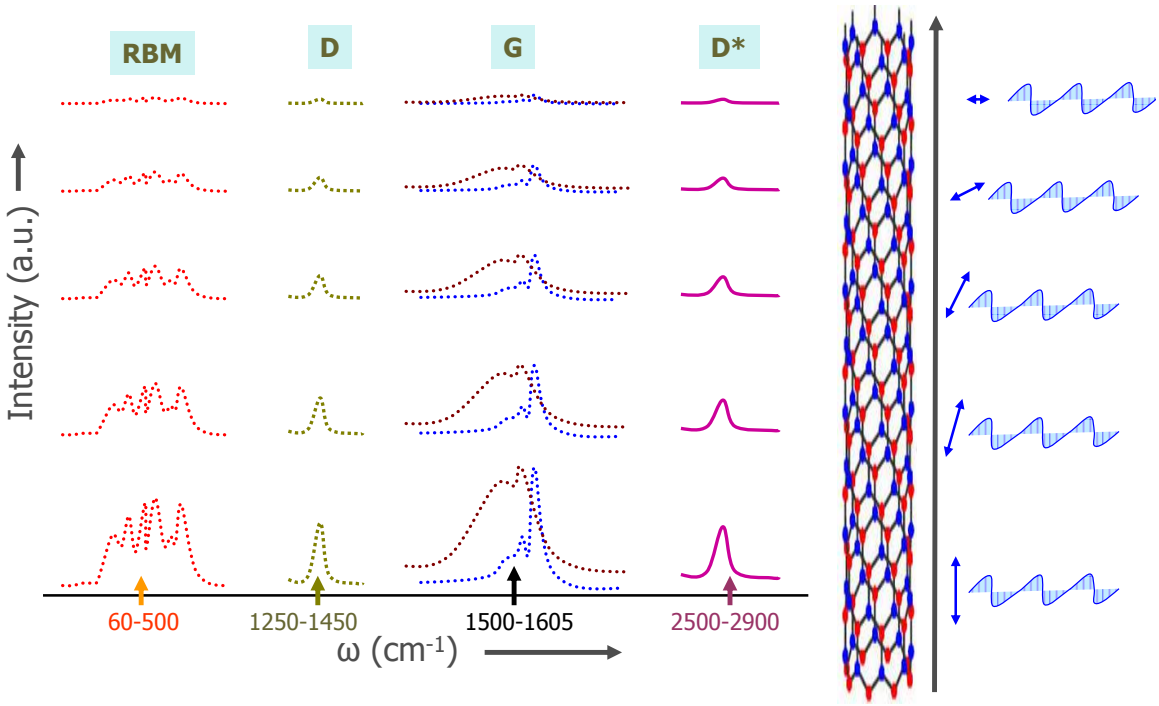

Figure D5. Effect of relative orientation of CNTs on the intensity of various bands of Raman spectrum. Maximum intensity is shown in the bottom-most spectrum when the nanotubes are aligned parallel to the plane of polarization of incident light. Minimum intensity (or total quenching) is shown in the top-most spectrum when the nanotubes alignment is perpendicular to the polarization of incident light. (figure adapted from [3])

References

1. Campbell D, Pethrick RA, and White JR. "Polymer Characterization: Physical Techniques", Stanley Thornes Ltd., Cheltenham, UK 2000:51.

2. Dresselhaus MS, Dresselhaus G, Jorio A, Souza AG, and Saito R. Carbon 2002;40(12):2043-2061.

3. Duesberg GS, Loa I, Burghard M, Syassen K, and Roth S. Physical Review Letters 2000;85(25):5436-5439.

APPENDIX E

DSC Thermograms of PEK-g-CNT Fibers

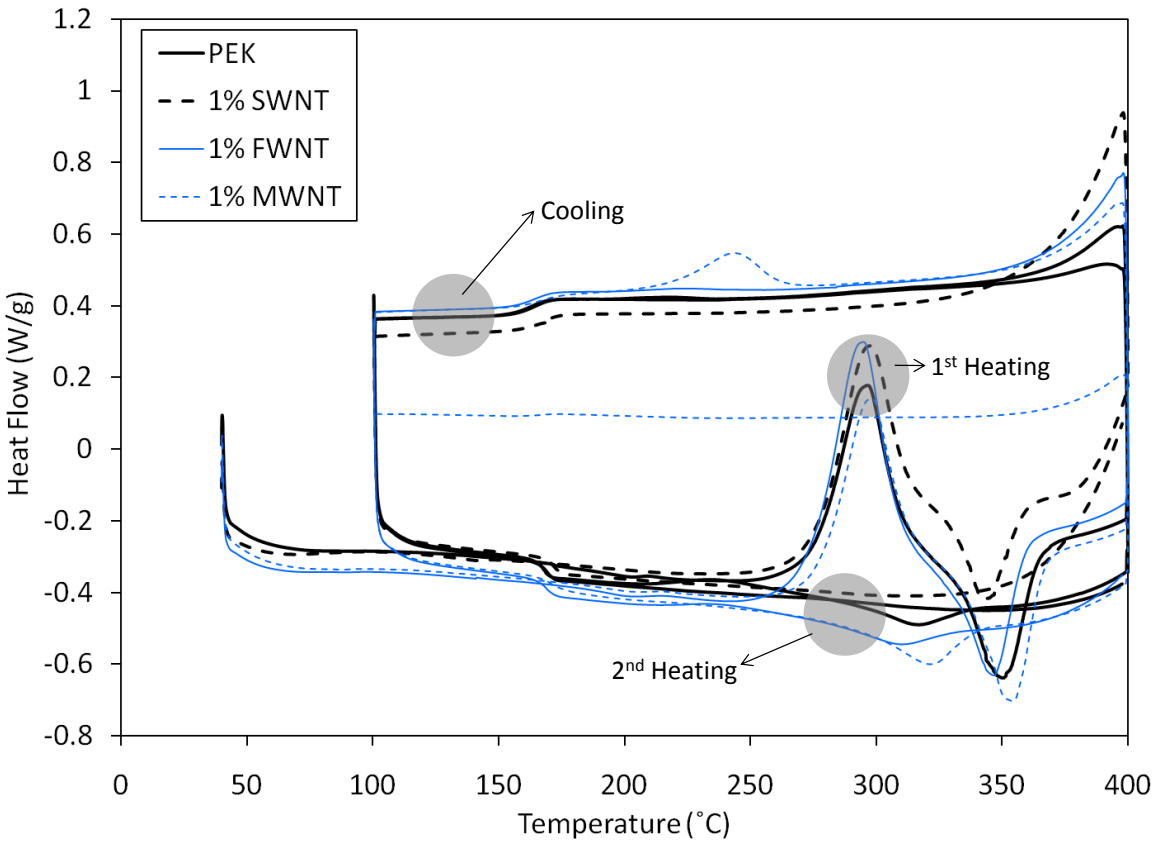

Figure E1. DSC thermograms (in air at a heating rate of 10 ˚C/min) of PEK (J2a), PEK-g-1%SWNT (K1a), PEK-g-1%FWNT (L2a), and PEK-g-1%MWNT (M1a) fibers (samples listed in Table 37) for heat-cool-heat cycles. A positive heat flow (upwards) represents exotherm and a negative heat flow (downwards) represents endotherm. All samples exhibited similar behavior except that MWNT containing fiber showed small exotherm for recrystallization during cooling.

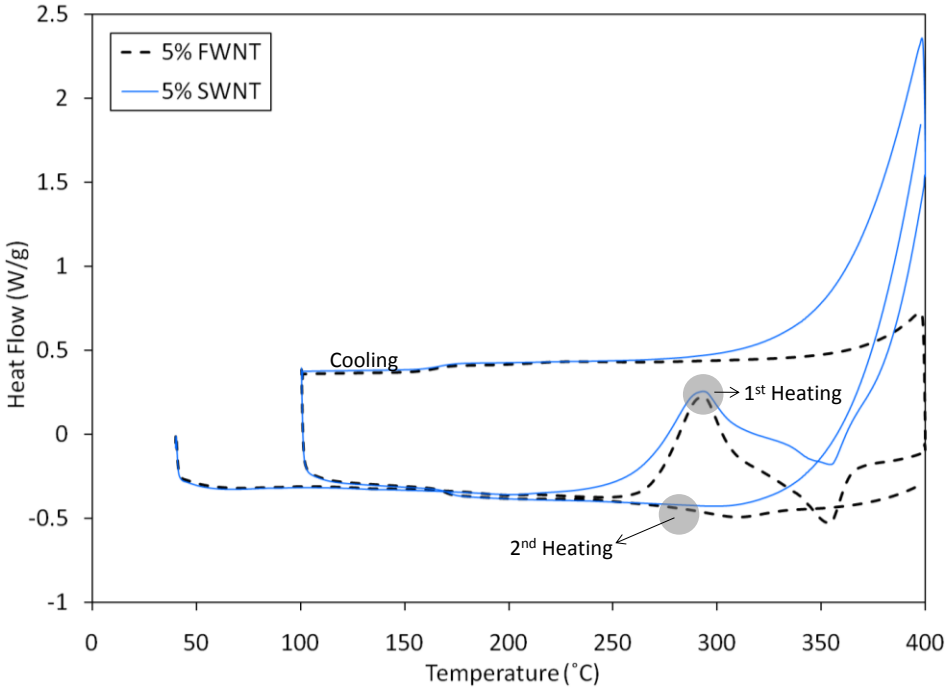

Figure E2. DSC thermograms (in air at a heating rate of 10 ˚C/min) of PEK-g-5%SWNT (K2a) and PEK-g-5%FWNT (L3a) fibers (samples listed in Table 37).

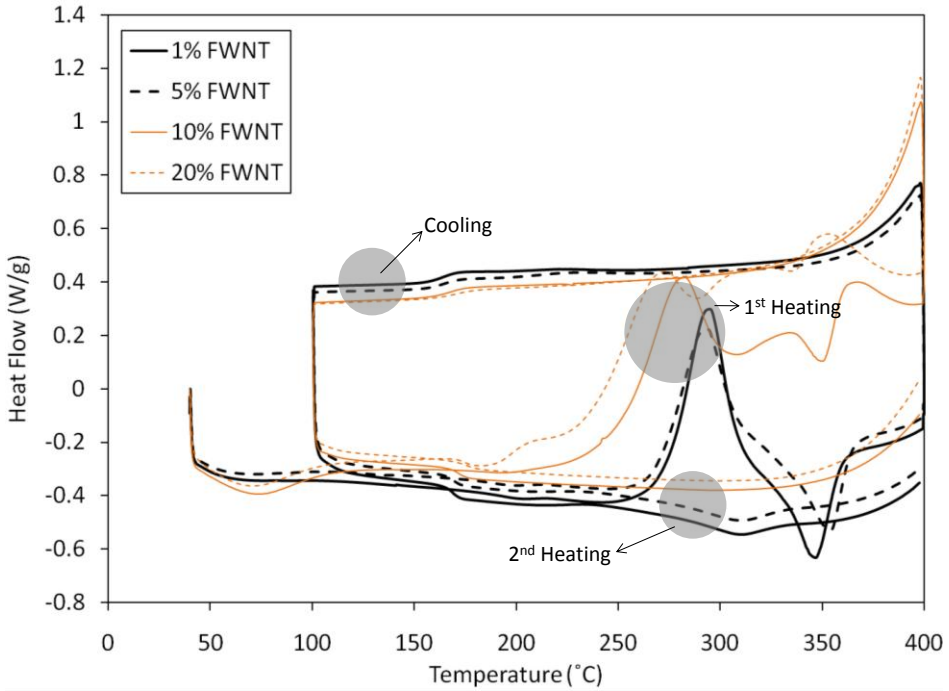

Figure E3. DSC thermograms (in air at a heating rate of 10 ˚C/min) of PEK with different concentrations of FWNTs. (1, 5, 10, and 20% correspond to samples L2a, L3a, L4a, and L5a in Table 37). The exotherm during first heating became larger and larger with increasing concentration of FWNTs.